Analysis of pollen development and pollen wall formation in *Arabidopsis thaliana* (L.) Heynh.

(シロイヌナズナにおける花粉発達と花粉表層形成に関する研究)

MOSTAFA AHMED ABOULELA MOHAMED

モスタファ アフメット アボレラ モハメッド

2017

Table of contents

Abbreviations

A. thaliana : *Arabidopsis thaliana*
ABRC : Arabidopsis biological resource center
aup : *aggregated unreleased pollen*
$BASTA^r$: BASTA resistance
BiFC : bimolecular fluorescence complementation
CLSM : confocal laser scanning microscopy
Cm^r : chloramphenicol resistance
COPII : coat protein complex II
DAPI : 4',6-diamidino-2-phenylindole
DD : destination donor
dnb : *dense-baculate exine*
DS : dual-site
DSB : dual-site binary
EMS : ethyl methanesulfonate
ER : endoplasmic reticulum
ERESs : endoplasmic reticulum exit sites
fcg : *faceless granulate pollen*
fcp : *faceless psilate pollen*
frx : *fragmented exine*
GC : guard cells
GMC : guard mother cells
GUS : β-glucuronidase
Hyg^r : hygromycin resistance
inp : *irregular aperture numbers and positions*
int : *interrupted tectum*
Km^r : kanamycin resistance
lpp : *less pollen-production*
lvc : *mild variable-size collapsed*
MAR : matrix attachment region
MS : Murashige and Skoog

mvc : *moderate variable-size collapsed*

nfa : *no flower anthesis*

O. sativa : *Oryza sativa*

P35S : 35S promoter

PCR : Polymerase chain reaction

Pnos : nopaline synthase promoter

qrtl : *quartet-like pollen*

R4DD : R4 destination donor

R4DS : R4 dual-site

R4DSB : R4 dual-site binary

rux : *rugulate exine*

SDD1 : *STOMATAL DENSITY AND DISTRIBUTION1*

SEM : scanning electron microscope

SNARE : soluble *N*-ethylmaleimide-sensitive factor attachment protein receptors

svc : *severe variable-size collapsed*

T-DNA : transfer-DNA

TEM : transmission electron microscope

TGN : *trans*-Golgi network

thp : *tetrahedral pollen*

tml : *thickened muri and irregular lumina*

Tnos : nopaline synthase terminator

Tunica^{r} : tunicamycin resistance

vdp : *variable-size defective pollen*

vrx : *verrucate exine*

WT : wild type

Chapter 1

Introduction

Arabidopsis thaliana (L.) Heynh.

Arabidopsis thaliana is a small annual weed belongs to the mustard family Cruciferae (Brassicaceae, Capparales). *A. thaliana* is a cosmopolitan species distributed widely in many areas of the world with preferential existence in central, western and northern Europe. It has also been found in a less extent in Australia, parts of North Africa, Turkey, Korea and Japan [1, 2]. *A. thaliana* resides a wide variety of habitats such as sandy or loamy soils, rocky slopes, river banks, cultivated ground, road sides, waste places, and open areas [3]. Many accessions and ecotypes of *A. thaliana* have been collected from wild populations growing throughout different ecological and geographical regions. From these accessions, Landsberg erecta (Ler), Columbia (Col-0) and Wassilewskija (Ws) are commonly used [1, 4]. Generally Columbia (Col-0) ecotype is considered as the reference genotype based on available data collected from many physiological, biochemical, sequencing and microarray studies [5]. Moreover, many research tools, such as sequence indexed T-DNA insertion lines, were developed in the Col-0 background [6].

For *A. thaliana* having numerous advantages, it was suggested earlier the suitability of *A. thaliana* as a model plant system by Laibach (1943) [7]. *A. thaliana* has been the subject of intense research in recent years and it is the most widely studied plant species with thousands of publications dealt with its biochemistry, molecular genetics, and development and evolution. The focused research on *Arabidopsis* should contribute to better understanding of diverse biological processes not only in plants but also in animal and other organisms hence many genes are conserved in all eukaryotes.

A. thaliana has been adopted as the organism of choice in many disciplines in plant science for a number of reasons, including its small size that reduce the required space for growth, short generation time (four to six weeks), small genome (only five chromosomes 2n =10), naturally self-fertilizing, the ease of large scale mutagenesis because of its small sized seeds [4, 8, 9]. One of the critical factors for developing *Arabidopsis* as a favoured organism was its amenability to the efficient Agrobacterium-mediated transformation [10]. In addition to availability of the comprehensive research resources such as the Arabidopsis entire genomic sequence [11], the large collection of gene disruptions usually by T-DNA or transposon insertions, and full genome microarrays which are already exist in several fundamental information databases such as TAIR (http://www.arabidopsis.org/) and Arabidopsis Biological Resource Center (ABRC).

Mutagenesis

A well-designed mutagenesis screen at high magnification is a powerful strategy to identify genes affecting many aspects of anther and pollen development. Mutagenesis can be accomplished by exposure to chemical mutagens such as ethyl methanesulfonate (EMS) [12], by treating with ionizing radiation such as fast neutron [13], and by insertional elements such as Agrobacterium-mediated T-DNA disruption [6] and transposon tagging [14]. EMS mutagenesis is the most widely used technique for mutagenesis with several advantages, including the ease of application, the high rate of mutagenicity with low mortality percentages, the random non-biased distribution of mutation in the genome, and the capability of generation novel mutant phenotypes [15, 16]. However, its utility has been limited by the time-consuming mapping required for identification of the mutation responsible-gene. The availability of high-throughput sequencing techniques such as next generation sequencing will help to overcome such limitation and will facilitate the identification of the mutation location. In contrast to EMS mutagenesis, insertional mutagenesis by T-DNA or transposons usually results in low mutation frequencies per plant; this necessitates screening of large numbers of plants to isolate a mutant [17]. Although the generation of large T-DNA insertion collections is time-consuming, the identification of the mutation location is streamlined and can be conducted easily using PCR-based methods [6, 18, 19]. However, through recent large-scale genetic screens using T-DNA insertional mutagenesis, it was found that a high number of T-DNA insertions were not directly linked to the genes causing the phenotypes observed. Instead, single to multiple nucleotide substitutions, deletions, or insertions were responsible for the phenotypes [20, 21].

EMS induces chemical modifications and alkylation of guanine (G) nucleotides resulting in base mispairing; G will pair with thymine (T) instead of cytosine (C) and during DNA repair, an amino acid change will occur (G-C pair will be replaced with A (adenine)-T pair) [12]. Occasionally, EMS induces replacement of G-C to C-G, G-C to T-A or A-T to G-C [22]. In EMS Mutagenesis of Arabidopsis, the M1 generation is allowed to self-fertilize and the mutants are screened and isolated among M2 generation. For the recessive mutants, a ratio of 7:1 (divided as 4:0 or 3:1) in an M2 population is expected, depending on the sector (+/+ or m/+) from which the seeds were collected (Fig. 1-1).

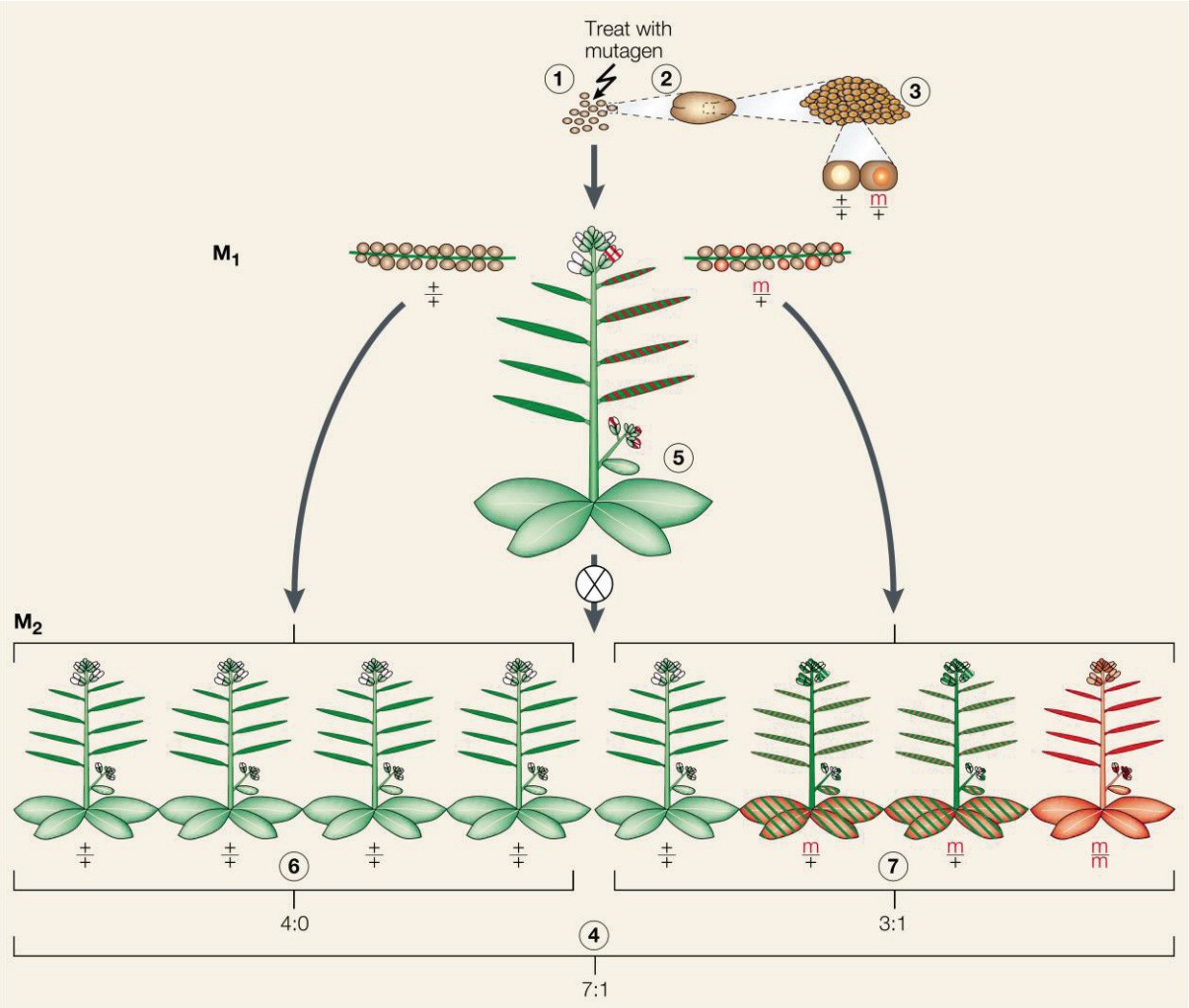

Fig. 1-1 Mutagenesis and segregation of recessive mutations. After treatment with a mutagen (e.g., EMS), seeds are collected and germinated to obtain M1 mutagenized plants. The M1 generation is allowed to self-fertilize and the resulting M2 generation are screened for mutants. In case of the recessive mutations, a ratio of 7:1 is expected in Arabidopsis. [Cited from Page D, Grossniklaus U. (2002) *Nat Rev Genet.* 3(2):124-36)]

Anther development and dehiscence

In *A. thaliana*, as in most flowering plant species, anther development initiates with the emergence of the stamen primordia in the meristemic floral third-whorl. In the stamen primordia, multiple cell-specification and differentiation events result in the formation of mature anther cell types (the epidermis, endothecium, middle layer, and tapetum) and generate the characteristic morphology of the anther and the filament [23]. In *A. thaliana*, the anther has a four-lobed structure inside which the pollen grains develop (Fig. 1-2). During development, the filament elongates, the anther enlarges and expands, the tapetum and middle layer degenerate, and the anther starts a dehiscence program [23].

Anther dehiscence (Fig. 1-2) is a multiple-step process that concludes with the release of pollen grains. At the beginning, expansion of the endothecium and accumulation of lignified materials in the walls of the endothecial cells occur [24]. Next, septum and stomium cells go through a cell degeneration program. The septum degenerates first, creating a bilocular anther. Then, a longitudinal weakness in the epidermis breaks at the stomium region of the anther wall. Finally, retraction of the anther wall leads to the full opening of the stomium and pollen release.

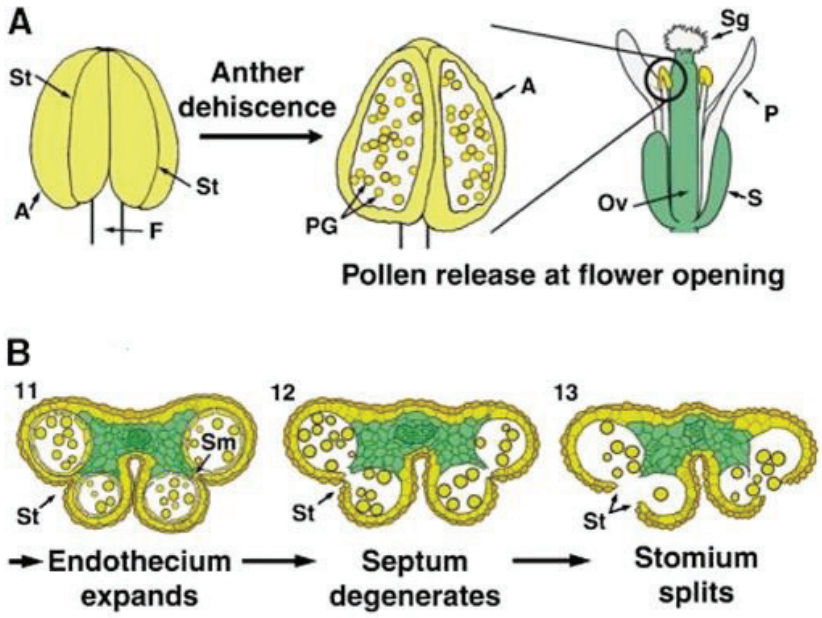

Fig. 1-2 Schematic representation for Anther structure and dehiscence. A An illustration of an anther showing its structure before and after dehiscence. **B** An illustration of transverse sections of anthers showing the key steps in dehiscence process. A, anther; F, filament; Ov, ovary; P, petal; PG, pollen grains; S, sepal; Sg, stigma; Sm, septum; St, stomium. [Adopted from Sanders PM *et al.* (2000) *The Plant Cell* 12 (7):1041-1061]

Pollen development in *Arabidopsis*

The development of the male gametophyte (pollen) (Fig. 1-3) is initiated in the anther when the callose-encased microsporocyte (diploid) goes through two meiotic divisions and cytokinesis to form haploid microspores arranged in a tetrad. The microspores are released from tetrads by the act of callase, an enzyme contributed by the tapetum. The microspores enlarged in size and produced a single large vacuole (vacuolated microspores). This large vacuole pushes the microspore nucleus to migrate to the periphery of the cell. Subsequently, each microspore undergoes the first mitosis (pollen mitosis I) to generate bicellular pollen with a generative cell (small) surrounded by a large vegetative cell. Then, the small generative cell undergoes a second mitosis (pollen mitosis II) to complete the last stage of pollen development and generates two sperm cells [25]. Upon pollination, the two sperm cells migrate to the ovule in the female gametophyte to form the zygote.

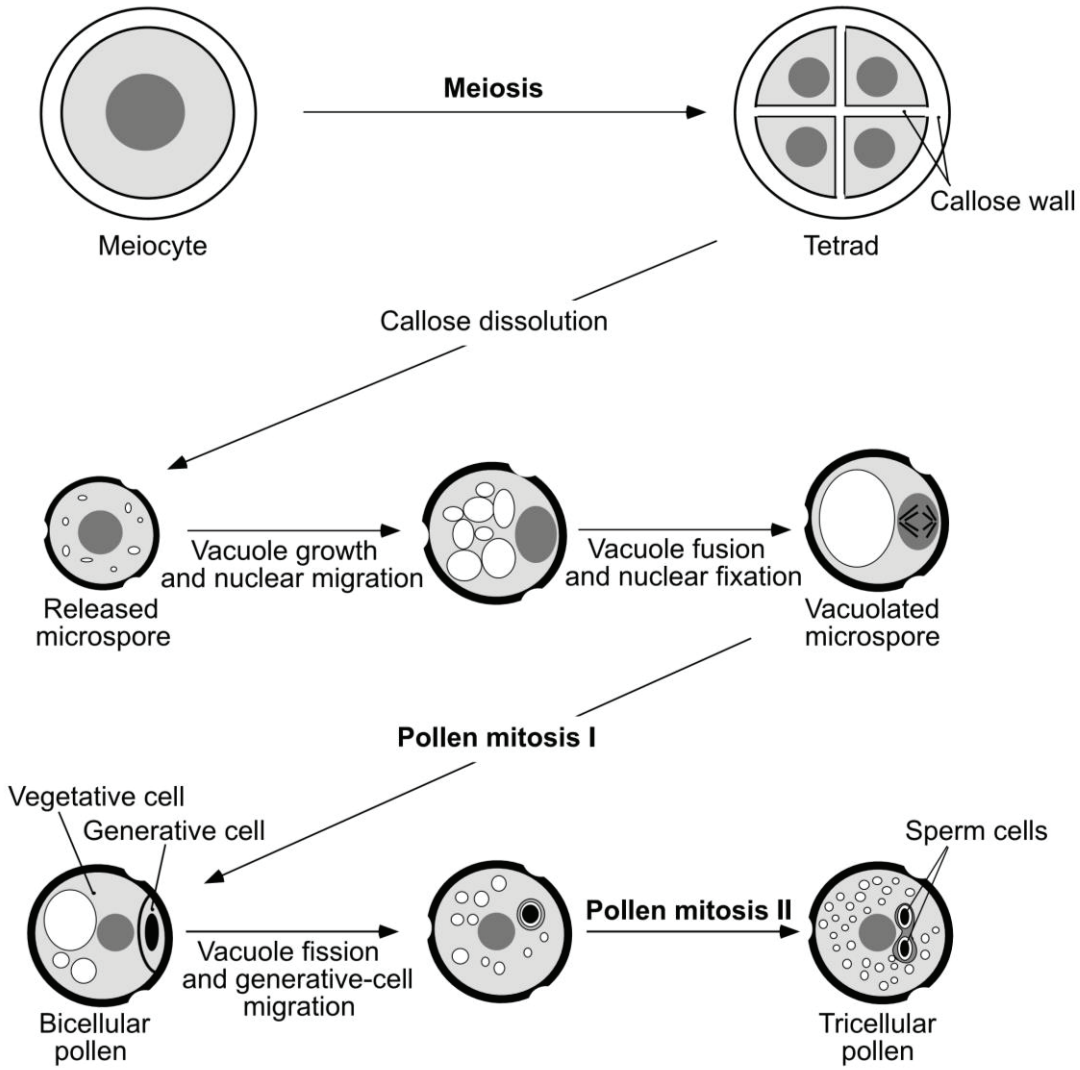

Fig. 1-3 Pollen development in *A. thaliana* showing major division events. The meiocyte divides meiotically to produce four identical microspores. Microspores undergo two mitotic divisions to produce mature pollen having two sperm cells and one vegetative cell. [Cited from Twell D, et al. (1998) *Trends in Plant Science* 3 (8):305-310]

Pollen wall stratification and pollen wall development in *Arabidopsis*

The *Arabidopsis* pollen wall has an architecturally-complex structure (Fig. 1-4) consists of two layers; the inner pectocellulosic-based intine and the outer sporopollenin-based exine. The exine wall covers the entire pollen surface except for apertures (the places specified for tube germination) where it is absent or greatly reduced. The exine wall is divided into two layers; inner nexine and outer sexine, which is further, subdivided into two structures the bacula and the tectum [26]. Both structures are responsible for the characteristic and taxon-specific architecture of the exine which is reticulate in *A. thaliana*. The nexine is composed of two layers, an outer nexine I, which represents the base for the bacula, and an inner nexine II [27, 28]. Additionally, in dry stigma species including *A. thaliana*, a lipid-based pollen coat is formed as a third wall component covering the exine layer.

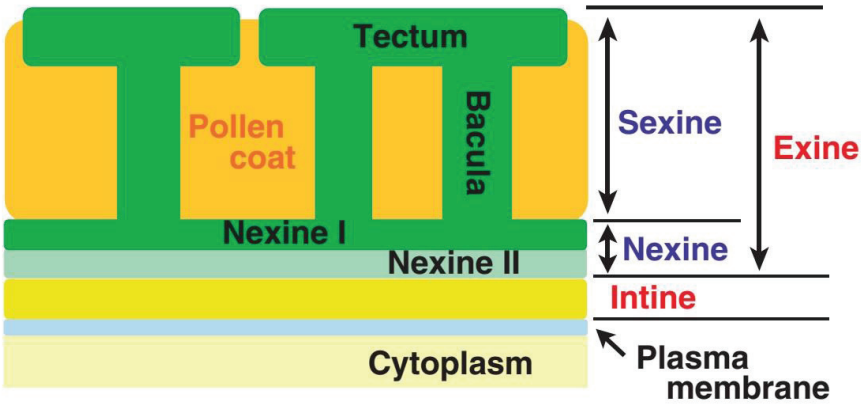

Fig. 1-4 Pollen wall structure in *A. thaliana*. Mature *Arabidopsis* pollen grains have a typical wall consisting of inner intine (surrounding the plasma membrane) and outer exine. Exine comprises two layers, sexine (subdivided into tectum and bacula) and nexine (subdivided into nexine I and nexine II). At the last stage, pollen coat materials fill the spaces in between the bacula. [Cited from Suzuki T, *et al.* (2008) *Plant and Cell Physiology* 49(10): p. 1465-1477]

Pollen wall development requires contributions from both the sporophytic and gametophytic tissues. For example, the exine and pollen coat constitutes are derived from the surrounding sporophytic tapetum cells while the intine is manufactured by microspore itself (gametophytic origin) [26]. Pollen wall development (Fig. 1-5) can be summarized as follows. At the tetrad stage, the four haploid microspores are surrounded by the callose wall. Next, primexine layer (matrix of polysaccharides) is deposited between the microspore plasma membrane and the callose wall. Then, the microspore plasma membrane develops an undulated structure. The undulated membrane represents anchoring sites of sporopollenin forming what known probacula and protecta [28-30]. After the microspores release (uninucleate stage), high sporopollenin fluxes from the tapetum are deposited on the microspore surface forming the bacula and the tectum. By the end of this stage, a pectocellulosic intine is developed around the microspores [31]. The bacula, tectum, and intine continue in development in the bicellular stage. At the tricellular stage, pollen coat materials (also known as tryphine or pollen kitt) fill the space in between bacula giving the pollen wall its characteristic structure.

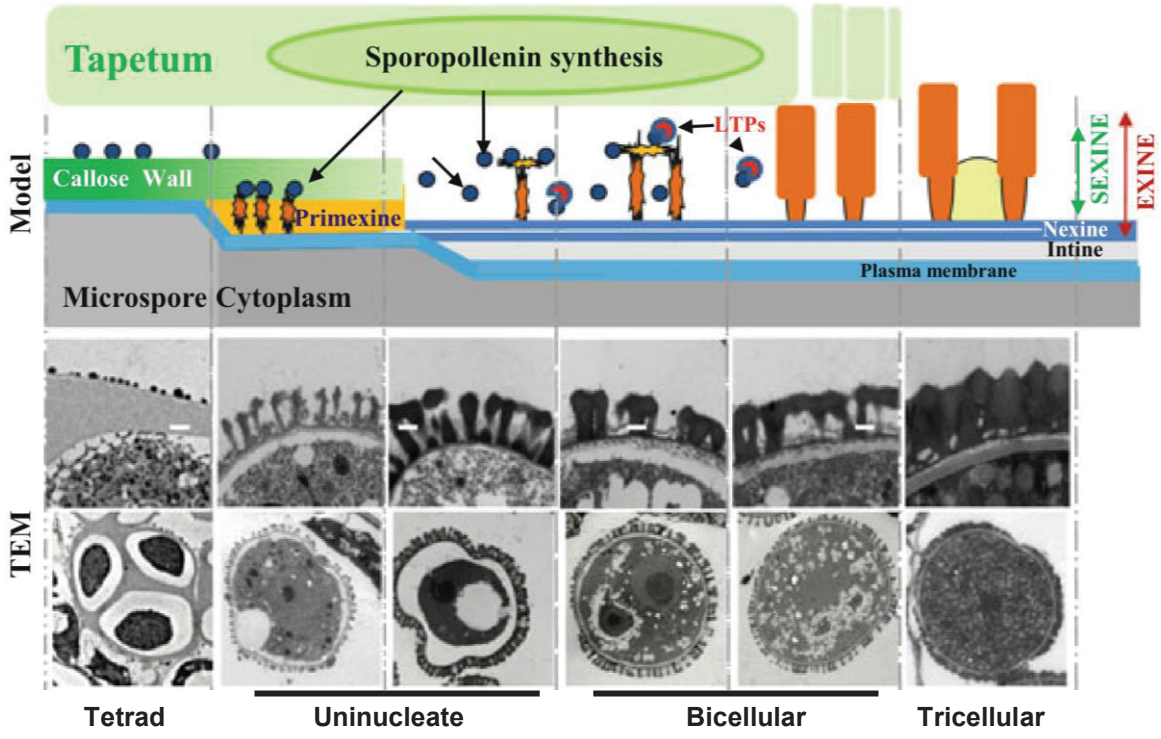

Fig. 1-5 Current model of Arabidopsis pollen wall development. Sporopollenin synthesis occurs in the tapetum and starts to accumulate around the callose wall surrounding the microspores at the tetrad stage. Primexine deposition, probacula, and protectum polymerization occur subsequently on the microspores. At the uninucleate stage, true bacula and tectum are formed and the intine layer is initiated. At the bicellular stage, bacula and tectum become longer and intine layer continues in growing. At the tricellular stage, pollen coat (tryphine) is deposited as a final pollen wall component. [Adopted from Zhang D, *et al.* (2016) *Subcell Biochem.* 86:315-37]

Coat protein complex II (COPII) assembly and vesicle formation

The COPII vesicle formation includes the sequential recruitment of five proteins, Sar1, SEC23/24, and SEC13/31 [32, 33] (Fig. 1-6). The COPII vesicle formation initiated by recruitment of Sar1 to the ER membrane via the activity of its guanine nucleotide exchange factor SEC12 [34, 35]. Activated Sar1 further recruits the SEC23/24 complex (the "inner" coat) by the direct interaction with SEC23 and forms a ‘‘prebudding complex’’ [36]. The prebudding complex captures the cargo protein and initiates vesicle curvature. Then, SEC13/31 heterotetramer (the "outer" coat) is finally recruited onto the prebudding complex, by the interaction between SEC31 and SEC23, to complete the vesicle formation process by promoting further membrane curvature and fission [37, 38].

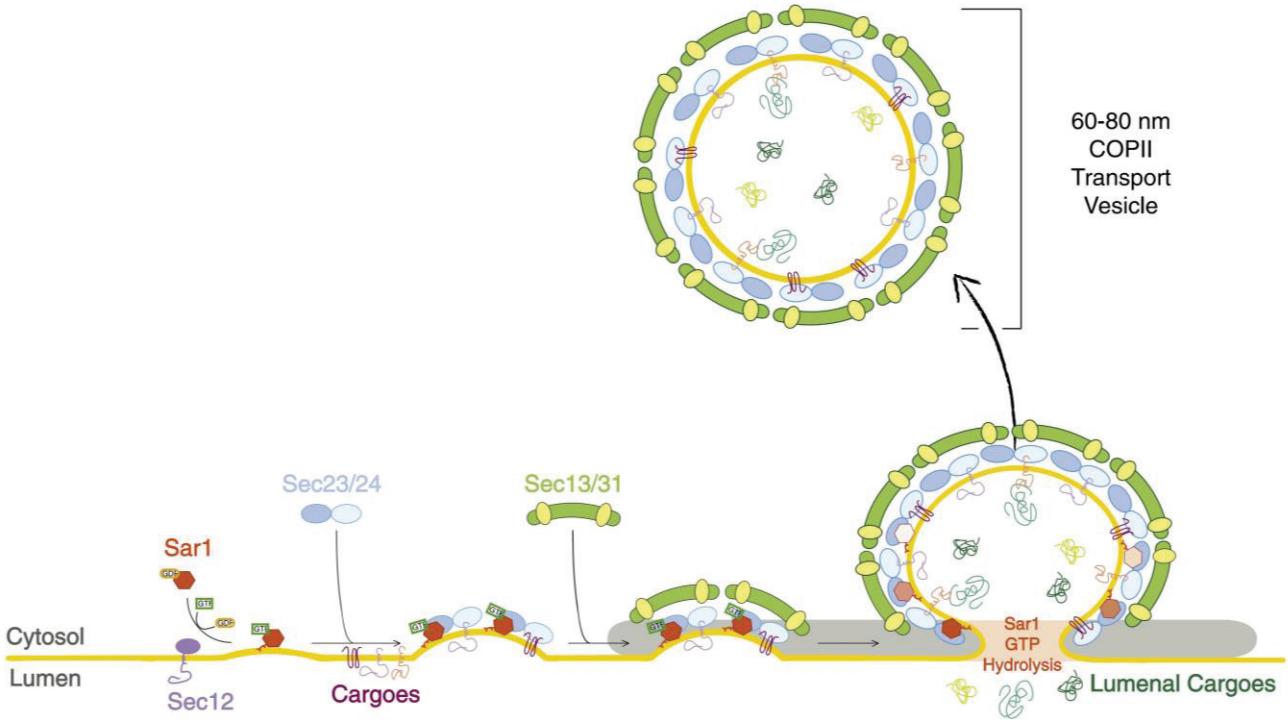

Fig. 1-6 Schematic representation of COPII vesicle formation. The process of vesicle formation is accomplished by the sequential recruitment of five proteins, Sar1, SEC23/24, and SEC13/31. Lipids and proteins assembled in the detached COPII vesicles are shuttled from the ER to the Golgi. [Adopted from D'Arcangelo JG, *et al.* (2013) *Biochimica et Biophysica Acta - Molecular Cell Research* 1833 (11):2464-2472]

Gateway cloning technology

In recent years, the Gateway cloning system [39] has proved to be extremely useful for cloning of foreign genes in high-throughput investigations and for constructing large cDNA libraries. Gateway cloning technology is based on a specific site recombination technology in which the integration and excision of λ phage DNA into and from *E.coli* genome occurs through two reversible clonase reactions named BP reaction and LR reaction [39, 40]. The *att*P sites of the λ phage are recombined with the *att*B site of the *E.coli* in a BP reaction to obtain the integrated λ phage genome flanked by *att*L and *att*R. This reaction is catalyzed by the BP Clonase enzyme mix. In the LR reaction, the phage DNA is excised from the bacterial chromosome by recombination between *att*L and *att*R sites. The LR reaction is catalyzed by the LR clonase enzyme mix (Fig. 1-7).

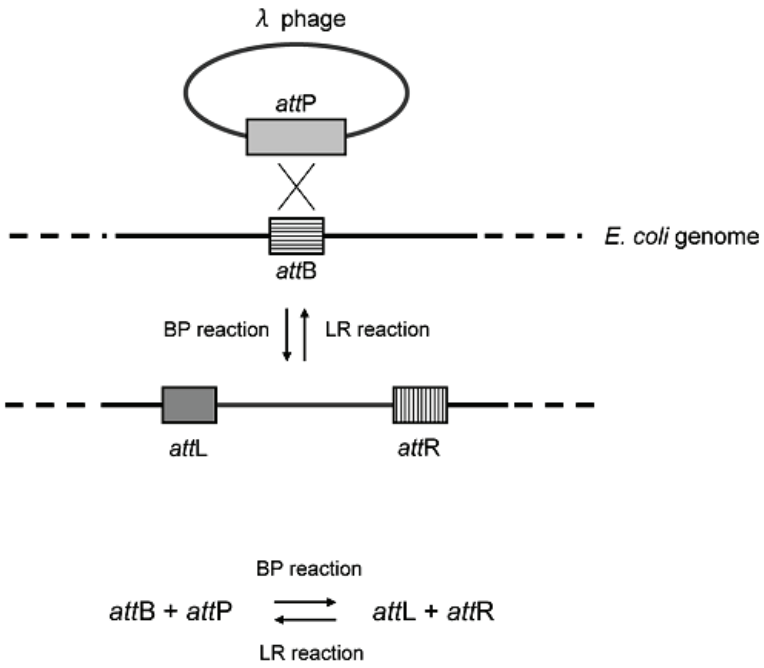

Fig. 1-7 Outline of Gateway cloning showing the site specific recombination and the BP and LR reactions. [Cited from (Nakagawa T, *et al.* (2009) *Plant biotechnol.* 26**:** 275-284]

The adaptable and streamlined Gateway cloning methodology represents a significant advance over the classical restriction approach and overcomes many of its limitations especially the speed and ease with which recombinant constructs can be generated and the convenience of transfer of these constructs between vectors regardless of their sequence. Increasing the number of *att* recombination signals to six different high specified ones [41] has enabled the simultaneous subcloning of multiple DNA fragments in a single LR reaction and has made the recombination of multiple expression elements such as promoters, ORFs, terminators, and reporters much easier [42]. The MultiRound Gateway technology [43, 44] and the Gateway recycling cloning system [45] have been developed as alternative applications of multiple *att* sites. These systems enable the step-by-step repetitive cloning of an expression cassette into a vector to make a multi-gene binary construct using multiple rounds of LR reactions. Although these are outstanding methods to clone an unlimited number of expression cassettes into a binary vector, they are limited by the laborious traditional cloning steps required to prepare a promoter:ORF construct on a prerequisite donor vector.

Stomatal development

The development of stomata is an ideal model for examining intra- and intercellular signaling networks, cell polarity, and cell-type differentiation [46]. In *A. thaliana*, the development of stomata goes through a specialized cell lineage (Fig. 1-8), which consists of the following five cell types; meristemoid mother cells (MMCs), meristemoids, stomatal lineage ground cells (SLGCs), guard mother cells (GMCs) and guard cells (GCs) [47-49]. All stomata are developed through at least one asymmetric and one symmetric division. A protodermal cell turns to MMCs which, in turn, goes an asymmetric division to produce a small triangular meristemoid cell and a larger cell called SLGC. Meristemoid divisions are called amplifying divisions and can occur up to three times or four times [50, 51]. The meristemoid cells lose their stem cell activity and develop into GMCs (characterized by their oval shape). A GMC divides once symmetrically to yield two GCs.

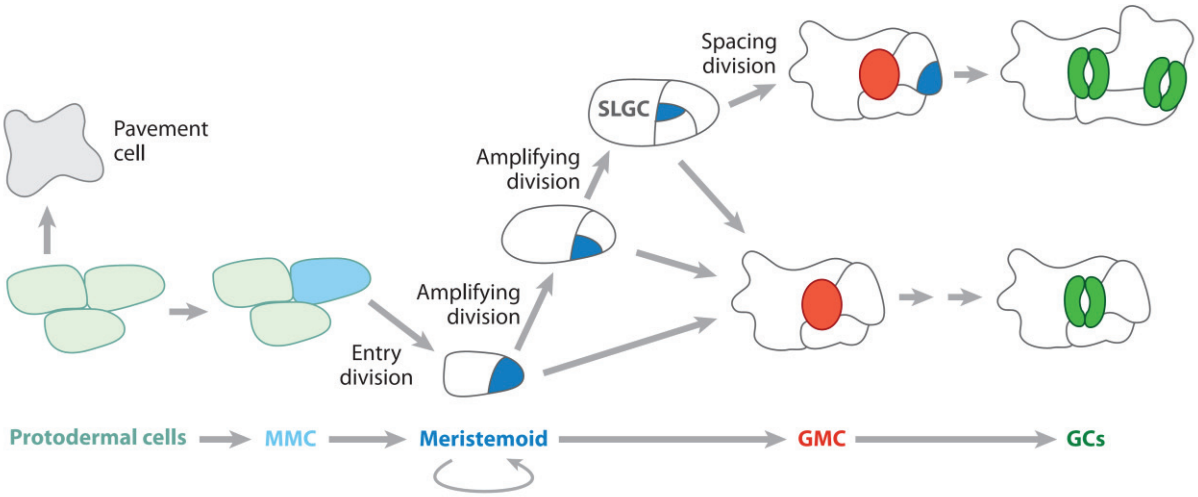

Fig. 1-8 The stomatal lineage development in *Arabidopsis*. A protodermal cell differentiates to a meristemoid mother cell (MMC) or a further pavement cell. MMCs divide asymmetrically to form a meristemoidal cell and a stomatal-lineage ground cell (SLGC). The meristemoidal cell undergo a limited number of asymmetric amplifying divisions and eventually a guard mother cell (GMC) is formed. The GMC divides once symmetrically to two identical guard cells (GCs). [Cited from Pillitteri L and Torii K (2012) *Annual review of plant biology* 63, 591-614]

Chapter 2

Screening for mutations affecting anther/pollen development and pollen wall formation in *Arabidopsis thaliana*

Introduction

Production of functional pollen for successful plant reproduction requires proper pollen development and exine formation. Pollen development and exine formation are complex biological processes that go through several well-documented stages [24, 26, 52, 53]. In the first stage of pollen development, the callose-encased microsporocyte goes through two meiotic divisions and cytokinesis to form haploid microspores arranged in a tetrad. At this stage, while tetrads are still encased by the callose wall, the primexine layer is formed between the microspore plasma membrane and the callose wall. Then, the microspore plasma membrane develops an undulated structure. On the top of these undulations, which represent anchoring sites of sporopollenin, probacula and protecta emerge [28-30]. After the microspores release, high sporopollenin fluxes from the tapetum are deposited on the microspore surface forming the characteristic exine structure. By the end of this stage, a pectocellulosic intine is developed around the microspores [31]. Subsequently, each microspore undergoes the first mitosis to generate bicellular pollen with a small generative cell surrounded by a large vegetative cell. Then, the small generative cell undergoes a second mitosis to complete the last stage of pollen development and generates two sperm cells [25]. Defects in any of these stages will affect the pollen development and exine formation processes and may result in male sterility phenotypes.

Recent genetic and molecular studies have revealed a large number of genes that are involved in pollen development and exine formation, including *ACYL COENZYME A SYNTHETASE5* (*ACOS5*) [54], *CALLOSE SYNTHASE5* (*CALS5*) [55], *MALE STERILE2* (*MS2*) [56], two CYTOCHROME P450s (CYP703A2 and CYP704B1) [57, 58], *MYB103* [59], *ATAXIA-TELANGIECTASIA MUTATED* (*ATATM*) [60], *QUARTET* (*QRT1* to *QRT3*) [61-63], *RUPTURED POLLEN GRAIN1* (*RPG1*) [64], *FACELESS POLLEN1* (*FLP1*) [65], *DEFECTIVE IN EXINE PATTERNING1* (*DEX1*) [66], *NO EXINE FORMATION1* (*NEF1*) [67], *TWO-IN-ONE* (*TIO*) [68, 69], *STUD/TETRASPORE* (*STD/TES*) [70-72], *POLYKETIDE SYNTHASES A* (*PKSA*) and *PKSB* [73, 74], *TETRAKETIDE α-PYRONE REDUCTASE1* (*TKPR1*) and *TKPR2* [75, 76], *ABCG26* [77, 78], KNS4 [79], *SPONGY2* (*SPG2*), and *UNEVEN PATTERN OF EXINE1* (*UPEX1*) [80].

Using ethyl methanesulfonate (EMS) for mutagenesis has many advantages over other mutagenesis strategies. EMS mutagenesis is simple, resulting in mutations distributed randomly across the genome, and most importantly it has the capability for generating novel

mutant phenotypes [15, 16]. However, it requires a time-consuming mapping to identify the mutation responsible-gene; thus, utilizing the advanced mapping techniques such as next generation sequencing will help to overcome such limitation. In contrast, although it is hypothesized that identification of the mutation location of insertional mutagenesis is streamlined and can be conducted easily using PCR-based methods, recent large-scale genetic screens using T-DNA insertional mutagenesis revealed a high number of T-DNA insertions that not directly linked to the genes causing the observed phenotypes. Instead, point mutations, small and large deletions, and genomic rearrangements were responsible for the phenotype [20, 21].

Identifying of *Arabidopsis* mutants with phenotypic changes in anther and pollen have provided powerful tools to improve our understanding of the function of genes controlling anther and pollen development [28, 81, 82]. In order to understand the whole molecular mechanism of specific processes in anther and pollen development such as pollen wall formation, sporopollenin synthesis, polymerization, and transport, and exine patterning, there is still a need to saturate the anther- and pollen-defective mutants. Previously, many mutant screenings were performed to isolate and identify genes affecting anther and pollen development. However, most of the previous screens were mainly focusing on the male sterile or semi-sterile mutants [24, 83-90], neglecting a large number of mutants with severe to mild defects that developed with normal fertility. Only a few screens have used fertility-independent approaches to isolate the mutants [21, 27].

In the present study, the author aimed to screen and identify genes disrupting anther/pollen development and exine formation. The screening strategy described here utilized a similar approach with that used by Suzuki *et al* [27] but with a larger scale (five folds). The screen was performed at a high-magnification level using scanning electron microscope (SEM) among large populations of EMS-mutagenized M2 plants (~ 10,000 plants). A total of 101 mutant plants were recovered and classified according to their phenotypic characters into three classes with multiple subclasses and types. Twenty-three mutations (some of them were found to be allelic) were successfully mapped to specific regions at the chromosomes of the Arabidopsis genome. This screen provides an additional resource for plant researchers to analyze functions of genes involved in pollen development and exine patterning processes and will help unrevealing previously unknown players in such processes.

Materials and methods

Plant materials and growth condition

EMS-mutagenized seeds (M2 population) of *Arabidopsis thaliana* Col-0 background were obtained from (Lehle Seeds, TX, USA). *A. thaliana* of the ecotype Landsberg erecta (Ler) was used for crossing and mapping. *A. thaliana* of the ecotype Columbia (Col-0) was used as the wild type for comparison with mutants. The seeds were surface-sterilized and vernalized on a Murashige and Skoog agar plates at 4°C for 3 days. The seeds were grown at 22°C under 24 h continuous lights for two weeks before transplanting to Jiffy-7 (Jiffy Preforma Production K. K, Yokohama, Japan) and continued to grow under the same conditions.

Screening for mutants

M2 populations belong to three different parental groups of EMS-mutagenized *Arabidopsis thaliana* Col-0 background were used for the mutant screening. To isolate the mutant plants, stamens of at least three flowers from different branches of each M2 plant were examined using SEM. The stamens were loaded on the double adhesive carbon tape and examined directly without coating with a TM3000 miniscope (Hitachi High-Tech). The mutants with fine pollen-surface structures were further examined after coating with platinum/palladium using an S-4800 field emission SEM (Hitachi High-Tech, Tokyo, Japan) as previously described [91].

DNA extraction for mapping

DNAs were extracted from flowers (100 mg) of the mutant plants using the DNeasy Mini Kit (Qiagen, Tokyo Japan). The concentration and the quality of the obtained DNA were analyzed by a Nanodrop-1000 spectrophotometer (Thermo Fisher Scientific, Kanagawa, Japan) and a Qubit 2.0 Fluorometer (Thermo Fisher Scientific).

Molecular mapping

Each mutant plant was crossed with *A. thaliana* Ler ecotype. Mutant plants were surgically emasculated and used as a female for cross-pollinating with pollen of *A. thaliana* Ler ecotype. F1 plants were screened for existence or absence of the mutant phenotype to determine the nature of the mutation (recessive or dominant). About 400 F2 plants for each

mutant were examined by SEM to isolate an adequate number of plants with the mutant phenotype for mapping analyses (about 100 if the mutation was recessive). Map positions were determined by bulked-segregant analysis. Adequate amount of extracted genomic DNA (5 μg) was prepared for sequencing using the NextSeq 500 High Output v2 kit (75 cycles) and samples were sequenced using the Illumina NextSeq 500.

Alexander's staining

Anthers of the largest closed bud (anther stage 12) were placed in Alexander's staining solution as described previously [91] and were examined by an All-in-One Fluorescent Microscope BZ-X710 (KEYENCE, Osaka, Japan).

4',6-diamidino-2-phenylindole (DAPI) staining

Pollen of fully opened flowers were placed in a drop of DAPI staining solution following [91] and fluorescence signals were detected using a BX51 fluorescence microscope (Olympus, Tokyo, Japan) equipped with a UV mirror unit.

Results and discussion

Screening framework

To better understand the molecular mechanisms of pollen development and exine formation, the author performed a high-magnification level screen for *Arabidopsis* mutants among large populations (~ 10,000 plants) of EMS-mutagenized M2 plants. Several mutant lines (101) with various abnormalities were isolated and classified into three main classes: flower-level, anther-level, and pollen-level mutants as described below. All mutants were examined for their male functionality by the Alexander's test. Next, the mutants were crossed with the wild type Ler (different ecotype) and the resulting F1 plants were screened to score the dominancy of alleles. Approximately 400 F2 plants were screened for the defective phenotypes and DNAs of selected plants were extracted for mapping. All the identified mutations were recessive with F1 plants exhibiting the wild-type phenotype and F2 plants segregating 3:1 (normal: defective) (data not shown). Due to the large number of isolated mutants, it was difficult to perform cross-based allelism tests in a round-robin fashion; instead, the author used bulked-segregant analysis by next generation sequencing to identify the mutants. Twenty-two of the 23 mutants chosen for further analyses were mapped by this method, whereas the *quartet-like* mutant was identified by capillary sequencing. These

include five mutants from the *defective reticulate-exine* subclass, five mutants from the *faceless pollen* subclass, five mutants from the *variable-size collapsed pollen* subclass, four mutants from the *irregular aperture-numbers and positions* subclass, and three mutants from the *aggregated unreleased pollen* subclass.

Class 1: Flower-level mutants

This class includes flowers missing one or more of the floral parts (sepal, petal, stamen, and pistil) and also flowers with defective floral parts. This class is divided into four subclasses as follows.

1A: no stamen-thick pistil (one line)

This subclass is represented only by one mutant in which the stamens and petals were missing (Fig. 2-1a, b). The plants were sterile (Fig. 2-1c, d). According to the ABC model of flower development, class B genes affect petals and stamens [92, 93]. The function of class B genes allows the differentiation of petals from sepals in the secondary whorl, as well as the differentiation of the stamen from the carpel on the tertiary whorl. In *A. thaliana*, the type-B function mainly comes from two genes, *APETALA3* (*AP3*) and *PISTILLATA* (*PI*), both of which are MADS-box genes [94, 95]. A mutation of one of these genes causes conversion of petals into sepals and of stamens into carpeloid structures and to date all *AP3 and PI* identified alleles show defects of the secondary and tertiary whorls. Strong mutations of *AP3 and PI* cause complete missing of stamen and petals whereas weak ones result in partial missing of these structures [96].

1B: irregular female gametophyte (two lines)

Two mutants were isolated with defects in female-gametophyte development. This subclass is represented by two types:

1B.1. branched style and stigma (one line)

In this type, the female gametophyte was ended with abnormal branched style and stigma and styles contained only a few papillae (Fig. 2-2a-d) resulting in non-functional pistils. The anthers and pollen grains were visibly indistinguishable from those of the wild type (Fig. 2-2e, f). No seeds were obtained of this mutant and the plant was sterile (Fig. 2-2g, h).

1B.2. open ovary and uncovered ovules (*ouo*; two lines)

One significant character of the angiosperms is developing multiple layers around seeds known as the seed coat. Through the seed development, ovules are always covered and enclosed in ovary, but in these two mutants the ovary was open and ovules were naked (Fig. 2-3a, b, e, f), resulting in immature seeds and consequently sterile plants. The anthers and pollen grains were comparable to those of the wild type (Fig. 2-3c, d, g, h).

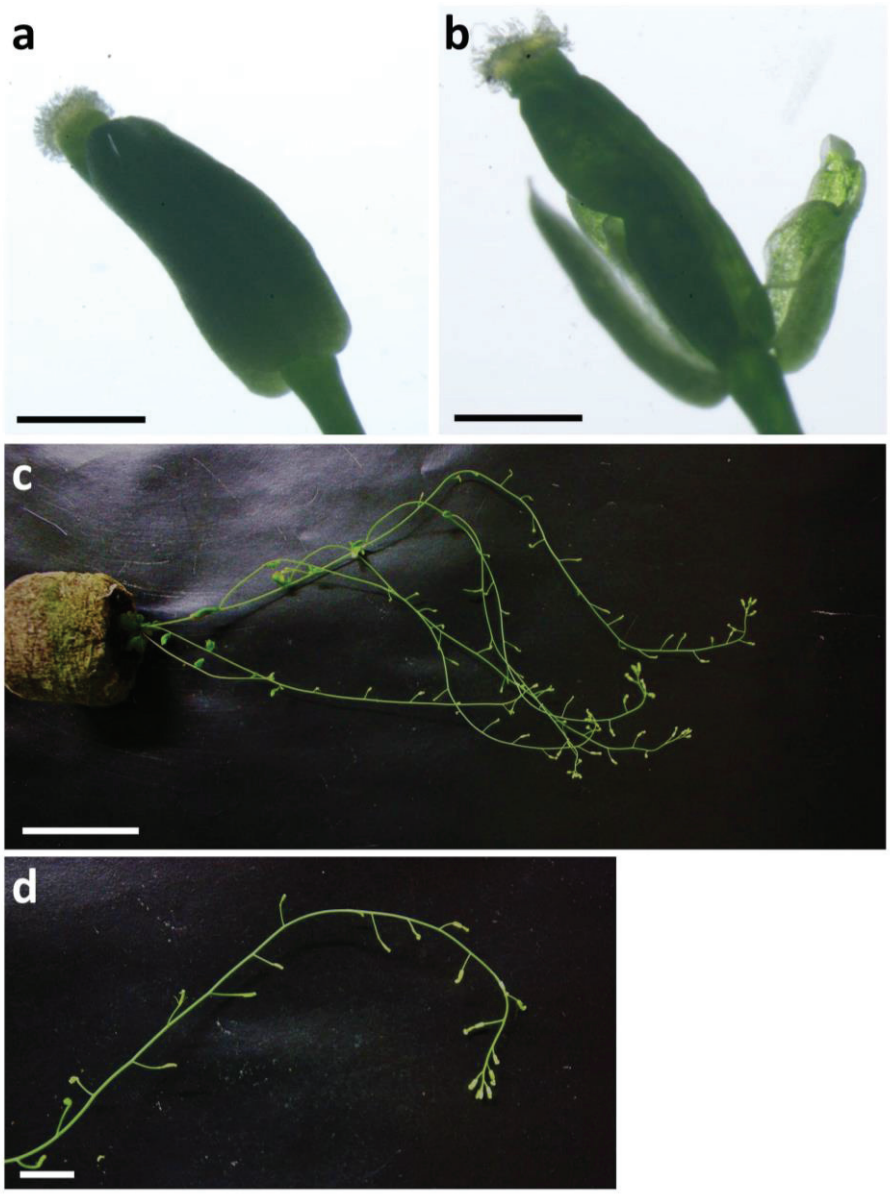

Fig. 2-1 Sterility and absence of petals and stamens in the *no stamen-thick pistil* mutant. a, b A mature flower closed (a) and dissected (b) showing the absence of petals and stamens and the more thickness in the female gametophyte. **c** A two-month-old plant with male-sterility. **d** A flowering branch with no elongated siliques. This mutant was isolated among populations of the parental group 35. Scale bars = 1 mm in (a, b), 5 cm in (c), and 1 cm in (d).

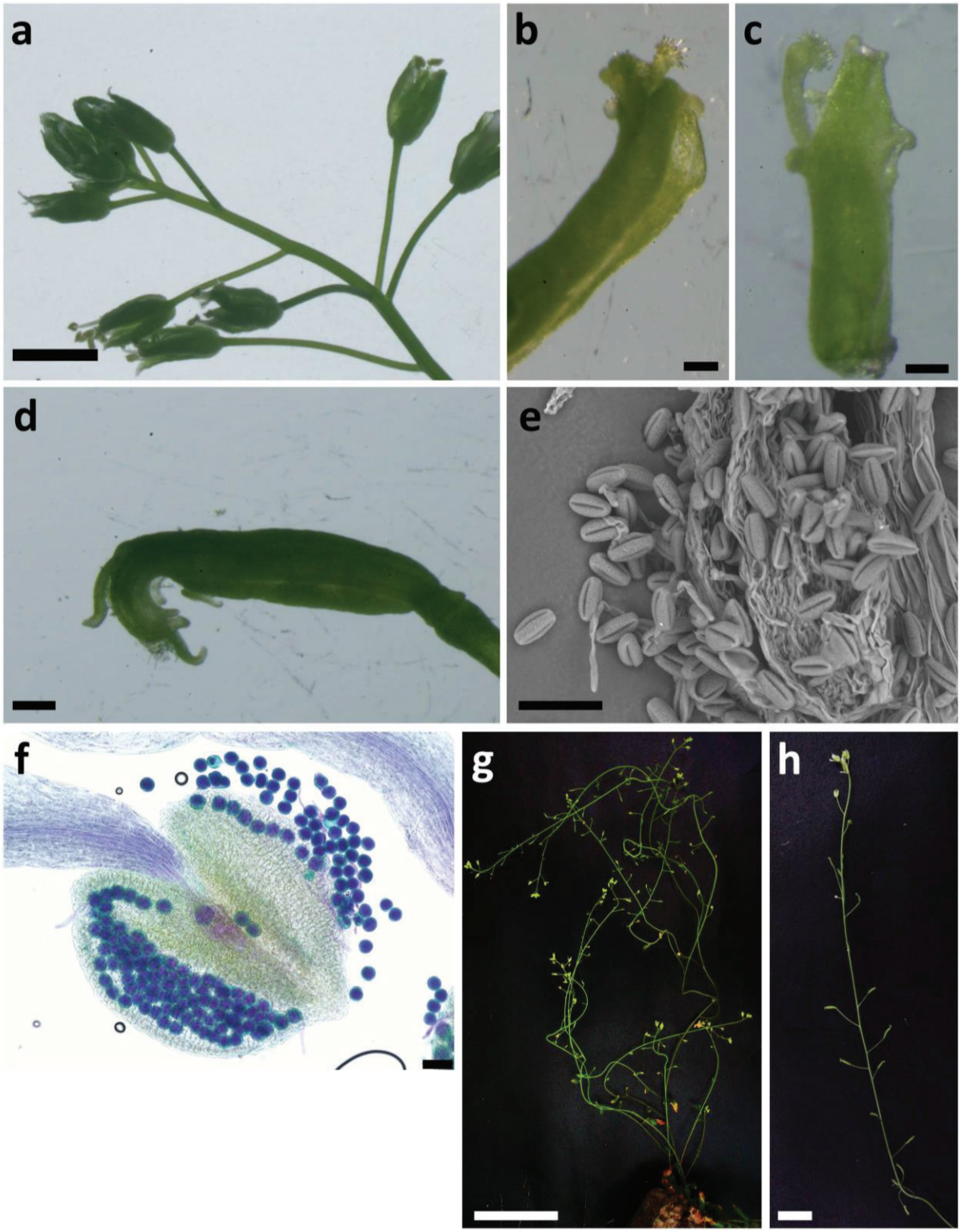

Fig. 2-2 Abnormal female gametophytes in the *branched style and stigma* mutant. a-d Stereomicroscope micrographs showing the defects in the female gametophytes. A part of a flowering branch (a) and pistils of flowers (b-d) showing the abnormal branched style and stigma. **e** A SEM micrograph of an anther full with normal pollen. **f** Alexander's staining of an anther indicating the normal viability of the pollen of this mutant type. **g** A two-month-old plant with female-sterility. **h** A flowering branch showing the female-sterility. This mutant was isolated among populations of the parental group 35. Scale bars = 2 mm in (a), 200 µm in (b-d), 50 µm in (e, f), 5 cm in (g), and 1 cm in (h).

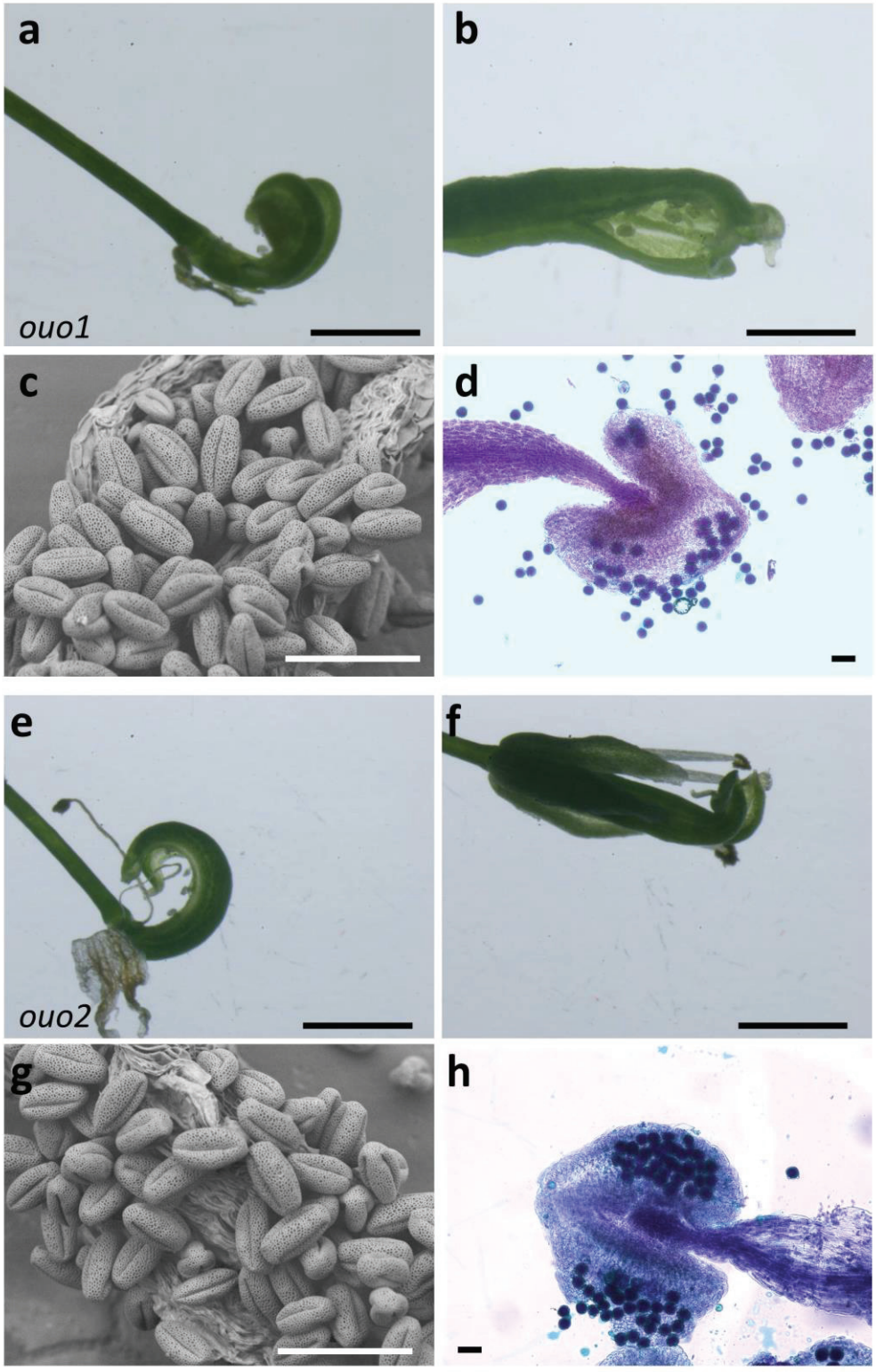

Fig. 2-3 Abnormal female gametophytes in the *open ovary and uncovered ovules* mutants. a, b, e, f Stereomicroscope micrographs showing the defects in the female gametophytes. Note that the naked ovules and unfused carpels. **c, g** SEM micrographs of *ouo*-mutants anthers showing normal pollen development. **d, h** Alexander's staining of *ouo*-mutants anthers indicating the normal viability of the pollen of these mutants. **a-d** *ouo1* and **e-h** *ouo2*. *ouo1* and *ouo2* were isolated among populations of the parental group 35. Scale bars = 1 mm in (a, b, e, f), and 50 µm in (c, d, g, h).

1C: connected sepals (one line)

This subclass is represented only by a single mutant in which the sepals were fused together through their margins (Fig. 2-4a) preventing the pollination process and consequently lead to a semi-sterile plant. Occasionally, short siliques with a few seeds were seen (arrows in Fig. 2-4e). The anthers and pollen grains were viable and functional as revealed by SEM and Alexander's staining (Fig. 2-4c, d). A similar phenotype was previously identified in a male-sterile based screen [24].

1D: no flower anthesis (one line)

In wild-type plants, flowers are naturally opened at stage 13 of development (Fig. 2-5f) and pollen released from the anthers and pollination process occurs at this stage, however, anthesis of flowers in *no flower anthesis (nfa)* mutant plant did not occurred. The author compared the flowers of wild type and the mutant at stages 13-15 and showed that no flower anthesis and no pollination were observed (Fig. 2-5f) and consequently resulted in a sterile plant (Fig. 2-5a-c). However, in rare cases, a few flowers could self-pollinate and resulted in a semi-sterile plant (Fig. 2-5b). The few developed seeds were larger is size than those of the wild type (Fig. 2-5g, h). The anthers and pollen grains were normal in the mutant plant (Fig. 2-5d, e). A mutant with a similar phenotype was identified in a previous study and named *megaintegumenta* (*mnt*) to indicate the increased size of the integuments of seeds, when produced. The *mnt* mutant plants had a low degree of self-fertility consistent with the failure of floral bud opening. The self-sterility was reasoned to the mechanical failure of pollination [97]. None of the mutants of this class were analyzed further.

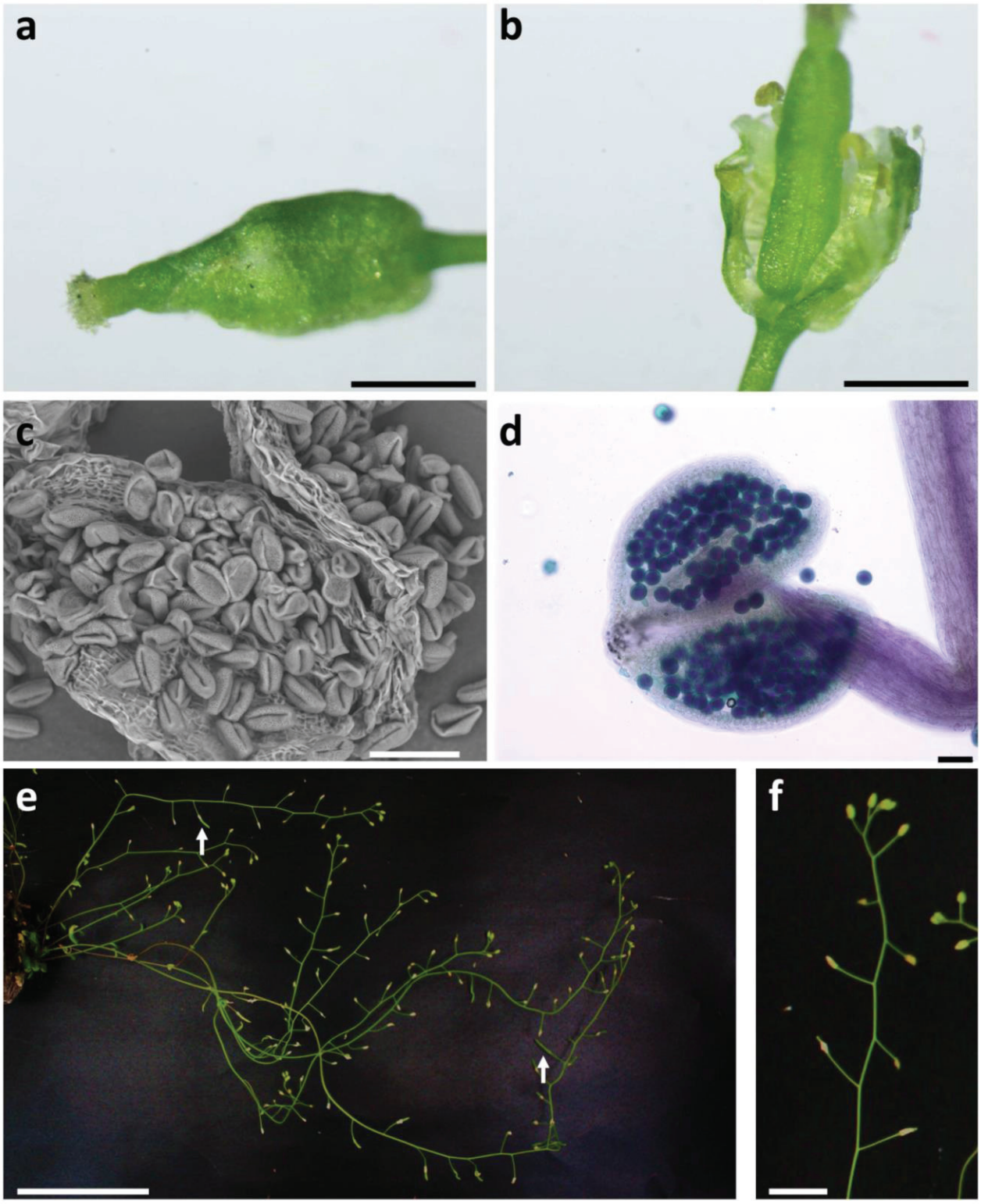

Fig. 2-4 Phenotypic characterization of the *connected sepals* mutant. a, b Stereomicroscope micrographs showing the fusion of sepals. **c** A SEM micrograph of an anther showing numerous of functional pollen grains. **d** Alexander's staining of an anther full with normal viable pollen grains. **e** A two-month-old plant with a semi-sterility phenotype. Arrows indicate the few elongated siliques occasionally developed. **f** A flowering branch showing the semi-sterility phenotype. This mutant was isolated among populations of the parental group 34. Scale bars = 1 mm in (a, b), 50 μm in (c, d), 5 cm in (e), and 1 cm in (f).

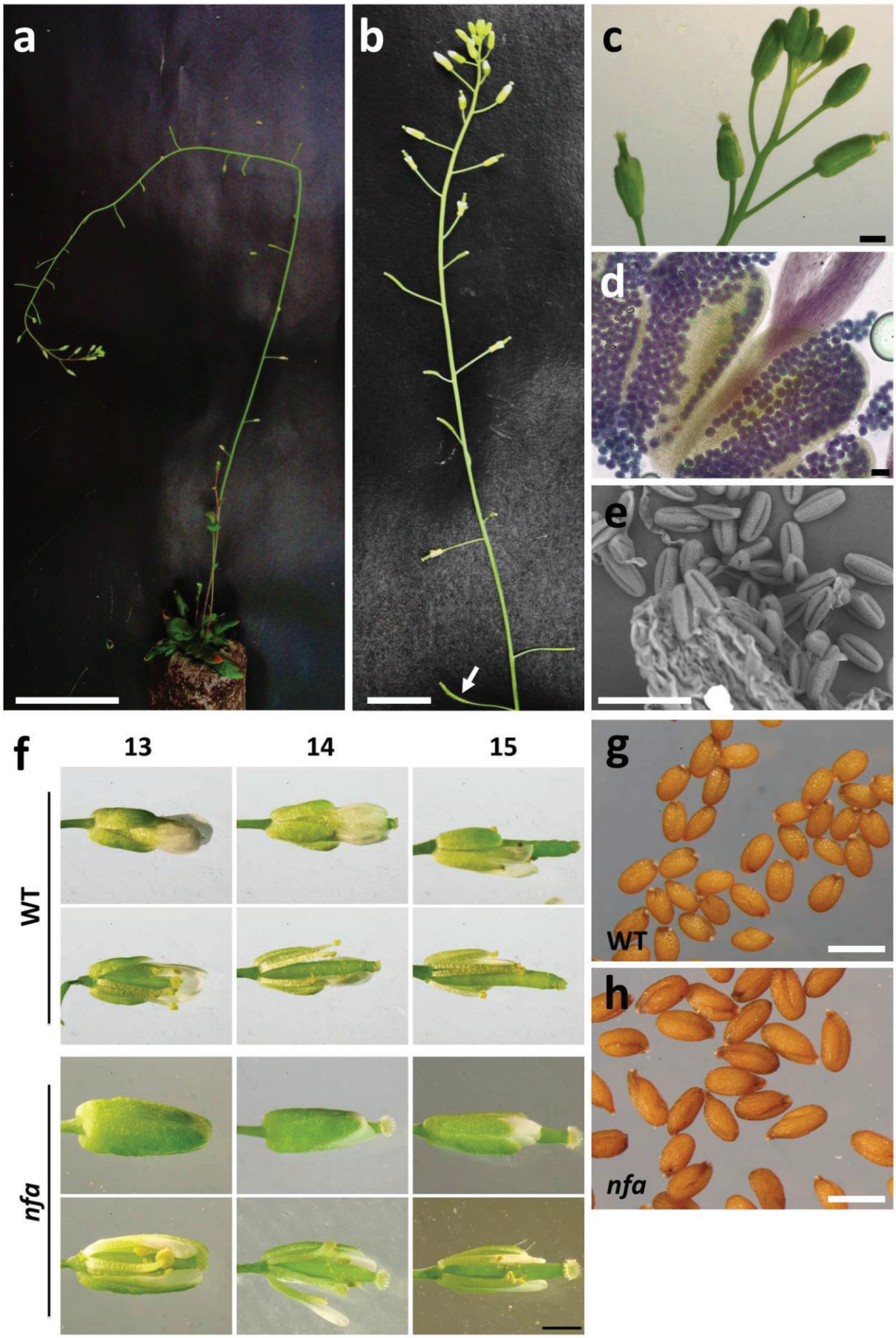
a
b
c
d
e
f
13
14
15
WT
nfa
g
WT
h
nfa

Fig. 2-5 Phenotypic characterization of the *no flower anthesis* mutant. a A forty five-day-old plant with a semi-sterility phenotype. **b** A flowering branch showing the semi-sterility phenotype. The arrow indicates one of the elongated siliques occasionally seen. **c** The top part of a flowering branch showing abnormal flower anthesis. **d** Alexander's staining of an anther full with normal viable pollen grains. **e** A SEM micrograph of an anther showing functional pollen grains. **f** A comparison of flower morphology of the wild type and the *nfa* mutant at stages 13, 14, and 15 of development. Upper panels show un-dissected flowers and lower panels show dissected flowers. Note that there is no flower anthesis in the *nfa* mutant at all stages and consequently no pollination, although numerous pollen can be seen on the pistils of the *nfa* mutant. **g, h** A comparison of seed size and morphology between the wild type and the *nfa* mutant. Note the larger size of *nfa* seeds. This mutant was isolated among populations of the parental group 35. Scale bars = 5 cm in (a), 1 cm in (b),1 mm in (c, f, g, h), and 50 μm in (d, e).

Class 2: Anther-level mutants

This class compromises the plants with defects in anther development. The mutant lines are characterized by either delaying the anther dehiscence or preventing the anther dehiscence and impairing the pollination process which resulted in sterile/ semi-sterile plants and this class is divided into two subclasses as follows.

2A: late-dehiscence (five lines)

In which opening (dehiscence) of anthers was delayed and stomium breaking postponed after the flower opening, preventing the pollen to reach the stigma at the appropriate time for pollination. Pollen release from anthers was delayed and did not occur at stage 13 (black arrows in Fig. 2-6); however, later, pollen grains were released during stage 15 (black arrows in Fig. 2-6). But by this time the stigmas are out of the pollen reach because they already grow high (Fig. 2-6; 2nd column). The anthers contained a lot of functional pollen grains as revealed by SEM and these pollen were viable as shown by Alexander's staining (Fig. 2-6; 3rd and 4th columns). A few siliques with seeds were occasionally seen in these mutants, indicating the semi-sterility phenotypes (Fig. 2-7). The late-dehiscence mutants showed a reduction in growth and height and the siliques were closer to each other (Fig. 2-7).

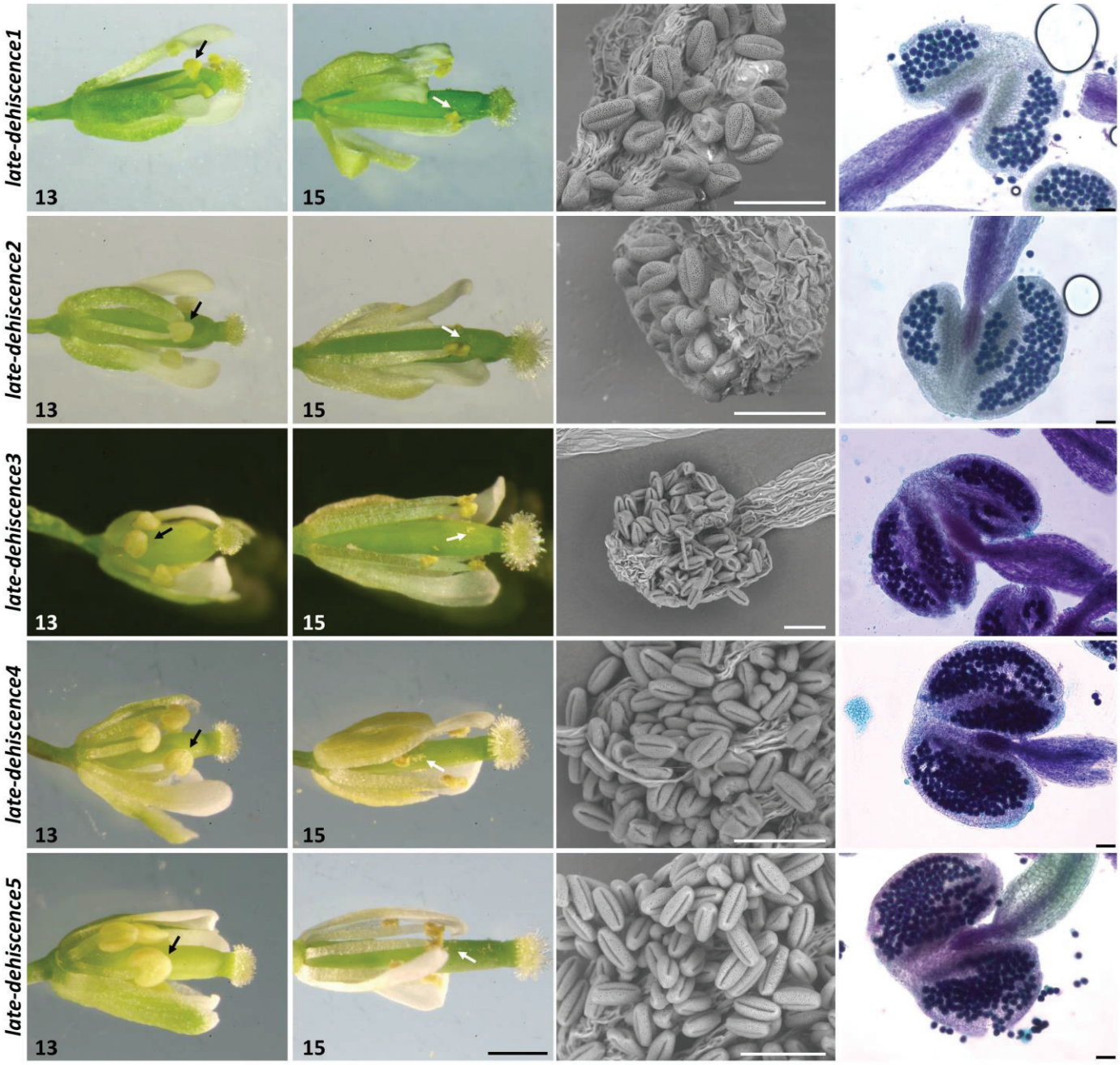

Fig. 2-6 Phenotypic characterization of the *late-dehiscence* mutants. The first and second columns show dissected flowers at stages 13 and 15, respectively. The black arrows indicate the yet indehiscent anthers. The white arrows show the dehiscent anthers and pollen release. Scale bars = 1 mm. For a comparison with the wild type, refer to Fig. 5f. The third column shows SEM micrograph of anther with numerous functional pollen grains. The fourth column shows Alexander's staining of anthers with normal viable pollen grains. All the five *late-dehiscence* mutants were isolated among populations of the parental group 35. Scale bars = 50 µm.

Fig. 2-7 Sterility or semi-sterility phenotypes of the *late-dehiscence* mutants. Upper panel shows two-month-old plants. Lower panel shows a flowering branch with a majority of undeveloped siliques. Scale bars = 5 cm in the upper panel and 1 cm in the lower panel.

2B: indehiscence/less pollen-production (lpp; two lines)

In this subclass, the anthers were prevented from normal opening and no stomium breaking occurred at all flower stages. Pollen of *lpp* were similar to wild-type pollen when manually open and observed by SEM (data not shown). Pollen release from anthers was not observed at stage 13 (black arrows in Fig. 2-8) or later at stage 15 (black arrows in Fig. 2-8). The anthers were smaller in size, intact with no stomium breaking (Fig. 2-8; 3rd column), and produced only a small amount of functional pollen grains as revealed by Alexander's staining (Fig. 2-8; 4th column).

Several mutants have recently been shown to cause late-dehiscence or indehiscence phenotypes by regulating genes in the jasmonate biosynthesis pathway [98-100] or in the biosynthesis and deposition of lignin [101, 102]. None of the mutants of this class were studied further.

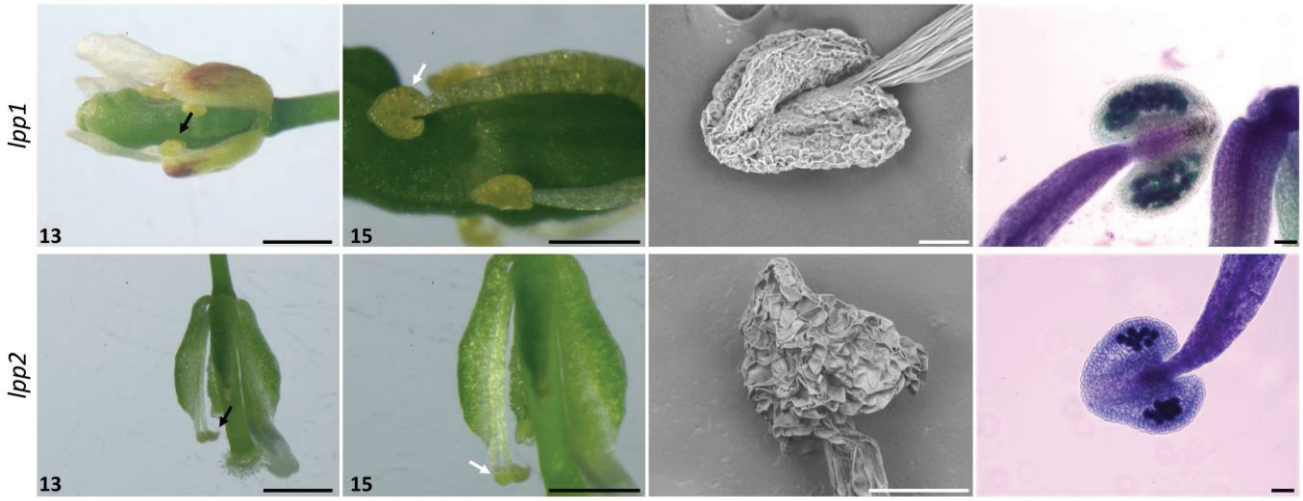

Fig. 2-8 Phenotypic characterization of the *indehiscence/less pollen-production* mutants. The first and second columns show dissected flowers at stages 13 and 15. The black and white arrows indicate the indehiscent anthers at stages 13 and 15, respectively. Scale bars = 1 mm. For a comparison with the wild type, refer to Fig. 5f. The third column shows SEM micrograph of indehiscent anthers of *lpp* mutants. The fourth column shows Alexander's staining of anthers of *lpp* mutants with only a few pollen grains. These pollen were with normal viability. *lpp1* and *lpp2* were isolated among populations of the parental groups 35 and 34, respectively. Scale bars = 50 μm.

Class 3: Pollen-level mutants

This class contains most of the isolated mutants and includes diverse defects in pollen development, wall formation, and pollen shape and size. This class is divided into eight subclases as follows.

3A: defective reticulate exine (14 lines)

The defective reticulate exine comprises six types with various defects in the surface structure and exine patterning, summarized as follows.

3A.1: rugulate exine (*rux*; three lines)

In this type, pollen grains were missing the sporopollenin deposition in some areas of the tectum leaving the remaining tectum surface similar to the rugulate type of exine sculpturing (Fig. 2-9a). SEM comparison with the wild type showed that pollen of *rux* mutants had lost the reticulate pattern characteristic to the wild type (Fig. 2-9a). Alexander's staining indicated that the pollen of *rux* mutants were viable similar to the wild type (Fig. 2-9b). These mutant plants were fertile with many elongated siliques (Fig. 2-9c).

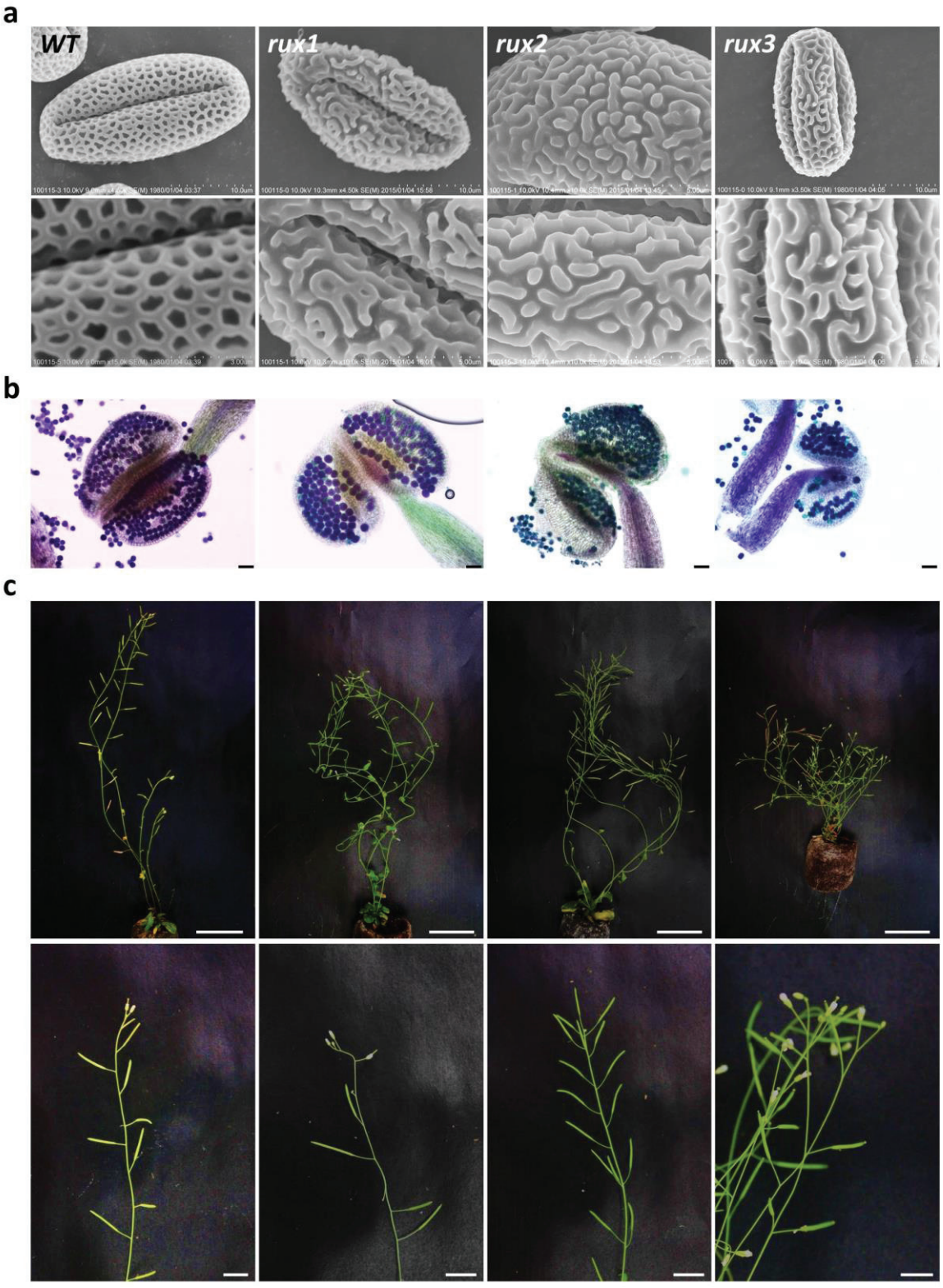

Fig. 2-9 Phenotypic characterization of the wild-type *and rugulate exine*-type mutants. a SEM micrographs comparing the surface structure of the wild type and *rux* mutants (upper panel). Lower panel shows magnified parts of the pollen surface structures in the upper panel. **b** Alexander's staining of wild-type and *rux* anthers showing pollen grains of normal viability. **c** Plant and silique morphology of the wild type and *rux* mutants. The upper panel shows two-month-old wild-type and *rux* plants with full fertility. Lower panel shows flowering branches with normal elongated siliques. All *rux* mutants were isolated among populations of the parental group 35. Use the wild-type images shown here for a comparison with the other mutants. Scale bars = 50 µm in (b), 5 cm in (upper panel of c), 1 cm in (lower panel of c), and as indicated on SEM micrographs.

3A.2: interrupted tectum (*int*; four lines)

Pollen grains of this type were characterized by a less sporopollenin deposition in areas of the tectum, resulting in interrupted tectum with a wider spacing between the muri (the walls that separate the lumina) (Fig. 2-10a). SEM analysis showed that the mutant pollen had exine with a partial reticulate pattern (Fig. 2-10a). Alexander's staining showed that the anthers of *int* mutants contained numerous viable pollen grains (Fig. 2-10b). These mutant plants were fertile and produced a large number of siliques and seeds (Fig. 2-10c).

3A.3: thickened muri and irregular lumina (*tml*; four lines)

tml-type pollen had more thickened muri walls than those of the wild type and the lumina were irregular in shape with an unequal spacing between muri (Fig. 2-11a). The pollen of this type exhibited a reticulate ornamentation and only can be seen with high magnifications. To the author's knowledge, this phenotype has not yet been isolated before and encodes a novel phenotype. Anthers of *tml* mutants contained a large number of viable pollen grains as revealed by Alexander's staining (Fig. 2-11b). All plants of this type were fertile with normal seed-set number (Fig. 2-11c).

3A.4: fragmented exine (*frx*; one line)

In this type, pollen grains had walls with irregular sporopollenin deposition resulting in a tectum structure resembling the perforate type of exine sculpturing (Fig. 2-12a). SEM showed that pollen of *frx* mutant completely lacked the reticulate exine pattern (Fig. 2-12a). However, Alexander's staining showed that the pollen of *frx* mutant were viable with cytoplasm stained purple and aggregates of sporopollenin materials forming walls stained green (Fig. 2-12d). These mutant plants were fertile and produced a large number of elongated siliques (Fig. 2-12g).

3A.5: verrucate exine (*vrx*; one line)

The surface of pollen grains of this type was covered with sporopollenin aggregations that formed a tectum with verrucate sculpturing-type. Many dome-like structures of were scattered on the outer exine wall instead of the characteristic reticulate pattern of the exine (Fig. 2-12b). Alexander's staining showed that the anthers of *vrx* mutants contained only a few viable pollen grains (stained purple) and a majority of collapsed pollen (stained green)

(Fig. 2-12e). The *vrx* mutant showed a semi-sterile phenotype and produced only a few fertile siliques (Fig. 2-12h).

3A.6: dense-baculate exine (*dnb*; one line)

This mutant pollen also lacked the regular reticulate exine and alternatively many densely arranged bacula were formed the fragmented tectum (Fig. 2-12c). It is expected that the number of bacula of *dnb* mutant pollen is significantly higher and placed closer than those of the wild type. Anthers of *dnb* mutant contained a mixture of viable pollen grains (stained purple) and non-viable pollen (stained green) as revealed by Alexander's staining (Fig. 2-12f). Plants of *dnb* type were normally fertile (Fig. 2-12i). *dnb*-type of pollen has a similar phenotype to a previously described mutant, *kns12*, which isolated through a similar screening strategy [27].

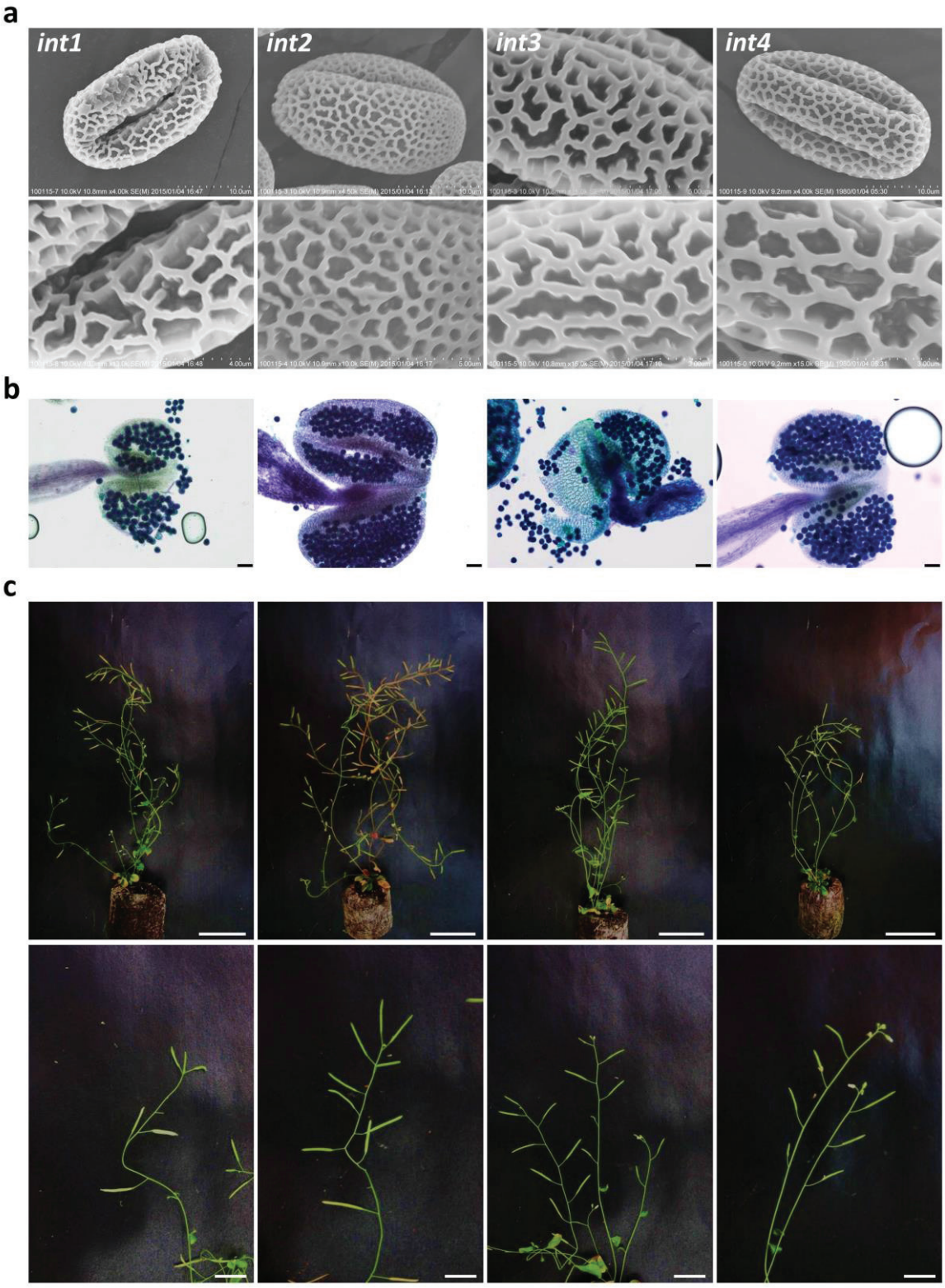

Fig. 2-10 Phenotypic characterization of the *interrupted tectum*-type mutants. a SEM micrographs showing the surface structure of *int* mutants (upper panel). Lower panel shows magnified parts of the pollen surface structures in the upper panel. **b** Alexander's staining of anthers of *int*-type mutants showing pollen grains of normal viability. **c** Plant and silique morphology. The upper panel shows two-month-old *int* plants with full fertility. Lower panel shows flowering branches with normal elongated siliques. *int1*, *int2*, and *int3* mutants were isolated among populations of the parental group 35 whereas *int4* belongs to parental group 36. Scale bars = 50 μm in (b), 5 cm in (upper panel of c), 1 cm in (lower panel of c), and as indicated on SEM micrographs.

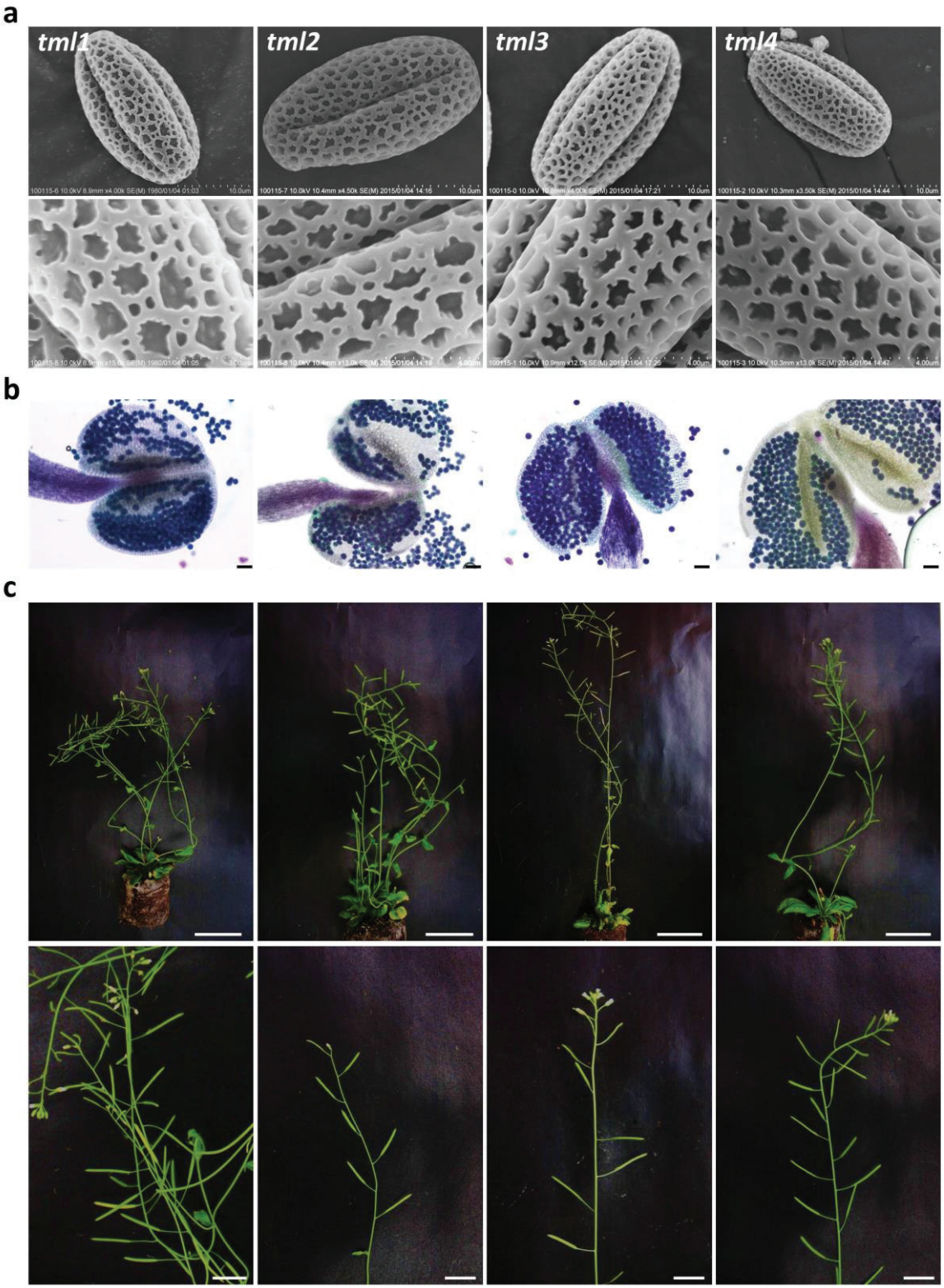

Fig. 2-11 Phenotypic characterization of the *thickened muri and irregular lumina*-type mutants. a SEM micrographs showing the surface structure of *tml* mutants (upper panel). Lower panel shows magnified parts of the pollen surface structures in the upper panel. **b** Alexander's staining of anthers of *tml*-type mutants showing pollen grains of normal viability. **c** Plant and silique morphology of the *tml*-type mutants. The upper panel shows two-month-old *tml* plants with full fertility. Lower panel shows flowering branches with normal elongated siliques. All *tml* mutants were isolated among populations of the parental group 35. Scale bars = 50 μm in (b), 5 cm in (upper panel of c), 1 cm in (lower panel of c), and as indicated on SEM micrographs.

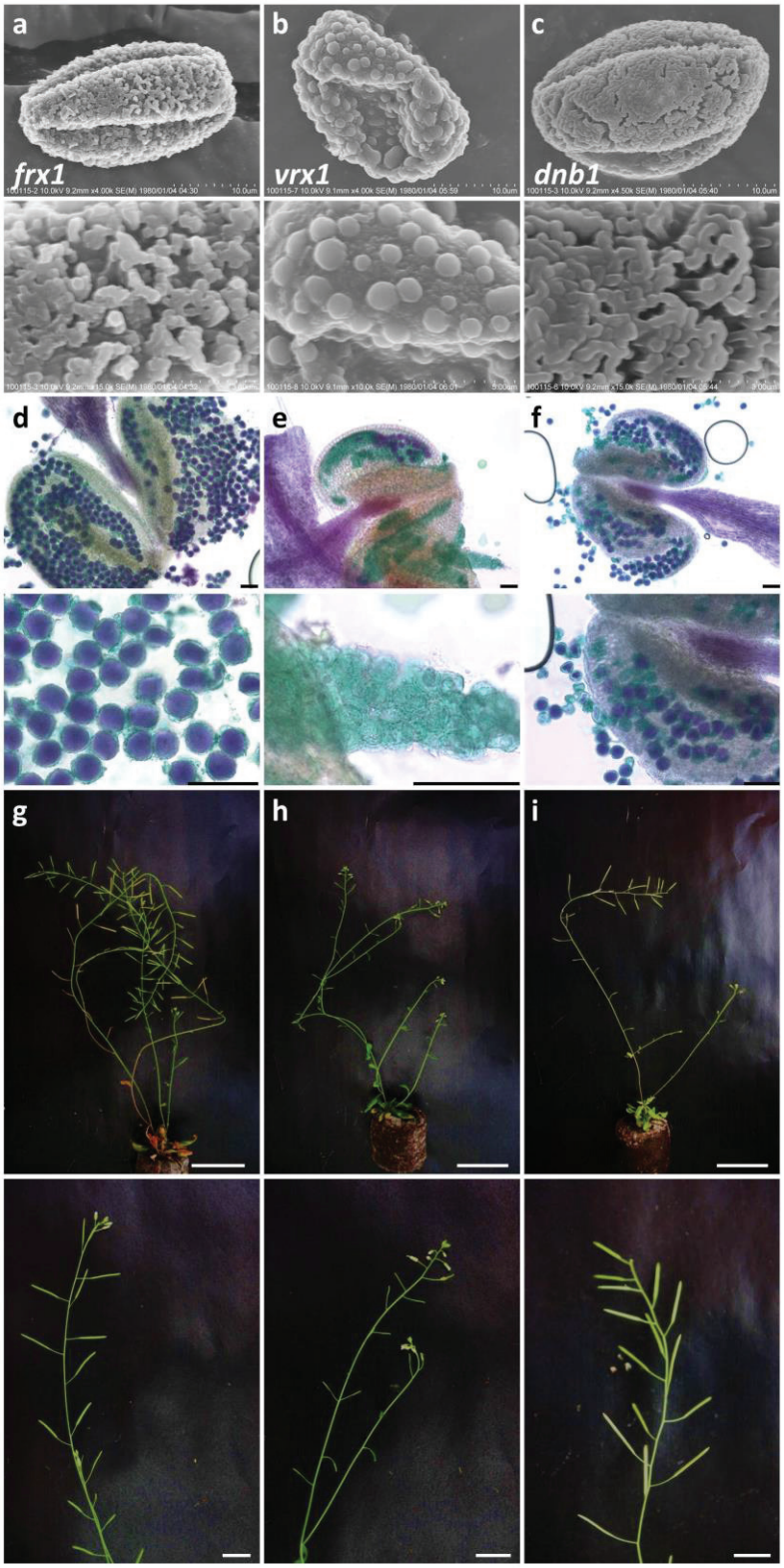

Fig. 2-12 Phenotypic characterization of the *fragmented exine*-type, *verrucate exine*-type, and *dense-baculate exine*-type mutants. a-c SEM micrographs showing the surface structure of *frx*-type, *vrx*-type, and *dnb*-type mutants (upper panel). Lower panel shows magnified parts of the pollen surface structures in the upper panel. **d-f** Alexander's staining of anthers of *frx*-type, *vrx*-type, and *dnb*-type mutants. Lower panel shows magnified parts of the anthers in the upper panel. **g-i** Plant and silique morphology of the *frx*-type, *vrx*-type, and *dnb*-type mutants. The upper panel shows two-month-old plants. Lower panel shows flowering branches with siliques. *frx* mutant was isolated among populations of the parental group 34 whereas *vrx* and *dnb* mutants were isolated among populations of the parental group 36. Scale bars = 50 µm in (d-f), 5 cm in (upper panel of g-i), 1 cm in (lower panel of g-i), and as indicated on SEM micrographs.

According to the characteristics of pollen-surface phenotypes of the *defective reticulate exine* subclass, the author speculate that the encoding genes may be involved in pollen wall formation and exine patterning by organizing specific developmental processes such as callose wall synthesis, spacing of the probacula, sporopollenin synthesis, polymerization, or transport, and tectum formation. These genes may be function sporophytically in the tapetal cells, since most building materials required for formation of pollen wall are synthesized in the tapetal cells [26, 28, 103, 104]. In a previous SEM-based mutant screen, 12 kaonashi (kns) mutants with defects of pollen exine were described and the functions of these genes were speculated. Type 1 KNS genes may involve in callose synthesis, Type 2 KNS genes may regulate the thickening of the primexine layer, Type 3 KNS genes may participate in tectum formation or in the synthesis, polymerization, or deposition of sporopollenin on the developing tectum, and Type 4 KNS genes may function in formation of spacers for correct distribution of the probacula [27]. The author isolated similar mutants as well as mutants with novel phenotypes and the variation of mutants isolated during the screen reflects the complexity of pollen wall formation process and the possibility of the existence of new genes controlling this process.

Five mutants of the *defective reticulate exine* subclass were further identified using bulked-segregant mapping by next generation sequencing. These were *rux1*and *rux2* from the *rugulate exine*-type which mapped to the bottom of chromosome 4 (data not shown), *int1* from the *interrupted tectum*-type which mapped to the bottom of chromosome 1 (data not shown), and *tml2* and *tml3* from the *thickened muri and irregular lumina*-type which mapped to the bottom of chromosome 3 (data not shown). Summary of mapping results is listed in Table 2-1.

Table 2-1: Mapping analysis of some selected mutants.

Mutant phenotype	Mutation ID[a]	Plant fertility[b]	Chromosome mapping	Candidate gene(s)[c]
defective reticulate-exine				
rugulate exine	*rux1, rux2*	++	bottom of chromosome 4	nd
interrupted tectum	*int1*	++	bottom of chromosome 1	nd
thickened muri and irregular lumina	*tml2, tml3*	++	bottom of chromosome 3	nd
faceless pollen				
faceless psilate pollen	*fcp1, fcp4*	-	bottom of chromosome 4; between 13-18 Mbp	AT4G35420/*DRL1/TKPR1*
	fcp3	-	bottom of chromosome 5; between 20-27 Mbp	AT5G56110/*MYB103/MYB80*
faceless granulate pollen	*fcg2, fcg3*	++	top of chromosome 1; between 0-3 Mbp	AT1G01280/*CYP703A2*
variable-size collapsed pollen				
severe variable-size collapsed	*svc1, svc2, svc5*	-	bottom of chromosome 3; between 15-20 Mbp	AT3G48190/*ATATM*
	svc3	-	bottom of chromosome 3; between 15-20 Mbp	nd
moderate variable-size collapsed	*mvc8*	+	top of chromosome 1; between 0-3 Mbp	nd
irregular aperture-numbers and positions				
	inp1	+	middle of chromosome 1; between 17-23 Mbp	AT1G50240/*TIO*
	inp2, inp3, inp5	+	middle of chromosome 3; between 12-17 Mbp	AT3G43210/*STD/TES*
aggregated unreleased pollen				
	aup2	-	bottom of chromosome 1	nd
	aup3	-	middle of chromosome 2	nd
	aup4	-	bottom of chromosome 4	nd
quartet-like pollen[d]	*qrtl*	++	nd	AT5G55590/*QRT1*

[a] all identified mutations were recessive. [b] ++, fully fertile; +, partial fertile; -, sterile. [c] nd, not determined.
[d] the only mutation identified by capillary sequencing was *qrtl*, whereas all others were identified by next generation sequencing.

3B: faceless pollen (seven lines)

A complete lack of the reticulate ornamentation was characteristic to the pollen of this subclass and a smooth surface was observed. This subclass has two types:

3B.1: faceless psilate pollen (*fcp;* four lines)

Pollen of this type had a smooth surface and lacking any reticulate sculpture. No granular structures were observed on the pollen surface of these mutants. Most pollen of the *fcp* type had lost the oblong shape characteristic to the wild type and became a more or less rounded with less integrity of the walls (Fig. 2-13a). Anthers of the *fcp* type contained a few viable pollen grains (stained purple) (Fig. 2-13b). As a result of the a few functional pollen grains, a semi-sterility phenotype was observed (Fig. 2-13c).

3B.2: faceless granulate pollen (*fcg*; three lines)

The phenotype of this type of mutants was very similar to the *fcp* type except for having numerous granular structures on the top of the smooth surface (Fig. 2-14a). Such granular structures indicate an extra deposition of sporopollenin in the exine layer and also may indicate more thickened exine layer. This type also totally lacked the reticulate sculpture. The majority of pollen were viable and indistinguishable from the wild-type pollen (Fig. 2-14b). Full fertile siliques were developed in the *fcg* mutant plants (Fig. 2-14c).

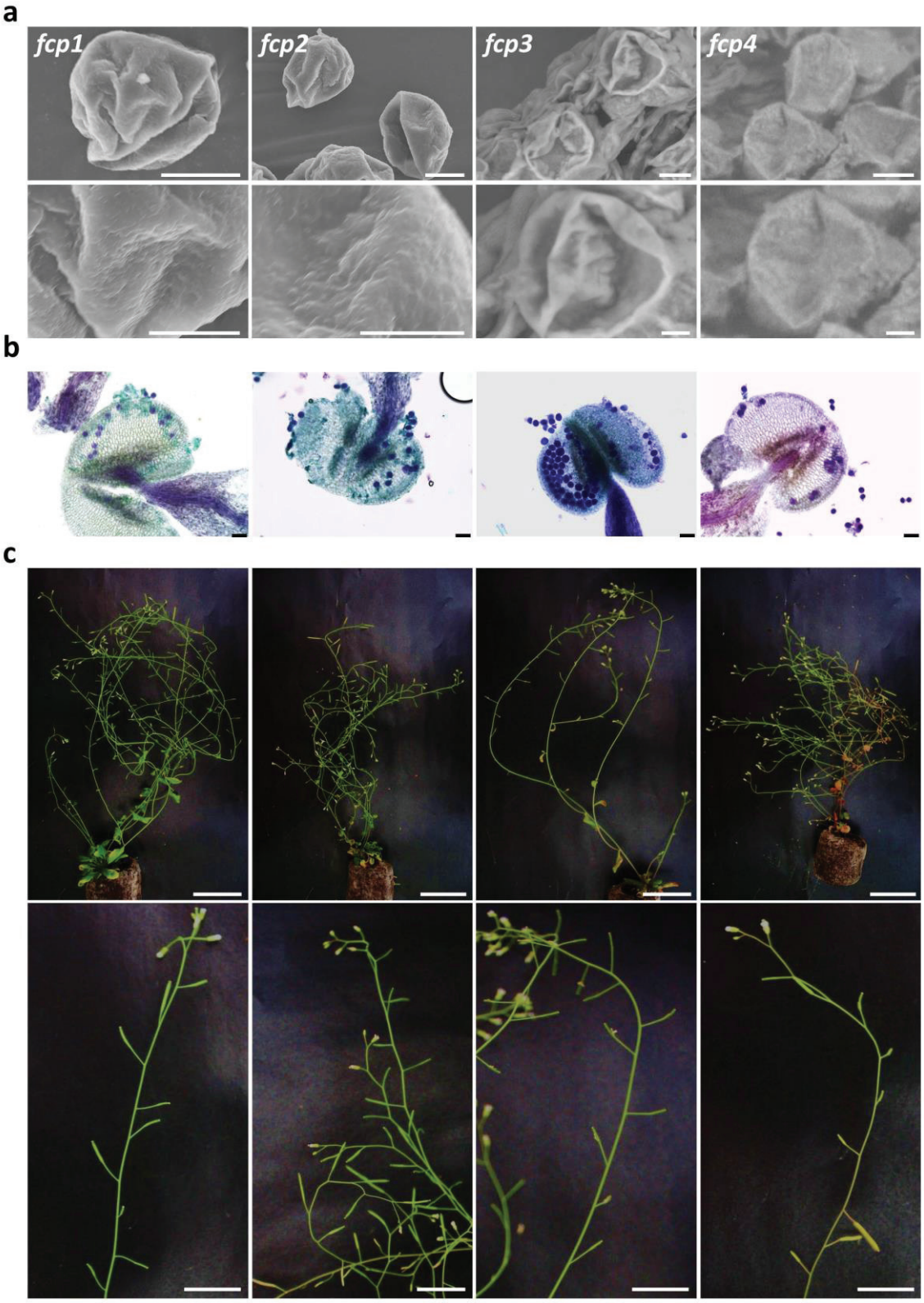

Fig. 2-13 Phenotypic characterization of the *faceless psilate pollen*-type mutants. a SEM micrographs showing the surface structure of *fcp* mutants (upper panel). Lower panel shows magnified parts of the pollen surface structures in the upper panel. **b** Alexander's staining of anthers of *fcp*-type mutants. **c** Plant and silique morphology of the *fcp*-type mutants. The upper panel shows two-month-old *fcp* plants with sterility/semi-sterility phenotypes. Lower panel shows flowering branches with majority of undeveloped siliques. All *fcp* mutants were isolated among populations of the parental group 35. Scale bars = 10 µm in (upper panel of a), 4 µm in (lower panel of a), 50 µm in (b), 5 cm in (upper panel of c), 2 cm in (lower panel of c), and as indicated on SEM micrographs.

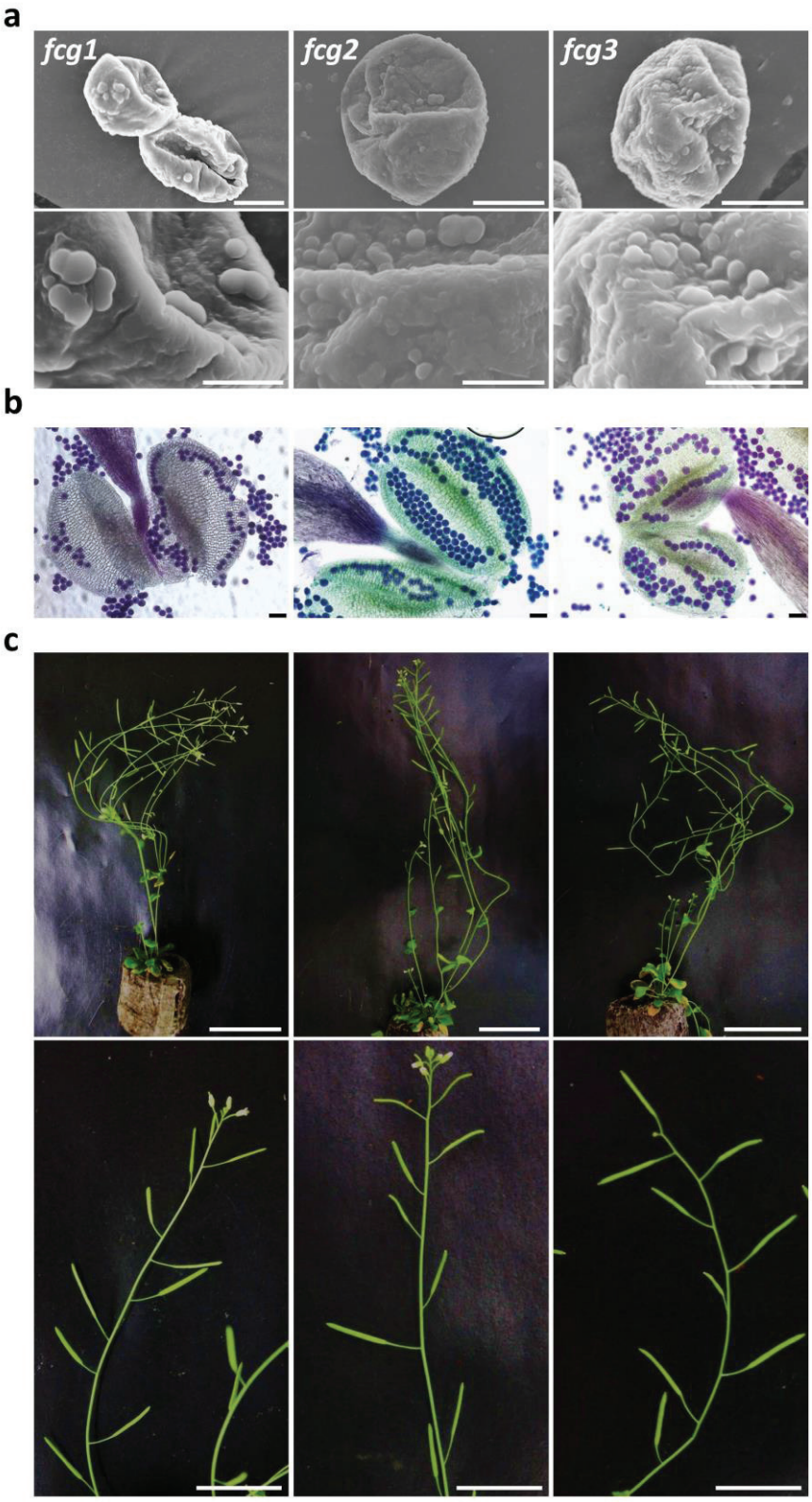

Fig. 2-14 Phenotypic characterization of the *faceless granulate pollen*-type mutants. a SEM micrographs showing the surface structure of *fcg*-type mutants (upper panel). Lower panel shows magnified parts of the pollen surface structures in the upper panel. **b** Alexander's staining of anthers of *fcg*-type mutants. **c** Plant and silique morphology of the *fcg*-type mutants. The upper panel shows two-month-old *fcg* plants with normal fertility phenotypes. Lower panel shows flowering branches with majority of fertile siliques. All *fcg* mutants were isolated among populations of the parental group 35. Scale bars = 10 µm in (upper panel of a), 4 µm in (lower panel of a), 50 µm in (b), 5 cm in (upper panel of c), 2 cm in (lower panel of c), and as indicated on SEM micrographs.

The *faceless pollen*-subclass mutants had a smooth surface and a thinner exine walls. Disruption of genes involved in sporopollenin synthesis and callose formation has been reported to cause similar phenotypes. For example, the *CYP703A2* and *DRL1/TKPR1* genes have been shown to be required for fatty acid hydroxylation and synthesis of hydroxylated tetraketide α-pyrones, two key steps for sporopollenin synthesis [57, 75, 76]. *MYB103/MYB80*, an *Arabidopsis* gene that may control glucanase enzymes, has been reported to be involved in callose wall formation or dissolution [59]. Accordingly, the author expected that the *fcp* and *fcg* responsible genes may participate in similar processes or may be alleles to these genes. In addition, the production of fully fertile plants in the *faceless granulate pollen*-type mutants indicated that the reticulate pattern of exine is not essential for the pollen functionality and completion of the pollination process. But rather than that the thickness of exine wall may be necessary for the functionality of pollen. It seems that the *faceless psilate pollen*-type mutants had a reduction of exine thickness and when more sporopollenin deposition occurred (e.g., the granular structures in the *faceless granulate pollen*-type), normal functionality of pollen was observed.

Five mutants of the *faceless pollen* subclass were identified by next generation sequencing analysis. Three mutants of the *faceless psilate pollen*-type and two mutants of the *faceless granulate pollen*-type were identified. *fcp1* and *fcp4* mutations were mapped to the bottom of chromosome 4 between the region 13-18 Mbp (Fig. 2-15a, b). The AT4G35420 gene was the mutation causative gene and both mutations were new alleles of the *DRL1/TKPR1*. The *fcp1* and *fcp4* phenotype was identical to that of the *DRL1/TKPR1*. The *fcp3* mutation was identified in the region between 20-27 Mbp bottom of chromosome 5 (Fig. 2-15c). The AT5G56110 gene was linked to this mutation and was a new allele of *MYB103/MYB80* with a very similar phenotype. Mutations of *fcg2* and *fcg3* were mapped to the top of chromosome 1 between the region 0-3 Mbp (Fig. 2-15d, e) and AT1G01280 was identified as the responsible gene for these mutations. These two mutations are new alleles of *CYP703A2* with identical phenotype. Mapping results are summarized in Table 2-1.

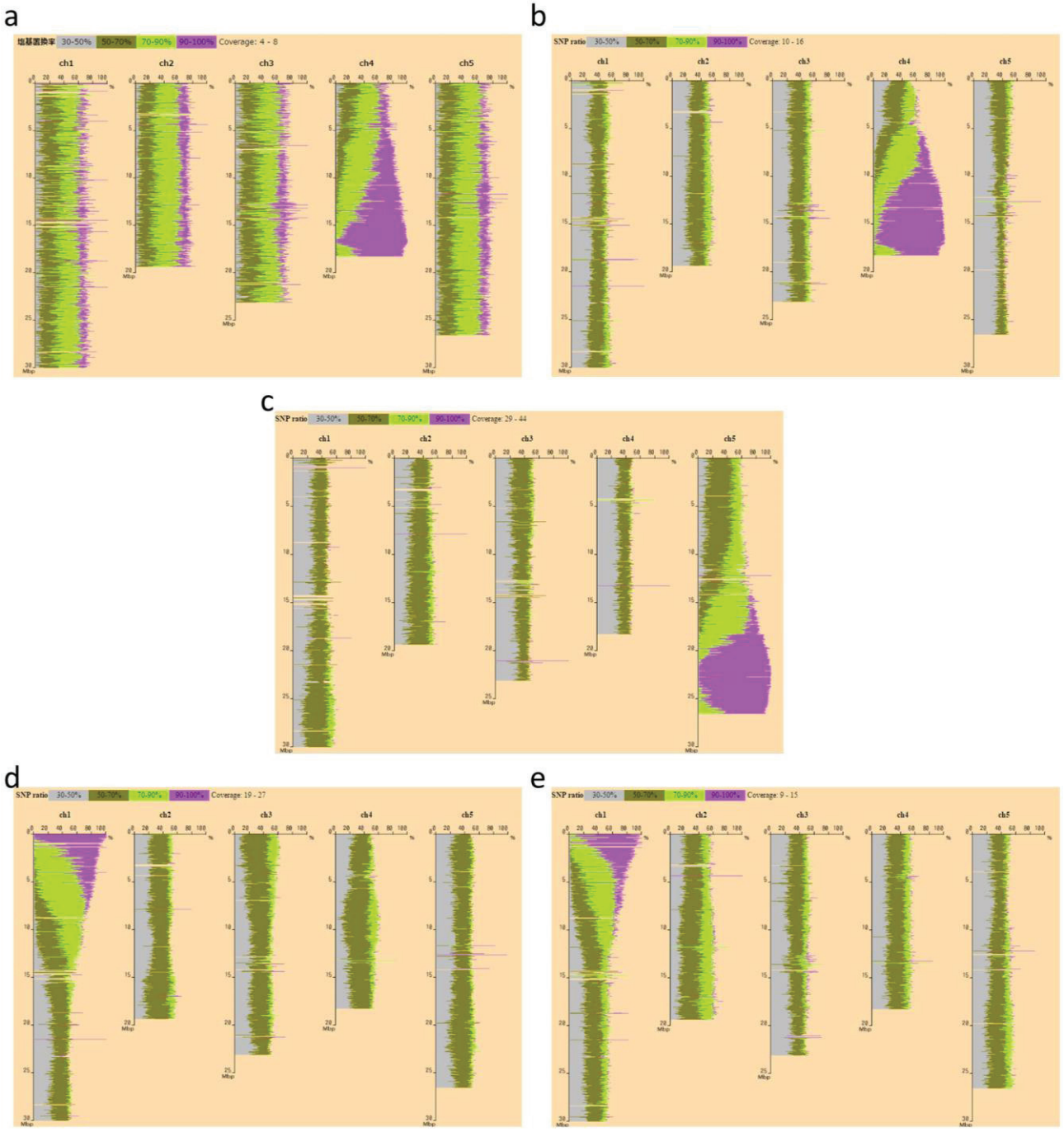

Fig. 2-15 Chromosome mapping of selected members from the *faceless pollen* subclass. a-c Bulked-segregant analysis of three members of the *faceless psilate pollen*-type, *fcp1* (a), *fcp4* (b), and *fcp3* (c). Both *fcp1* and *fcp4* were mapped to the same region bottom of chromosome 4. *fcp3* was mapped to the bottom of chromosome 5. **d, e** Bulked-segregant analysis of two members of the *faceless granulate pollen*-type, *fcp2* (d) and *fcp3* (e). Both *fcp2* and *fcp3* were mapped to the same region top of chromosome 1.

3C: variable-size collapsed pollen (45 lines)

The *variable-size collapsed pollen* subclass included the largest number of mutants isolated through the screen. Anthers of this subclass contained two groups of pollen: normal well-developed pollen (like the wild type) and collapsed smaller (shriveled) pollen. All pollen, the normal and the collapsed, had the reticulate ornamentation. Various percentages of pollen in this subclass remained smaller in size and did not undergo further developmental stages and collapsed. Mainly the collapsed pollen were about two times smaller than the well-developed ones, indicating that the pollen abortion has occurred at the uninucleate to bicellular stages of development. This subclass is represented by three types according to the severity of the phenotype, as follows.

3C.1: severe variable-size collapsed (*svc*; 14 lines)

The majority of pollen of this type were small and collapsed (Fig. 2-16; upper panels). Anthers with~ 70-100% collapsed pollen were included in the *svc*-pollen type. The viability test (Alexander's staining) was used with the SEM images to roughly estimate the severity of the phenotype. Results from Alexander's staining showed that no or few pollen grains were viable (stained purple) whereas the majority stained with green, indicating the non-viable dead pollen (Fig. 2-16; lower panels). Most of these mutants were sterile or at least show a severe reduction in fertility (data not shown).

3C.2: moderate variable-size collapsed (*mvc*; 19 lines)

Approximately half of pollen of this type were small and collapsed and the other half were fertile, identical to the wild type (Fig. 2-17; upper panels). Anthers with~ 40-60% collapsed pollen were included in the *mvc*-pollen type. Alexander's staining showed that about half of pollen grains were viable (stained purple), whereas the remaining half were dead and green-stained (Fig. 2-17; lower panels). Most of these mutants were fertile or at least partially fertile (data not shown) and probably some of them were heterozygous lines.

3C.3: mild variable-size collapsed (*lvc*; 12 lines)

Most pollen of this type were normal, identical to the wild type and only a few were small and collapsed (Fig. 2-18; upper panels). Anthers with less than 20% collapsed pollen were included in the *lvc*-pollen type. Alexander's staining showed that the majority of pollen

grains were viable, whereas only a few pollen grains were negatively stained and dead (Fig. 2-18; lower panels). All lines of *lvc* mutants were fully fertile (data not shown).

The shriveled pollen phenotype observed in the *variable-size collapsed* subclass is previously described in several mutants and it seems that this phenotype may be caused by disruption of genes with a wide range of functions. For example, disruption of TPLATE, a gene functions in vesicle-trafficking events to regulate somatic cytokinesis and pollen maturation leads to a shriveled pollen phenotype [105]. *ATAXIA-TELANGIECTASIA MUTATED (ATATM)* gene is essential for the response of DNA damage during meiosis [60]. *PIG1,* an allele to the *ATATM* isolated in a screening for mutants with programmed cell death phenotype during male gametogenesis, is involved in the male gametophyte-specific programmed cell death and may organize the DNA damage-induced apoptosis during pollen development [106]. Moreover, many mutants showing the variable size collapsed phenotype were isolated in a previous screen aimed to identify early meiotic recombination functions [20].

Four mutants of the *severe variable-size collapsed*-type and one mutant of the *moderate variable-size collapsed*-type were identified by mapping. Mapping results are summarized in Table 2-1. Mutations in *svc1, svc2,* and *svc5* were mapped to the region between 15-20 Mbp, at the bottom of chromosome 3 (Fig. 2-19a, b, c), in the AT3G48190 gene. These mutations were alleles of *ATATM* and showed similar phenotypes. *svc3* mutation was linked to the region 15-20 Mbp at the bottom of chromosome 3 (Fig. 2-19d). *mvc8* belonging to the *moderate variable-size collapsed*-type had a mutation mapped to the top of chromosome 1 at the region between 0-3 Mbp (Fig. 2-19e). The responsible genes of *svc3 and mvc8* mutations have not yet determined.

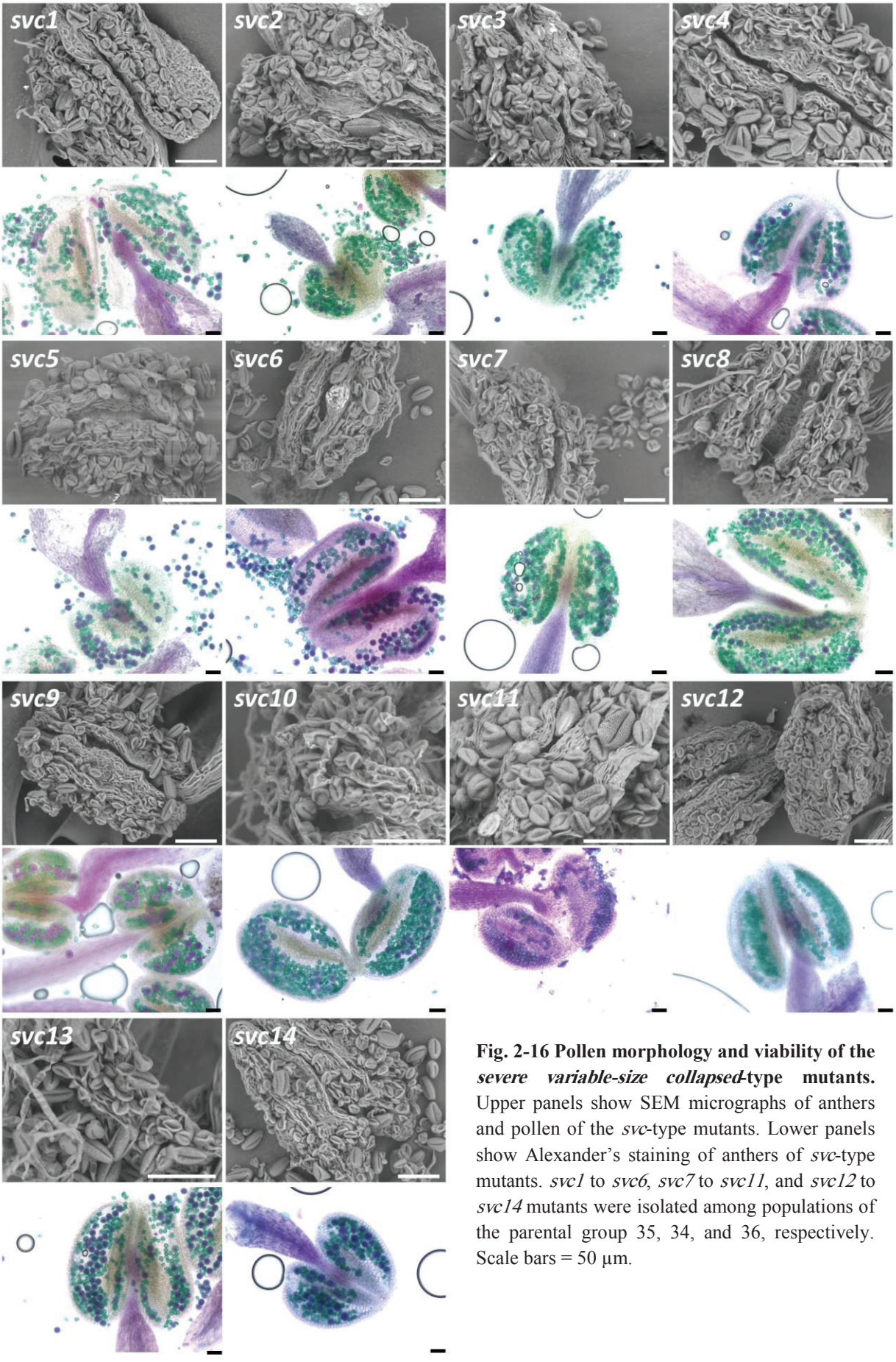

Fig. 2-16 Pollen morphology and viability of the *severe variable-size collapsed*-type mutants. Upper panels show SEM micrographs of anthers and pollen of the *svc*-type mutants. Lower panels show Alexander's staining of anthers of *svc*-type mutants. *svc1* to *svc6*, *svc7* to *svc11*, and *svc12* to *svc14* mutants were isolated among populations of the parental group 35, 34, and 36, respectively. Scale bars = 50 μm.

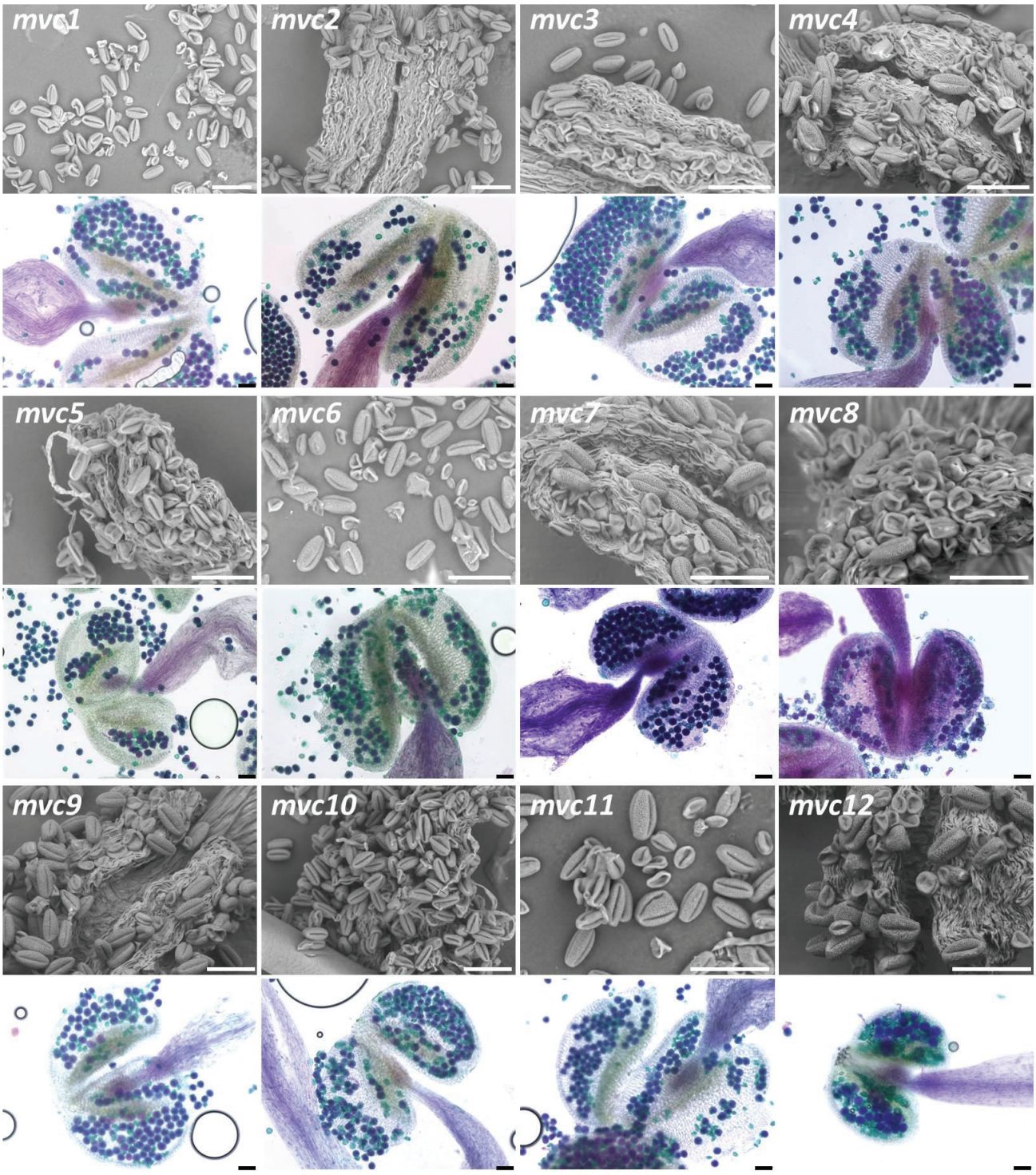
mvc1
mvc2
mvc3
mvc4
mvc5
mvc6
mvc7
mvc8
mvc9
mvc10
mvc11
mvc12

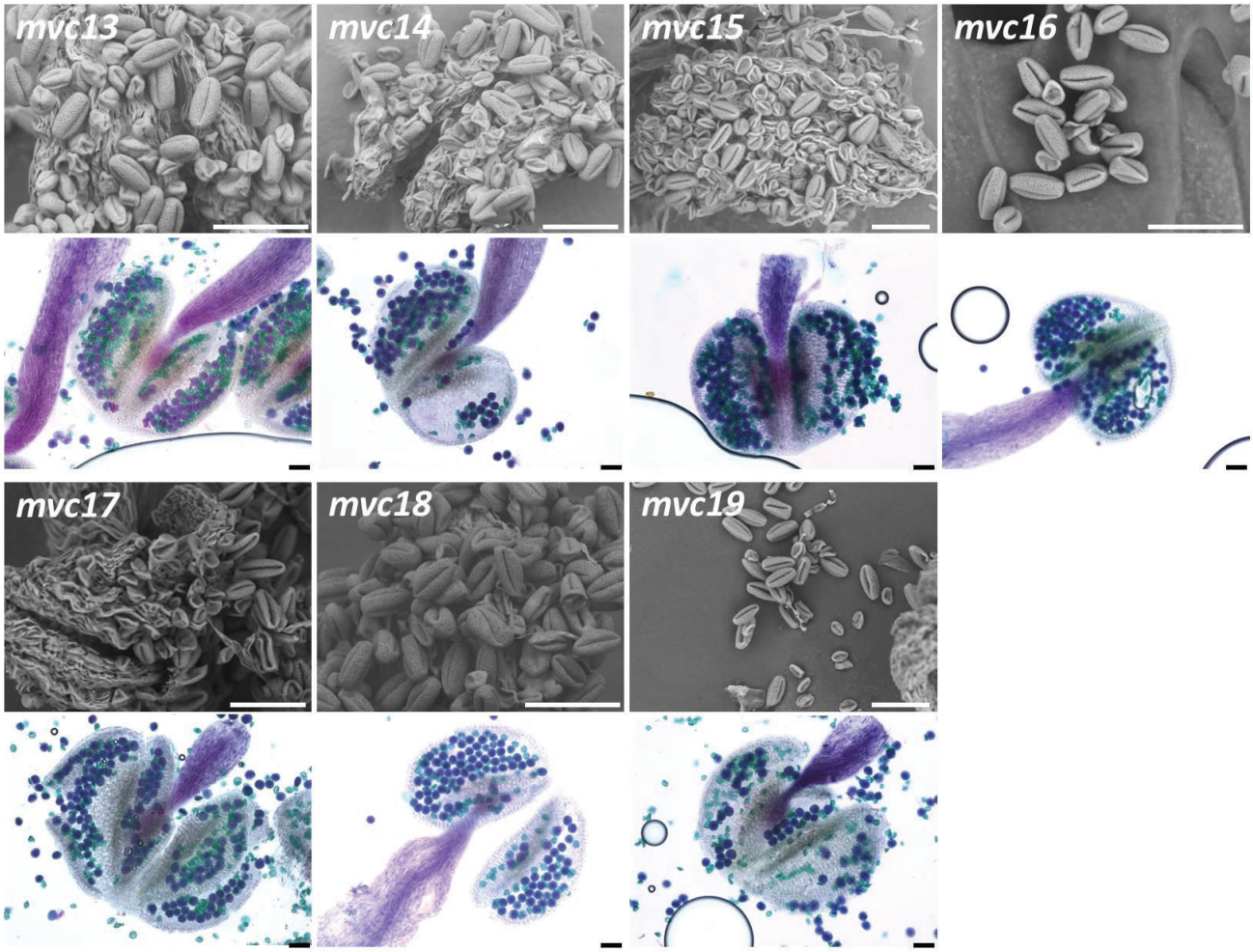

Fig. 2-17 Pollen morphology and viability of the *moderate variable-size collapsed*-type mutants. Upper panels show SEM micrographs of anthers and pollen of the *mvc*-type mutants. Lower panels show Alexander's staining of anthers of *mvc*-type mutants. *mvc1* to *mvc8*, *mvc9* to *mvc11*, and *mvc12* to *mvc19* mutants were isolated among populations of the parental group 35, 34, and 36, respectively. Scale bars = 50 µm.

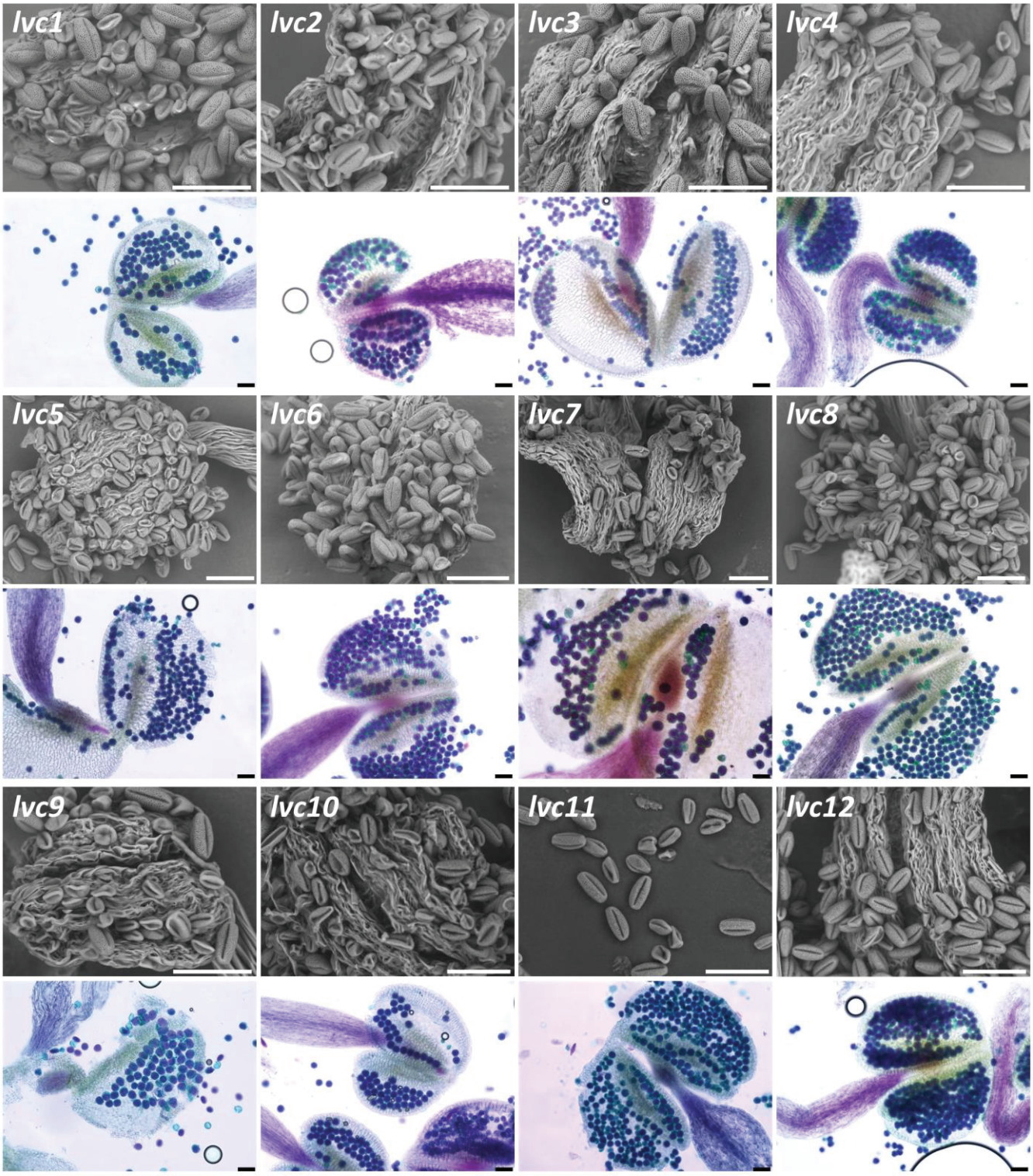

Fig. 2-18 Pollen morphology and viability of the *mild variable-size collapsed*-type mutants. Upper panels show SEM micrographs of anthers and pollen of the *lvc*-type mutants. Lower panels show Alexander's staining of anthers of *lvc*-type mutants. *lvc1* to *lvc7*, (*lvc8* and *lvc9*), and *lvc10* to *lvc12* mutants were isolated among populations of the parental group 35, 34, and 36, respectively. Scale bars = 50 μm.

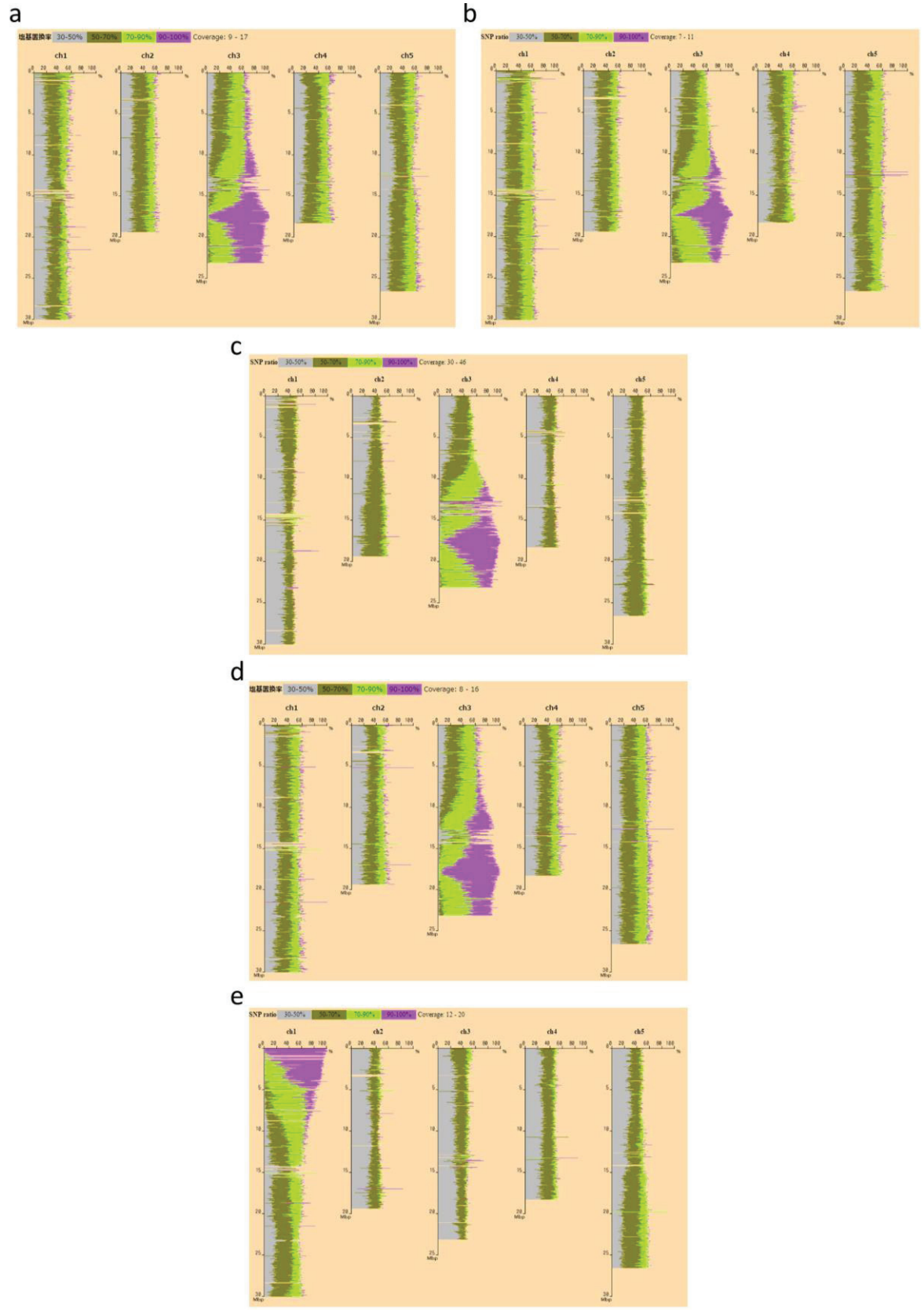

Fig. 2-19 Chromosome mapping of selected members from the *variable-size collapsed pollen* subclass. a-d Bulked-segregant analysis of four members of the *severe variable-size collapsed*-type, *svc1* (a), *svc2* (b), *svc5* (c), and *svc3* (d). *svc1*, *svc2*, and *svc5* were mapped to the same region bottom of chromosome 4 and linked to the same gene. *svc3* was mapped to the bottom of chromosome 4 and the gene responsible for the phenotype is not yet identified. **e** Bulked-segregant analysis of a member of the *moderate variable-size collapsed*-type. *mvc8* was mapped to the top of chromosome 1.

3D: variable-size defective pollen (vdp; two lines)

The difference between the *variable-size collapsed pollen* subclass and *variable-size defective pollen* subclass is that pollen of the latter had pollen with developmental abnormalities. Most pollen, the large and the small, tended to aggregate together and lost the integrity of the pollen walls (Fig. 2-20a, b, g, h). A few pollen grains were remarkably larger in size. Pollen of *vdp1* mutant exhibited a defective exine with depositions in the lamina, resulting in a reticulate exine with narrower lamina (Fig. 2-20a, b). These depositions likely are excess aggregations of pollen coat materials. Pollen of *vdp2* mutant lacked a clear reticulate ornamentation and only some of the larger size pollen had faintly observable reticulate ornamentation (Fig. 2-20g, h). The total number of pollen in a single anther was reduced in both mutants compared with those of the wild type. Alexander's staining showed that only a small number of pollen were viable (Fig. 2-20c, i). Flowers of these mutants were dissected and compared with the wild type. Anthers of both mutants exhibited shrinkage with no or few released pollen and the stigmas were devoid of any pollen, indicating a failure of self-pollination (Fig. 2-20d, j). The *vdp* mutant plants were semi-sterile and only at rare cases develop seed-bearing siliques (Fig. 2-20e, f, k, l). None of these two mutants were analyzed further.

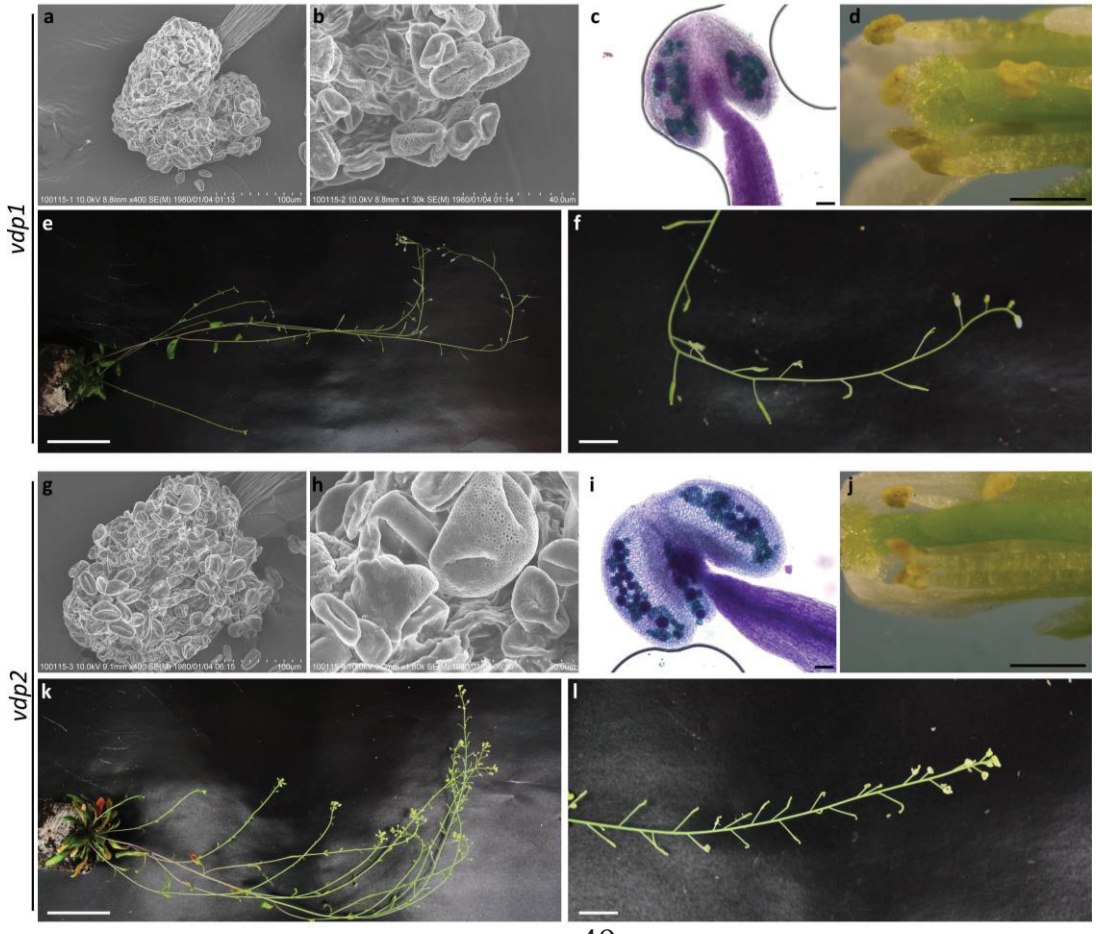

Fig. 2-20 Phenotypic characterization of the *variable-size defective pollen* mutants. a, b, g, h SEM micrographs showing the surface structure of *vdp*-type mutants. **g, h** are magnified parts of the pollen surface structures in (a, g). **c, i** Alexander's staining of anthers of *vdp*-type mutants. **d, j** A dissected flower showing defective anthers and unfertilized stigmas. **e, f, k, l** Plant and silique morphology of the *vdp*-type mutants. The upper panel shows two-month-old *vdp* plants with sterility/semi-sterility phenotypes. Lower panel shows flowering branches with majority of undeveloped siliques. **a-f** *vdp1* and **g-l** *vdp2*. *vdp1* and *vdp2* mutants were isolated among populations of the parental group 35 and 36, respectively. Scale bars = 50 μm in (c, i), 1 mm in (d, j) 5 cm in (e, k), 1 cm in (f, l), and as indicated on SEM micrographs.

3E: irregular aperture numbers and positions (inp; five lines)

Pollen of this subclass were larger in size than those of the wild type and contained abnormal number and position of apertures (Fig. 2-21a). In some cases, more than one pollen were fused together to form a giant pollen grain (Fig. 2-21b; lower panels). Alexander's staining indicated that most pollen were viable, however, a few pollen grains were negatively stained (Fig. 2-21b). The seed morphology of *inp* mutants and the wild type was compared and showed that, in contrast to the wild type which had a majority of normal seeds, most seeds of the mutant plants *inp*2 to *inp5* were unfunctional leaving only dark empty seed-coats without embryos. Approximately half seeds of *inp*1 showed a similar phenotype with other *inp* mutants whereas the other half resembled the wild type (Fig. 2-21c). The *inp* mutants showed a reduced fertility phenotype and produced only some normal siliques (Fig. 2-22).

DAPI staining for pollen of *inp*1 mutant were performed to determine its nuclear content. Results from DAPI staining demonstrated that numerous pollen had an abnormal distribution of the nuclear content (Fig. 2-23a, b). Some pollen showed normal nuclear content (Fig. 2-23c). A large proportion of the pollen were incompletely separated, resulting in distorted shapes (Fig. 2-23a, b, d). The abnormalities in pollen separation and nuclear content suggested that defects in meiotic cytokinesis have occurred.

Interestingly, *inp*1 mutant plants had stomata with defective development. In the wild type, guard mother cell divides symmetrically to form a new cell wall (known as the ventral wall) between two guard cells leaving a central pore. In contrast, in the *inp*1 mutant, many stomata lacked the stomata pore (Fig. 2-23e, h), whereas others developed pores but not separated into two guard cells (Fig. 2-23f, g). The ventral walls were completely missing (Fig. 2-23h) or partially formed (Fig. 2-23e; left). Mutations in stomata cytokinesis have resulted in defective stomata with identical phenotypes. For example, the Arabidopsis

cytokinesis defective1 [107] developed stomata with a range of defects similar to those described here.

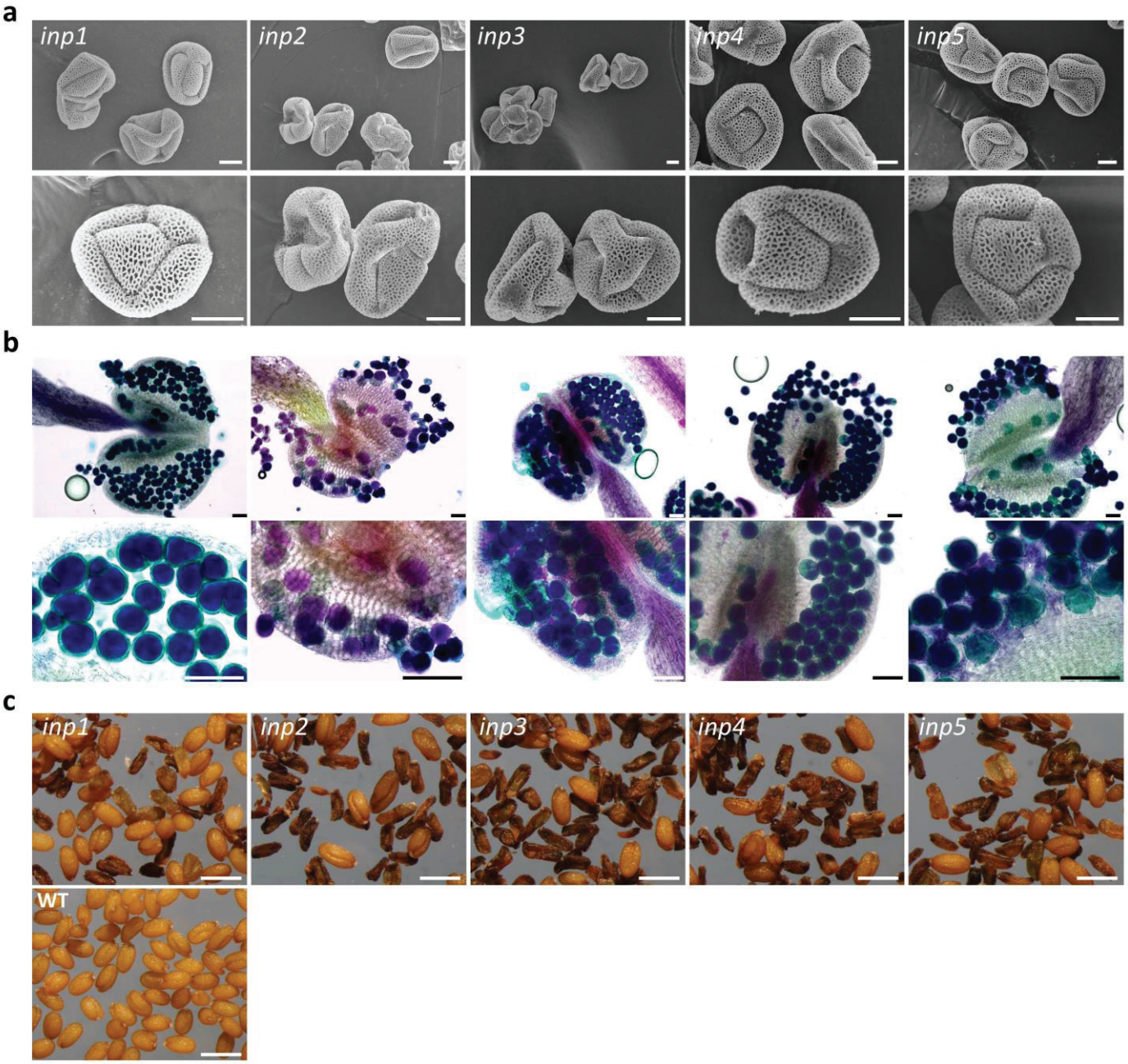

Fig. 2-21 Phenotypic characterization of the *irregular aperture numbers and positions* mutants. a SEM micrographs showing the surface structure of the *inp* mutants (upper panel). Lower panel shows magnified one or two pollen from the upper panel. **b** Alexander's staining of anthers of the *inp* mutants showing pollen grains of normal viability. Lower panel shows magnified parts of the anthers in the upper panel. **c** A comparison of the seed morphology of the *inp* mutants and the wild type. Many seeds of the *inp* mutants were dark-colored, empty. All *inp* mutants were isolated among populations of the parental group 35. Scale bars = 10 μm in (a), 50 μm in (b), and 500 μm in (c).

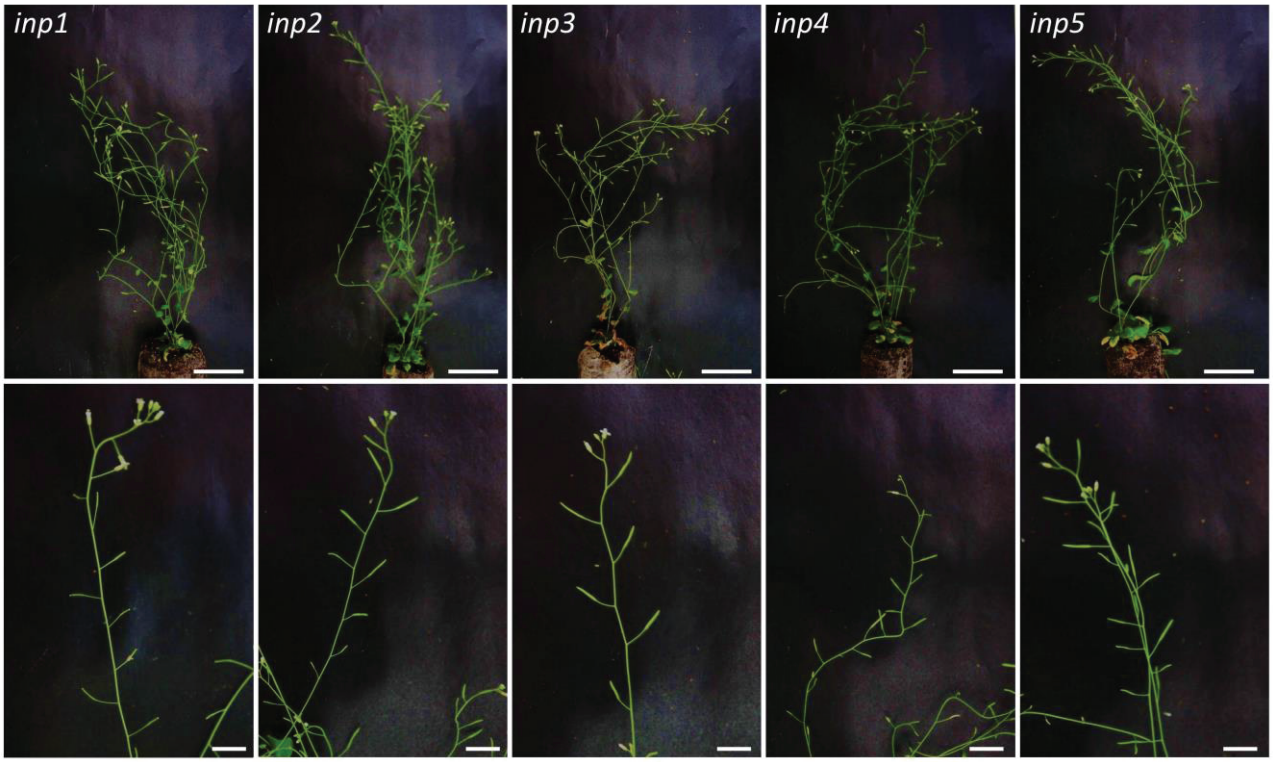

Fig. 2-22 Plant and silique morphology of the *irregular aperture numbers and positions* mutants. Upper panel shows two-month-old plants. Lower panel shows flowering branches with siliques. Scale bars = 5 cm in the upper panel and 1 cm in the lower panel.

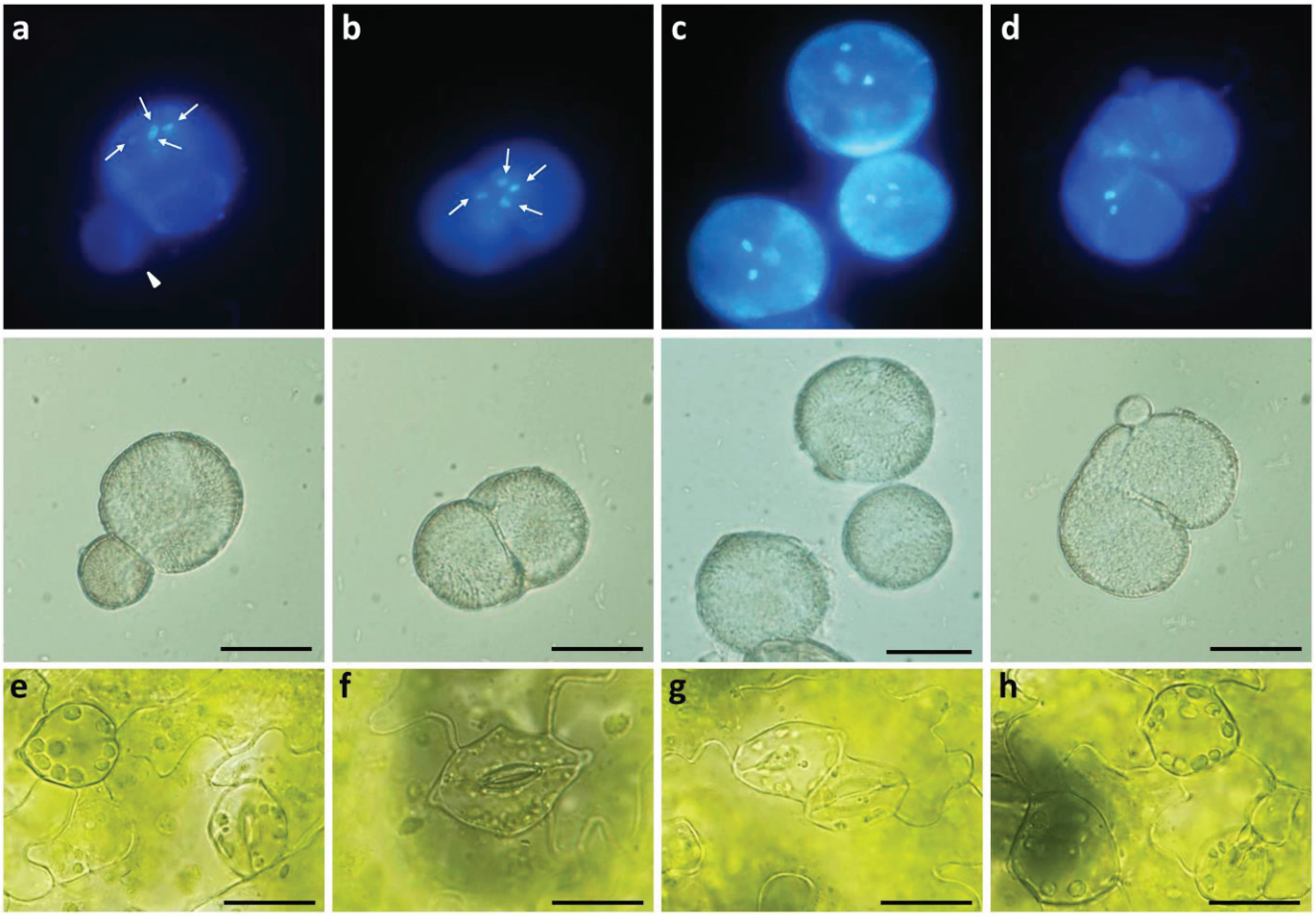

Fig. 2-23 Abnormal cytokinesis in the *inp1* mutant. a-d DAPI staining (upper panel) and bright field images (lower panel) of *inp1* pollen showing abnormal nuclear content (a, b, d) or normal nuclear content (c). The four arrows in (a, b) indicate the four sperm cells that distributed unequally. The arrowhead in (a) shows no DAPI signals. **e-h** Defective stomata development in the *inp1* mutant. Scale bars = 20 μm.

Mutants with similar pollen defects were isolated previously in a genetic screen for pollen exine genes [21] and in a screen for mutants affecting cytokinesis in the embryos [108]. Dobritsa et al. (2011) named such mutants *large and square pollen* and they stated that these mutants or at least some of them were likely dominant, however the *inp* mutants were all recessive with F1 plants exhibiting the wild-type phenotype and F2 plants segregating 3:1 (wild type: *inp*) as expected in recessive mutations (data not shown).

It was reported that mutants with abnormal meiotic divisions or cytokinesis of the microsporocyte show abnormal number and arrangement of apertures in developing microspores. For example, a mutation in the kinesin-encoding *STUD/TETRASPORE (STD/TES)*, a gene required for male-specific meiotic cytokinesis in *Arabidopsis*, leads to the formation of larger pollen with irregular aperture numbers and positions. In *std/tes* mutants, the separation of microspores does not occur due to failure of meiotic cytokinesis [70-72]. Mutations in *TWO-IN-ONE* (*TIO*), a gene regulates both somatic and gametophytic cell cytokinesis, result in enlarged pollen with irregular apertures often in increased number and with abnormal nuclear content [68, 69].

Four out of the five mutants were analyzed by bulked-segregant mapping. Mapping results are summarized in Table 2-1. These four were classified into two groups: *inp1 in one group and inp2, inp3, and inp5* in the other. *inp1* was mapped to the middle of chromosome 1 (the region between 17-23 Mbp) (Fig. 2-24a) and the gene AT1G50240 was identified as the mutation causative gene, indicating that *inp1* is a new allele of *TIO*. Whereas *inp2, inp3, and inp5* mutations were mapped to the middle of chromosome 3 (the region between 12-17 Mbp) (Fig. 2-24b-d), and the gene AT3G43210 was identified as the mutation causative gene, suggesting that *inp2, inp3, and inp5* were new alleles of *STD/TES*.

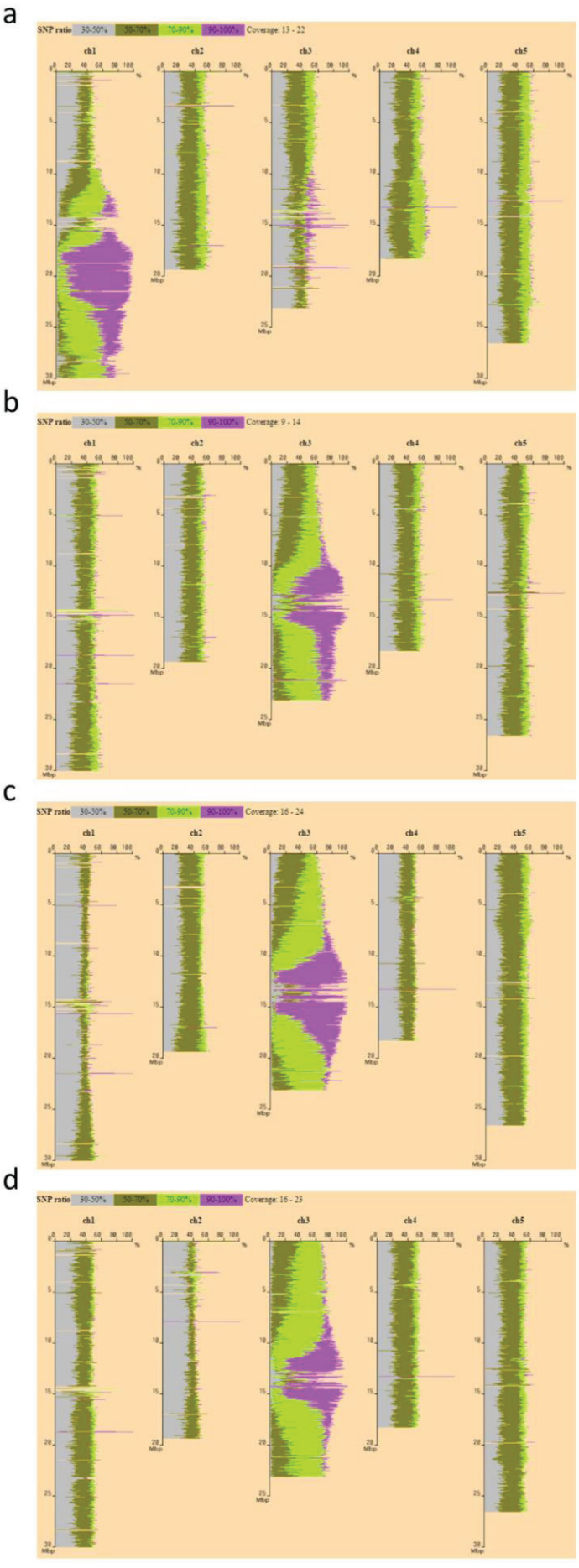

Fig. 2-24 Chromosome mapping of four members from the *irregular aperture numbers and positions* subclass. a-d Bulked-segregant analysis of *inp1* (a), *inp2* (b), *inp3* (c), and *inp5* (d). *inp1* was mapped to the middle of chromosome 1. *inp2*, *inp3*, and *inp5* were mapped to the same region middle of chromosome 3.

3G: aggregated unreleased pollen (aup; five lines)

Flowers of this subclass contained anther that developed normally with similar height and dehiscence to the wild type. Anther dehiscence proceeded normally as the pollen debris can be seen when examined by SEM. However, anthers were filled with pollen debris and bulks of dead pollen that aggregate to form *aup* phenotype (Fig. 2-25a). Pollen were adhesive to the anther walls and failed to release from anthers (Fig. 2-25a). Occasionally a few intact pollen, although collapsed, were observed imbedded on the pollen debris. These pollen had abnormal shapes and surface structures; some of them showed a smooth surface with or without granular structures as in *aup*1, 2, 4, and 5; these few pollen exhibited a similar phenotype to the *faceless pollen* subclass. Whereas pollen of *aup3* had exine with numerous irregular sporopollenin aggregations resembling the *defective reticulate exine* subclass. Anthers of these mutants were filled with dead materials (green-stained) with no or few pollen that were positively stained (Fig. 2-25b). The *aup* subclass produces sterile/semi-sterile plants (Fig. 2-25c).

Three mutants of the *aggregated unreleased pollen* subclass were further identified by next generation sequencing. The *aup2*, *aup3*, and *aup4* were mapped to the bottom of chromosome 1 (data not shown), the middle of chromosome 2 (data not shown), and the bottom of chromosome 4 (data not shown), respectively. Mapping results are summarized in Table 2-1.

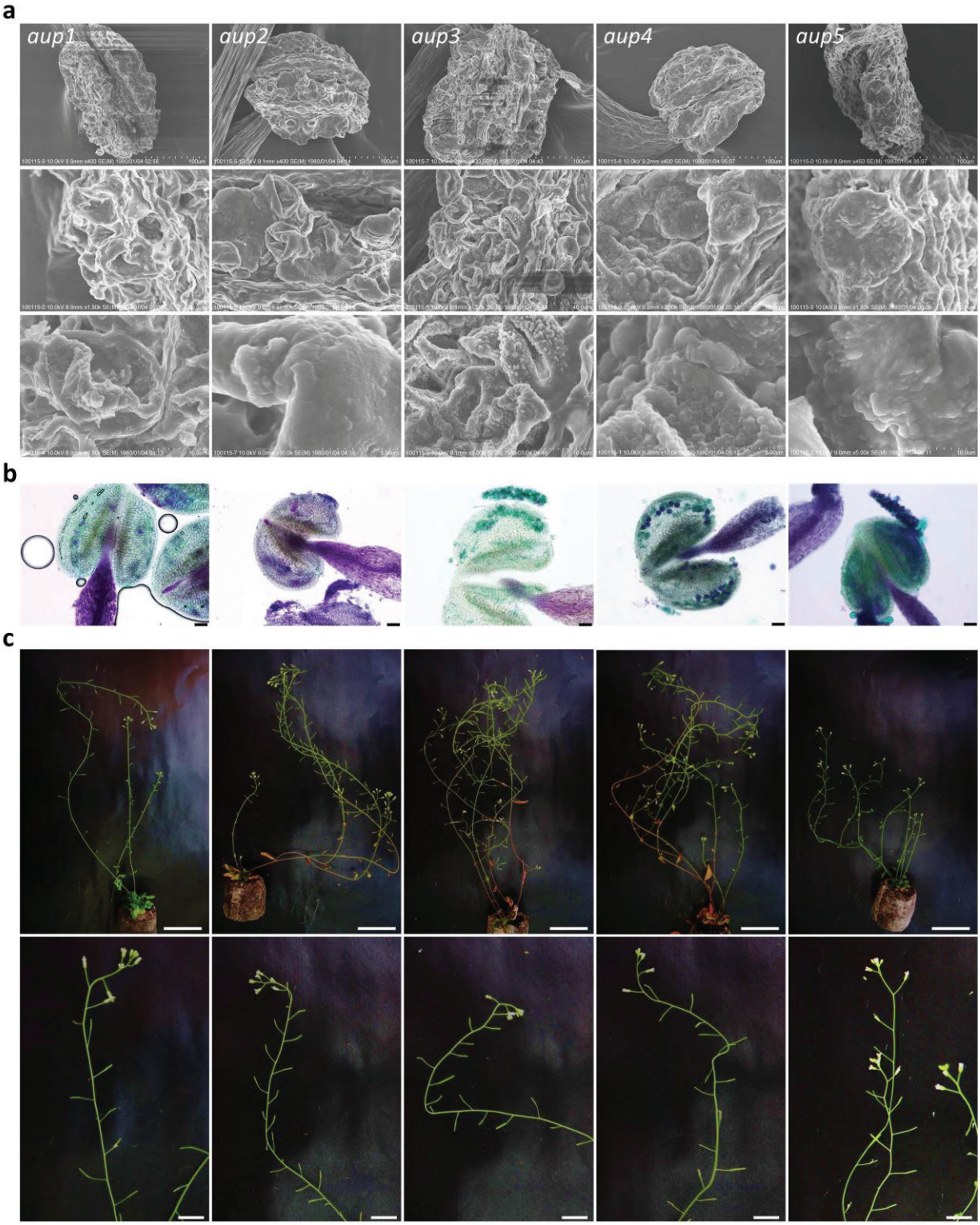

Fig. 2-25 Phenotypic characterization of the *aggregated unreleased pollen* mutants. a SEM micrographs showing anthers of the *aup* mutants (upper panel). Middle panel shows magnified parts of anthers in the upper panel. Lower panel shows the pollen surface structure magnified from the middle panel. **b** Alexander's staining of anthers of the *aup* mutants showing a majority of non-viable pollen. Lower panel shows magnified parts of the anthers in the upper panel. **c** Plant and silique morphology of the *tml*-type mutants. The upper panel shows two-month-old *aup* plants with sterility/semi-sterility phenotypes. Lower panel shows flowering branches with a majority of undeveloped siliques. *aup1*, (*aup2* to *aup4*), and *aup5* mutants were isolated among populations of the parental group 35, 34, and 36, respectively. Scale bars = 50 μm in (b) 5 cm in (upper panel of c), 1 cm in (lower panel of c), and as indicated on SEM micrographs.

3H: tetrahedral pollen (thp; nine lines)

Many of the pollen of *thp* subclass have different shapes losing the characteristic oblong shape of the wild-type pollen and tend to form more or less tetrahedral shaped pollen (Fig. 2-26a, c). In a single anther, a mixture of pollen with wild-type phenotype, tetrahedral phenotype, and rarely rounded phenotype was seen (Fig. 2-26a, c). The arrangement of apertures was also altered in these mutants and in many occasions an extra aperture was developed resulting in a tetracolpate pollen grains (Fig. 2-26b, d). Anthers of *thp* subclass were full of viable pollen as revealed by Alexander's staining (Fig. 2-26b, d). All members of *thp* subclass produce fully fertile plants (Fig. 2-27). Some members of this class were likely dominant as F1 plants resulting of a backcross with Ler showed the *thp* phenotype. None of these mutants were studied further.

3I: quartet-like pollen (qrtl; one line)

This mutant produces tetrads with microspores failed to separate during pollen development. The pollen of this mutant had a reticulate surface indistinguishable from the wild type (Fig. 2-28a). Alexander's staining revealed that all pollen were viable (Fig. 2-28b).the plants were fully fertile with a large number of siliques comparable to the wild type (Fig. 2-28c).

Till now, three quartet (*qrt*) mutants were isolated and the genes responsible for the mutations were identified (*QRT1*3; AT5G55590.1, AT3G07970.1, and AT4G20050.1, respectively) [61-63]. These genes are required for pectin degradation of spore mother cell to separate microspores. To confirm whether this mutant is a novel mutant or an allele of one of these genes and because of the limited number of previously identified genes known to result in quartet phenotype, the author compared the nucleotide sequence of these genes in the *qrtl* mutant. The sequence results confirmed that this mutation is a new allele to *qrt1* gene. The mutation site was detected by DNA capillary sequencing at the first base in the first intron (360 b from the ATG initiation codon). This mutation is a substitution mutation from G to A.

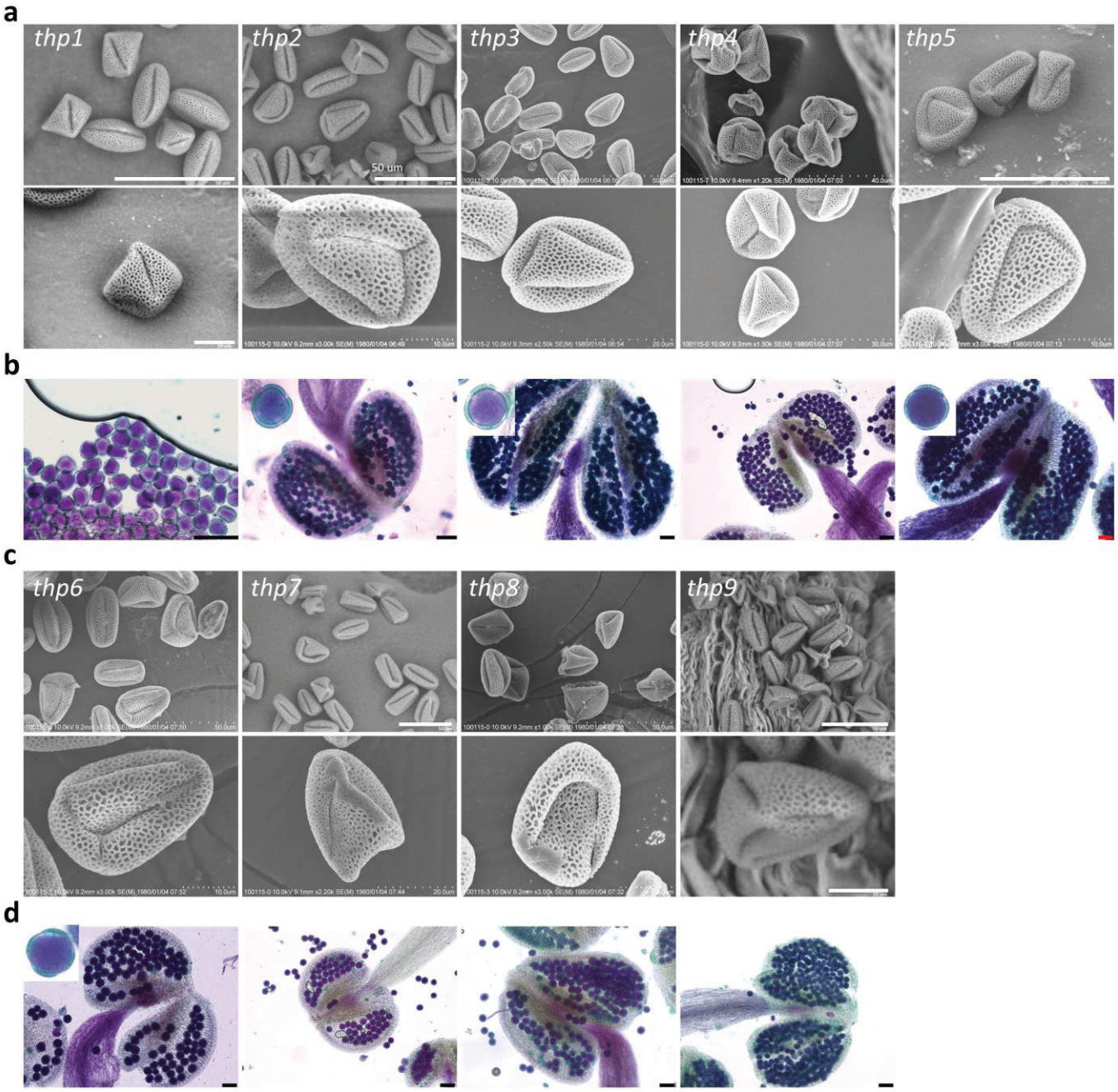

Fig. 2-26 Phenotypic characterization of the *tetrahedral pollen* mutants. a, c SEM micrographs of pollen of the *thp* mutants (upper panel). Lower panel shows pollen grain(s) at a higher magnification. **b, d** Alexander's staining of anthers of the *thp* mutants showing a majority of viable pollen. Some pollen exhibited tetracolpate phenotype with four apertures. *thp1* to *thp5*, (*thp6* and *thp7*), and (*thp8* and *thp9*) mutants were isolated among populations of the parental group 35, 34, and 36, respectively. Scale bars = 50 μm in (b, d) and as indicated on SEM micrographs.

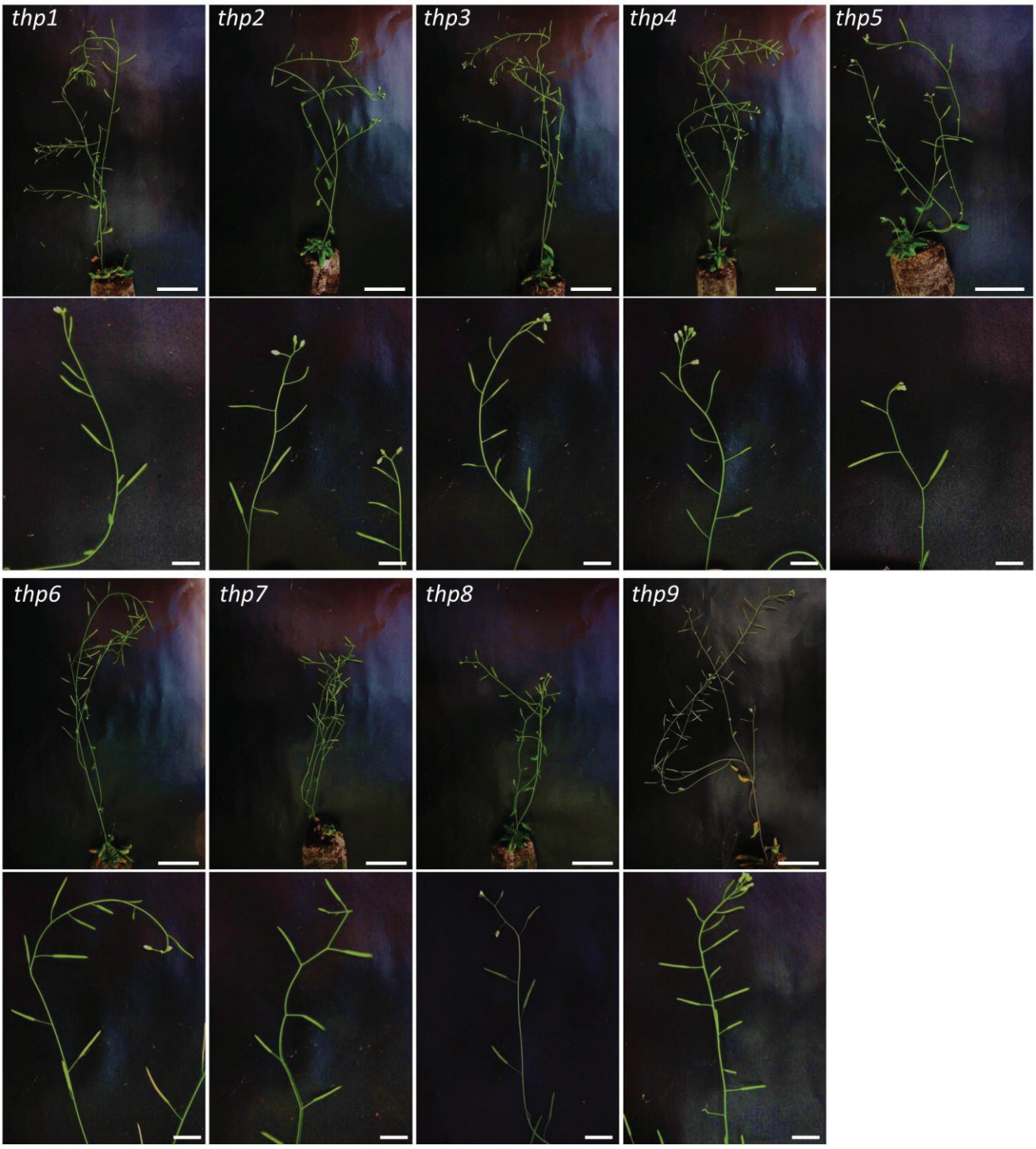

Fig. 2-27 Plant and silique morphology of the *tetrahedral pollen* mutants. Upper panel shows two-month-old plants with high fertility. Lower panel shows flowering branches with a majority of elongated siliques. Scale bars = 5 cm in the upper panel and 1 cm in the lower panel.

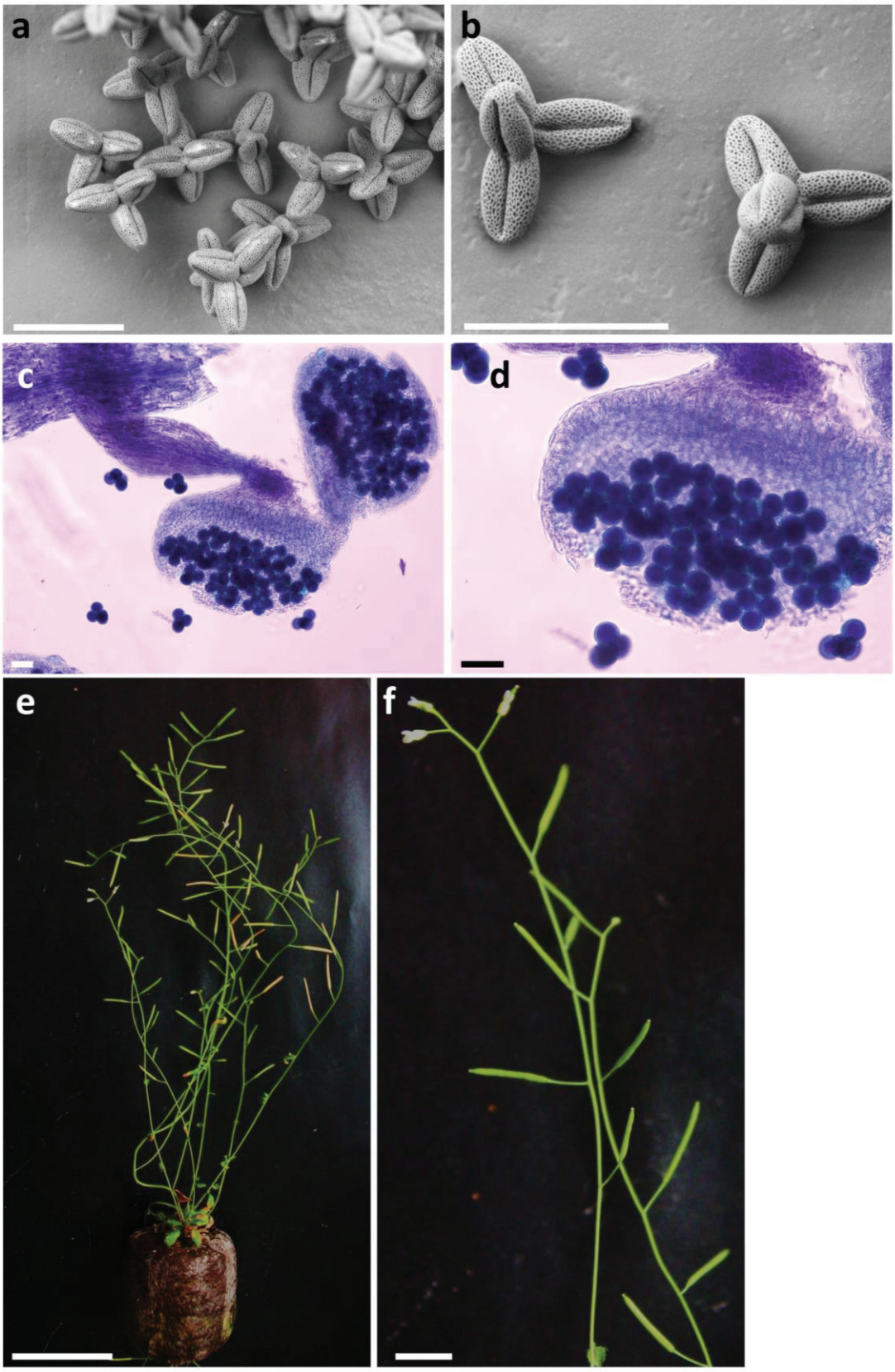

Fig. 2-28 Phenotypic characterization of the *quartet-like pollen* mutants. a, b SEM micrographs of pollen grains of the *qrtl* mutant. **c, d** Alexander's staining of anthers of the *qrtl* mutant. **e, f** Plant and silique morphology of *qrtl* mutant. **e** Two-month-old *qrtl* plants with normal fertility phenotypes. **f** Flowering branches with majority of fertile siliques. *qrtl* mutant was isolated among populations of the parental group 35. Scale bars = 50 μm in (a-d), 5 cm in (e), and 1 cm in (f)

The author used SEM at high magnification to screen a large population (~ 10,000) of M2 mutagenized *Arabidopsis thaliana* (Col-0 accession). The strategy used in this screen, although laborious, has shown to be effective for isolation of numerous mutants with a wide range of defects in anther and pollen development, some of them showing novel phenotypes.

The isolated mutant lines (101) were classified into three classes: flower-level, anther-level, and pollen-level mutants. Flower-level class included the mutants with defects in flower development (missing or abnormal structure of one or more of the floral parts) and flowers with defective floral parts. Mutants of anther-level had defects in anther dehiscence or production of pollen. Pollen-level class contained the largest number of mutants showing a remarkably variable defects, including altered pollen wall structure or ornamentation, altered shapes and sizes, failure in separation from tetrads, and failure to release from anthers.

The distinctiveness of the screen described here resides in the capability to isolate mutants with mild defects in the exine surface structure that would be neglected with using other screening strategies e.g., visual screen by the naked eye, dissecting microscope-based, or confocal microscope-based screens and in using the simple streamlined mapping by next generation sequencing to identify the mutations' causative gene(s). Most of mutants in the *defective reticulate exine* subclass showed stunning phenotypes and potentially they may encode novel genes. To get maximum benefits of this screen, future work will include the identification of the genes responsible for the remaining unmapped mutations and also examining more T-DNA lines to link the mutations with the observed phenotypes.

Chapter 3

AtSEC23A and AtSEC23D, two Arabidopsis COPII components, are essential for pollen wall development and exine patterning

Introduction

The multi-layered pollen wall plays multiple functions in a plant reproduction. Besides the structural and physical support that it provides to the microspore cytoplasm, it helps the male gametes survive severe environmental conditions such as abrasion, desiccation, UV radiation, and microbial attack [109]. The wall also facilitates pollination and male-female interaction processes. In addition, it allows normal microspore development by maintaining the integrity of the microspore plasma membrane [64]. The pollen wall has an architecturally-complex structure comprises two main layers; the inner pectocellulosic-based intine and the outer sporopollenin-based exine. Additionally, in dry stigma species including *Arabidopsis thaliana*, a lipid-based pollen coat (also known as tryphine or pollen kitt) is formed as a third wall component covering the exine layer. The exine wall is divided into two layers; inner nexine and outer sexine, which is further, subdivided into two structures the bacula roofed by the tectum [26]. The bacula and the tectum are responsible for the characteristic and taxon-specific architecture of the exine which is reticulate in *A. thaliana*. The highly resistant character of the pollen wall is attributed to the robust biopolymer material called sporopollenin [28, 81]. Due to its complexity and extreme recalcitrance to degradation, the exact composition of sporopollenin is still elusive, but chemical evidence suggests that it made up of a mixture of phenolics and long-chain fatty acid derivatives, coupled by ester and ether linkages [110-113].

Pollen wall development relies largely on the adjacent sporophytic anther layers, especially the tapetum, which plays a major secretory role and provides the developing microspores with metabolites, enzymes, nutrients, and structural components necessary to build up the outer exine layer [26, 28, 103, 104]. In particular, during the early stages of pollen development, tapetum cells secrete β-1,3-glucanase (callase) to degrade the callose wall around tetrads to release the microspores [114, 115]. Immediately, after the microspore release, tapetal cells synthesize lipidic-sporopollenin precursors as major components of the exine wall. And finally, during the late stages of pollen development, tapetal cells synthesize and store lipidic materials required for pollen coat formation in two specialized organelles, the plastid-derived elaioplasts and the endoplasmic reticulum-derived tapetosomes. When tapetal cells undergo programmed cell death, the stored materials in those organelles are discharged to the locule and deposited on pollen exines, completing the final pollen-wall structure. Thus, normal pollen wall development relies, in turn, on the normal development of

the tapetum. Premature or delayed differentiation of tapetal cells, as well as alteration of their internal structure, usually result in defective pollen development and reduced fertility [28, 116, 117]. Several male sterile mutants exhibit abnormal or delayed tapetal development such as *ABORTED MICROSPORES* (AMS), *MALE STERILITY1* (*MS1*), *DYSFUNCTIONAL TAPETUM1* (*DYT1*), *TAPETAL DEVELOPMENT AND FUNCTION1* (*TDF1*), and *TAPETUM DETERMINANT1* (*TPD1*) [118-124].

The coat protein complex II (COPII)-mediated vesicle transport from the endoplasmic reticulum (ER) to the Golgi apparatus represents the first step of the secretory pathway [125]. Newly synthesized lipids and proteins exit the ER through COPII-coated vesicles heading to the Golgi apparatus for further modification and sorting before reaching their final destinations (i.e., plasma membrane, extracellular space, or other storage and lytic organelles [126, 127]). According to the current model in yeast and mammals, the COPII-coated vesicle formation requires the sequential recruitment of the five cytosolic components, Sar1, SEC23/24, and SEC13/31 [32, 33]. At first, Sar1 is recruited to the ER membrane by the activity of its guanine nucleotide exchange factor SEC12 [34, 35]. Activated Sar1 further recruits the SEC23/24 complex by the direct interaction with SEC23 and forms a ‘‘prebudding complex’’ [36]. The prebudding complex captures the cargo protein and initiates vesicle curvature. In the prebudding complex, SEC23 acts as Sar1 GAP (GTPase-activating protein) and plays a role in cargo recognition with SEC24 [128-130]. At last, SEC13/31 heterotetramer is subsequently recruited onto the prebudding complex, by the interaction between SEC31 and SEC23, to complete the vesicle formation process [37, 38]. Previous studies have revealed a part of conservative amino acids functions of SEC23 homologs in yeast and human. The arginine residue 722 of the yeast ScSEC23 has shown to be necessary to stimulate Sar1 GTPase activity [36]. SEC23 inserts this “arginine finger” into the active site of SAR1 during SEC23-SAR1 interaction [36]. In human, a missense mutation in hSEC23A at the conservative phenylalanine residue 382 (to leucine) has shown to be responsible for the disorder cranio-lenticulo sutural dysplasia disease [131, 132]. In plants, an amino acid substitution in AtSEC23A at the conserved aspartate residue 484 (to cysteine) has reported to be essential for the unique interaction with AtSAR1in *Arabidopsis* [133].

A growing body of evidence demonstrates the involvement of COPII components in regulating plant growth and development. The characterization of two *AtSEC24* proteins showed that both *AtSEC24B* and *AtSEC24C* were redundantly involved in male- and female-gametophyte development in *A. thaliana* [91]. *AtSEC24A* is essential for male fertility [134],

ER-Golgi integrity [135, 136], and for maintaining cell-size patterning in sepals [137]. The specific interaction between *AtSAR1* and *AtSEC23A* is required for their function in ER export of proteins in *A. thaliana* [133]. More recently, *AtSEC31B* is required for pollen wall development probably by regulating the early secretory pathway of tapetal cells [138].

Although SEC23 is an essential component of the COPII vesicle formation, its phenotypic characterization and involvement in regulating plant growth and development have yet to be elucidated. Moreover, the functional differences among the SEC23 homologs remain to be determined. In this study, the author identified and characterized two SEC23 homologs, *AtSEC23A* and *AtSC23D*, which are required for proper pollen wall formation, exine patterning, and tapetum development. Both *AtSEC23A* and *AtSEC23D* exhibited the characteristic COPII localization at ER exit sites (ERESs). Double *atsec23ad* mutant plants had defective pollen walls, and altered development of tapetal cells with morphological abnormalities of the ER, Golgi, elaioplasts, and tapetosomes. Our results indicate that ER export of proteins in the early secretory pathway of tapetal cells is a key factor for pollen wall development. Our work provides a direct link between the tapetum early secretory pathway and sporopollenin deposition and exine patterning. Also, this work points to the functional diversity of SEC23 homologs in plants.

Materials and methods

Plant materials, growth condition, and transformation

Seeds of *A. thaliana* T-DNA insertion lines (Col-0 background), and *quartet1* (*qrt1*) mutant were obtained from the ABRC, Ohio State University, USA. *A. thaliana* ecotype Col-0 was used as the wild type. The seeds were surface-sterilized, plated on a Murashige and Skoog (MS) agar medium, and cold treated at 4°C for 2-3 days. The seeds were then germinated at 22°C under 24 h continuous lights. After 10-14 days, seedlings were transplanted to Jiffy-7 (Jiffy Preforma Production K. K, Yokohama, Japan) and grown at 22°C under long-day conditions (16 h light/8 h dark) or under 24 h continuous light. Transformations of *A. thaliana* was carried out by the floral-dip method [10] or the floral inoculating method [139] and transgenic plants were screened on MS agar medium containing 100 mg L^{-1} Cefotax (Chugai Pharmaceutical, Tokyo, Japan) and appropriate antibiotics (20 mg L^{-1} hygromycin B or 20 mg L^{-1} kanamycin). *Nicotiana benthamiana* seeds

were planted directly on soil and vernalized for 3 days at dark, then move to a growth chamber to grow at 25°C under 24 h continuous light.

Table 3-1. Oligonucleotides used in this study.

Oligos	Sequence
*att*B1 adaptor	5'-GGGGACAAGTTTGTACAAAAAAGCAGGCT-3'
*att*B2 adaptor	5'-GGGGACCACTTTGTACAAGAAAGCTGGGT-3'
P_{nos}-*att*B4	5'-GGGGACAACTTTGTATAGAAAAGTTGGCTGAGACACTATCATGAGCGGAGAATTAAGG-3'
P_{nos}- *att*B1r	5'-GGGGACTGCTTTTTTGTACAAACTTGTGACACTAGATCCGGTGCAGATTATTTG-3'
$P_{AtSEC23A}$-*att*B1	5'-GGGGACAAGTTTGTACAAAAAAGCAGGCTCCGACACTCGGGATTATTGATGGGAAATC-3'
$P_{AtSEC23A}$-*att*B2	5'-GGGGACCACTTTGTACAAGAAAGCTGGGTAGACACTCGGATTCCGAAGTTTCTACTT-3'
$P_{AtSEC23A}$-*att*B4	5'-GGGGACAACTTTGTATAGAAAAGTTGGCTGAGACACTCGGGATTATTGATGGGAAATC-3'
$P_{AtSEC23A}$-*att*B1r	5'-GGGGACTGCTTTTTTGTACAAACTTGTGACACTCGGATTCCGAAGTTTCTACTT-3'
$P_{AtSEC23D}$-*att*B1	5'-GGGGACAAGTTTGTACAAAAAAGCAGGCTCCGACACTCTGGAAAACCTATTCAAGCCA-3'
$P_{AtSEC23D}$-*att*B2	5'-GGGGACCACTTTGTACAAGAAAGCTGGGTAGACACTTGTTTCAGATCAGATCCTTCC-3'
$P_{AtSEC23D}$-*att*B4	5'-GGGGACAACTTTGTATAGAAAAGTTGGCTGAGACACTCTGGAAAACCTATTCAAGCCA-3'
$P_{AtSEC23D}$-*att*B1r	5'-GGGGACTGCTTTTTTGTACAAACTTGTGACACTTGTTTCAGATCAGATCCTTCC-3'
AtSEC23A-*att*B1	5'-AAAAAGCAGGCTCCGACACTATGGCTAACTTACCGAAATC-3'
AtSEC23A-*att*B2	5'-AGAAAGCTGGGTAGACACTCCTGGGCTCAGGAGGCAC-3'
AtSEC23D-*att*B1	5'-AAAAAGCAGGCTCCGACACTATGGCAGTGAGAGCAACGGT-3'
AtSEC23D-*att*B2	5'-AGAAAGCTGGGTAGACACTCTTCATGTATTCAGTGACAC-3'
RT-*AtSEC23A*-F	5'-CACATTCAGAAACTCACGAG-3'
RT-*AtSEC23A*-R	5'-CCTGGGCTCAGGAGGCAC-3'
RT-*AtSEC23D*-F	5'-GCCTCTCTGGAAGATGGAGT-3'
RT-*AtSEC23D*-R	5'-CTTCATGTATTCAGTGACAC-3'
ACT2-F	5'-CATCTTCTTCCGCTCTTTCTTTCCA-3'
ACT2-R	5'-CTCTTACAATTTCCCGCTCTGCTGT-3'
GN-*AtSEC23A*-F	5'-CATAAGGTGAGTCTGCAGCT-3'
GN-*AtSEC23A*-R	5'-GACGTCGGTTAATACCACGT-3'
GN-*AtSEC23D*-R	5'-GAGATTAGCTTGTAAGCTTG-3'
T-DNA-LB	5'-GCAATCAGCTGTTGCCCGTCTCACTGGAG-3'

Genotyping analysis

Genomic DNAs were extracted from mutant-plant leaves following [140]. The T-DNA insertions were analyzed by PCR genotyping with the specific primers GN-*AtSEC23A*-F and GN-*AtSEC23A*-R for *AtSEC23A* or RT-*AtSEC23D*-F and GN-*AtSEC23D*-R for *AtSEC23D*. The T-DNA-LB was used as a common primer for detection of T-DNA. The primers are listed in Table 3-1.

RNA extraction and RT-PCR

Total RNAs were extracted from various tissues of the wild-type plants using the RNeasy Mini Kit (Qiagen, Tokyo Japan), and 1.0 mg of total RNAs was used as a template to synthesize cDNAs using ReverTraAce (TOYOBO, Osaka, Japan), according to the manufacturer's instructions. The *ACTIN2* (At3g18780) was used as an internal reference. RT-PCR was carried out with a 0.2 mg of cDNAs using KOD-Plus-Neo DNA polymerase (TOYOBO) for 26 cycles. The specific primers RT-*AtSEC23A*-F, RT-*AtSEC23A*-R, RT-*AtSEC23D*-F, RT-*AtSEC23D*-R, *ACT2*-F, and *ACT2*-R used for RT-PCR are listed in Table 3-1.

Preparation of promoter and ORF entry clones

Two types of promoter entry clones were prepared for each of *AtSEC23A* and *AtSEC23D*. Approximately 2kbp upstream of the start codon were used for construction of pDONR201-$P_{AtSEC23A}$ (*att*L1-$P_{AtSEC23A}$-*att*L2), pDONRP4-P1R-$P_{AtSEC23A}$ (*att*L4-$P_{AtSEC23A}$-*att*R1), pDONR201-$P_{AtSEC23D}$ (*att*L1-$P_{AtSEC23D}$-*att*L2) and pDONRP4-P1R-$P_{AtSEC23D}$ (*att*L4-$P_{AtSEC23A}$-*att*R1) entry clones. For ORF entry clones, nucleotide sequences corresponding with translation initiation site to last amino acid of AtSEC23A and AtSEC23D were used for construction of pDONR201-*AtSEC23A* (*att*L1-AtSEC23A-*att*L2) and pDONR201-*AtSEC23D* (*att*L1-AtSEC23D-*att*L1) ORF entry clones, respectively. The detailed description of construction method can be summarized as follows. The DNA fragment corresponding to nucleotides -1996 to -1 (A of initiation codon is +1) of *AtSEC23A* was amplified from *A. thaliana* wild-type genomic DNA with the primers $P_{AtSEC23A}$-*att*B1 and $P_{AtSEC23A}$-*att*B2, or $P_{AtSEC23A}$-*att*B4 and $P_{AtSEC23A}$-*att*B1r (Table 3-1), to add *att*B1 and *att*B2, or *att*B4 and *att*B1 sequences to its 5' and 3' ends, respectively. The resulting fragments *att*B1-$P_{AtSEC23A}$-*att*B2 and *att*B4-$P_{AtSEC23A}$-*att*B1 were individually subjected to a BP reaction with pDONR201 or pDONRP4-P1R, following the manufacturer's instructions (Thermo

Fisher Scientific, Kanagawa, Japan), to construct pDONR201-$P_{AtSEC23A}$ (*att*L1-$P_{AtSEC23A}$-*att*L2) and pDONRP4-P1R-$P_{AtSEC23A}$ (*att*L4-$P_{AtSEC23A}$-*att*R1) promoter entry clones. With the same method, pDONR201-$P_{AtSEC23D}$ (*att*L1-$P_{AtSEC23D}$-*att*L2) and pDONRP4-P1R-$P_{AtSEC23D}$ (*att*L4-$P_{AtSEC23D}$-*att*R1) promoter entry clones were generated by amplifying the DNA fragment corresponding to nucleotides -2126 to -1 of *AtSEC23D* using the primers $P_{AtSEC23D}$-*att*B1 and $P_{AtSEC23D}$-*att*B2 or $P_{AtSEC23D}$-*att*B4 and $P_{AtSEC23D}$-*att*B1r (Table 3-1), respectively. The nopaline synthase promoter was amplified using pGWB401 [141] as a template with the primers P_{nos}-*att*B4 and P_{nos}-*att*B1r (Table 3-1). The resulting *att*B4-P_{nos}-*att*B1 was subjected to BP reaction with pDONRP4-P1r to construct pDONRP4-P1R-P_{nos} (*att*L4-P_{nos}-*att*R1) promoter entry clone. Nucleotide sequences corresponding to the translation initiation site to the last amino acid of *AtSEC23A* was amplified from Arabidopsis full-length cDNA clone pda01836 obtained from RIKEN BRC (RIKEN, Tsukuba, Japan) by two-step adaptor PCR. In the first PCR, the primers *AtSEC23A*-*att*B1 and *AtSEC23A*-*att*B were used for the amplification. In the second PCR, the *att*B1 adaptor and *att*B2 adaptor primers were used to add *att*B1 and *att*B2 sequences to their 5' and 3' ends, respectively. The resulting *att*L1-*AtSEC23A*-*att*L2 was subjected to a BP reaction with pDONR201 to construct the pDONR201-*AtSEC23A* (*att*L1-*AtSEC23A*-*att*L2) ORF entry clone. Similarly, pDONR201-*AtSEC23D* (*att*L1-*AtSEC23D*-*att*L2) ORF entry clone was constructed using *att*B1-*AtSEC23D*-*att*B2 fragment amplified from pda04203 (RIKEN) with *AtSEC23D*-*att*B1 and *AtSEC23D*-*att*B2 as primers in the 1st PCR (Table 3-1).

Preparation of GFP fusion constructs for complementation and expression analyses

The pDONRP4-P1R-$P_{AtSEC23A}$ and pDONR201-*AtSEC23A* entry clones were subjected to LR reaction with R4pGWB550 [142] to generate the $P_{AtSEC23A}$:*AtSEC23A-G3GFP*. The $P_{AtSEC23D}$:*AtSEC23D-G3GFP* was prepared by the same procedure using pDONRP4-P1R-$P_{AtSEC23D}$ and pDONR201-*AtSEC23D* entry clones.

Staining and semi-thin sectioning

Alexander's and 4',6-diamidino-2-phenylindole (DAPI) staining were performed as described in [91]. For Alexander's staining, anthers were observed by a BZ-X710 All-in-One Fluorescent Microscope (KEYENCE, Osaka, Japan). DAPI fluorescence was detected using a BX51 fluorescence microscope (Olympus, Tokyo, Japan) equipped with a UV mirror unit. For the aniline blue staining, buds at the tetrad stage were squeezed onto a slide containing a

drop of aniline blue solution (100 mg L^{-1} in 50 mM potassium phosphate buffer, pH 7.5) and observed by the BX51 fluorescence microscope. For the auramine O staining, pollen grains were placed on a slide containing a drop of auramine O solution (0.001% auramine O in 50 mM Tris-HCl, pH 7.5; [21]) and viewed by the below-mentioned confocal microscopy.

Floral buds with different developmental stages were fixed in 4% paraformaldehyde solution, dehydrated in a graded ethanol series, embedded in Technovit 7100 resin (Heraeus Kulzer, Wehrheim, Germany), and sectioned (2-3 μm) by an RV-240 rotary microtome (Yamato Kohki Industrial, Saitama, Japan). Semi-thin sections were stained in a toluidine blue solution (1% toluidine blue, 1% sodium borate), shortly heated on a hot plate (46°C), rinsed with water, and viewed by the all-in-one fluorescent microscope.

Promoter:β-glucuronidase (*GUS*) assay

For the promoter:*GUS* assays, pDONR201-$P_{AtSEC23A}$ and pDONR201-$P_{AtSEC23D}$ entry clones were applied for LR reactions with pGWB233 [143] to make $P_{AtSEC23A}$:*GUS* and $P_{AtSEC23D}$:*GUS* constructs. These constructs were transferred to *Agrobacterium tumefaciens* strain C58C1 (pMP90) by electroporation and then used for transformation of *A. thaliana* wild type. T2 or T3 lines were stained and examined following the method described previously [144].

In vitro pollen germination

Pollen of at least six recently-opened flowers of wild type, *atsec23a*, *atsec23d*, *atsec23ad*, and complemented *atsec23a* lines carrying $P_{AtSEC23A}$:*AtSEC23A-G3GFP* were tested for germination *in vitro* according to [145]. Images were captured using a SZX16 stereo-microscope (Olympus) and germination rate was calculated by counting at least 500 pollen grains for each sample with the ImageJ (http://rsbweb.nih.gov/ij/).

Transient co-localization analyses in *N. benthamiana* leaves

R4 dual-site Gateway cloning system (Chapter 4) was used to express two genes in co-localization analysis. The pDONRP4-P1R-P_{nos} promoter entry clone, pDONR201-*AtSEC23A*, pDONR201-*AtSEC23D*, pDONR201-*AtSEC24A* [91], pDONR201-*SYP31* [91], and pRbcSTP221 (Chapter 4) ORF entry clones were used for preparation of various two-gene constructs with R4pDD650-MD8 and R4pGWB6459-MD8 according to the cloning protocol described in (Chapter 4). P_{nos}:*AtSEC24A-TagRFP*-P_{nos}:*AtSEC23A-G3GFP*,

P_{nos}:AtSEC24A-TagRFP-P_{nos}:AtSEC23D-G3GFP, *P_{nos}:SYP31-TagRFP-P_{nos}:AtSEC23A-G3GFP*, *P_{nos}:SYP31-TagRFP-P_{nos}:AtSEC23D-G3GFP*, *P_{nos}:RbcsTP-TagRFP-P_{nos}:AtSEC23A-G3GFP*, *P_{nos}:RbcsTP-TagRFP-P_{nos}:AtSEC23D-G3GFP*, and *P_{nos}:AtSEC23A-TagRFP-P_{nos}:AtSEC23D-G3GFP* were generated as the final two-gene constructs.

A. tumefaciens strain EHA101 carrying each two-gene construct or the gene-silencing suppressor vector p19 [146] was cultured in 5ml of Luria broth (LB) medium supplemented with appropriate antibiotics at 28°C with shaking for 2 days. Agrobacterium cultures were centrifuged at 4500 × *g* for 10 min and the cell pellets were re-suspended in adequate amount of an infiltration medium (10 mM MES, 10 mM $MgCl_2$, and 150 mM acetosyringone) to adjust the OD_{600} to 1.0. After incubation of 3 to 4 h at room temperature, each culture of two-gene construct were mixed with p19 at a 1:1 ratio and diluted by the infiltration medium to a total volume of 1ml. The diluted mixture was used to infiltrate the abaxial side of *N. benthamiana* leaves by a syringe. After incubation of 3 to 4 days at 25°C the leaves were examined by the below-mentioned confocal microscopy.

Confocal microscopy

The fluorescent signals of G3GFP and TagRFP were viewed with a TCS SP5 confocal laser scanning microscope (CLSM) (Leica Microsystems, Wetzlar, Germany) using an HCX IRAPO L 25.0 X 0.95 water-immersion objective lens or an HCX PLAPO 100.0 X1.40-0.70 oil-immersion objective lens. In observation of anthers, setting described in [147] was applied to distinguish the G3GFP signals from the chlorophyll auto-fluorescence in anthers of transgenic *A.thaliana*. In the co-localization experiments in *N. benthamiana*, G3GFP was excited with the argon laser line (488 nm) and its fluorescence was captured using the dichroic mirror BP500-530 nm. TagRFP was excited with the helium-neon laser line (543 nm) and its fluorescence was detected using the dichroic mirror BP555-615 nm. The fluorescence of pollen stained with auramine O was detected with the CLSM using the fluorescein isothiocyanate (FITC) settings an HCX PLAPO 100.0 X1.40-0.70 oil-immersion objective lens. Images were processed and converted to the TIFF format using Photoshop 8.0 (Adobe Systems Incorporated, CA, USA).

Electron microscopy

Scanning electron microscope (SEM) observations were performed as described [91] using either an S-4800 field emission SEM (Hitachi High-Tech, Tokyo, Japan) or a TM3000 miniscope (Hitachi High-Tech).

Floral buds containing appropriate developmental stages were detached form the wild-type, *atsec23a*, *atsec23d*, and *atsec23ad* inflorescences and immediately fixed in 2.5% glutaraldehyde in 50 mM sodium phosphate buffer (pH 7.2). The specimens were further treated with 1.5% osmium tetroxide in 100 mM cacodylate buffer (pH 7.4) for 90 min and embedded in EPON 812 (TAAB, Berkshire, UK). Ultrathin sections (70 nm) were double-stained with 3% uranyl acetate and lead citrate then observed with a JEM-1400 transmission electron microscope (JEOL, Tokyo, Japan).

Results

AtSEC23A and *AtSEC23D* are divergent from other Arabidopsis SEC23 homologs

Within *A. thaliana* genome, there are five homologs for SAR1, seven for SEC23, three for SEC24 and two for each SEC12, SEC13, SEC16 and SEC31 [148, 149]. The seven SEC23 homologs, At4g01810, At1g05520, At2g21630, At2g27460 At3g23660, At4g14160, and At5g43670 were named AtSEC23 A, B, C, D, E, F, and G, respectively, following Chung et al. (2016). Phylogenetic analysis of SEC23 homologs in yeast, green algae, plants, and mammals showed that five of the *A. thaliana* SEC23 homologs were clustered in a single clade with rice and green algae homologs (Fig. 3-1a). While both AtSEC23A and AtSEC23D were divergent from other AtSEC23 proteins; each was separated in a distinct clade with only homologs of rice. AtSEC23A and AtSEC23D showed no significant identity with other AtSEC23 homologs (Fig. 3-2).

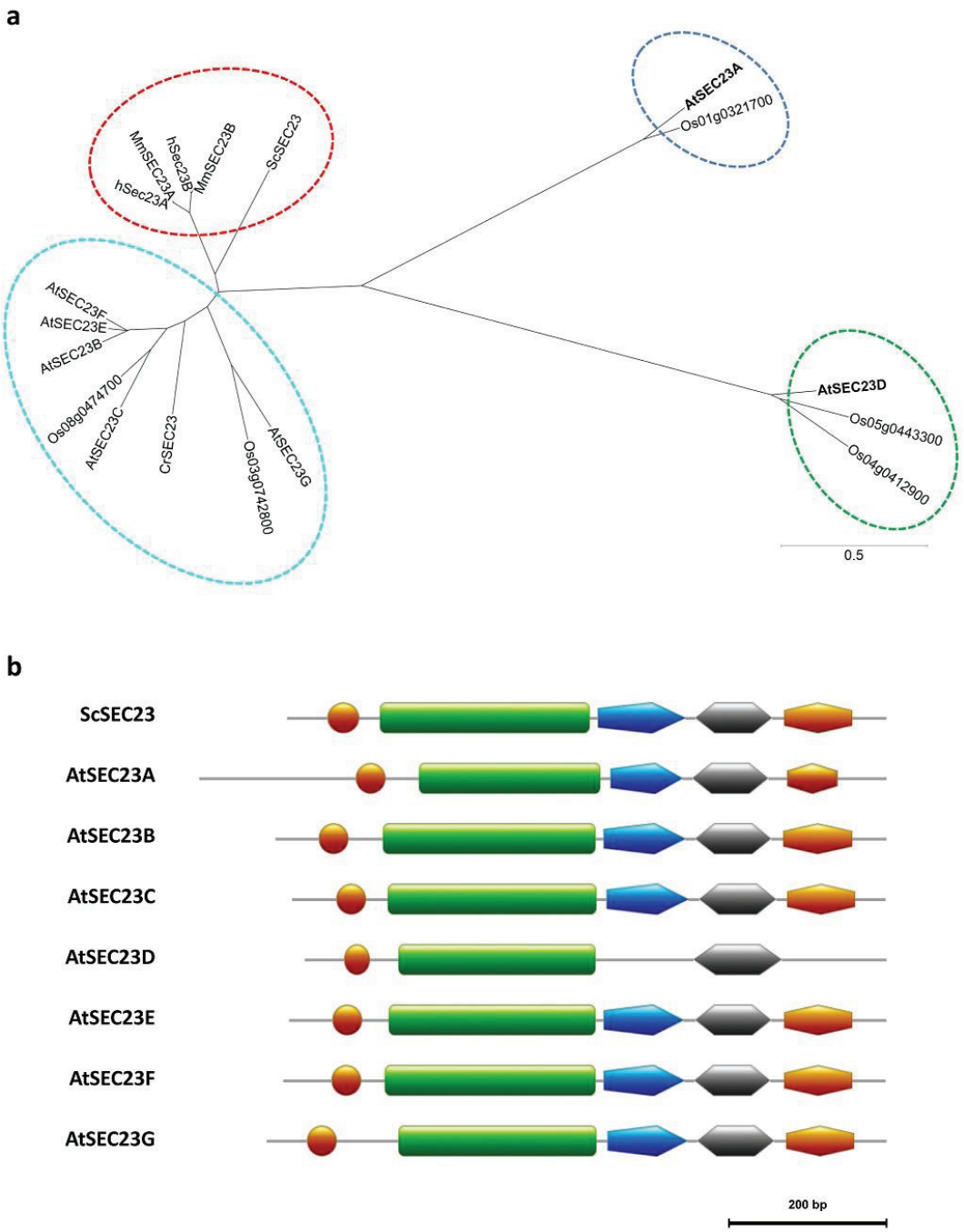

Fig. 3-1 Phylogenetic and domain structure analyses of SEC23 homologs. a A phylogenetic tree of SEC23 homologs in plants (*Arabidopsis thaliana* and *Oryza sativa*), green algae (*Chlamydomonas reinhardtii*) mammals (*Homo sapiens* and *Mus musculus*), and yeast (*Saccharomyces cerevisiae*). Amino acid sequences were aligned using the neighbor-joining method by the ClustalW ver. 1.83 program (http://clustalw.ddbj.nig.ac.jp/) and bootstrap values of 1,000 replications. The tree was drawn by GENETYX-Tree software (Genetyx, Tokyo, Japan) based on the alignment results. The scale bar demonstrates the evolutionary distance. Accession nos.: AtSEC23A (NP_567217), AtSEC23B (NP_563741), AtSEC23C (NP_179757), AtSEC23D (NP_565651), AtSEC23E (NP_189008), AtSEC23F (NP_193152), AtSEC23G (NP_568626), Os01g0321700 (*O. sativa*, XP_015621728), Os03g0742800 (AAR87299), Os04g0412900 (XP_015636882), Os05g0443300 (BAF17587), Os08g0474700 (XP_015650237), CrSEC23 (*C. reinhardtii*, XP_001702936), hSec23A (*H. sapiens*, CAA65774), hSec23B (CAA65775), MmSEC23A (*M. musculus*, NP_033173), MmSEC23B (NP_062761), ScSEC23 (*S. cerevisiae*, NP_015507). **b** Domain structures of SEC23 protein in yeast and its seven homologs in *Arabidopsis*. The domains were predicted with the motif database Pfam (http://pfam.xfam.org/) and drown using the image creator, MyDomains (http://prosite.expasy.org/mydomains/). The predicted five domains were indicated as following: circle, zinc finger; rectangle, trunk; pentagon, β-barrel; gray hexagon, all-helical; and orange hexagon, gelsoline-like.


ScSEC23 MDFETN EDINGVR FTWNVFPST 22
AtSEC23A MANLPKSSVNYPGTLTPLEPNRPSPQPDRTPVPHSPPVVASPIPPRFPQPSFRPDQMSSPSMKSPSLLSPANGIRTGSPIPRLSTPPGPPVFNTPVKPAAVPFRTSPATPQPMAYSSANS 120
AtSEC23B MSEMAS MDPEGIDGVR MTWNVWPRT 25
AtSEC23C MAEFGE LEAQDGVR MPWNIIPVATK 25
AtSEC23D MAVR ATVSRFPID 13
AtSEC23E MAETAN TDLEGIDGVR MTWNVWPHS 25
AtSEC23F MAEMADKAKVEEMDWEGIDGVR MTWNLWPRT 31
AtSEC23G MDFLE LEAIEGLR WSWNSWPTT 22
ScSEC23 RSDANSNVVPVGCLYTPLK EYDELNVAPYNPVVCSGPHCKSILNPYCVIDPRNSSWSCPICNSRNHL 89
AtSEC23A SLPVSTPSFYSNGSSVGSQRDLPDVVRMEEPIAADSPYVLFSANKVLKQKKLANVASLGFGAIVSAGRE ISPGPQIIQRDPHRCLN CGAYSNPYSSILIGSGQWQCVICENMNGS 235
AtSEC23B KVEASKCVIPVAACISPIR YHRDIPSVEYAPLRCR ICTAALNPFARVDFLAKIWICPICFQRNHF 90
AtSEC23C KEQSIDSEVPVSAIYTPLKP LRSQSLLLPYSPLRCR TCRSVLNPYSVVDFSACNWGCPFCFNRNPF 91
AtSEC23D SDAQEASGLPWGLTVTPFAAKDENGIGPACGSNGHLLPRCENCYAYFNTYCELD QWAWNCSLCGTLNGL 82
AtSEC23E KAEASKCVIPLAACISPIR RHADIPTLPYAPLRCR TCSAALNAYAQVDFTAKLWICPFCYQRNHF 90
AtSEC23F KVEASKCVIPLAASISPIR RHPLILDLPYAPLDCK TCKALLNAFARVDFAAMNWVCPFCYHRNHF 96
AtSEC23G KSDCESLVVPLSIMYTPLM HFSELPTIPYDPLICS RCGAVLNPYARVDYQSRIWSCPFCFHKNLF 87
ScSEC23 PPQYTN LSQENMPLEL QSTTIEYITNKP VTVP PIFFFVVDLTSETENLDSLKESIITSLSLLPPNALIG 158
AtSEC23A KGEYVA SSKNELQNFPELSLPLVDYVQTGNKRPG FVPASDSRTS APVVLVIDECLDEPHLQHLQSSLHAFVDSLPQTTRLG 316
AtSEC23B PPHYHV MSETNVPCELYPQYTTVEYTLPNPSQP TGVGNFDQTGAVSGQPSP SVFVFVLDTCMIEEEFGYAKSALKQAIGLLPENALVG 178
AtSEC23C PLNYSS VADNNLPPELFPHSTTVEYLCDS FSSPSP PVFLFVVDTCLISEELDFLKSSLFQALDLLPDTSILG 163
AtSEC23D PSDAIARYSNPHSIPEMTSSFIDLEMPLDGS EEEMTQAR PVYVAAIDISSSEEFLELTKSALLAALEALSPGALFG 158
AtSEC23E PPHYHV ISETNLPGELYPQYTTVEYTLPPP VANGEGLVDP PVFVFVLDTCMIEEELDFAKSALKQAIGLLPENALVG 167
AtSEC23F PSHYHS ISEINLPGELYPQYTTVEYTLPP DPSRVPPP PVFVFVLDTCMIEEELGYAKSALKQAIGLLPENALVG 170
AtSEC23G PRSYSG ITETNLPAELFPTYSAVEYSPLPSRQSGSNTTTPTAAASWSNGFNQGVRSMPSNSSFSSLASSTVGGGGGVISELGPAFVFVVDASMVEDELRAVRSDVLFVIEQLPENCLVA 206
ScSEC23 LITYGNVVQLHDLS SETIDRCNVFRGDREYQLEALTEMLTGQKPTGPGGAASHLPNAMN KVTPFSLNRFFLPLEQVEFKLNQLLENLSPDQWSVPAGHRPL RATGSA 265
AtSEC23A IILYGRTVSIYDFS EDSVASADVISGAKSPSAESMKALIYGTG VYLSPMHASLKVAHEIFSSLRPYTLNVPEASRD RCLGTA 398
AtSEC23B FVSFGTQAHVHELG FSDLTKVYVFRGDKEISKDQVLEQLGLGASGRRNPVGGFPMGRDNSANFGYSGVNRFLLPASDCEFTIDLLLEELQTDQWPVQAGRRQS RCTGVA 287
AtSEC23C LITFDSLVRVYELG FPHCTKSYFFHGNKDCTKDQLLDQLSFFVKNPK PSSGVIAGARD GLSSDDIARFLLPASDCHFTLHSVLEELGNSPWPVAADHRPA RCTGVA 269
AtSEC23D LVTFSHKIGLYDVQGPIPVVKNVFIPPDGESSLSLELEDVMP LLQFLAPVETCKDRIAAALETLRPITSWERSAGAGQGMDSVLMGGRGFGTA 251
AtSEC23E FVSFGTQAHVHELG FSEMSKVFVFKGDKEISKDQILDQLGLGGSSRR GGSKGPQN GFPSSGLNRFLLPASECEFTLNSLLDELQSDQWPVKPGHRSQ RCTGVA 270
AtSEC23F FVSFGTQAHVHELG FSEMSKVFVFKGNKEVTKDQILDQLGLGSSSRRAPTSGFSKGAQN GFQSSGVDRFLLPASECEYTLDLLLDELQSDQWPVQPGHRPQ RCTGVA 277
AtSEC23G LITFDSMVRVYDLG FSECSKVVVFHGERDLSPDQIQQFLGLG YSKQFHHG KMSAIRKQSFLLPLVECEFNLTSAFEEIIP LVDVKPGHRPH RSTGAA 303
ScSEC23 LNIASLLLQGCY KNIPARIILFASGPGTVAPGLIVNSELKDPLRSHHDIDSDHAQHYKKACKFYNQIAQRVAANGHTVDIFAGCYDQIGMSEMKQLTDSTGGVLLLTDAFSTAIFKQS 383
AtSEC23A VEAALAIIQGPS AEMSRGVVRRAGGNSRIIVCAGGPITYGPGSVPHSMSHPNYPYMEKTAIKWMENLGREAHRHNTVVDILCAGTCPLRVPILQPLAKASGGVLVLHDDFG EAFGVD 515
AtSEC23B ISVATGLLGACF PGTGARIVALIGGPCSEGPGTIVSKDLSEPLRSHKDLDKDAAPFYKKAEKFYDALANQLVNQGHVLDLFASALDQVGVAEMKAAVERTGGLVVLSESFGHSVFKDS 405
AtSEC23C LRIAASLLGACF PGSAARIMAFIGGPSTQGPGAIVSRELSDPIRSHKDIDKDSAMYYHKAVEFYEMLAKQLVHQGHVLDVFASSVDQVGIAELKVAVEQTGGFVVLAESFGHSVFRDS 387
AtSEC23D MEALFNYLGSEFGNTFALARVFAFLSGPPDYGRGQLDTSRYGEQYASKRVDADR ALLPEQTPFYKDLATIAVQSGVCVDLFAVTNEYTDLASLKFLSIESGGSLFLYSSTDDSTLPQD 369
AtSEC23E LSVAAGLLGACL PGTGARIVALIGGPCTEGPGTIVSKDLSDPVRSHKDLDKDAAPYYKKAVKFYDSIAKQLVTQGHVLDLFASALDQVGVAEMKVAVERTGGLVVLSESFGHSVFKDS 388
AtSEC23F LSVAAGLLGACL PGTGARIVALVGGPCTEGPGTIISKDLSDPVRSHKDLDKDAAPYYKKAVKFYDSIAKQLVAQGHVLDLFASALDQVGVAEMKVAVESTGGLVVLSESFGHSVFKDS 395
AtSEC23G ISTALGLLEGCS VTTGSRIMVFTSGPATRGPGIIVDSDLSNSIRTHRDIITGHVSYYDKSCGFYKKLAKRLCDSSVVLDVFACSLDQVGAAELRYAVEMSGGFLLLGETFESEQFKKC 421
ScSEC23 YLRLFAKDEEGYLKMAFNGNMAVKTSKDLKVQGLIGHAS AVKKTDANNISESEIGIGATSTWKMASLSPYHSYAIFFEIANTAANSNPMMSAPGSADRPHLAYTQFITTYQHSSGTNRI 502
AtSEC23A LQRAAT RAAGSHGLLEVRCSDDILITQVIGPGE EAHSETHE TFKSDAALSIQMLSVEETQSFSLSME NKRDIKSD HVFFQFAFHYSDVYQADVS 609
AtSEC23B FKRVFE DGEESLGLCFNGTLEICCSKDIKIQGIIGPCA SLQKKGPS VADTVIGEGNTTQWKMCGLDKRTCLTVFFDLSSSDQSSAPGGVN NQLYLQFMTSYQNSKGKTLQ 515
AtSEC23C LKRVCQ SGENDLGLSSCGIFEINCSKDIKVQGIIGPCA SLEKKGPL CSDTAIGQGHTSAWKMCGLDNNTSICLVFEIAKIDTADVVLQSQS NQFYFQFLTYYQHSNGQTRL 498
AtSEC23D MFRMLN RPYAFNCVLRLRTSTEFKPGNSFGHFFPDPQYENLQHIICCDSYATYAYDFEFADNTGFSRHSGEQPVVQIAFQYTVVVPP EGLSNSEMSSSSRGKHTLQ 475
AtSEC23E FKRVFE DGDQALGLCFNGTLEICCSQDIKIQGAIGPCS SLEKKGAS VADTVIGEGNTSAWRLCGLDKTTCLTIFFDISSSG SNTPGAAN PQFYLQFLTSYQNPEGQTLL 497
AtSEC23F FKRMFE DGEHSLGLCFNGTLEINCSKDIKIQGVIGPCS SLEKKGPN VADTVIGEGNTSAWKLCGLDKSTCLTVFFDLSSTG STAPGALN QQLYLQFITRYQNSEGKSLA 504
AtSEC23G LRHIFIRDADGNLSMYFDVSLEVVTTKDMRICGALGPVV SLRQKNDI VSETEIGEGGTYMWKTSTVTNKTCVSFFFHVSNEQ NRKPQPGS AFFIQFITRYRYGNGAMRK 530

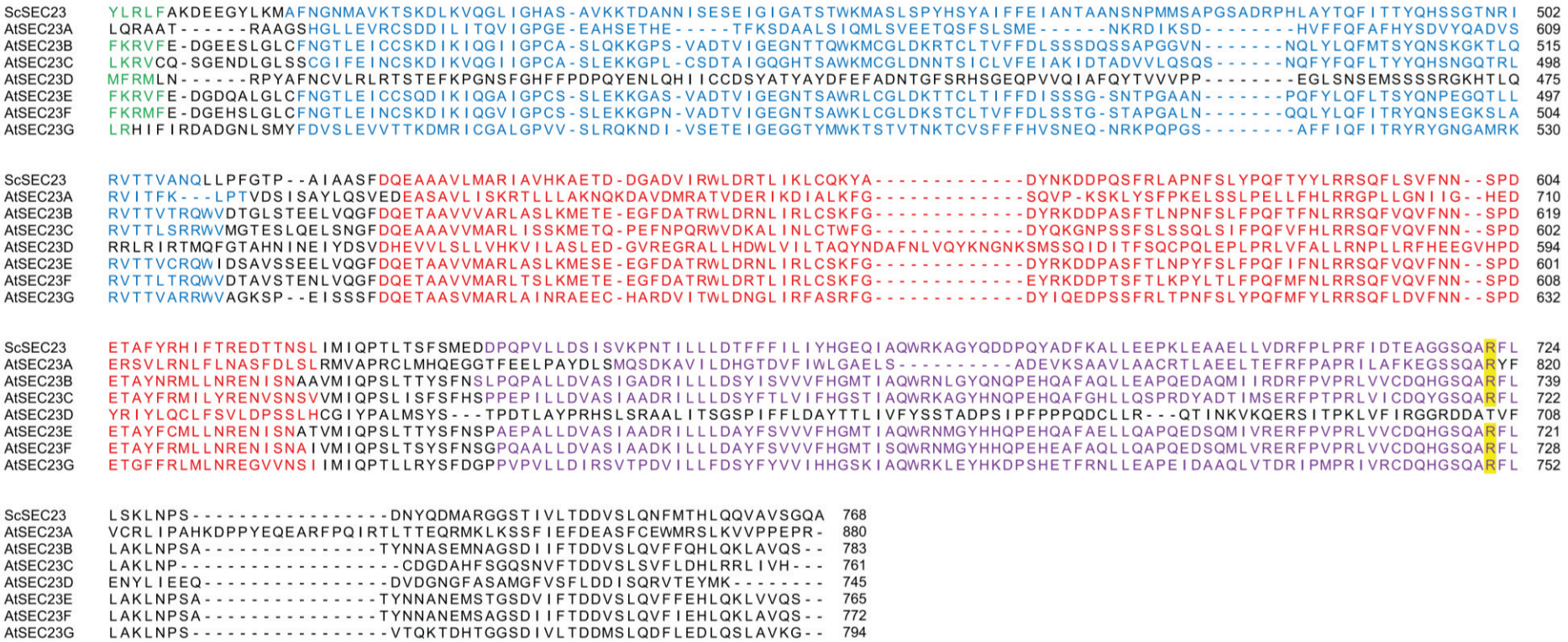

Fig. 3-2. Multiple sequence alignment of SEC23 family proteins in yeast and *Arabidopsis*. The amino acid sequences used in Fig. 3-1 were aligned by ClustalW ver. 1.83 program (http://clustalw.ddbj.nig.ac.jp/). The five domains shown in Fig. 3-1 are indicated by colored letters: zinc finger (orange), trunk (green), β-barrel (blue), all-helical (red), and gelsolin-like (purple). The conserved amino acid residues previously reported are highlighted by yellow background (see results and discussion sections for more details).

In *Saccharomyces cerevisiae*, SEC23 and SEC24 include five domains, namely, zinc finger, trunk, β-barrel, all-helical, and gelsolin-like domains [36]. These five domains are well conserved within all *A. thaliana* SEC23 members, except for *AtSEC23D* which misses the β-barrel and gelsolin-like domains (Fig. 3-1b). Notably, *AtSEC23A* has a longer N-terminal extension than *S. cerevisiae* SEC23 (ScSEC23) and other AtSEC23s (Fig. 3-1b). Sequence alignment of SEC23 homologs in *A. thaliana* and yeast revealed that both AtSEC23A and AtSEC23D have an amino acid substitution at the conserved aspartate residue in the trunk domain (Asp351 of ScSEC23) to cysteine (Cys484 of AtSEC23A) [133] or glutamate residue (Glu337 of AtSEC23D), respectively, while all other AtSEC23 homologs have no substitution at that position (Fig. 3-2). Interestingly, AtSEC23D also misses the phenylalanine residue 366 (equivalent to phenylalanine residue 382 of human SEC23A [131, 132]) and the catalytic arginine residue 706 (722 of ScSEC23 [36]), which are conserved in ScSEC23 and other AtSEC23s (Fig. 3-2). Taken together, these results indicated that both AtSEC23A and AtSEC23D are distinct from other *A. thaliana* SEC23 homologs.

atsec23a and *atsec23d* single-mutant plants show defects in exine patterning

To understand the functions of *A. thaliana* SEC23 homologs during plant development, homozygous T-DNA inserted lines of the seven *AtSEC23s* were prepared (ABRC (www.arabidopsis.org)) and screened for any obvious developmental abnormalities. Among all AtSEC23s examined, the author found abnormalities of pollen wall structure in T-DNA inserted lines for only *AtSEC23A* (At4g01810) and *AtSEC23D* (At2g27460) (Fig. 3-3 and Fig. 3-4). These T-DNA inserted lines, SALK_021996 (for *AtSEC23A*) and SALK_012411 (for *AtSEC23D*) [6] were named *atsec23a* and *atsec23d*, respectively, and used for further experiments. In *atsec23a* and *atsec23d*, T-DNAs were inserted upstream of the 5' untranslated region and in the last (14th) exon of *AtSEC23A* and *AtSEC23D*, respectively (Fig. 3-3a). RT-PCR analysis revealed that the *atsec23a* and *atsec23d* plants were knockdowns and knockouts, respectively (Fig. 3-3b). In contrast to wild-type pollen which had a reticulate exine with the characteristic net-like structure (Fig. 3-3c, g), the pollen of *atsec23a* and *atsec23d* showed an abnormal exine phenotype represented by partial loss of the net-like structure and incomplete tectum formation in some surface areas (Fig. 3-3d, e, h, i). In particular, *atsec23a* pollen showed much less tectum formation with larger surface areas lacking the net-like structure when compared to *atsec23d* pollen.

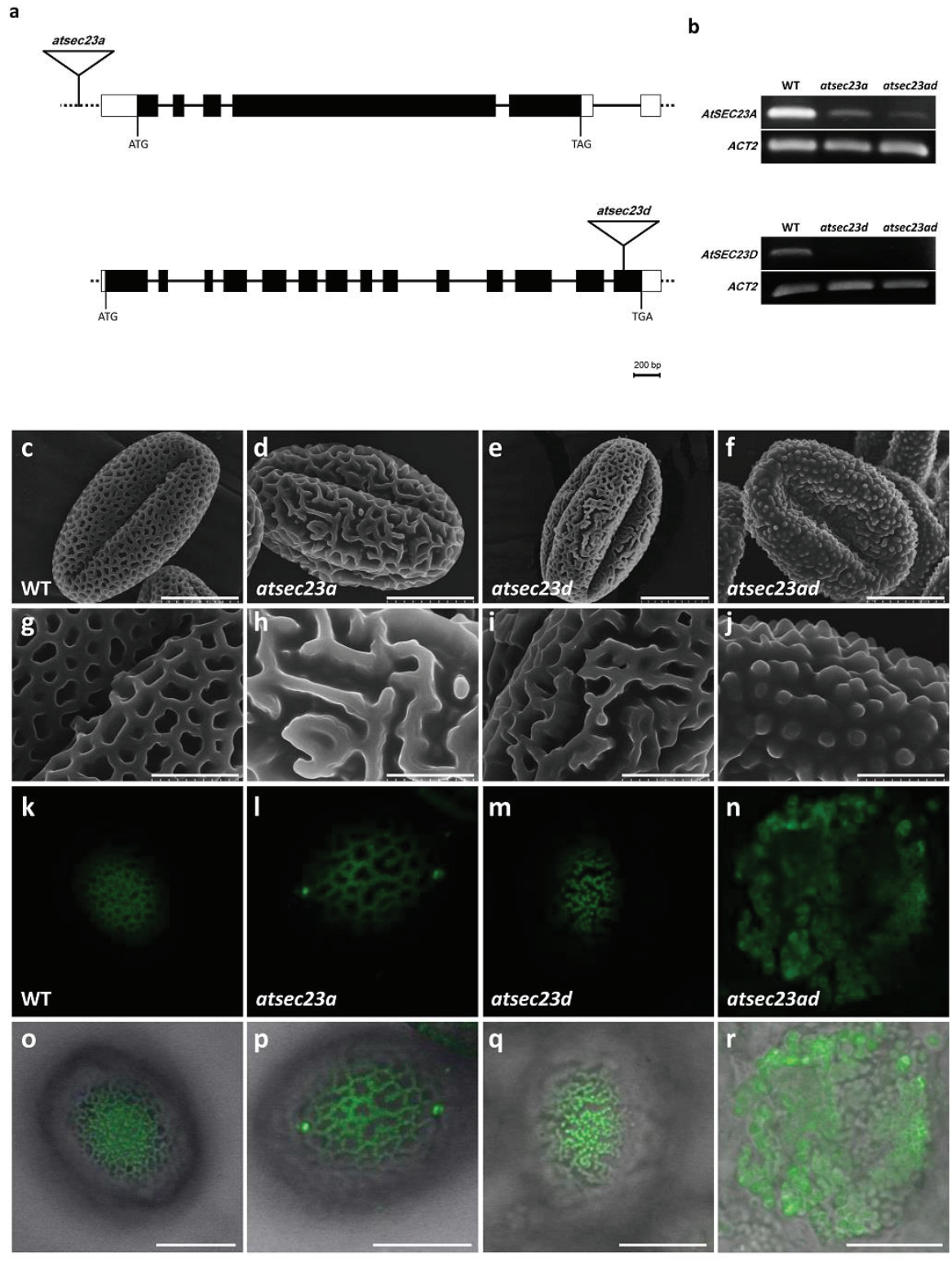

Fig. 3-3 Defective exine patterning caused by depletion of *AtSEC23A* and *AtSEC23D*. **a** Schematic diagrams of *AtSEC23A* and *AtSEC23D* genes showing T-DNA insertion sites. Black boxes, white boxes, and black solid lines represent the exons, untranslated regions, and introns, respectively. The triangles indicate the locations of T-DNA insertions. **b** Expression analysis of *AtSEC23A* and *AtSEC23D* by RT-PCR in wild type, single, and double mutants. The transcription level of *Actin2* was used as an internal reference. **c-j** SEM images showing pollen surface structures of wild-type (c, g), *atsec23a* (d, h), *atsec23d* (e, i), and *atsec23ad* (f, j) plants. Lower panels (g-j) indicate magnified parts of the pollen surface structures in upper panels (c-f). **k-r** Auramine O staining of wild-type (k, o), *atsec23a* (l, p), *atsec23d* (m, q), and *atsec23ad* (n, r) plants. Upper panels (k-n) and lower panels (o-r) show the fluorescence images of auramine O and merged images of the auramine O fluorescence with bright field images, respectively. Scale bars = 10 μm in (c-f), 3 μm in (g-j), and 20 μm in (k-r).

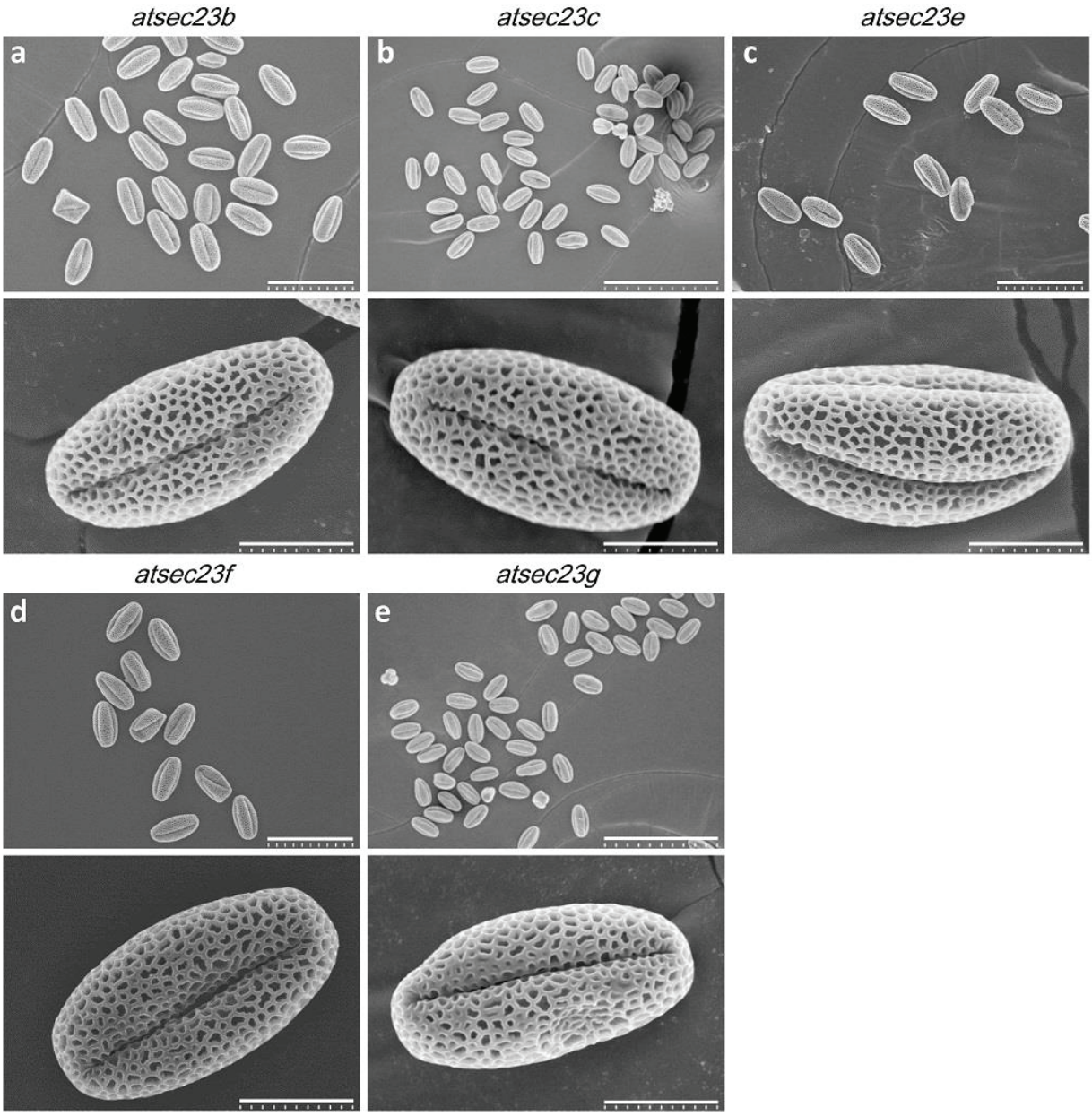

Fig. 3-4. Scanning electron micrographs of pollen of the remaining members of *Arabidopsis* SEC23 family genes (T-DNA inserted lines). The lines, SALK_051290, SALK_075252, SALK_080595, SALK_104305, and SALK_027036 were used as gene disrupted lines for *AtSEC23B*, *C*, *E*, *F*, and *G,* respectively. Scale bars = 50 µm in (upper panels of a, c, and d), 100 µm in (upper panels of b, e), and 10 µm in the lower panels.

In addition, the author used the exine-specific fluorescent dye (auramine O) to observe the differences in pollen surface structure using CLSM. Pollen grains of both *atsec23a* and *atsec23d* had profound alterations in exine formation with some areas showing no auramine O staining in comparison to the wild-type (Fig. 3-3k-m, o-q), being consistent with SEM observations. Next, a genetic complementation test was conducted to confirm whether the defect in exine patterning is directly linked to the T-DNA insertions in *AtSEC23A* and *AtSEC23D*. AtSEC23A and AtSEC23D fused with GFP driven by their own promoters were expressed in *atsec23a* and *atsec23d*, respectively. Several complemented lines showing normal exine patterning with the characteristic net-like structure were obtained (Fig. 3-8p-u). These results indicated that the depletion of AtSEC23A or AtSEC23D leads to defects in exine patterning of pollen grains.

To check whether *AtSEC23A* and *AtSEC23D* have overlapping functions, the author generated the double-mutant *atsec23ad* by cross-fertilization (Fig. 3-3b). The *atsec23ad* exhibited a more aberrant pollen phenotype. Most pollen of *atsec23ad* did not maintain their original shapes and became collapsed and flattened (Fig. 3-3f, j, n, r). Many granules of different shape and size were irregularly scattered on and around the pollen surface. These granules showed auramine O staining, indicating that their surface structure are composed of a material similar to sporopollenin (Fig. 3-3n, r). A few pollen showed a less severe phenotype and were not collapsed nor flattened. Their surface lacked the net-like structure and was instead covered with many granules of uniform shape and size (Fig. 3-5b). These results indicated that the pollen surface of *atsec23ad* exhibited more severe defects than that of *atsec23a* and *atsec23d*, and clearly showed that the exine formation and sporopollenin deposition were incomplete in *atsec23a* and *atsec23d*, and thoroughly defective in *atsec23ad*.

Double-mutant *atsec23ad* shows semi-sterile phenotype with impaired male gametogenesis

The author compared the fertility of wild-type, *atsec23a*, *atsec23d*, and double-mutant *atsec23ad* by analyzing the average silique and seed yields per plant (Fig. 3-5b-d). The *atsec23a* and *atsec23d* contained elongated siliques with a full set of developing seeds comparable to the wild-type (Fig. 3-5a-c). The total seed yield in the wild type was about 5,000 seeds per plant with no significant difference with *atsec23a* and *atsec23d* (Fig. 3-5d). In contrast, the *atsec23ad* mutant showed a dramatically reduced fertility, and the majority of siliques was short and devoid of any seeds (Fig. 3-5a). However, occasionally a few seed-

bearing siliques were observed (labelled by an arrow in Fig. 3-5a) and these siliques were with a reduced set of developing seeds (Fig. 3-5c), resulting finally in a semi-sterile phenotype with less than 100 seeds per plant (Fig. 3-5d). Moreover, *atsec23ad* plants grew taller for a longer time than the wild-type, and last few flowers showed distorted shapes (Fig. 3-6a).

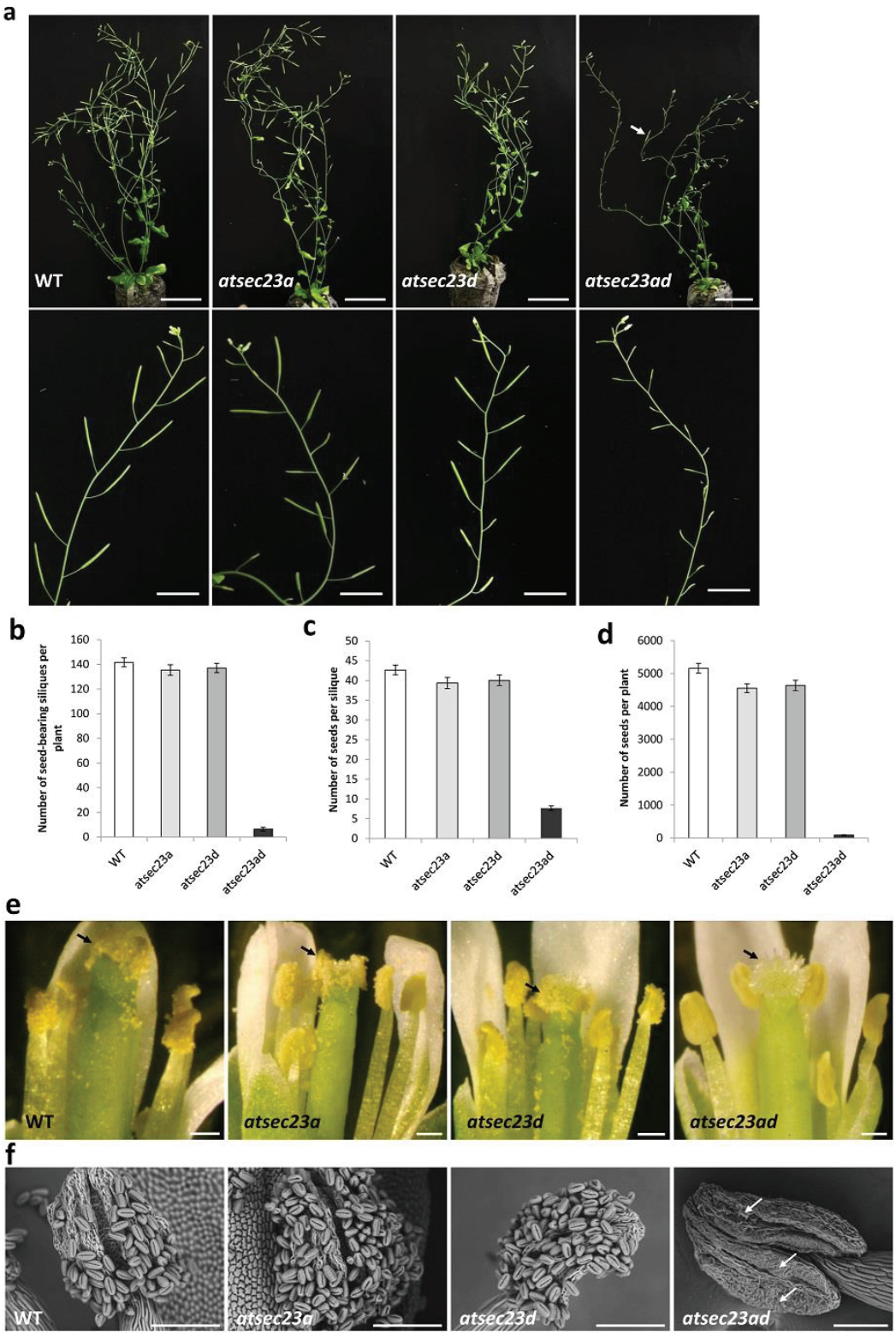

Fig. 3-5 Fertility analysis of *atsec23a*, *atsec23d*, and *atsec23ad* plants in comparison to the wild type. a Two-month-old wild-type, *atsec23a*, *atsec23d*, and *atsec23ad* plants. The arrow indicates one of the few seed-bearing siliques. The lower panel shows a flowering branch of wild-type, *atsec23a*, *atsec23d*, and *atsec23ad* plants. **b-d** Seed- and silique-set analyses in the mutant plants. The analyses include number of seed-bearing siliques per plant (b; $n = 13$), number of seeds per silique (c; $n = 40$), and number of seeds per plant (d; $n = 10$). Bars indicate standard errors. **e** Dissected flowers showing a lack of pollination in *atsec23ad*. Note that single- and double-mutant plants have normal anther height similar to the wild type. Arrows show stigmas with abundant pollen (wild type, *atsec23a* and *atsec23d*) or with no pollen (*atsec23ad*). **f** SEM micrographs comparing the anther dehiscence and pollen release in wild-type and mutant plants. Arrows indicate aggregations of pollen as a collapsed bulk adhesive to anthers. Scale bars = 5 cm in (upper panel of a), 2 cm in (lower panel of a), 200 μm in (e), and 100 μm in (f).

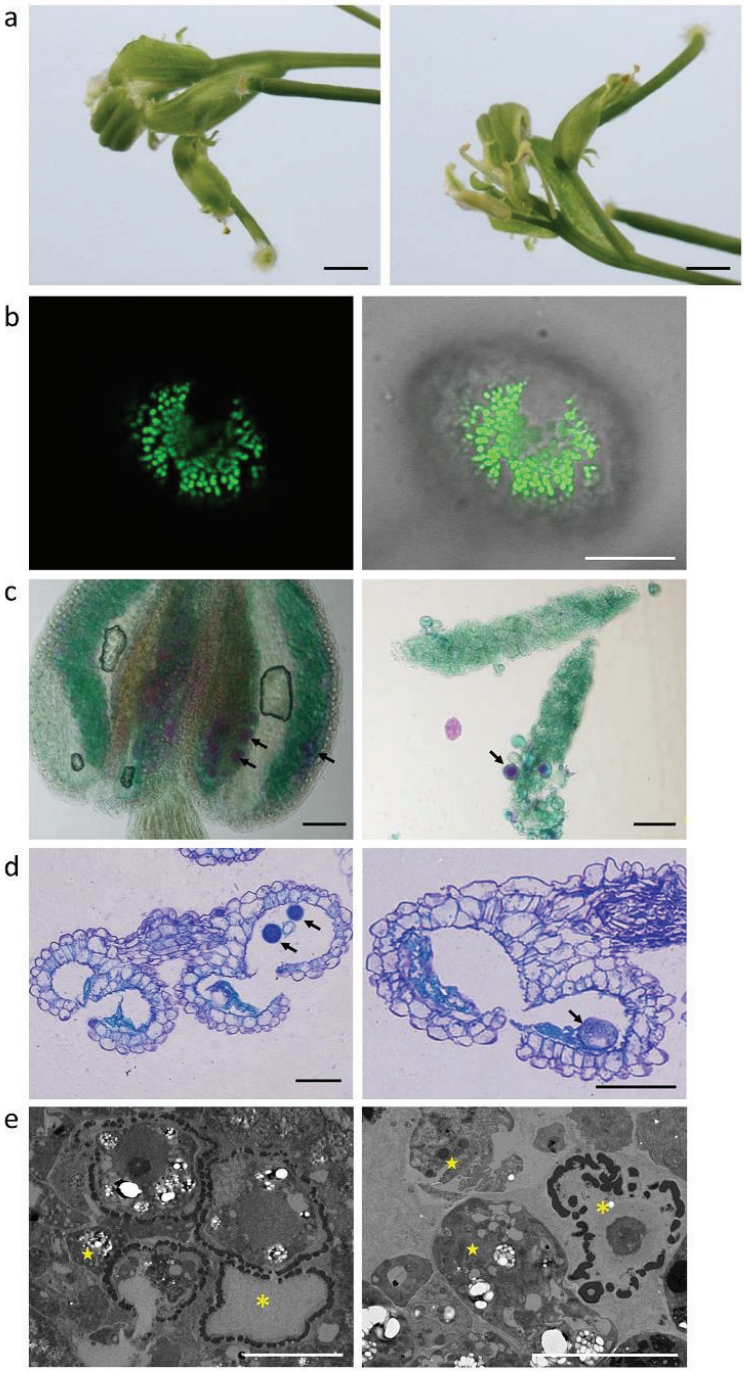

Fig. 3-6. Defective phenotypes in the double mutant *atsec23ad* plants. a Distorted morphology of last flowers of *atsec23ad* plants. **b** Auramine O staining of *atsec23ad* pollen showing a less severe phenotype. **c** Alexander's staining of *atsec23ad* pollen showing a few positively stained pollen (purple). **d** Technovit semi-thin sections of *atsec23ad* anthers showing a few intact (potentially functional) pollen. **e** Transmission micrographs of *atsec23ad* microspores at bicellular stage showing the severe defects in microspores. Stars and asterisks show naked microspores with no walls and empty pollen shells with no cytoplasm, respectively. Scale bars = 1mm in (a), 10 μm in (b, e), and 50 μm in (c, d).

To investigate the reason behind the reduced fertility, the author observed open flowers of wild-type, *atsec23a*, *atsec23d* and *atsec23ad* after completion of self-fertilization. An abundant amount of pollen grains was adhered to anthers and stigma of wild-type, *atsec23a* and *atsec23d*, whereas no pollen grains were seen on the surface of these tissues in the *atsec23ad* flower (Fig. 3-5e). The *atsec23a*, *atsec23d* and *atsec23ad* contained anthers with comparable height to wild-type (Fig. 3-5e), and these anthers showed normal dehiscence (Fig. 3-5f). However, most pollen in the *atsec23ad* tended to aggregate as a collapsed bulk of remnant materials (potentially dead pollen) which were strongly adhesive to anther walls failing to be released. These findings suggested that the reduced fertility in the *atsec23ad* was caused by a defect in pollen development but not in anther development. To determine whether the semi-sterility phenotype in *atsec23ad* linked to defects in the female gametophyte, the author cross-pollinated the stigmas of the *atsec23ad* with wild-type pollen grains. Normal elongated siliques with a full set of seeds indistinguishable from that of the wild-type were produced (Fig. 3-7), indicating that female gametophytes function normally in *atsec23ad*. These results suggested that the semi-sterility phenotype caused by the insufficiency of AtSEC23A and AtSEC23D is linked to defects in male reproduction (pollen development).

To examine whether the incomplete exine pattern in *atsec23a* and *atsec23d*, and the abortion of pollen in *atsec23ad* attribute to gametophytic or sporophytic defects, the author performed genetic analyses using heterozygous lines. Heterologous lines of both +/*atsec23a* and +/*atsec23d* generated normal pollen with the characteristic reticulate exine indistinguishable from wild-type pollen (Fig. 3-8a-f), indicating that the incomplete exine pattern was caused by defects in sporophytic tissues. Furthermore, the author observed pollen produced by heterozygous line *atsec23a* in the homozygous *atsec23d* and *qrt1-2* background (+/*atsec23a*, *atsec23d*/*atsec23d*, *qrt1-2*/*qrt1-2*). The *qrt1-2* causes incomplete separation of microspores in tetrads and finally generates pollen-tetrads enabling precise segregation analysis of pollen derived from a single microsporocyte [150]. As revealed by SEM and Alexander's staining [151], the majority of pollen-tetrads had four uncollapsed pollen (the exine pattern phenotype is resulted by the effect of *atsec23d*/*atsec23d*) similar to those from *qrt1-2* (Fig. 3-8g-o), indicating that the failure of pollen development was due to a sporophytic aberration. Therefore, these findings suggested that the pollen defects in *atsec23a* and *atsec23d* mutants are sporophytic in nature and both *AtSEC23A* and *AtSEC23D* function sporophytically.

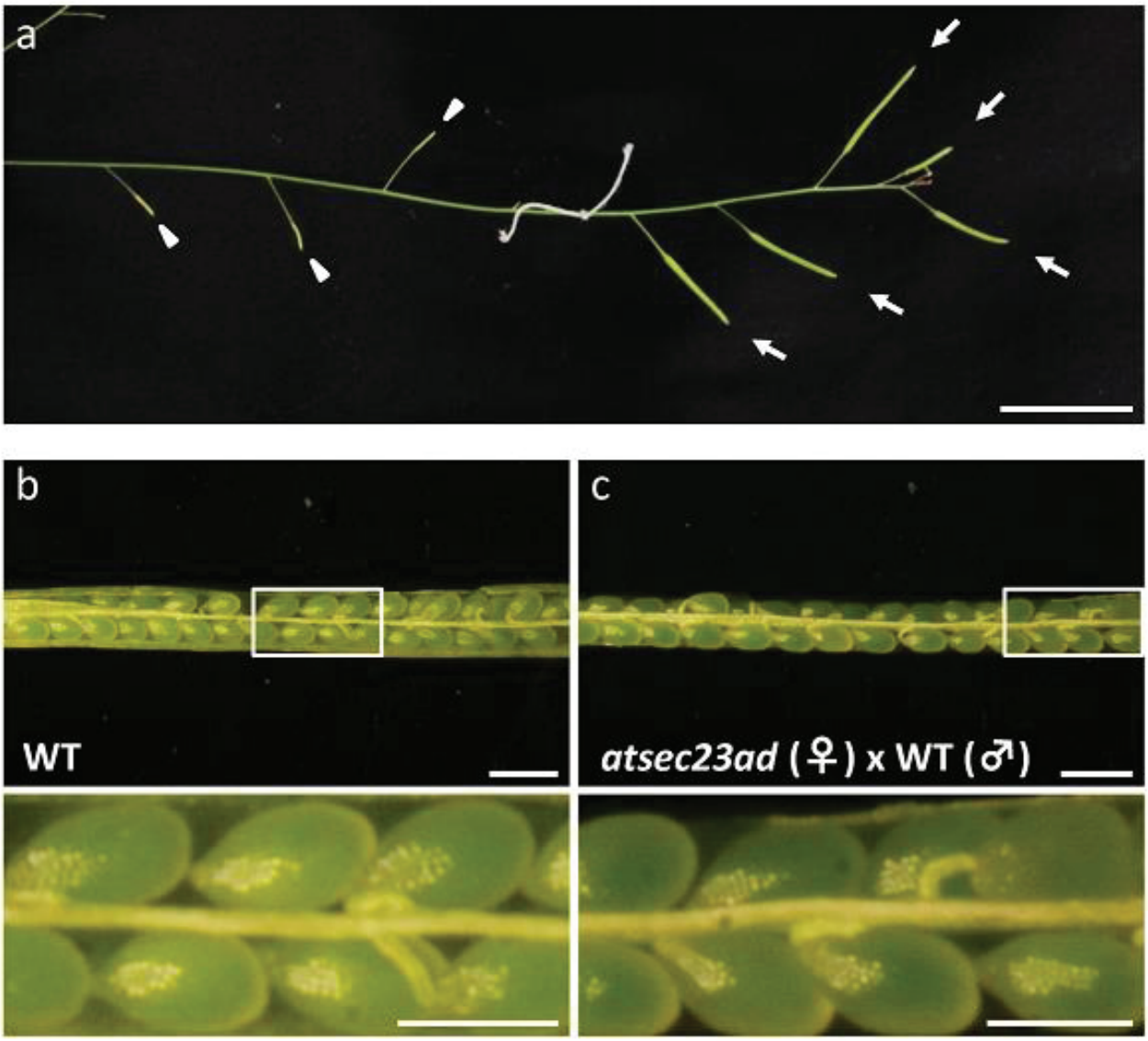

Fig. 3-7. Normal functionality of the female gametophyte of *atsec23ad* plants. a An *atsec23ad* flowering branch with normal elongated siliques after cross-pollination with wild-type pollen. Arrows and arrowheads indicate crossed and self-pollinated siliques, respectively. **b, c** Comparison of seed development between a wild-type silique and an *atsec23ad* silique pollinated by wild-type pollen. Scale bars = 2 cm in (a), 1 mm in (upper panel of b, c), and 0.5 mm in (lower panel of b, c).

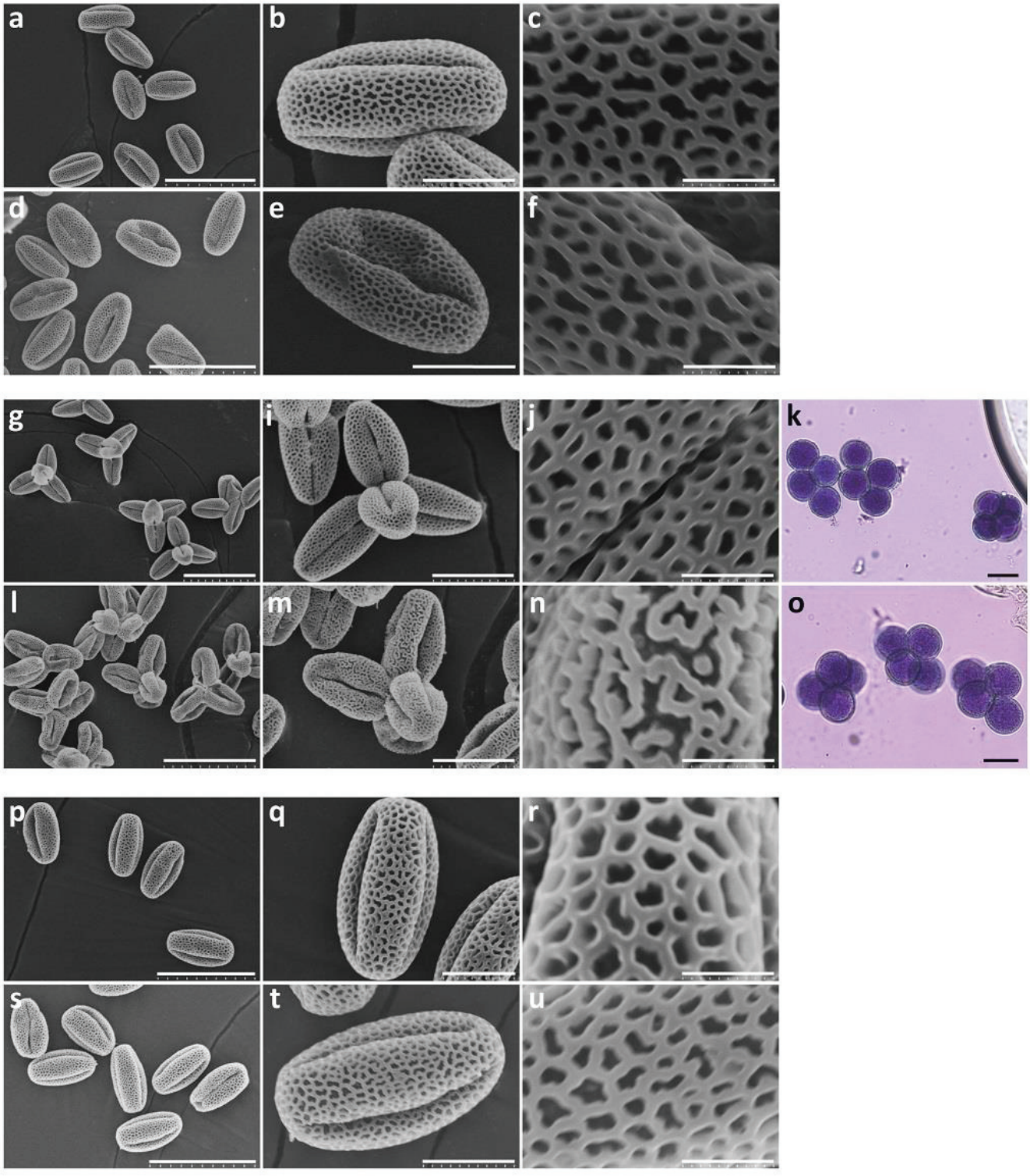

Fig. 3-8. Sporophytic control of *AtSEC23A* and *AtSEC23D* and rescue of the mutant phenotype. a-f Scanning electron micrographs of pollen grains and their surface structure in heterozygous *atsec23a* (a-c) and *atsec23d* (d-f) mutants showing normal pollen with the characteristic reticulate pattern. **g-o** Tetrad analysis of heterozygous *atsec23ad* using *qrt1-2* mutant. Scanning electron micrographs of pollen tetrads of *qrt1-2* (g-j) and heterozygous *atsec23a* in the *qrt1-2* mutant background (*+/23a, 23d/23d, qrt1-2/qrt1-2*) (l-n). Alexander's staining of pollen tetrads of *qrt1-2/qrt1-2* (k) and *+/23a, 23d/23d, qrt1-2/qrt1-2* (o). Note that all the four pollen in a tetrad are uncollapsed. **p-u** Scanning electron micrographs of *atsec23a* or *atsec23d* mutant pollen complemented by expressing $P_{AtSEC23A}$:*AtSEC23A-GFP* (p-r) or $P_{AtSEC23D}$:*AtSEC23D-GFP* (s-u). Scale bars = 50 µm in (a, d, g, l, p, and s), 10 µm in (b, e, i, m, q, and t), 3 µm in (c, f, j, n, r, and u), and 20 µm in (k, and o).

atsec23a single- and *atsec23ad* double-mutants exhibit impaired pollen germination

Since the *atsec23ad* showed male sterility and severe phenotype in pollen morphology, the author next performed Alexander's and DAPI staining to examine the viability of pollen. In contrast to the wild-type, *atsec23a* and *atsec23d* anthers which contained purple-stained viable pollen (Fig. 3-9a-c), most anthers of the *atsec23ad* contained green-stained dead pollen (Fig. 3-9d), however, a small number of purple-stained normal pollen were observed in some anthers (Fig. 3-6c), being consistent with the production of few seeds in *atsec23ad*. DAPI staining showed that wild-type, *atsec23a*, and *atsec23d* pollen contained two sperm nuclei and one vegetative nucleus indicating normal development and male mitosis (Fig. 3-9e-g). By contrast, the majority of *atsec23ad* pollen did not show any DAPI signals and were smaller in size and collapsed, while only a small number of pollen possessed the three nuclei (Fig. 3-9h), indicating that the *atsec23ad* pollen often failed to reach the final stages of development. To investigate that whether the abortion of pollen occurred during developmental stage earlier than pollen mitosis, the author observed callose deposition on microspores at tetrad and early uninucleate stages by aniline blue staining. Tetrads and microspores just released from tetrads in *atsec23a*, *atsec23d* and *atsec23ad* showed comparable levels of aniline blue staining to that of the wild-type (Fig. 3-9i-p), indicating a normal callose wall deposition and suggesting that the defect of pollen was started in later developmental stages.

Next, the author performed *in vitro* pollen germination assay. Pollen of *atsec23d* showed germination rate of 82% comparable to wild-type pollen (80.5%), while only 41.6% of *atsec23a* pollen could germinate (Fig. 3-9q-s, v). The quantitative analysis of the germination rate of *atsec23ad* pollen was difficult to be accurately determined because most pollen were collapsed and adhesive to anther walls. However, after forcing pollen to separate from anther walls (*i.e.*, by the tip of a forceps), very few germinated pollen were seen on the germination medium or within the anther itself (Fig. 3-9u). Complemented *atsec23a* lines expressing *AtSEC23A* fused with GFP showed similar pollen germination rates to that of the wild-type (Fig. 3-9t, v). These results indicated that pollen germination was normal in *atsec23d* but impaired in *atsec23a*, and also showed a presence of few functional pollen in *atsec23ad*, which agreed with the few seeds obtained from *atsec23ad*.

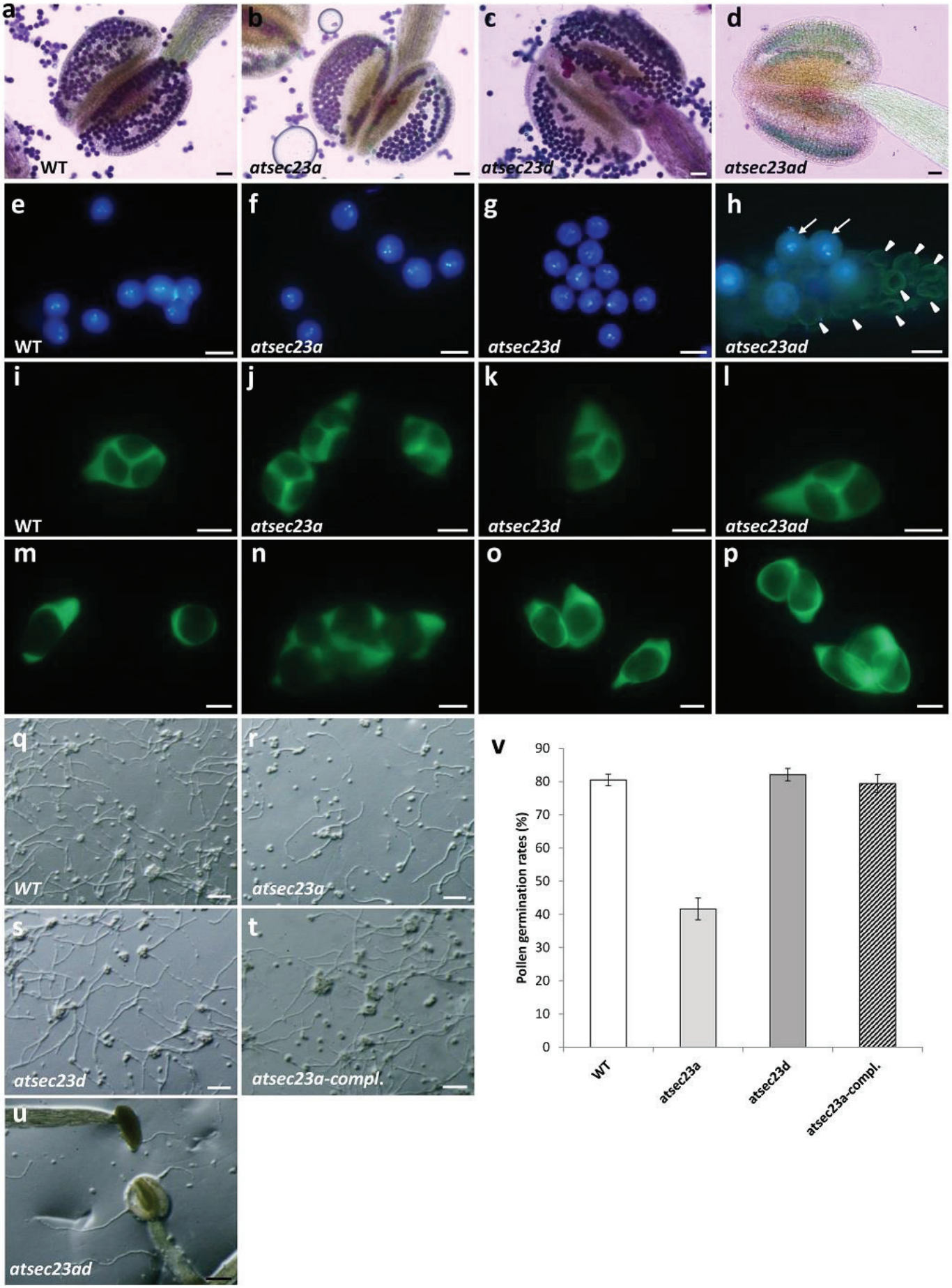
a
WT
b
atsec23a
c
atsec23d
d
atsec23ad
e
WT
f
atsec23a
g
atsec23d
h
atsec23ad
i
WT
j
atsec23a
k
atsec23d
l
atsec23ad
m
n
o
p
q
WT
r
atsec23a
s
atsec23d
t
atsec23a-compl.
u
atsec23ad
v
Pollen germination rates (%)
0
10
20
30
40
50
60
70
80
90
WT
atsec23a
atsec23d
atsec23a-compl.

Fig. 3-9 Phenotypic analyses of wild-type, *atsec23a*, *atsec23d*, and *atsec23ad* pollen. a-d Alexander's staining of wild-type, *atsec23a*, *atsec23d*, and *atsec23ad* pollens. **e-h** DAPI staining of mature pollen of wild-type, *atsec23a*, *atsec23d*, and *atsec23ad* plants. Arrows and arrowheads indicate normally developed (possessed three nuclei) and non-stained pollen, respectively. **i-p** Aniline blue staining showing normal pollen development at tetrad stage (i-l) and early uninucleate stage (m-p) of wild-type and mutant plants. **q-u** Light microscopy images of germinated pollen of wild-type, *atsec23a*, *atsec23d*, *atsec23a-compl.*, and *atsec23ad* plants. **v** Pollen germination rate in wild-type, *atsec23a*, *atsec23d*, and *atsec23a-compl.* plants. Error bars indicate the standard errors. Scale bars = 50 μm in (a-d), 20 μm in (e-h), 10 μm in (i-p), and 200 μm in (q-u).

AtSEC23A and *AtSEC23D* are highly expressed in tapetum and mature pollen of developing anthers

Expression of *AtSEC23* genes was anticipated to be universally distributed throughout the whole plant using the GENEVESTIGATOR [148]. However, the exact expression profiles of AtSEC23 homologs were not yet determined. The author investigated the expression pattern of both *AtSEC23A* and *AtSEC23D*. By RT-PCR analysis, *AtSEC23A* was expressed almost equally in all investigated organs but siliques, which showed a weak expression (Fig. 3-10a). *AtSEC23D* was expressed in all investigated organs but were most abundant in closed floral buds. Similar to *AtSEC23A*, *AtSEC23D* expression was also weak in siliques (Fig. 3-10a). The author further conducted promoter:GUS assays to explore the spatial and temporal pattern of expression of both *AtSEC23A* and *AtSEC23D*. The GUS activity in transgenic plants expressing $P_{AtSEC23A}$*:GUS* was widely detected in all flower parts including sepals, petals, stamen filaments, anther walls, mature pollen, pollen tubes and young siliques (Fig. 3-10f-j) but not in the mature siliques (Fig. 3-10k). In young developing seedlings (5-day-old), GUS activity was detected in root, cotyledons, and leaf primordia but not in the hypocotyl (Fig. 3-10b). In 15-day-old seedlings, the GUS activity was observed throughout the whole plant including roots, cotyledons, true leaves, trichomes, and leaf primordia with a higher level of expression in root tips and leaf veins (Fig. 3-10c-e). Transgenic plants expressing $P_{AtSEC23D}$*:GUS* did not show the universal expression pattern of *AtSEC23D* but exhibited a specific expression pattern. The GUS activity was detected mainly in floral buds and open flowers (Fig. 3-10p, q), specifically in mature pollen, pollen tubes (Fig. 3-10q-s) and fertilized ovules (Fig. 3-10t), but not observed in other floral parts including sepal, petal, stamen filaments, anther walls (Fig. 3-10p-r) or mature siliques (Fig. 3-10u). In young developing seedlings (5-day-old), no expression was detected (Fig. 3-10i). In 15-day-old seedlings, only a negligible amount of GUS staining was observed in roots and leaf primordia (Fig. 3-10m-o).

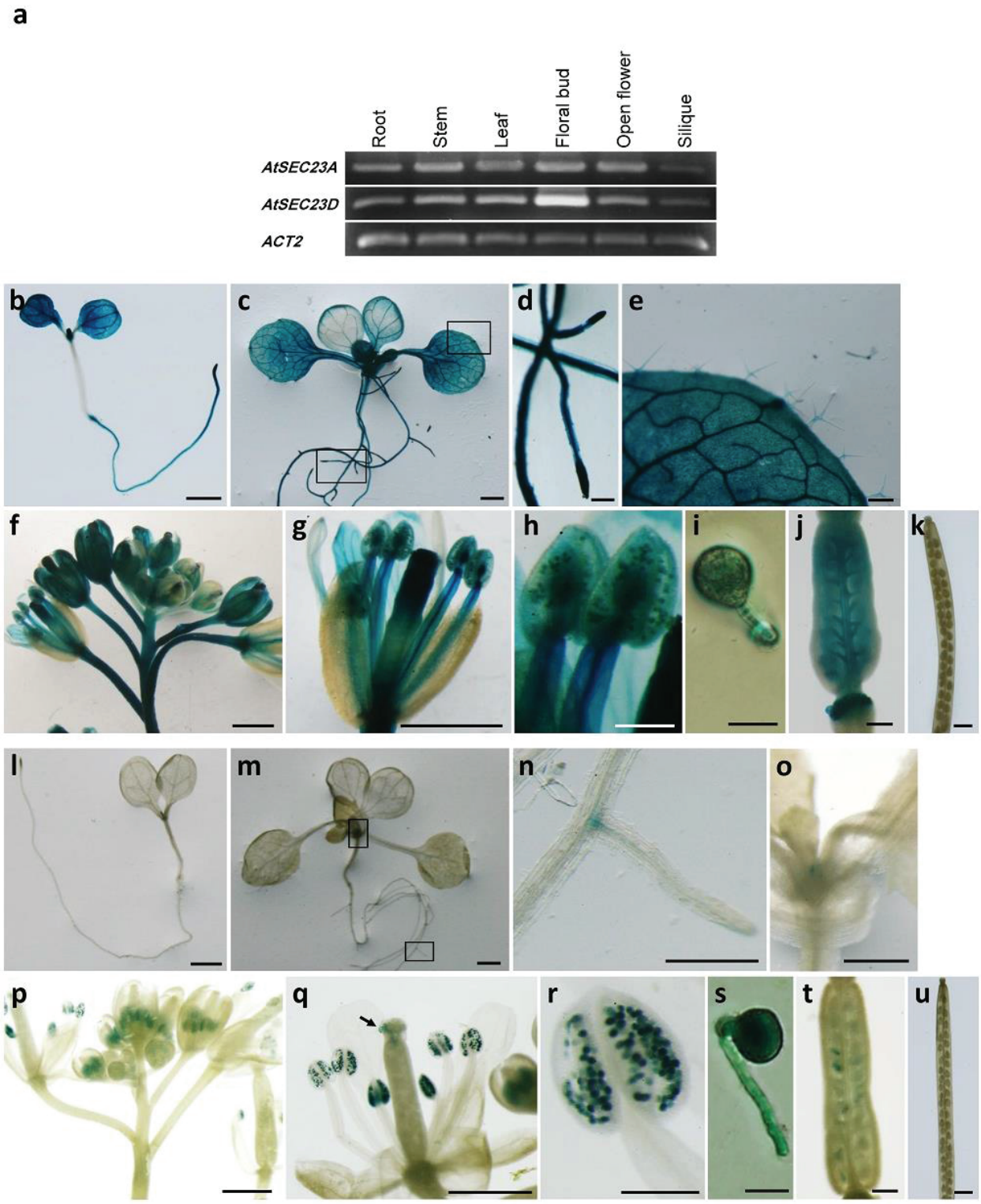

Fig. 3-10 *AtSEC23A* and *AtSEC23D* expression patterns in different organs of *A. thaliana.* **a** RT-PCR analysis of *AtSEC23A* and *AtSEC23D* using RNA extracted from roots, stems, leaves, floral buds, open flowers, and siliques of the wild-type plants. The transcription level of *Actin2* was monitored as a control. **b-u** GUS staining of *Arabidopsis* plants expressing $P_{AtSEC23A}$:*GUS* (a-k) or $P_{AtSEC23D}$:*GUS* (l-u). The staining was performed with five-day-old seedlings (b, l), fourteen-day-old seedlings (c, m), inflorescences (f, p), flowers (g, q), anthers (h, r), germinated pollen (i, s), fertilized ovaries (j, t), and mature siliques (k, u). **d, e** and **n, o** are enlargements of the boxed areas in (c) and (m), respectively. The arrow in (q) indicates germinated pollen on stigmatic papillae. Scale bars = 1 mm in (b, c, f, g, k, l, m, p, q, and u), 200 μm in (d, e, h, j, n, o, r, and t), and 20 μm in (i-s).

Next, the author followed the expression closely in anthers by promoter:*GUS* assays and GFP-fusion protein localizations. GUS signals were observed predominantly in tapetal cells at uninucleate and bicellular stages in $P_{AtSEC23A}$*:GUS* and $P_{AtSEC23D}$*:GUS* transgenic plants; meanwhile, no or little signals were detected in developing microspores (Fig. 3-11a, b, d, e). During these stages, the tapetum is active in manufacturing and secreting exine components into the locule [28]. At tricellular pollen stage, when tapetum degeneration has completed, strong GUS signals were observed in mature pollen (Fig. 3-11c, f). The author further traced the expression of both genes in complemented plant lines by constructs identical to those used in complementation tests of Fig. 3-8 (*atsec23a* carrying $P_{AtSEC23A}$*:AtSEC23A-GFP* and *atsec23d* carrying $P_{AtSEC23D}$*:AtSEC23D-GFP*). In both cases, GFP fluorescence was detected mainly in the tapetum (Fig. 3-11g, h, k, l) and mature pollen (Fig. 3-11i, j, m, n), consistent with GUS staining results in anthers. In summary, although *AtSEC23A* and *AtSEC23D* have shown different expression patterns in the whole plant body, both of them are highly expressed in the tapetum and mature pollen.

AtSEC23A and AtSEC23D were localized to the cytosol and ERES

AtSEC23A has shown ERES localization when co-expressed with SAR1A in *A. thaliana* protoplast in a previous report [133]. To examine the subcellular localization of AtSEC23D, AtSEC23D-G3GFP with AtSEC23A-tagRFP were transiently co-expressed in *Nicotiana benthamiana* leaves. AtSEC23D-G3GFP exhibited a similar localization pattern to AtSEC23A-tagRFP; both were localized to cytosol with existence of many dot-like structures (Fig. 3-12a). To confirm that these dot-like structures were ERES, the author used the ERES marker AtSEC24A [152, 153] and the *cis*-Golgi marker SYP31, which is transported as a cargo to Golgi apparatus via the secretory pathways [154], in a co-localization experiment with AtSEC23A-G3GFP and AtSEC23D-G3GFP. The AtSEC24A fused with tagRFP (AtSEC24A-tagRFP) was co-localized with AtSEC23A-G3GFP and AtSEC23D-G3GFP, and the dot-like structures labeled with AtSEC23A-G3GFP or AtSEC23D-G3GFP overlapped with ERESs indicated by AtSEC24A-tagRFP (Fig. 3-12b, c). Furthermore, a time-lapse analysis showed that these GFP and RFP signals moved together as a single unit in the cytoplasm (data not shown), confirming that these dots were ERES.

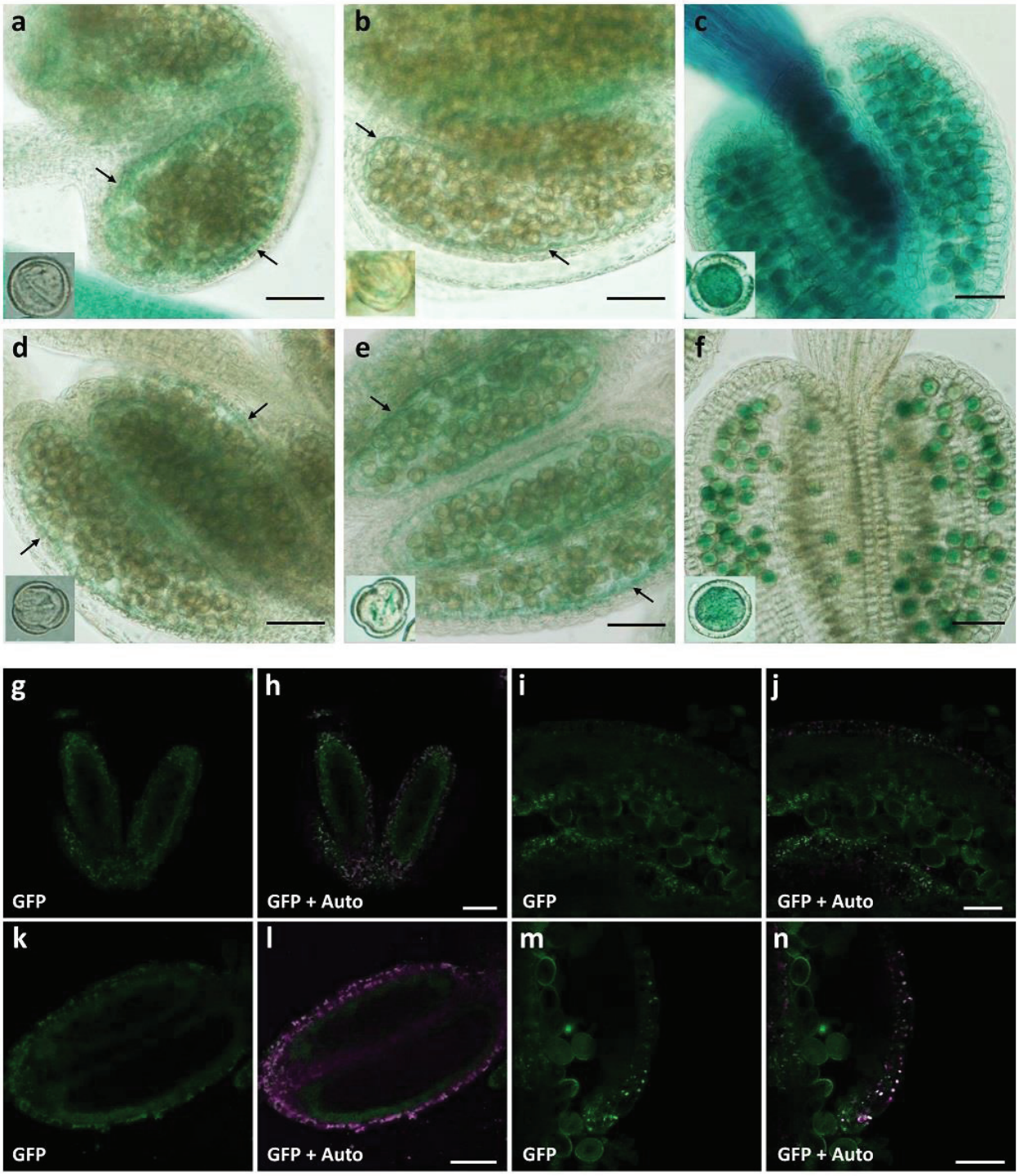

Fig. 3-11 *AtSEC23A* and *AtSEC23D* expression patterns in anthers. a-f GUS activity in the tapetum and pollen of transgenic *Arabidopsis* expressing $P_{AtSEC23A}$:*GUS* (a-c) or $P_{AtSEC23D}$:*GUS* (d-f). GUS staining was performed with anthers at uninucleate stage (a, d), bicellular stage (b, e), and tricellular stage (c, f). Arrows highlight the expression in the tapetum. **g-n** GFP fluorescence in the tapetum and pollen of transgenic *Arabidopsis* expressing $P_{AtSEC23A}$:*AtSEC23A-GFP* (g-j) or $P_{AtSEC23D}$:*AtSEC23D-GFP* (k-n). GFP fluorescence was observed with anthers at uninucleate stage (g, h, k, l) and tricellular stage (i, j, m, n). GFP, signal of G3GFP (green); Auto, auto-fluorescence of chlorophyll (magenta). Scale bars = 40 μm.

Moreover, RFP signal of SYP31-tagRFP was detected in a close proximity to the ERES to which AtSEC23A-G3GFP and AtSEC23D-G3GFP were localized (Fig. 3-13a, b). These results indicated that both AtSEC23A and AtSEC23D exhibit the characteristic localization of COPII coat in *N. benthamiana* leaf epidermal cells, suggesting that they contribute to COPII formation and ER-Golgi vesicle transport.

Because *AtSEC23A* was anticipated to be a putative chloroplast-localized protein by bioinformatics tools [155, 156], the author co-expressed *AtSEC23A* and *AtSEC23D* with a chloroplast marker which contains an RFP joined to a chloroplast-targeting signal of the *A. thaliana* RuBisCO small subunit. Like AtSEC23D, AtSEC23A showed no plastid localization in a transient expression system using *N. benthamiana* (Fig. 3-13c, d).

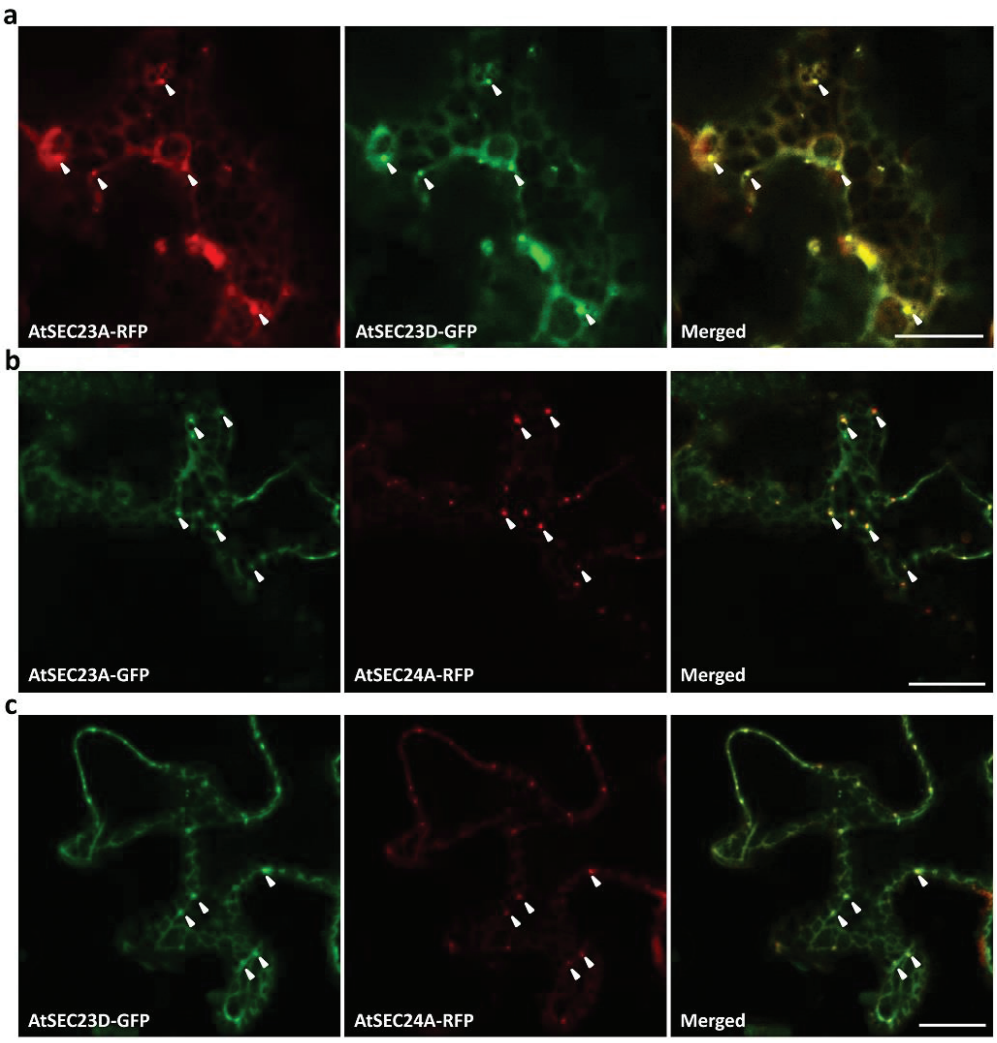

Fig. 3-12 Intracellular localization of AtSEC23A and AtSEC23D in *N. benthamiana* leaf epidermal cells. a Fluorescent images of epidermal cell co-expressing AtSEC23D-GFP with AtSEC23A-RFP. **b, c** Fluorescent images of epidermal cells co-expressing AtSEC23A-GFP (b) or AtSEC23D-GFP (c) with the ERES marker AtSEC24A-RFP. Arrowheads indicate ERESs. Scale bars = 20 μm.

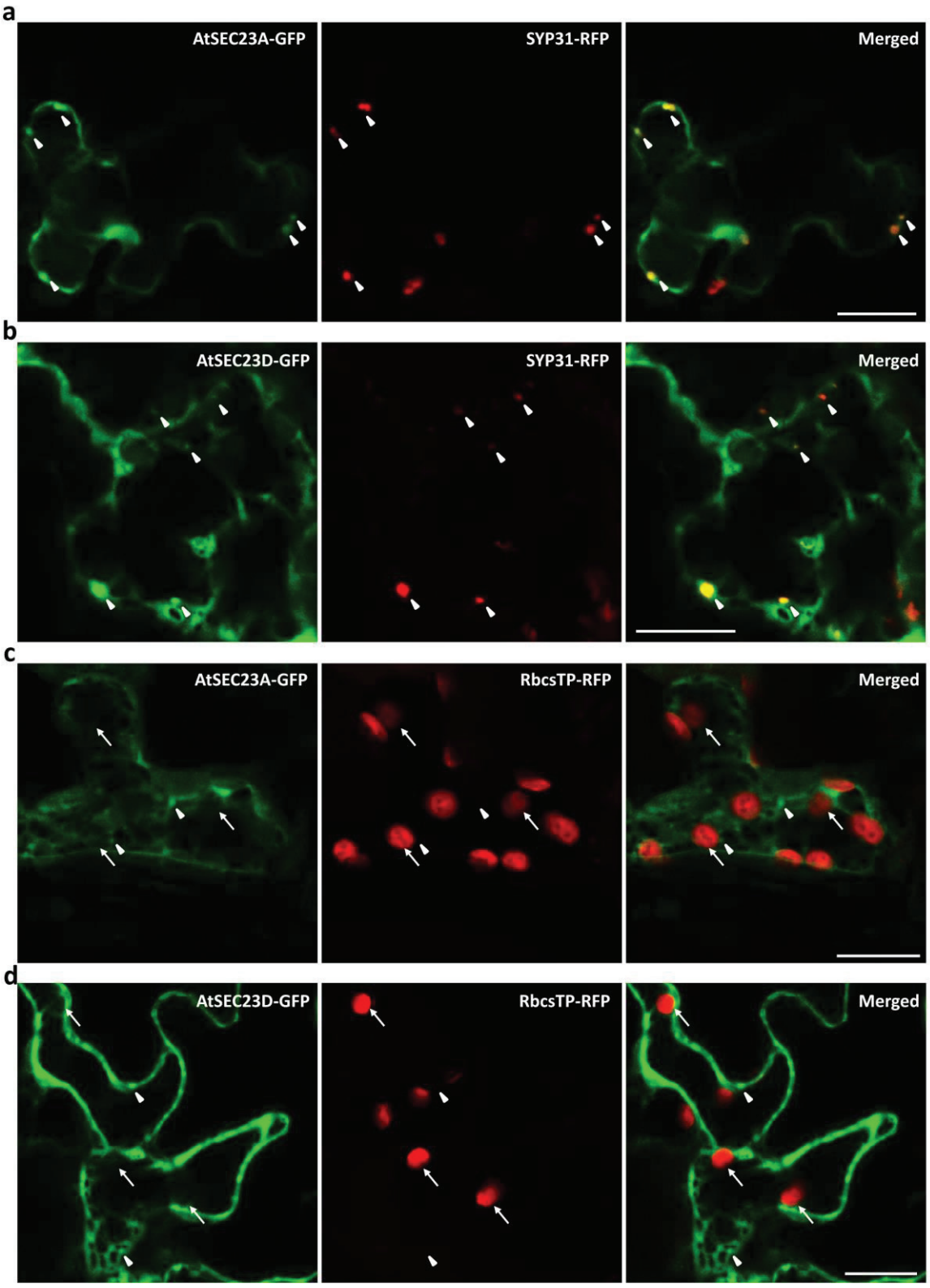

Fig. 3-13. Co-localization analyses of AtSEC23A and AtSEC23D in *N. benthamiana* leaf epidermal cells. **a, b** Confocal images of *N. benthamiana* leaf epidermal cells co-expressing the *cis*-Golgi marker SYP31-RFP with AtSEC23A-GFP (a) and AtSEC23D-GFP (b). Arrowheads label ERESs where GFP- and RFP-fused proteins co-localize. **c, d** Confocal images of *N. benthamiana* leaf epidermal cells co-expressing the chloroplast marker RbcsTP-RFP with AtSEC23A-GFP (c) and AtSEC23D-GFP (d). Arrows and arrowheads label the plastids and ERESs, respectively. Scale bars = 20 μm.

The decrease of AtSEC23A and AtSEC23D give rise to significant defects in microspore development at late uninucleate stage

To determine the precise timing of pollen defect appearance, the author analyzed the microspore and pollen development from the tetrad to the tricellular stage in *atsec23a*, *atsec23d* and *atsec23ad* by semi-thin sectioning. The major events of anther development in *A. thaliana* were classified into 14 well-defined stages [24]. At the tetrad stage (corresponding to anther stage 7), like wild-type anthers, *atsec23a*, *atsec23d* and *atsec23ad* anthers showed no obvious differences in microspores and tapetum development (Fig. 3-14a-d), however, tapetum was more vacuolated in the *atsec23ad* than that in the wild-type, *atsec23a* and *atsec23d* (Fig. 3-14d). At the early uninucleate stage (anther stage 8), individual microspores were released normally from the tetrads in wild-type, *atsec23a*, *atsec23d* and *atsec23ad* anthers, indicating yet normal microspore development (Fig. 3-14e-h). However, the tapetum of *atsec23ad* was highly vacuolated compared with that of wild-type, *atsec23a* and *atsec23d* (Fig. 3-14e-h). At the late uninucleate stage (anther stage 9), microspores and tapetal cells of the *atsec23a* and *atsec23d* showed comparable development with those of wild-type anthers (Fig. 3-14i-k). The large vacuole characteristic to this stage was seen in wild-type, *atsec23a* and *atsec23d* microspores (Fig. 3-14i-k). In contrast, apparent defects in microspore development were observed in *atsec23ad* anthers (Fig. 3-14l). Most microspores had irregular shapes with abnormal exine walls that mostly detached from the microspore plasma membrane. Although some microspores with large vacuole were observed, they lost their integrity and became concave in shape. At bicellular stage (anther stages 10-11), microspore development proceeded in wild-type, *atsec23a* and *atsec23d* anthers with no detectable differences (Fig. 3-14m-o). Microspores successfully completed the pollen mitosis I and possessed a cytosol with several small vacuoles instead of a solely large vacuole, and two distinctive vegetative and generative cells (Fig. 3-14m-o). By contrast, the defects of *atsec23ad* pollen became more obvious with a majority of pollen misshapen and shrunken which displays some signs of degeneration (Fig. 3-14p). Many pollen have shown a clear separation of the vegetative and the generative cells with detached exine walls (arrowheads in Fig. 3-14p), while others had no exine wall at all (arrows in Fig. 3-14p). The tapetum degeneration was initiated normally in the *atsec23a* and *atsec23d* as in wild-type anthers (Fig. 3-14m-o), while a metabolically active tapetum with many vacuoles and enlarged swollen tapetal cells was evident in the *atsec23ad* anthers, which indicates a delayed programmed cell death compared with the wild-type, *atsec23a* and *atsec23d* (Fig. 3-14p). At

tricellular stage (anther stage 12), the pollen mitosis II was completed and numerous tricellular pollen were found in wild-type, *atsec23a* and *atsec23d* anther locules (Fig. 3-14q-s). In contrast, only some remnants of tapetal cells, pollen materials, and empty pollen surface structures adhered to locule walls in the *atsec23ad* anther (Fig. 3-14t). However, few intact pollen were occasionally seen in some anther locules (Fig. 3-6d). These observations indicated that *atsec23a* and *atsec23d* plants showed no detectable defects in this analysis whereas *atsec23ad* plants were defective in exine wall formation which directly affected the whole process of pollen development and subsequently the seed yield.

Exine and intine formation are impaired in *atsec23ad* double-mutant plants

To examine whether the microspores and/or tapetal cells exhibited ultrastructural defects that might be undetectable by semi-thin sectioning, the author compared wild-type, *atsec23a*, *atsec23d* and *atsec23ad* anthers at higher resolutions using transmission electron microscope (TEM). In the wild-type at the tetrad stage, microspores enveloped in callose wall showed undulation of plasma membrane and primexine matrix synthesis followed by successful probacula deposition on the top of undulated membrane (Fig. 3-15a). Similar processes were observed in *atsec23a*, *atsec23d* and *atsec23ad* (Fig. 3-15b-d). In late uninucleate stage, where the microspores included a large vacuole, the wild-type, *atsec23a* and *atsec23d* developed well-defined bacula, tectum, and a thin layer of nexine (Fig. 3-15e-g). In addition, a primary intine layer was seen at this stage (black arrows in Fig. 3-15e-g). In *atsec23ad* microspores, such typical exine structures were completely missing except for a fragmented nexine-like layer around which many electron-dense semi-spherical sporopollenin-like aggregations were accumulated (Fig. 3-15h). Some *atsec23ad* microspores showed signs of degeneration with a pollen wall separated from the cytoplasm. In the bicellular stage, wild-type, *atsec23a* and *atsec23d* microspores continued development with expanded bacula and thicker tectum (Fig. 3-15i-k). In addition, the inner intine layer became more obvious at this stage (black arrows in Fig. 3-15i-k). In contrast, the *atsec23ad* microspores showed more damaged pollen wall in which the sporopollenin-like aggregations increased in size and fused together with clear separation from microspore plasma membrane (Fig. 3-15l). Some pollen grains were seen as naked cells without walls (yellow star(s) in Fig. 3-15l and Fig. 3-6e), while others had only empty walls without microspore cells (yellow asterisks in Fig. 3-6e), being consistent with semi-thin sectioning observations (Fig. 3-14p). Moreover, the nexine and intine layers were indistinguishable in the *atsec23ad* microspores (Fig. 3-15l). The inner compartments of *atsec23a* and *atsec23d* microspores were comparable

to those of the wild-type (Fig. 3-15j, k). In contrast, most cellular inclusions of *atsec23ad* microspores were degenerated and only few distinguishable organelles remain (i.e., plastids and mitochondria) (arrows and arrowheads in Fig. 3-15l). Interestingly, the plastids in the incompletely degenerated *atsec23ad* bicellular pollen showed profound alternation in their morphologies comparing with those of the wild-type, *atsec23a* and *atsec23d*. At the tricellular stage, mature pollen walls were completed by deposition of pollen coat materials released from tapetal cells into the cavities between bacula of wild-type, *atsec23a* and *atsec23d* pollen (Fig. 3-15m-o). At this stage, wild-type and *atsec23d* pollen developed a thin uniformly-distributed intine layer around the plasma membrane (Fig. 3-15m, n), while this layer was developed thicker and less electron-dense in *atsec23a* pollen (Fig. 3-15o and Fig. 3-16a-c). By contrast, most pollen in the *atsec23ad* anthers were degenerated and only flattened pollen shells and remnants of tapetum and dead pollen materials were left inside the locules (Fig. 3-15p). However, few undegenerated pollen grains with incomplete pollen walls were occasionally seen. Some of them had walls consisted of sporopollenin-like aggregations with little pollen coat materials which contained numerous rod-shaped electron-lucent structures (Fig. 3-15p), while others had walls consisted of elongated bacula that not roofed by tectum and with much depositions of pollen coat materials (Fig. 3-16d, e). These depositions were less electron-dense and less compacted than those of the wild-type, *atsec23a* and *atsec23d*, and contained many electron-lucent vesicle-like structures of different sizes, that did not observed in the wild-type, *atsec23a*, and *atsec23d* (Fig. 3-16d, e). This suggested incomplete pollen coat depositions and a possible defect in development of tapetal cells, the main sources of pollen coat materials. Therefore, these results indicated that the depletion of both *AtSEC23A* and *AtSEC23D* result in defective pollen wall development and consequently leads to pollen degeneration.

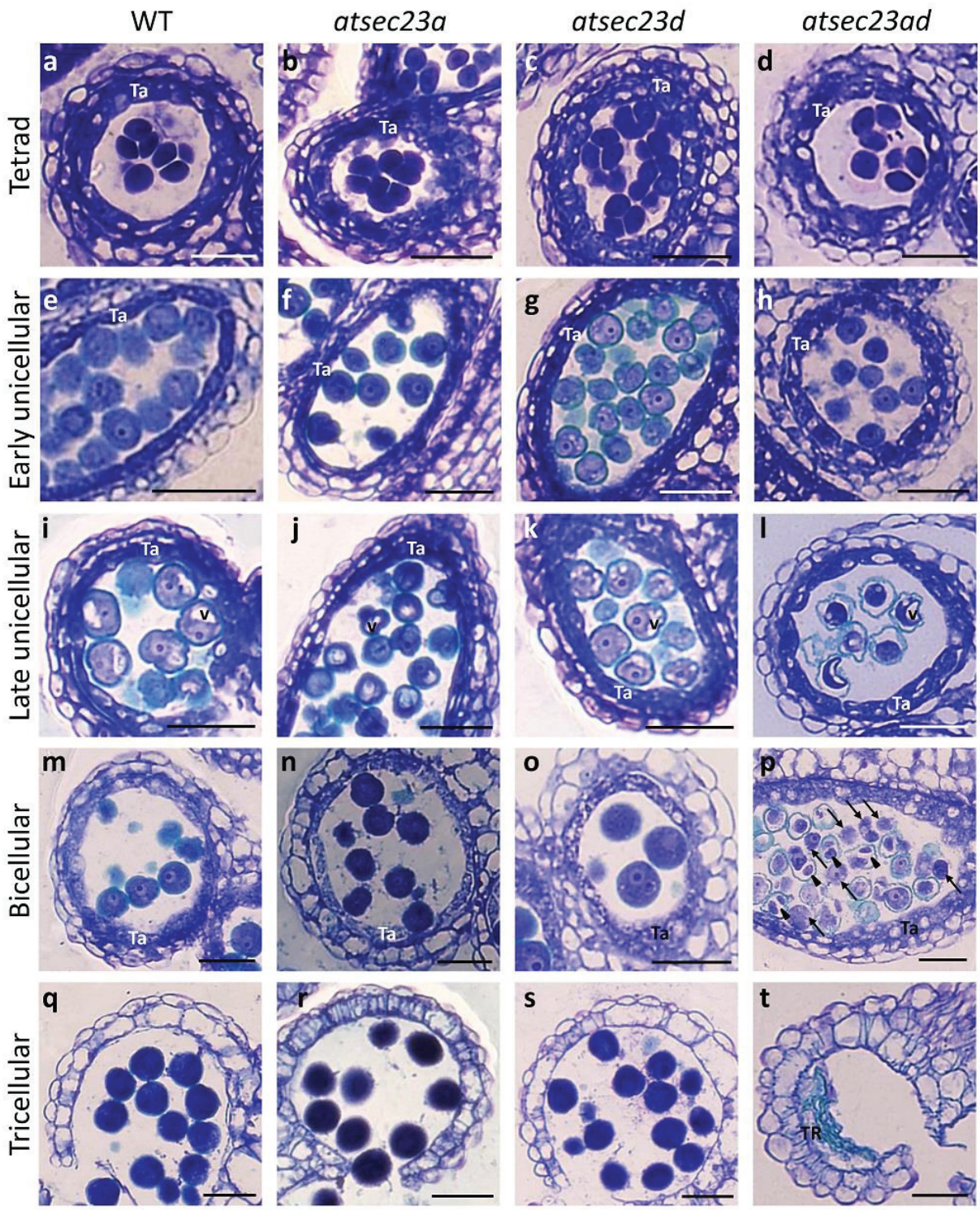

Fig. 3-14 Semi-thin sections showing anther and microspore development in wild-type, *atsec23a*, *atsec23d*, and *atsec23ad* plants. The sections were prepared from anthers at tetrad (a-d), early uninucleate (e-h), late uninucleate (i-l), bicellular (m-p), and tricellular stages (q-t). No obvious defects were observed in the *atsec23a* and *atsec23d* single-mutant anthers compared to the wild type. Defects in the double mutant, *atsec23ad*, were seen at the late uninucleate stage. The severity of phenotype increased at bicellular stage and almost empty locules remained at tricellular stage. Arrowheads and arrows indicate microspore with detached pollen walls and without pollen walls, respectively. Ta, tapetum; TR, tapetum residue; V, vacuole. Scale bars = 30 μm.

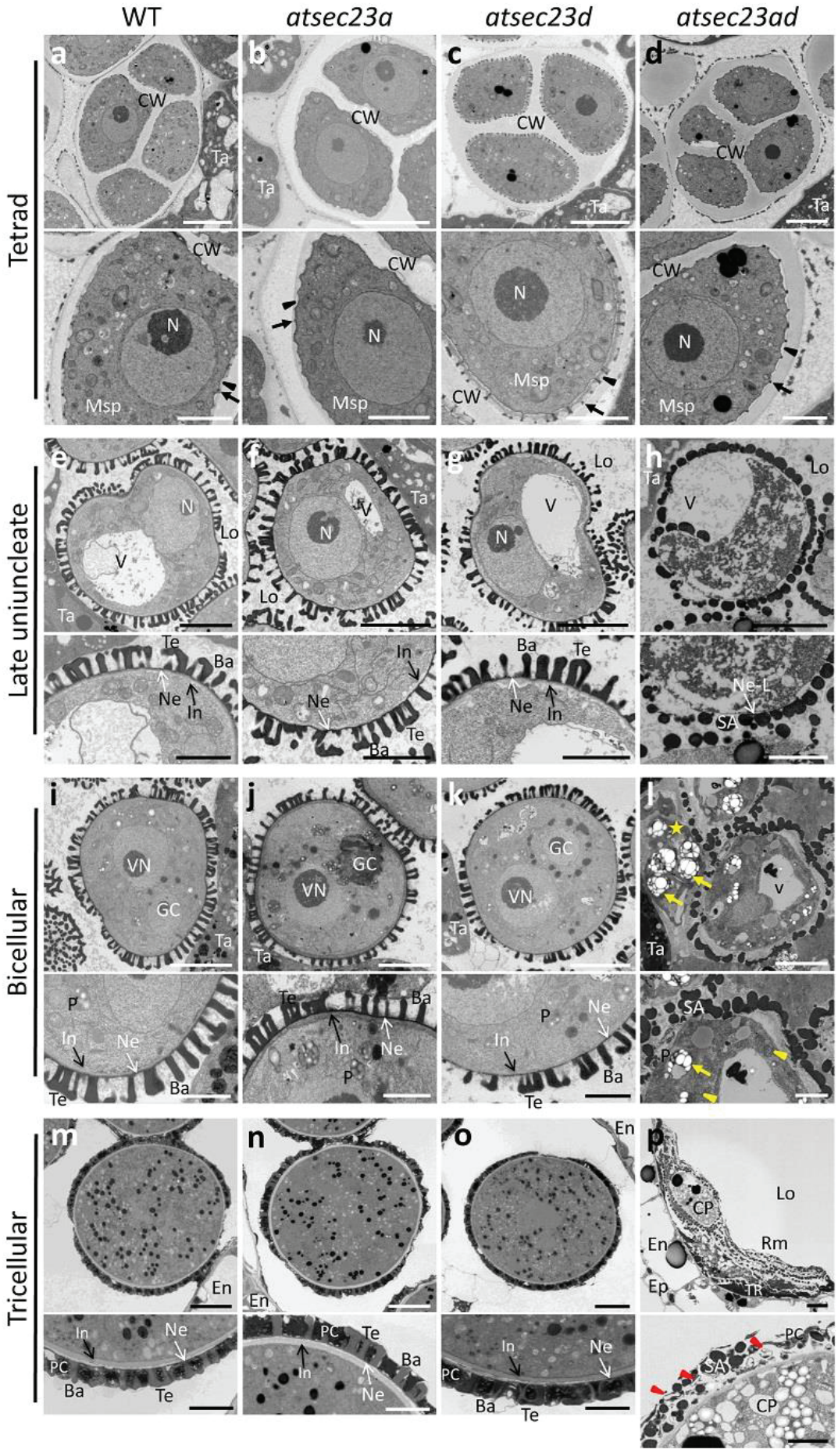
WT
atsec23a
atsec23d
atsec23ad
Tetrad
Late uniuncleate
Bicellular
Tricellular
a
b
c
d
e
f
g
h
i
j
k
l
m
n
o
p
CW
Ta
N
Msp
V
Lo
Te
Ba
Ne
In
Ne-L
SA
VN
GC
v
P
PC
En
CP
Rm
Ep
TR

Fig. 3-15 Transmission electron micrographs comparing microspore development of wild-type, *atsec23a*, *atsec23d*, and *atsec23ad* plants. a-d Ultrastructure of microspores at tetrad stage. Arrows and arrowheads label primexine and protecta, respectively. The tetrad in *atsec23d* is little advanced than tetrads of other samples. **e-h** Ultrastructure of microspores at late uninucleate stage. **i-l** Ultrastructure of microspores at bicellular stage. A star, arrows, and arrowheads indicate a naked microspore with no walls, plastids, and mitochondria, respectively. **m-p** Ultrastructure of pollen at tricellular stage. Arrowheads show the irregular electron-lucent structures in the pollen coat. Lower panels are magnifications of pollen structures in the upper panels. Ba, baculum; CP, collapsed pollen; CW, callose wall; En, endodermis Ep, epidermis; GC, generative cell; In, intine; Lo, locule; Msp, microspore; N, nucleus with a dark stained nucleolus; Ne, nexine; Ne-L, nexine-like structure; P, plastid; PC, pollen coat; Rm, remnants of dead pollen; Sa, sporopollenin-like aggregations; Ta, tapetum; Te, tectum; TR, tapetum residue; V, vacuole; VN, vegetative nucleus. Scale bars = 5 μm in upper panels, and 2 μm in lower panels.

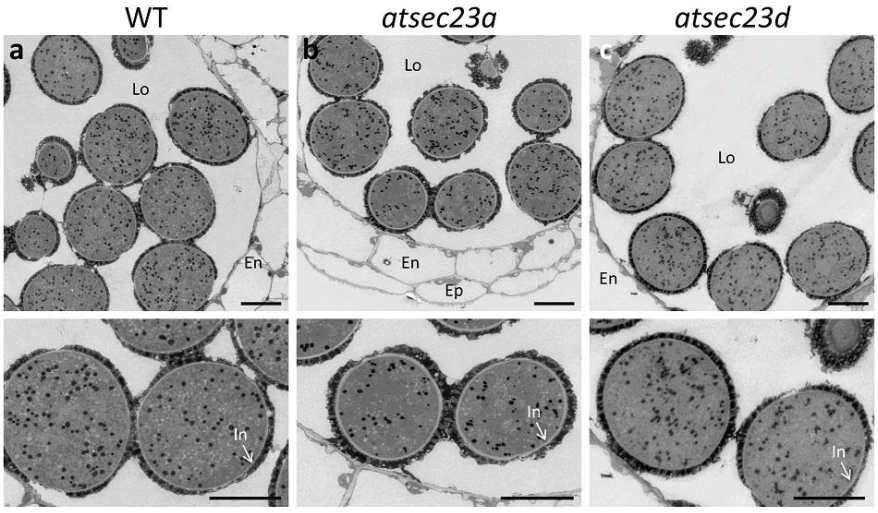

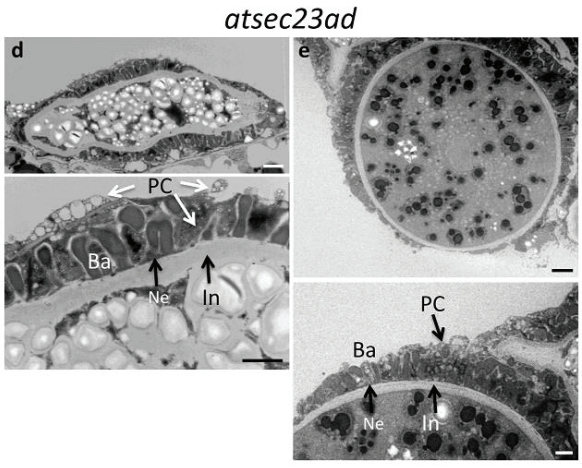

Fig. 3-16. Abnormal thickening of the intine layer of *atsec23a* pollen and defective wall development in *atsec23ad* pollen. a-c Scanning electron micrographs comparing intine layer of mature wild-type (a), *atsec23a* (b), and *atsec23d* (c) pollen at the tricellular stage. **d, e** Scanning electron micrographs showing defective walls of *atsec23ad* pollen at the tricellular stage. Note the abnormal, less compacted pollen coat, thickened intine layer, and missing of the tectum in *atsec23ad* pollen. Ba, baculum; En, endodermis Ep, epidermis; In, intine; Lo, locule; Ne, nexine; PC, pollen coat. Scale bars = 10 μm in (a-c), 2 μm in (upper panel of d, e), and 1μm in (lower panel of d, e).

Loss of *AtSEC23A* and *AtSEC23D* causes a delay in tapetum development and abnormalities in tapetal inner organelles

Tapetal cells supply pollen wall materials such as sporopollenin to developing microspores, and provide pollen coat materials accumulated in elaioplasts and tapetosomes to mature pollen after the degeneration of tapetal cells [28, 81]. The occurrence of apparent defects in microspores at the time of formation of significant exine walls and the incomplete pollen coat in *atsec23ad*, led us to suspect the possibility of dysfunction of tapetal cells. Thus, the author performed TEM observation focused on the endomembrane system and organelles in tapetal cells along different developmental stages. At the tetrad stage, tapetal cells in wild-type, *atsec23a* and *atsec23d* showed several small and few large vacuoles (Fig. 3-17a-c), whereas, smaller vacuoles and clusters of tiny vesicles were observed in the *atsec23ad* (Fig. 3-17d). In the wild-type, *atsec23a* and *atsec23d*, tapetal cells contained elongated stacks of rough ER with clear ribosomes and well-defined Golgi bodies (Fig. 3-17a-c). By contrast, tapetal cells of *atsec23ad* contained rough ER surrounded with less clear ribosomes and abnormal Golgi stacks swollen at their ends and connected with numerous small vesicles (Fig. 3-17d). The tapetum at the late uninucleate stage is characterized by the formation of two specialized storage organelles, the elaioplast and tapetosome. Well-developed elaioplasts with numerous electron-lucent plastoglobules and clusters of small electron-dense tapetosomes were evident in tapetal cells of the wild-type, *atsec23a* and *atsec23d* (Fig. 3-17e-g). By contrast, undifferentiated proplastids (precursors of elaioplasts) were observed and the formation of tapetosomes was net not initiated in the *atsec23ad* tapetal cells (Fig. 3-17h), indicating that a delay in tapetum development has occurred in the *atsec23ad*. In addition, several sporopollenin-like aggregations deposited on the middle layer cell wall facing to the tapetum (arrows in Fig. 3-17h), coinciding with the occurrence of clear defects in microspore wall development (Fig. 3-15h). At the bicellular stage in wild-type, *atsec23a* and *atsec23d*, tapetal cells continued to develop more abundant mature elaioplasts and fully developed tapetosomes (Fig. 3-17i-k). The tapetosomes became larger and contained numerous fragmented electron-dense structures (Fig. 3-17i-k). In contrast, the *atsec23ad* tapetal cells had elaioplasts without definite membranes consisted of fewer and larger plastoglobules (Fig. 3-17l). In addition, tapetosomes had lost their integrity and had unclear fragmented inner structures (Fig. 3-17l). Moreover, deposited sporopollenin-like aggregations became more abundant on the middle layer wall (arrows in Fig. 3-17l). At the tricellular stage, the tapetal cells were completely degenerated in wild-type, *atsec23a* and *atsec23d* (Fig. 3-17m-o).

However, the remnants of tapetal cells still can be observed in *atsec23ad* anthers (Fig. 3-17p), indicating a delay in tapetum degeneration. These findings suggested that lack of *AtSEC23A* and *AtSEC23D* causes structural abnormalities and a developmental delay in the tapetal organelles, elaioplasts and tapetosomes.

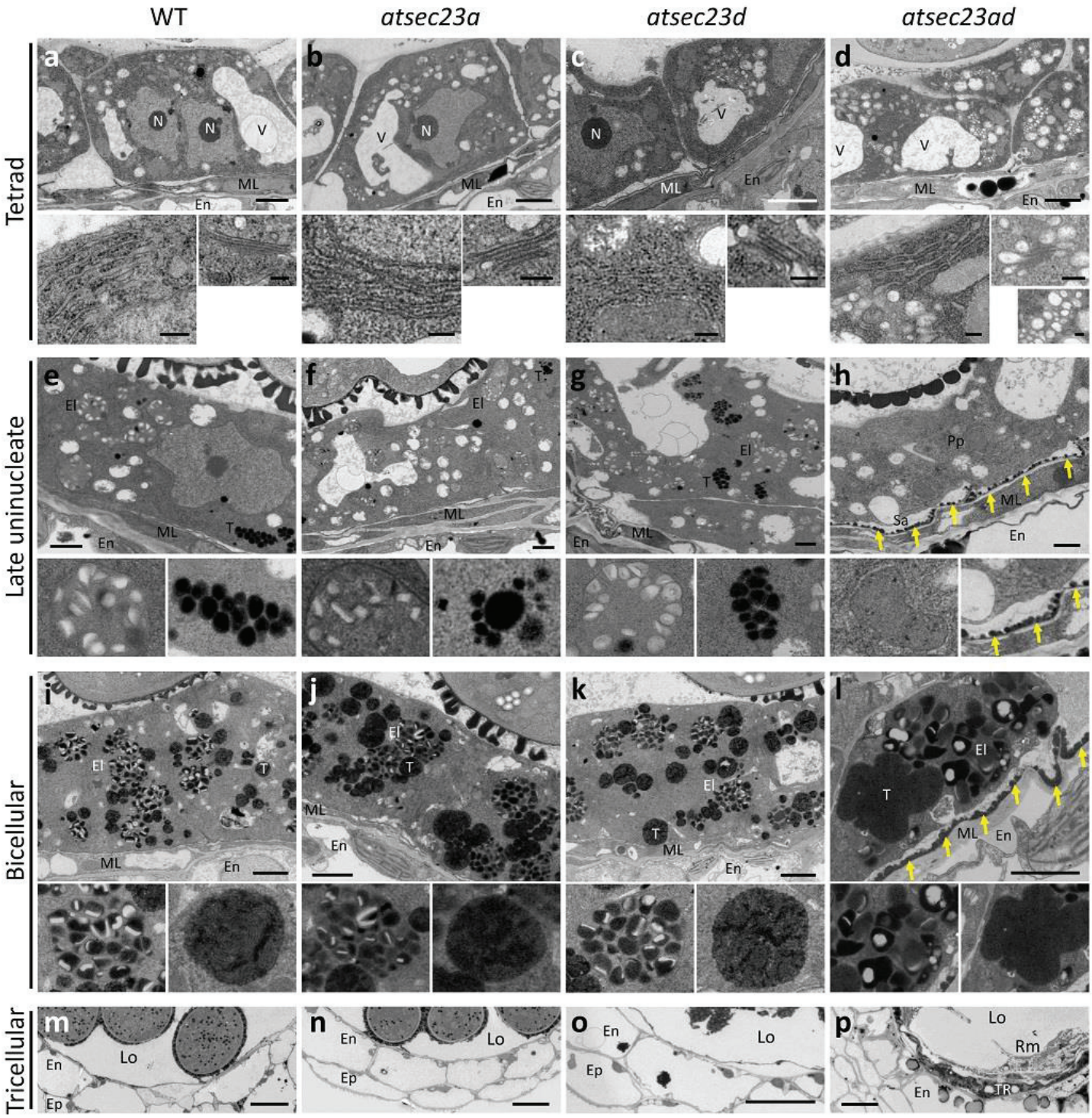

Fig. 3-17 Transmission electron micrographs comparing the development of tapetum and inner organelles in wild-type, *atsec23a*, *atsec23d*, and *atsec23ad* plants. a-d Ultrastructure of tapetal cells at tetrad stage. The left side of lower panels in (a-d) shows enlargements of the ER. The right side of lower panels indicates enlargements of Golgi in (a-c) or Golgi (top) and clusters of tiny vesicles (bottom) in (d). **e-h** Ultrastructure of tapetal cells at late uninucleate stage. Left and right lower panels in (e-g) show enlargements of elaioplasts and tapetosomes, respectively. Elaioplasts and tapetosomes are not yet developed in *atsec23ad*. Left and right lower panels in (h) indicate enlargements of proplastids (precursors of elaioplast) and sporopollenin-like aggregations accumulated on the middle layer wall, respectively. The enlarged parts are labeled by letters in the upper panels. Arrows indicate the sporopollenin-like aggregations accumulated on the middle layer wall. **i-l** Ultrastructure of tapetal cells at ~~B~~bicellular stage. Left and right lower panels show enlargements of elaioplasts and tapetosomes labeled by letters in the upper panels, respectively. Arrows indicate the sporopollenin-like aggregations that became more abundant on the middle layer wall. **m-p** Ultrastructure in anther locule at tricellular stage. Note that tapetum residue remains only in *atsec23ad* locule with remnants of dead pollen and cell debris. El, elaioplast; En, endodermis Ep, epidermis; Lo, locule; ML, middle layer; N, nucleus; PP, proplastid; Rm, remnants of dead pollen; Sa, sporopollenin-like aggregations; T, tapetosome; Ta, tapetum; TR, tapetum residue; V, vacuole. Scale bars = 2 μm in (upper panels of a-d and i-l), 250 nm in (upper panels of a-d), 1 μm in (e-h), and 10 μm in (m-p).

Discussion

The involvement of SEC23 proteins in regulating plant growth and development and the functional differences among them have remained unknown. In the present study, the author revealed that out of the seven *A. thaliana*. SEC23 homologs, *AtSEC23A* and *AtSEC23D* have an essential role in pollen wall formation, exine patterning, and tapetum development. The author also provides an evidence for the partially overlapping functions of SEC23 homologs in plants.

The results of the primary structure analyses (phylogenetic tree, domain structure analysis, and sequence alignments) suggested that both AtSEC23A and AtSEC23D may be involved in cellular processes distinct from other AtSEC23 homologs. AtSEC23A and AtSEC23D showed limited sequence similarities with other AtSEC23 homologs and substitutions in some conservative amino acids such as Cys484 of AtSEC23A and Glu337, Phe366, and Arg706 of AtSEC23D. However, like AtSEC23A, AtSEC23D showed a subcellular localization being characteristic of COPII component with distribution into ERES (Fig. 3-12), suggesting that they may have specific functions in ER export at the early secretory pathway. Although there is no available information about the significance of the substitution of these amino acids in AtSEC23D, they may be required for selective cargo export from the ER or for specific interaction with other SAR1 homologs as the case of Cys484 in AtSEC23A. It will be interesting to analyze the specific effects of these substitutions in a further study.

Knockout of *AtSEC23D* caused a defect in the microspore outer layer (exine) but did not affect the inner layer (intine) (Fig. 3-15). Pollen of *atsec23d* plants exhibited less sporopollenin deposition which led to incomplete tectum formation and reticulate architecture (Fig. 3-3). In contrast, knockdown of *AtSEC23A* caused defects in both exine and intine layers. The exine layer of *atsec23a* also missed the reticulate architecture with wide areas showed incomplete tectum formation and less sporopollenin deposition (Fig. 3-3), whereas the intine layer was thicker and less electron dense when observed by TEM (Fig. 3-15 and Fig. 3-16). Moreover, pollen of *atsec23a* plants showed impaired germination rate, almost half of those in the case of the wild-type (Fig. 3-9q, r, v). Despite the limited pollen germination rate, the *atsec23a* was normally fertile which may be due to the large amount of yet functional pollen compared with the limited number of ovules to be fertilized. Mutations in *AtSEC24A*, *AtSEC24B*, and *AtSEC31B*, other members of COPII proteins, have shown to cause compromised pollen germination rate [91, 134, 138]. During pollen germination, the growing pollen tube is encased only by the intine [157]. Possibly, the thickened intine in *atsec23a* is responsible for the impaired pollen germination rate by increasing the required pressure for pollen germination. In *Brassica campestris*, a mutation in the BcMF8 which encodes a putative arabinogalactan protein causes reduced pollen germination and retarded pollen tube growth as a result of remarkable thickening of the intine layer [158]. Similarly, double knockdown plants of two polygalacturonase genes (BcMF26a and BcMF26b) exhibited defective pollen development, pollen germination, and pollen tube elongation by formation of an abnormal thick intine layer [159].

By genetic analyses (Fig. 3-8), the author showed that *atsec23a* and *atsec23d* mutants in the heterozygous state generate normal pollen with the characteristic exine reticulate pattern, suggesting that the defect of exine pattern is caused by sporophytic effect. Also, tetrad analysis of the heterozygous *atsec23a* in the *atsec23d* and *qrt1-2* mutant background (+/*23a*, *23d/23d*, *qrt1-2*/*qrt1-2*), supported that the failure of pollen development is due to defects in sporophytic tissues. However, the reduced pollen germination rates and the abnormally thickened intine of *atsec23a* plants indicate a gametophytic function of AtSEC23A in the male gametophyte. Therefore, these findings suggest that *AtSEC23D* functions only sporophytically while *AtSEC23A* functions both sporophytically and gametophytically.

AtSEC23A and *AtSEC23D* showed different temporal and spatial expression patterns (Fig. 3-10), however, the close investigation in anthers revealed that both genes were

expressed primarily in the tapetal cells but slightly or not expressed in developing microspores (Fig. 3-11). After tapetum degeneration, the expression was detected in the mature pollen. The timing of appearance of obvious defects in microspores correlates well with the timing of *AtSEC23A* and *AtSEC23D* expression in the tapetum and also with the timing at which sporopollenin-like aggregations accumulated on the middle layer walls, indicating that loss of *AtSEC23A* and *AtSEC23D* in sporophytic tapetal cells may be responsible for the defects observed in the microspores.

TEM analysis of microspore development showed that membrane undulation, primexine synthesis, and probacula deposition have occurred normally in single and double mutants similar to those in the wild type (Fig. 3-15). Release of microspores from the callose wall was not affected in single and double mutants as revealed by aniline blue staining (Fig. 3-9i-p) and semi-sectioning analysis (Fig. 3-14). The aberrant exine observed at the late unicellular stage of anther development indicates a postmeiotic function of *AtSEC23A* and *AtSEC23D*. Double-mutant plants exhibited a wide range of defects, including: (1) defective sexine with incorrect deposition of sporopollenin-like materials around the microspore cytoplasm and on the locule wall, (2) microspore degeneration or leakage as many microspores were seen naked without walls while others had empty shells with no cytoplasm and only few distinguishable organelles remain (i.e., plastids and mitochondria), (3) altered or missing nexine and intine layer, (4) altered development of the inner organelles (i.e., ER, Golgi, elaioplasts, and tapetosomes) in the tapetal cells, and (5) abnormal pollen coat depositions.

The frequent microspore degeneration or leakage observed in double-mutant locules was linked with loss of the intact cell wall. Pollen wall integrity must be maintained to ensure normal pollen development. Mutations that affect pollen wall integrity such as *MS1, MS2, ACYL COENZYME A SYNTHETASE5* (*ACOS5*), *CALLOSE SYNTHASE5* (*CALS5*), *CYTOCHROME P450* (*CYP703A2*), *RUPTURED POLLEN GRAIN1* (*RPG1*), *DEFECTIVE IN EXINE PATTERNING1* (*DEX1*), *NO EXINE FORMATION1* (*NEF1*), *TRANSIENT DEFECTIVE EXINE* (*TDE1*), ATP-binding cassette (*ABCG26*), and *AtSEC31B* have resulted in collapsed pollen with degenerated cytoplasm [54-57, 64, 66, 67, 77, 78, 118, 138, 160]. Interestingly the mutants *cals5*, *dex1*, *nef1*, *tde1*, *abcg26*, and *atsec31b* have accumulated sporopollenin-like aggregations on the outer tapetum walls similar to those found in the *atsec23ad* double-mutant plants [55, 66, 67, 78, 138, 160]. These sporopollenin-like aggregations indicate an unsuccessful sporopollenin deposition and polymerization onto the

microspore plasma membrane. One explanation for the failure of sporopollenin deposition and polymerization onto the microspore plasma membrane is that the sporopollenin produced by the tapetal cells in *atsec23ad* double-mutant plants has an altered chemical composition missing one or more of the essential components that are required for correct sporopollenin deposition and polymerization. This is further supported by the tendency of double-mutant microspores to aggregate and stick together, which may indicate an abnormal chemical composition of the sporopollenin. The collapsed microspores that tended to stick together in the *ms1* mutant plants were suggested to be a result of an unusual chemical composition of pollen-wall materials, and *MS1* possibly function by organizing materials such as sporopollenin correctly on the microspore plasma membrane [161]. Sporopollenin is mainly composed of fatty acid derivatives [162] and several enzymes that participate in the metabolism of fatty acids and their derivatives are associated with the ER [28, 163]. These include *ACOS5*, *MS2*, *CYP703A2*, *CYP704B1*, *POLYKETIDE SYNTHASES A* (*PKSA*), *PKSB*, *TETRAKETIDE α-PYRONE REDUCTASE1* (*TKPR1*), and *TKPR2* [54, 56-58, 73-76]. *ACOS5*, *PKSA*, *PKSB*, and *TKPR1* are involved in tetraketide α-pyrones synthesis pathway and localized in the ER of the tapetal cells where they interact together *in vivo* [163]. Most likely the majority of these genes and enzymes exit the ER through a COPII-dependent route. These fatty acids and polyketides as main components of the sporopollenin may be substrates of *AtSEC23A* and *AtSEC23D*. However, this question requires further investigations. Another hypothesis is that *AtSEC23A* and *AtSEC23D* may mediate signaling proteins necessary for the coordination of sporopollenin deposition and polymerization onto the microspore plasma membrane. It was suggested that *ABCG26* may transport some signaling molecules required for the coordination of exine formation and sporopollenin polymerization on the developing microspore wall [77]. The study of pollen development of the *tde1* mutant has suggested the existence of factors controlling the exine patterning. These factors were potentially active at uninucleate microspore stage [160].

Pollen wall development relies largely on normal tapetum development. Semi-sectioning analysis has revealed no detectable defects in tapetum development of single-and double-mutant plants, except for that the tapetal cells of double-mutant plants were more vacuolated (Fig. 3-14). However, TEM analysis has revealed the occurrence of morphological abnormalities in organelles of the tapetum (i.e., ER, Golgi, elaioplasts, and tapetosomes), and a delay in tapetum development and degeneration (Fig. 3-17). The endomembrane system in double-mutant tapetal cells was highly affected. Lack of *AtSEC23A*

and *AtSEC23D* causes aberrant ER and Golgi structures and leads to appearance of clusters of tiny vesicles; which ultimately affect the efficiency of COPII assembly. Despite these abnormalities in the tapetal cells of double *atsec23ad* mutant plants, the microspores were released normally, which indicate that the endomembrane system in tapetal cells still have a partial activity sufficient to support callase secretion. Several studies have shown that maintaining the integrity of ER and Golgi membranes is associated with successful assembly of COPII proteins. For example, a mutation of SAR1 proteins inhibits ER to Golgi trafficking and affects the Golgi integrity [164]. A missense mutation in *AtSEC24A* has resulted in defective ER and Golgi structures and has led to a formation of different sized vesicular clusters [135]. Moreover, a mutation in either *GLYCEROL-3-PHOSPHATE ACYLTRANSFERASE* (*GPAT1*) or *GPAT6* caused reduced ER profiles and compromised secretory activity in the tapetal cells which consequently resulted in reduced male fertility in *A. thaliana* [165, 166].

In addition to the defective ER and Golgi, the development of elaioplasts and tapetosomes in the double-mutant tapetum was significantly delayed and both organelles exhibited structural abnormalities (Fig. 3-17). These organelles are the places for storage of lipidic materials required for pollen coat formation. Tapetosomes are originated from the ER and enriched with triacylglycerols, flavonoids, and oleosins [167] while elaioplasts are developed from the proplastids and mainly filled with steryl esters and polar lipids [168, 169]. ER networks are in direct contact with plastids and it was suggested that lipid exchange between the ER and plastids may occur at membrane contact sites [170-172]. The structural abnormalities and the delayed development of elaioplasts and tapetosomes may be a consequence of the defective ER structure or a defective lipid exchange between the ER and plastids. Another possibility is that lack of functional *AtSEC23A* and *AtSEC23D* causes less efficient COPII assembly at the ERESs and disrupts transport of essential components (i.e., triacylglycerols, oleosins, and steryl esters) required for normal elaioplast and tapetosome development. It was reported that triacylglycerols and oleosins are synthesized in the ER cisternae and accumulated at specific centers in the ER to form tapetosomes [173]. *AtSEC31B*, another COPII component, also showed a retarded development of elaioplasts and tapetosomes with ultrastructure abnormalities [138]. However, the mechanisms by which COPII components affect the formation of elaioplasts and tapetosomes require further investigation.

Pollen of the double mutant also showed abnormal pollen coat depositions (Fig. 3-17). Some pollen had less deposition of coat materials with numerous rod-shaped electron-lucent structures. Similar structures were described in the pollen coat of *atsec31b* and *abcg9 abcg31* plants as reported previously [138, 174]. Occasionally, few pollen have developed walls with elongated bacula in between which much depositions of pollen coat materials accumulated (Fig. 3-16d, e). These depositions were less electron-dense and less compacted than those of the wild type and abnormally contained many electron-lucent vesicle-like structures (Fig. 3-15p). The abnormal pollen coat depositions may be the direct result of abnormal development of elaioplasts and tapetosomes in the tapetal cells, a delay in tapetum degeneration, or alternatively as a result of less efficient ER export of proteins that participate in pollen coat deposition. Recently, the ABCG9, which is involved in transport of lipidic components (e.g., steryl glycosides) required for pollen coat formation [174], is likely transported through ER-Golgi route [138].

In summary, the results described here show that *AtSEC23A* and *AtSEC23D* are required for proper pollen wall development and exine patterning, possibly by mediating efficient ER export of some essential proteins/enzymes participating in pollen wall formation. This work provides a direct link between the early secretory pathway in tapetal cells and sporopollenin deposition and exine patterning. These results indicate that *AtSEC23A* and *AtSEC23D* may only share partial redundant functions. From the phenotypes observed in the single mutants, it seems that both proteins do not fulfill exactly the same functions; *AtSEC23A* functions both sporophytically in the tapetum to form the exine wall and gametophytically in the microspore to form the intine wall and to support pollen germination, whereas, *AtSEC23D* functions only sporophytically in the tapetum to participate with *AtSEC23A* in the exine wall formation. Thus, the author proposes that *AtSEC23A* and *AtSEC23D* may have differing substrate preferences, providing an evidence of functional diversity of SEC23 proteins in plants. Identifying the specific substrate and the interaction partners of *AtSEC23A* and *AtSEC23D* will be the basis for a future study.

Chapter 4

Development of an R4 dual-site gateway cloning system for simultaneous cloning of two desired sets of promoters and open reading frames in a binary vector for plant research

Introduction

With advances in omics databases and bioinformatics, many genes and their products have been anticipated to work cooperatively. In order to verify and utilize information on relationships between genes evaluated by these studies, transgenic analyses of expression patterns, intracellular dynamics, and molecular interactions between two genes of interest are necessary. Several approaches such as crossing, re-transformation, co-transformation, polycistronic transgenes, a polyprotein production system, bi-directional promoter strategy, and multi-gene construction are performed for the delivery of two or more genes into plant genomes [175, 176]. Successive rounds of crossing or sequential re-transformation are laborious and time-consuming. In re-transformation, different selection markers are required in each transformation process. Furthermore, transgenes are integrated at different loci and segregate in subsequent generations, which is also the case in co-transformation. Other methods use one T-DNA carrying all genes to be introduced for transformation and these genes are integrated at the same loci and inherited concurrently by offspring in successive generations. However, polycistronic transgenes, the polyprotein production system, and bi-directional strategy only use one promoter for the production of all encoded proteins [175, 177]. In contrast, multi-gene constructs carrying all expression cassettes in one T-DNA permit the use of different promoters in each expression cassette in order to independently regulate the expression of genes in each cassette [178, 179]. This characteristic is critically important because researchers need to carry out interactive functional analyses with multiple genes that are individually expressed using their own or suitable promoters (e.g. inducible, site-, or stage-specific promoters).

A binary vector system that provides researchers with the flexibility to choose the desired promoter(s) is expected to be useful practically because it is very laborious to construct several promoter-open reading frame (ORF) cassettes and arrange them in one binary vector using traditional cloning methods. Gateway cloning technology [39] has recently proved to be extremely useful for gene construction, and a number of Gateway cloning technology-compatible binary vectors for various applications including fusion with useful tags have been developed [180]. In addition to the originally utilized *att*1 and *att*2 sites, the engineered variants *att*3, *att*4, *att*5, and *att*6 were developed as new highly specific recombination sites and these made possible the multisite Gateway technology [41]. In the commercial multisite Gateway system, these six *att* sites (*att*1 to *att*6) are applied to the

simultaneous linking and cloning of multiple DNA fragments (entry clones) into a vector by an LR reaction [181], for example, the linking of a promoter (*att*L1-promoter-*att*R5), ORF (*att*L5-ORF-*att*L4), tag (*att*R4-tag-*att*R3), and terminator (*att*L3-terminator-*att*L2) to make and clone expression cassettes (e.g. *att*B1-promoter-*att*B5-ORF-*att*B4-tag-*att*B3-terminator-*att*B2) [182]. Although this system is useful for assembling DNA fragments, it requires specialized entry clones, and the resources of universal entry clones accumulated in research communities are not available for this system. As alternative applications of multiple *att* sites, MultiRound Gateway technology [43, 44] and the Gateway recycling cloning system [45] have been developed for step-by-step repetitive cloning of an expression cassette into a vector to make a multi-gene binary construct using multiple rounds of LR reactions. Although these are outstanding methods to clone an unlimited number of expression cassettes into a binary vector, they require laborious traditional cloning steps to prepare a promoter:ORF construct on a prerequisite donor vector. Since many transgenic experiments require manipulations of up to two genes, the supportive binary vector system oriented simple cloning of just two expression cassettes is thought to be valuable as a practical tool.

In the present study, a novel Gateway cloning technology-compatible binary vector system, the R4 dual-site (R4DS) Gateway cloning system was developed to permit the easy and efficient cloning of two genes for various transgenic experiments in plants without the difficulties associated with other methods. In order to test this system, the author made two-gene constructs with a combination of stomatal lineage-specific promoters and organelle-targeted fluorescent proteins, and observed consistent expression and localization patterns in transgenic *Arabidopsis thaliana*. This system provides a versatile cloning tool with multiple flexibility features, e.g., 17 types of C-terminal tags and 4 kinds of plant selection markers. The R4DS Gateway cloning system will be an invaluable experimental tool in plant research.

Materials and methods

DNA manipulation and plasmid construction

All plasmids described in this study were handled according to standard DNA manipulation methods [183]. In PCR, KOD DNA polymerase (TOYOBO, Osaka, Japan) was used to amplify products with blunt ends. The nucleotide sequences of cloned PCR fragments, synthetic oligo DNAs, and their ligated junctions in all intermediate and final

vectors were confirmed by sequencing. All oligonucleotides used in this study as a linker, adaptors and primers are listed in Table 4-1.

pGWB400, 500 [141], 600 [184], and 700 [185] binary vectors, which are based on the pPZP vector [186], were used as a backbone to create R4pGWB6xxx-MD8. In brief, *att*R4-*ccd*B-*att*R2 and *att*R5-*ccd*B-*att*R6 sequences were generated on binary vectors as the first and second acceptor sites for Gateway cloning, respectively. The R4pDD6xx-MD8 series was constructed on the pUC119 vector by generating the *att*R4-Cm^r-*ccd*B-*att*R2 sequence nested between *att*L5 and *att*L6. MD8, a MAR of *A. thaliana* [187], was placed upstream of each *att*R4 site (cloning site for the promoter) in order to provide more stability for transgene expression. Plasmid construction and cloning strategies in detail are described as follows.

Construction of R4pGWB6x01-MD8

The 35S promoter was removed from pUGW2 [188] by digestion with *Xba*I to make pUGW2-Δ35S. The chloramphenicol resistance (Cm^r) fragment between *att*R1 and *att*R2 was removed from pUGW2-Δ35S by digestion with *Bam*HI to make pUGW2-Δ(35S, Cm^r). The *Swa*I-*Not*I-*Asc*I-*Eco*RI adaptor was introduced into the *Eco*RI site of pUGW2-Δ(35S, Cm^r) to make pUGW2-Δ(35S, Cm^r)-SNAE. Destruction of the *Eco*RI site in Cm^r was performed as follows. The outermost upstream region of the Cm^r fragment was amplified using pDONR201 (Thermo Fisher Scientific) as a template with the primers 5'-Cm^r-F and 5'-Cm^r-d*Eco*RI-R. The outermost downstream region of the Cm^r fragment was amplified using pDONR201 as a template with 3'-Cm^r-d*Eco*RI-F and 3'-Cm^r-R. Products were diluted, mixed, and used in a second PCR with the primers 5'-Cm^r-F and 3'-Cm^r-R. The amplified modified Cm^r fragment was introduced into the *Swa*I site of pUGW2-Δ(35S, Cm^r)-SNAE to make pUGW2-Δ35S-Cm^r-NAE (*att*R1-*ccd*B-*att*R2-Tnos-Cm^r). The *Sal*I site of pDONR-L1R1R2L2 [45] was destroyed by *Sal*I digestion followed by a treatment with the Klenow enzyme. The *Not*I-*Nco*I region within Gateway reading cassette A of the resulting plasmid was replaced with a *Swa*I adaptor to make pDONR-L1R1-*Swa*I-R2L2. The *Not*I-*att*R4-*Swa*I-*att*R3-*Asc*I sequence was amplified using pDONR-L1R1-*Swa*I-R2L2 as a template with the primers *Not*I-*att*R4 and *Asc*I-*att*R3. The amplified product was digested with *Not*I and *Asc*I, then introduced into the *Not*I and *Asc*I sites of pUGW2-Δ35S-Cm^r-NAE to make pUGW3001 (*att*R1-*ccd*B-*att*R2-Tnos-Cm^r-*att*R4-*ccd*B-*att*R3). The *Not*I-*att*R5-*ccd*B-*att*R6-*Asc*I sequence was amplified using pUGW3001 as a template with the primers *Not*I-*att*R5 and *Asc*I-*att*R6.

The amplified product was digested with *Not*I and *Asc*I, then *att*R4-*ccd*B-*att*R3 of pUGW3001 was replaced with *att*R5-*ccd*B-*att*R6 to make pUGW6001 (*att*R1-*ccd*B-*att*R2-Tnos-Cm^r-*att*R5-*ccd*B-*att*R6). The *att*R1 sequence of pUGW6001 was replaced with *att*R4 prepared from R4pUGW1 [142] by *Hin*dIII and *Xho*I digestion to make R4pUGW6001 (*att*R4-*ccd*B-*att*R2-Tnos-Cm^r-*att*R5-*ccd*B-*att*R6).

The *Swa*I linker was introduced into the *Hin*dIII site of pGWB400, pGWB500 [141], pGWB600 [184], and pGWB700 [185] to make pGWB400-*Swa*I, pGWB500-*Swa*I, pGWB600-*Swa*I, and pGWB700-*Swa*I, respectively. A recombinant (Fusion) PCR technique was used to link the MD8 sequence [187] with the Cm^r sequence. The MD8 fragment was amplified by PCR using *Arabidopsis thaliana* genomic DNA as a template with the MD8-F and MD8-*Hin*dIII-Cm^r (ATG)-R primers. The Cm^r sequence was amplified by PCR using pGWB401 [141] as a template with the Cm^r-F and Cm^r-*Hin*dIII-R primers**.** These products were diluted, mixed, and subjected to a second PCR with the MD8-F and Cm^r-*Hin*dIII-R primers to make the MD8-*Hin*dIII-Cm^r-*Hin*dIII fragment, and then introduced into the *Swa*I site of pGWB400-*Swa*I, pGWB500-*Swa*I, pGWB600-*Swa*I, and pGWB700-*Swa*I to make pGWB400-MD8-*Hin*dIII-Cm^r-*Hin*dIII, pGWB500-MD8-*Hin*dIII-Cm^r-*Hin*dIII, pGWB600-MD8-*Hin*dIII-Cm^r-*Hin*dIII, and pGWB700-MD8-*Hin*dIII-Cm^r-*Hin*dIII, respectively. The *Hin*dIII-Cm^r-*Hin*dIII fragment was excised by *Hin*dIII digestion followed by self-ligation to make pGWB400-MD8, pGWB500-MD8, pGWB600-MD8, and pGWB700-MD8, respectively (MD8-*Hin*dIII-*Xba*I-*Sac*I-Tnos). The *att*R4-*ccd*B-*att*R2-Tnos-Cm^r-*att*R5-*ccd*B-*att*R6 sequence of R4pUGW6001 was introduced into the *Hin*dIII-*Asc*I sites of pGWB400-MD8, pGWB500-MD8, pGWB600-MD8, and pGWB700-MD8 to generate R4pGWB6401-MD8, R4pGWB6501-MD8, R4pGWB6601-MD8, and R4pGWB6701-MD8, respectively (MD8-*att*R4-*ccd*B-*att*R2-Tnos-Cm^r-*att*R5-*ccd*B-*att*R6).

Construction of R4pGWB6xxx-MD8 for fusion with a tag

The 35S promoter was prepared from pGWB401 [141] and introduced into the *Hin*dIII-*Xba*I site of pUGW3001 to make pUGW3002. The Cm^r of pUGWxx [188], pGWnY, and pGWcY [143] was removed by digestion with *Bam*HI to make pUGWxx-ΔCm^r, pGWnY-ΔCm^r, and pGWcY-ΔCm^r, respectively. The *Xba*I-*Sac*I fragment containing the *att*R1-*ccd*B-*att*R2-tag was prepared from pUGWxx-ΔCm^r, pGWnY-ΔCm^r, and pGWcY-ΔCm^r, and introduced into pUGW3002 to make pUGW30xx, pUGW3000-nY, and pUGW3000-cY, respectively.

Construction of R4pGWB64xx-MD8 (kanamycin resistance) and R4pGWB66xx-MD8 (BASTA resistance)

The *Xho*I-*Bsp*EI adaptor was introduced into R4pGWB6401-MD8 and R4pGWB6601-MD8 to make R4pGWB6401-MD8/*Xho*I-*Bsp*EI and R4pGWB6601-MD8/*Xho*I-*Bsp*EI, respectively. The *Xho*I-*ccd*B-*att*R2-tag-Tnos-Cm^r-*Bsp*EI fragment was prepared from pUGW30xx, pUGW3000-nY, and pUGW3000-cY and inserted into R4pGWB6401-MD8/*Xho*I-*Bsp*EI to make R4pGWB6404-MD8 to R4pGWB6459-MD8, R4pGWB6400-MD8-NY2, and R4pGWB6400-MD8-CY2, respectively. Similarly, R4pGWB6604-MD8 to R4pGWB6659-MD8, R4pGWB6600-MD8-NY2, and R4pGWB6600-MD8-CY2 were generated by replacing R4pGWB6401-MD8/*Xho*I-*Bsp*EI with R4pGWB6601-MD8/*Xho*I-*Bsp*EI. In LUC containing the *Bsp*EI site in its sequence, *Xho*I-*ccd*B-*att*R2-mRFP-*Sac*I of R4pGWB6454-MD8 and R4pGWB6654-MD8 was replaced with *Xho*I-*ccd*B-*att*R2-LUC-*Sac*I obtained from pUGW3035. The resulting plasmids were designated R4pGWB6435-MD8 and R4pGWB6635-MD8, respectively.

Construction of R4pGWB65xx-MD8 (hygromycin resistance)

The *Hin*dIII-*att*R4-*ccd*B-*att*R2-tag-Tnos-Cm^r-*att*R5-*ccd*B-*att*R6-*Asc*I fragment was prepared from R4pGWB64xx-MD8 and R4pGWB6400-MD8-NY2 vectors and inserted into pGWB500-MD8 by *Hin*dIII and *Asc*I digestion. The resulting plasmids were designated R4pGWB65xx-MD8 and R4pGWB6500-MD8-NY2. Regarding LUC, G3GFP, mRFP, and cYFP having the *Hin*dIII site at their 3' terminals, *Xho*I-*ccd*B-*att*R2-EYFP-*Sac*I of R4pGWB6540-MD8 was replaced with *Xho*I-*ccd*B-*att*R2-LUC-*Sac*I (from R4pGWB6435-MD8), *Xho*I-*ccd*B-*att*R2-G3GFP-*Sac*I (from R4pGWB6450-MD8), *Xho*I-*ccd*B-*att*R2-mRFP-*Sac*I (from R4pGWB6453-MD8), and *Xho*I-*ccd*B-*att*R2-cYFP-*Sac*I (from R4pGWB6400-MD8-CY2) to make R4pGWB6535-MD8, R4pGWB6550-MD8, R4pGWB6553-MD8, and R4pGWB6500-MD8-CY2, respectively.

Construction of R4pGWB67xx-MD8 (tunicamycin resistance)

The *Hin*dIII-*att*R4-*ccd*B-*att*R2-tag-Tnos-Cm^r-*att*R5-*ccd*B-*att*R6-*Asc*I fragment was prepared from the R4pGWB64xx-MD8 and R4pGWB6400-MD8-NY2 vectors and inserted into pGWB700-MD8 by *Hin*dIII and *Asc*I digestion. The resulting plasmids were designated R4pGWB67xx-MD8 and R4pGWB6700-MD8-NY2. Regarding LUC, G3GFP, mRFP, and

cYFP containing the *Hin*dIII site at their 3' terminals, *Asc*I-(NPTII marker)-LB-*Age*I of R4pGWBB6435-MD8, R4pGWB6450-MD8, R4pGWB6453-MD8, and R4pGWB6400-MD8-CY2 was replaced with *Asc*I-(GPT marker)-LB-*Age*I from pGWB700-MD8 to make R4pGWB6735-MD8, R4pGWB6750-MD8, R4pGWB6753-MD8, and R4pGWB6700-MD8-CY2 respectively.

Construction of R4pDD6xx-MD8

The *Hin*dIII-*Xba*I-*Sac*I-*Eco*RI adaptor was introduced into the *Xba*I and *Hin*dIII sites between the *att*L1 and *att*L2 sites of the *A. thaliana BAGEL7* (AT2g43990) entry clone constructed on pDONR201 [45] to make pDONR-L1-(HXSE)-L2. The *Sac*I-*Eco*RI fragment containing the nopaline synthase terminator (Tnos) was prepared from pBI221 (Clontech) and introduced into pDONR-L1-(HXSE)-L2 to make pDONR-L1-(HX)-Tnos-L2. The *att*L4 sequence was prepared from the *att*L1 sequence as follows. The outermost upstream region of the *att*L4 sequence was amplified using pDONR-L1-(HX)-Tnos-L2 as a template with the primers proximal-to-*att*L1 and 5'-*att*L4-R. The outermost downstream region of the *att*L4 sequences was amplified using pDONR-L1-(HX)-Tnos-L2 as a template with the primers 3'-*att*L4-F and Tnos-R. The products were diluted, mixed, and used in a second PCR with the primers proximal-to-*att*L1 and Tnos-R. The amplified product was digested with *Hpa*I and *Hin*dIII, and the *att*L1 site of pDONR-L1-(HX)-Tnos-L2 was then replaced with *att*L4 to make pDONR-L4-(HX)-Tnos-L2. Similarly, the *att*L3 sequence was prepared from the *att*L2 sequence of pDONR-L1-(HX)-Tnos-L2 by using the Tnos-F, 5'-*att*L3-R, 3'-*att*L3-F, and proximal-to-*att*L2 primers in the first PCR and Tnos-F and the proximal-to-*att*L2 primers in the second PCR. The amplified product was digested with *Eco*RI and *Pvu*II, and the *att*L2 site of pDONR-L4-(HX)-Tnos-L2 was then replaced with *att*L3 to make L4L3pDD500 (*att*L4-*Hin*dIII-*Xba*I-*Sac*I-Tnos-*Eco*RI-*att*L3). Similarly, the *att*L5 sequence was prepared from the *att*L4 sequence of L4L3pDD500 by using the primers proximal-to-*att*L1, 5'-*att*L5-R, 3'-*att*L5-F, and Tnos-R in the first PCR and the primers proximal-to-*att*L1 and Tnos-R in the second PCR. The amplified product was digested with *Hpa*I and *Hin*dIII, and the *att*L4 site of L4L3pDD500 was then replaced with *att*L5 to make L5L3pDD500. The *att*L6 sequence was prepared from the *att*L3 sequence of L5L3pDD500 by using the primers Tnos-F, 5'-*att*L6-R, 3'-*att*L6-F, and proximal-to-*att*L2 in the first PCR and the primers Tnos-F and proximal-to-*att*L2 in the second PCR. The amplified product was digested with *Eco*RI and *Pvu*II, and the *att*L3 site of L5L3pDD500 was then replaced with *att*L6 to make

L5L6pDD500 (*att*L5-*Hin*dIII-*Xba*I-*Sac*I-Tnos-*Eco*RI-*att*L6). The *Pme*I adaptor was introduced into the *Hin*dIII site of L5L6pDD500 to make L5L6pDD500-*Pme*I. The MD8 sequence [187] was amplified using *A. thaliana* genomic DNA as a template with the primers MD8-F and MD8-*Hin*dIII-R, and then introduced into *Pme*I site of L5L6pDD500-*Pme*I to make L5L6pDD500-MD8 (*att*L5-MD8-*Hin*dIII-*Xba*I-*Sac*I-Tnos-*Eco*RI-*att*L6). The *Hpa*I and *Nru*I fragment of L5L6PDD500-MD8, containing *att*L5-MD8-Tnos-*att*L6, was introduced into the *Sma*I site of pUC119 (TAKARA BIO, Otsu, Japan) to make pDD600-MD8. The *att*R4-Cm^r-*ccd*B-*att*R2-tag sequences prepared from R4pGWB401 to R4pGWB459 [142] were introduced into the *Hin*dIII-*Sac*I sites of pDD600-MD8 to generate R4pDD601-MD8 to R4pDD659-MD8. Regarding LUC, G3GFP, and mRFP having the *Hin*dIII site in their sequences, the *Sal*I-*att*R2-tag-*Sac*I fragment was prepared from the pUGW35, pUGW51, and pUGW54 [141, 188] vectors and inserted into R4pDD601-MD8 to make R4pDD635-MD8, R4pDD650-MD8, and R4pDD653-MD8, respectively. Regarding nYFP and cYFP, the *Xho*I-*att*R2-tag-*Sac*I fragment was prepared from the pGWnY and pGWcY [143] vectors and inserted into R4pDD601-MD8 to make R4pDD600-MD8-NY2 and R4pDD600-MD8-CY2, respectively.

Construction of entry clones and final expression vectors

P_{MUTE} was amplified from *A. thaliana* (ecotype Col-0) wild-type genomic DNA using P_{MUTE}-*att*B4 and P_{MUTE}-*att*B1 primers (Table 4-1) to add the *att*B4 and *att*B1 sequences to its 5' and 3' ends, respectively. The resulting fragment was subjected to a BP reaction with pDONRP4-P1R (Thermo Fisher Scientific) to construct the *att*L4-P_{MUTE}-*att*R1 entry clone. PCR and BP reactions were performed according to the manufacturer's instructions (Thermo Fisher Scientific). The *att*L4-P_{SDD1}-*att*R1 entry clone was prepared as described previously [142]. In the construction of ORF entry clones, organelle-targeting sequences were PCR amplified from cDNA prepared from Col-0 wild-type seedlings that germinated for 5 days under dark conditions and 2 days under light conditions. The DNA fragment corresponding to the N-terminal amino acids (1-42) of the *A. thaliana* F_1-ATPase γ subunit (mitochondria-targeting signal) was amplified using F_1ATPg-*att*B1 and F_1ATPg-*att*B2 primers (Table 4-1). The amplified DNA fragment was further used in a second adaptor PCR with *att*B1 adaptor and *att*B2 adaptor primers (Table 4-1) to add the *att*B1 and *att*B2 sequences to its 5' and 3' ends, respectively. The resulting fragment was subjected to the BP reaction with pDONR221 (Thermo Fisher Scientific) in order to construct the pF1gLS221 entry clone. Similarly, the

DNA fragment corresponding to the N-terminal amino acids (1-55) of the *A. thaliana* RuBisCO small subunit (plastid-targeting signal) was amplified with the RBCS1A-*att*B1 and RBCS1A-*att*B2 primers and then with *att*B1 adaptor and *att*B2 adaptor primers (Table 4-1) and used for the construction of pRbcSTP221. F_1ATPg-*att*B2 and RBCS1A-*att*B2 primers were designed to insert one nucleotide between the last codon of ORF and the *att*B2 (*att*L2 in the entry clone) according to the manufacturer's instructions (Thermo Fisher Scientific) for in-frame fusion with fluorescent protein encoded in destination vector.

In the construction of two sets of the promoter:ORF-fluorescent protein genes on R4DSB vectors, the following two rounds of LR reactions were performed. *att*L4-P_{MUTE}-*att*R1 and *att*L4-P_{SDD1}-*att*R1 were used as the promoter entry clones. pF1gLS221, pRbcSTP221, and pPTS2-221 [189] were used as the ORF entry clones. In the first LR reaction, a promoter entry clone, ORF entry clone, and linearized R4pDD650-MD8 (or R4pDD659-MD8) by *Sal*I digestion were subjected to a tripartite LR reaction [142] in order to make the promoter:ORF-tag fusion gene on R4DD vectors (R4pDD6xx-MD8-Pro2:ORF2 in Fig. 4-1A). In the second LR reaction, a quadripartite LR reaction was performed using the following two-step procedure. R4pDD6xx-MD8-Pro2:ORF2 and linearized R4pGWB6450-MD8 (or R4pGWB6459-MD8) by *Sal*I digestion were subjected to the LR reaction. At the same time a promoter entry clone and ORF entry clone were subjected to the LR reaction. After an incubation for 5 hours, these two solutions were mixed and incubated further overnight with a boost of LR clonase to construct a binary clone carrying two sets of the promoter:ORF-tag fusion (R4pGWB6xxx-MD8-Pro1:ORF1-Pro2:ORF2 in Fig. 4-1B). Ten different combinations of Pro1:ORF1-tag1-Pro2:ORF2-tag2 were constructed as final binary clones (Fig. 4-3 and Table 4-3). The full procedure for constructing and confirming the two-gene constructs took less than one week (excluding the time required for preparing entry clones). For each of the first and second LR reaction, one day is required for vector construction and two days for vector confirmation.

Vector manipulation in *Escherichia coli* and *A. tumefaciens*

E. coli strains DH5α or One Shot® *ccd*B survival™ $2T1^R$ (Thermo Fisher Scientific) were used to construct plasmids. The transformation of *A. tumefaciens* strain C58C1 (pMP90) was performed by electroporation. *E. coli* with the recombinant plasmids was grown at 37˚C for approximately 12 to 16 h in Luria broth (LB) media supplemented with appropriate

antibiotics. *A. tumefaciens* was grown at 28˚ C for 48-72 h in LB media supplemented with the appropriate antibiotics.

Transformation and growth of *A. thaliana*

A. tumefaciens strains with the recombinant R4DSB vectors were used to transform *A. thaliana* ecotype Col-0 using the floral dip transformation method [10], and treated plants were allowed to set seeds at 22˚C under a long-day photoperiod (16/8-hr light/dark cycle). The seeds were vernalized at 4˚C for 3 days and selected on Murashige and Skoog (MS) agar medium containing kanamycin (30 mg /L) and cefotax (100 mg /L) under 24-hr continuous light conditions for two weeks. Fourteen-day-old seedlings of the selected lines (T1) were transplanted to soil pots and allowed to grow at 22˚C under a long-day photoperiod. T2 seeds were collected and the segregation of transgenes was analyzed by selection on MS medium containing kanamycin and cefotax.

Confocal microscopy

The abaxial surfaces of the fully expanded leaves of two-week-old T1 or T2 seedlings were viewed with a TCS SP5 confocal laser-scanning microscope (Leica Microsystems, Wetzlar, Germany) using an HCX PL APO CS 20.0 x 0.7 IMM UV water immersion objective lens. G3GFP was excited with the argon laser line (488 nm) and TagRFP was excited with the helium-neon laser line (543 nm). The fluorescence of G3GFP and TagRFP was detected using the emission filters, BP500-530 nm and BP555-615 nm, respectively. Images were acquired sequentially line-by-line with a resolution of 512×512 pixels and 400-Hz scanning speed. Image analyses were processed in Adobe Photoshop 8.0 (Adobe Systems Incorporated, CA, U.S.A.) and converted to the TIFF format.

Table 4-1. Oligonucleotides used in this study. Restriction sites are underlined.

Oligos	Sequence
Linker	
*Swa*I	5′-AGCTGGTGATTTAAATCACC-3′
Adaptors	
*Hin*dIII-*Xba*I-*Sac*I-*Eco*RI-F	5′-AGCTAGAATTCGGAGCTCGTCTAGAGAAGCTTAC-3′
*Hin*dIII-*Xba*I-*Sac*I-*Eco*RI-R	5′-CTAGTAAGCTTCTCTAGACGAGCTCCGAATTCT-3′
*Pme*I-F	5′-AGCTCACTCGTTTAAACACTGC-3′
*Pme*I-R	5′-AGCTGCAGTGTTTAAACGAGTG-3′
*Swa*I-*Not*I-*Asc*I-*Eco*RI-F	5′-AATTAATTTAAATGCGGCCGCGGCGCGCCG-3′
*Swa*I-*Not*I-*Asc*I-*Eco*RI-R	5′-AATTCGGCGCGCCGCGGCCGCATTTAAATT-3′
*Swa*I-F	5′-GGCCACATTTAAATG-3′
*Swa*I-R	5′-CATGCATTTAAATGT-3′
*Xho*I-*Bsp*EI-F	5'-TCGAGTCTCCCTCATT-3'
*Xho*I-*Bsp*EI-R	5'- CAGAGGGAGTAAGGCC-3'
Primers	
proximal-to-*att*L1	5′-TCGCGTTAACGCTAGCATGGATCTC-3′
3’-*att*L4-F	5′-TGCCAACTTTGTATAGAAAAGTAG-3′
5’-*att*L4-R	5′-AGCCTACTTTTCTATACAAAGTTG-3′
Tnos-F	5'-AATAAAGTTTCTTAAGATTGAATCC-3'
Tnos-R	5′-GATCTAGTAACATAGATGAC-3′
3’-*att*L3-F	5’-ACCCAACTTTATTATACAAAGTTG-3’
5’-*att*L3-R	5'-TGCCAACTTTGTATAATAAAGTTG-3'
proximal-to-*att*L2	5’-GTAACATCAGAGATTTTGAGACAC-3’
3’-*att*L5-F	5’-TGCCAACTTTGTATACAAAAGTAG-3’
5’-*att*L5-R	5’-AGCCTACTTTTGTATACAAAGTTG-3’
3’-*att*L6-F	5’-ACCCAACTTTTTAATACAAAGTTG-3’
5’-*att*L6-R	5’-TGCCAACTTTGTATTAAAAAGTTG-3’
*Not*I-*att*R4	5’-CTGCGGCCGCGTGGATCCCCCATCACAAC-3’
*Asc*I-*att*R3	5’-CTGGCGCGCCAGCTTGATATCACAACTTTGTAT-3’
*Not*I-*att*R5	5’-CTGCGGCCGCGTGGATCCCCCATCACAACTTTGTATACAAAAG-3’
*Asc*I-*att*R6	5’-CTGGCGCGCCAGCTTGATATCACAACTTTGTATTAAAAAG-3’
MD8-F	5′-TCATCACACGTAATATCATCC-3′

MD8-*Hin*dIII-R	5′-AAGCTTAGATTTTCAGCTTTCTTTTTTTTCC-3′
MD8-*Hin*dIII-Cm^r (ATG)-R	5′-GAAGCATAAAGTGTAAAGCCTAAGCTTAGATTTTCAGCTTTCTTTTTTTTCC-3′
5’-Cm^r-F	5’-TAAGAGGTTCCAACTTTCAC-3’
3’-Cm^r-R	5’-ACATATCAGTATATATTCTTATACC-3’
Cm^r-F	5′-AGGCTTTACACTTTATGCTTC-3′
Cm^r-*Hin*dIII-R	5′-AAGCTTCCTTACCAGACCGGAGATAT-3′
3’-Cm^r-d*Eco*RI-F	5’-CATCCGGAATTTCGTATGGCAA-3’
5’-Cm^r-d*Eco*RI-R	5’-TTGCCATACGAAATTCCGGATG-3’
P_{MUTE}-*att*B1	5'-GGGGACTGCTTTTTTGTACAAACTTGTGACACTGATACTTAATTGATCAAGATTC-3'
P_{MUTE}-*att*B4	5'-GGGGACAACTTTGTATAGAAAAGTTGGCTGAGACACTCCAGCAATTTGAAAAATCC-3'
F_1ATPg-*att*B1	5’-AAAAAGCAGGCTTTATGGCAATGGCTGTTTTCCG-3’
F_1ATPg-*att*B2	5’-AGAAAGCTGGGTTAGATCGAACTCCAAGAAGTCC-3’
RBCS1A-*att*B1	5’-AAAAAGCAGGCTTTATGGCTTCCTCTATGCTCTC-3’
RBCS1A-*att*B2	5’-AGAAAGCTGGGTTGCAGTTAACTCTTCCGCCG-3’
*att*B1 adaptor	5'-GGGGACAAGTTTGTACAAAAAAGCAGGCT -3'
*att*B2 adaptor	5'-GGGGACCACTTTGTACAAGAAAGCTGGGT-3'

Results and discussion

Preparation of two-gene constructs and characteristics of the R4DS Gateway cloning system

The author herein developed the R4DS Gateway cloning system, which permits the easy and fast cloning of two sets of promoters and ORFs in a binary vector for plant transformation using any combination of a promoter entry clone (*att*L4-promoter-*att*R1) and ORF entry clone (*att*L1-ORF-*att*L2). ORFs may be fused with various tags (visible reporters or epitope tags; see below), if necessary. Fig. 4-1 shows vector structures and the cloning procedure in this system. The system consists of two types of vectors, R4 destination donor (R4DD) vectors and R4 dual-site binary (R4DSB) vectors. MD8 [187], a matrix attachment region (MAR) of *A. thaliana*, was placed upstream of the expression cassettes of both vectors. MARs are expected to increase the overall levels of transgene expression and reduce variance in expression patterns in transgenic plants [190-195]. Two LR reactions are used to generate the two-gene constructs. The first LR reaction (tripartite LR reaction) connects promoter2 (Pro2) and ORF2 with tag2 in the R4DD vector and produces an intermediate clone (*att*L5-MD8-*att*B4-Pro2-*att*B1-ORF2-*att*B2-tag2-Tnos-*att*L6) [R4pDD6xx-MD8-Pro2:ORF2 in Fig. 4-1A]. Tnos represents the terminator region of the nopaline synthase gene. The second LR reaction (quadripartite LR reaction) connects the second set of the promoter [promoter1 (Pro1)] and ORF entry clones (*att*L4-Pro1-*att*R1 and *att*L1-ORF1-*att*L2) and incorporates the two genes into R4pGWB6xxx-MD8 (Fig. 4-1B). A final binary clone, MD8-*att*B4-Pro1-*att*B1-ORF1-*att*B2-tag1-Tnos-Cm^r-*att*B5-MD8-*att*B4-Pro2-*att*B1-ORF2-*att*B2-tag2-Tnos-*att*B6 can be transferred into the plant genome using Agrobacterium-mediated transformation. In fusion-type vectors, the *att*B2 linker sequence between ORF and tag encodes 12 amino acids. Whereas, 13 additional amino acids representing the *att*B2 linker sequence are added at the C-terminus of the protein of interest in the case of vectors without a tag. For a detailed description of linker sequences, see Fig. 2 and supplemental Fig. 1 of Nakagawa *et al* (2008) [142].

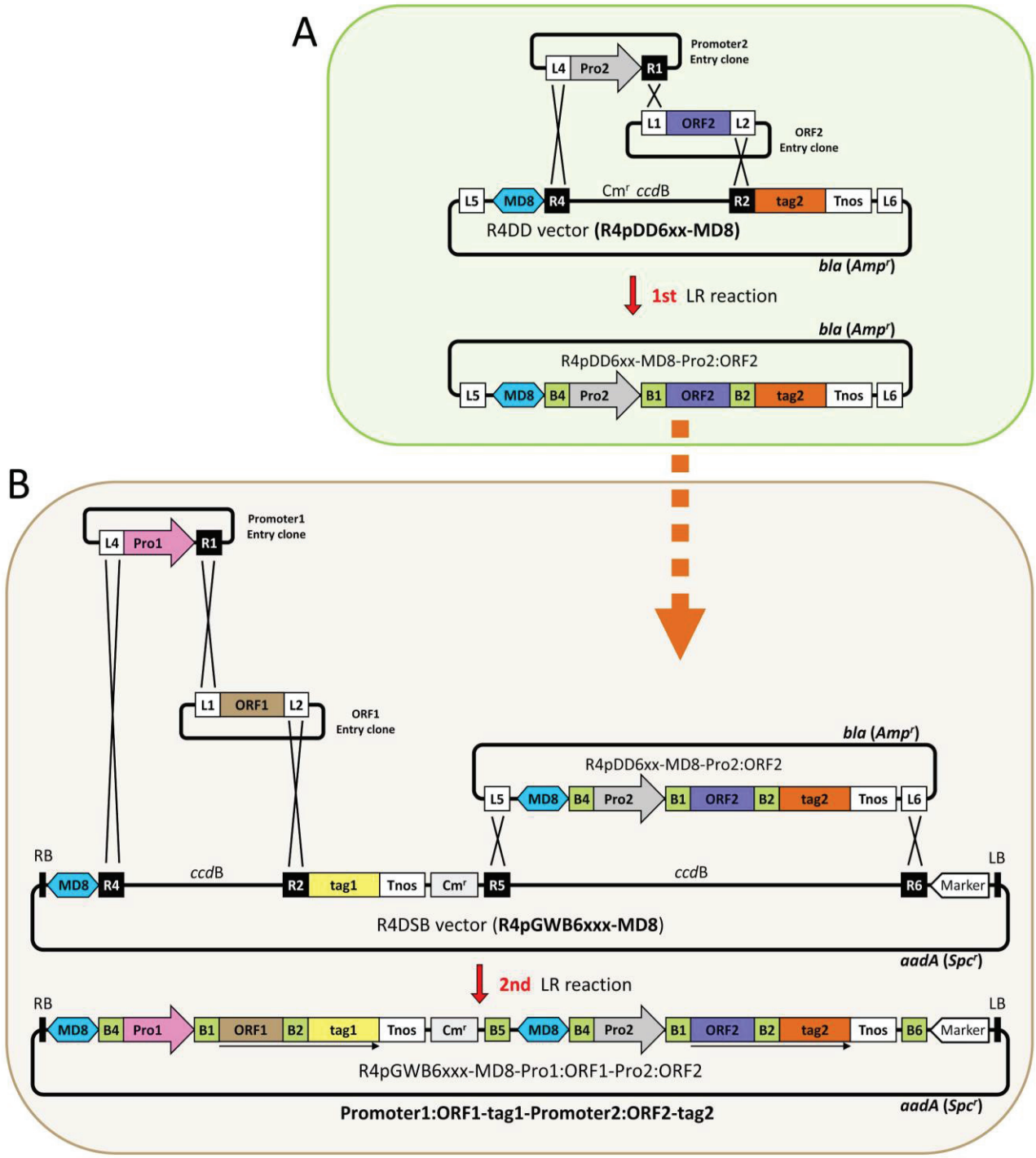

Fig. 4-1. Outline for cloning two sets of promoters and ORFs in the R4DS Gateway cloning system. (A) The 1st LR reaction. In the 1st LR reaction (tripartite LR reaction), Pro2 and ORF2 are linked and cloned into an R4DD vector to make R4pDD6xx-MD8-Pro2:ORF2. The dashed arrow indicates that established R4pDD6xx-MD8-Pro2:ORF2 is used further for the 2nd LR reaction. (B) The 2nd LR reaction. In the 2nd LR reaction (quadripartite LR reaction), Pro1 and ORF1 are linked and cloned into an R4DSB vector together with the Pro2:ORF2-tag2 constructed by the 1st LR reaction to make the binary clone R4pGWB6xxx-MD8-Pro1:ORF1-Pro2:ORF2 with two independent expression cassettes. MD8, the matrix attachment region; B1, *att*B1; B2, *att*B2; B4, *att*B4; B5, *att*B5; B6, *att*B6; L1, *att*L1; L2, *att*L2; L4, *att*L4; L5, *att*L5; L6, *att*L6; R1, *att*R1; R2, *att*R2; R4, *att*R4; R5, *att*R5; R6, *att*R6; *ccd*B, Control of Cell Death B as a negative selection marker for bacteria; Cm^r, chloramphenicol resistance; Marker, plant selection marker; Pro1, promoter1; Pro2, promoter2; LB, left border; RB, right border; Tnos, nopaline synthase terminator; *aadA*, the gene for spectinomycin resistance (Spc^r) in bacteria; *bla*, gene for ampicillin resistance (Amp^r) in bacteria. Arrows under ORF1-B2-tag1 and ORF2-B2-tag2 indicate expression. Figures are not drawn to scale.

The R4DS Gateway cloning system consists of four selection marker series (Fig. 4-2). R4DSB vectors with the MD8 sequence were named R4pGWB6xxx-MD8 (Fig. 4-2A and 2C). The first digit "6" of the four-digit number indicates the dual-site type (6xxx, vectors using *att*6 for cloning) and the next digit (4, 5, 6, or 7) refers to the types of plant selection markers. The R4pGWB64xx-MD8 series contains neomycin phosphotransferase II (NPTII) conferring kanamycin resistance (Km^r), the R4pGWB65xx-MD8 series contains hygromycin phosphotransferase (HPT) conferring hygromycin resistance (Hyg^r), the R4pGWB66xx-MD8 series contains phosphinothricin acetyl transferase (the bialophos resistance gene; bar) providing BASTA resistance ($BASTA^r$), and the R4pGWB67xx-MD8 series contains UDP *N*-acetylglucosamine: dolichol phosphate *N*-acetylglucosamine-1-P transferase (GPT) providing tunicamycin resistance ($Tunica^r$) (Fig. 4-2A). The availability of the four selection markers in this vector system is useful for transformation experiments and is of particular importance for repetitive transformation in order to introduce new transgenes into previously generated transgenic plants. All marker genes are driven by the nopaline synthase promoter (Pnos) and followed by Tnos. The last two digits represent the type of tag incorporated into these vectors. Seventeen different tags, visible reporters and epitope tags, were equipped in this system for fusion to both ORFs (Fig. 4-2E), namely; synthetic green fluorescent protein (sGFP) [196], the hexahistidine tag (6xHis) [197], FLAG tag (FLAG) [198], triple HA tag (3xHA), four or ten repeats of the Myc tag (4xMyc or 10xMyc) [197], glutathione S-transferase (GST) [199], the T7 epitope tag (T7) [200], β-glucuronidase (GUS) [201], luciferase (LUC) [202], enhanced yellow fluorescent protein (EYFP), enhanced cyan fluorescent protein (ECFP) [203], G3 green fluorescent protein (G3GFP) [204], monomeric red fluorescent protein (mRFP) [205], tag red fluorescent protein (TagRFP) [206], and the N- and C-terminal fragments of enhanced yellow fluorescent protein (nYFP and cYFP) [143]. With these tags, co-purification and co-immuno-precipitation analyses using different epitope tags, comparisons of the expression of two genes and the localization of gene products simultaneously using different visual reporter genes, and protein-protein interaction studies with bimolecular fluorescent complementation using nYFP and cYFP are possible. The two-digit number corresponding to each tag is consistent with that of R4 Gateway Binary Vectors (R4pGWBs) [142, 184, 185, 207].

The R4DD vectors with the MD8 sequence were named R4pDD6xx-MD8 (Fig. 4-2B and 2D). The first digit "6" of the three-digit number indicates the destination donor-type

vector compatible with R4pGWB6xxx-MD8. The last two digits indicate the types of tags that are consistent with R4DSB vectors.

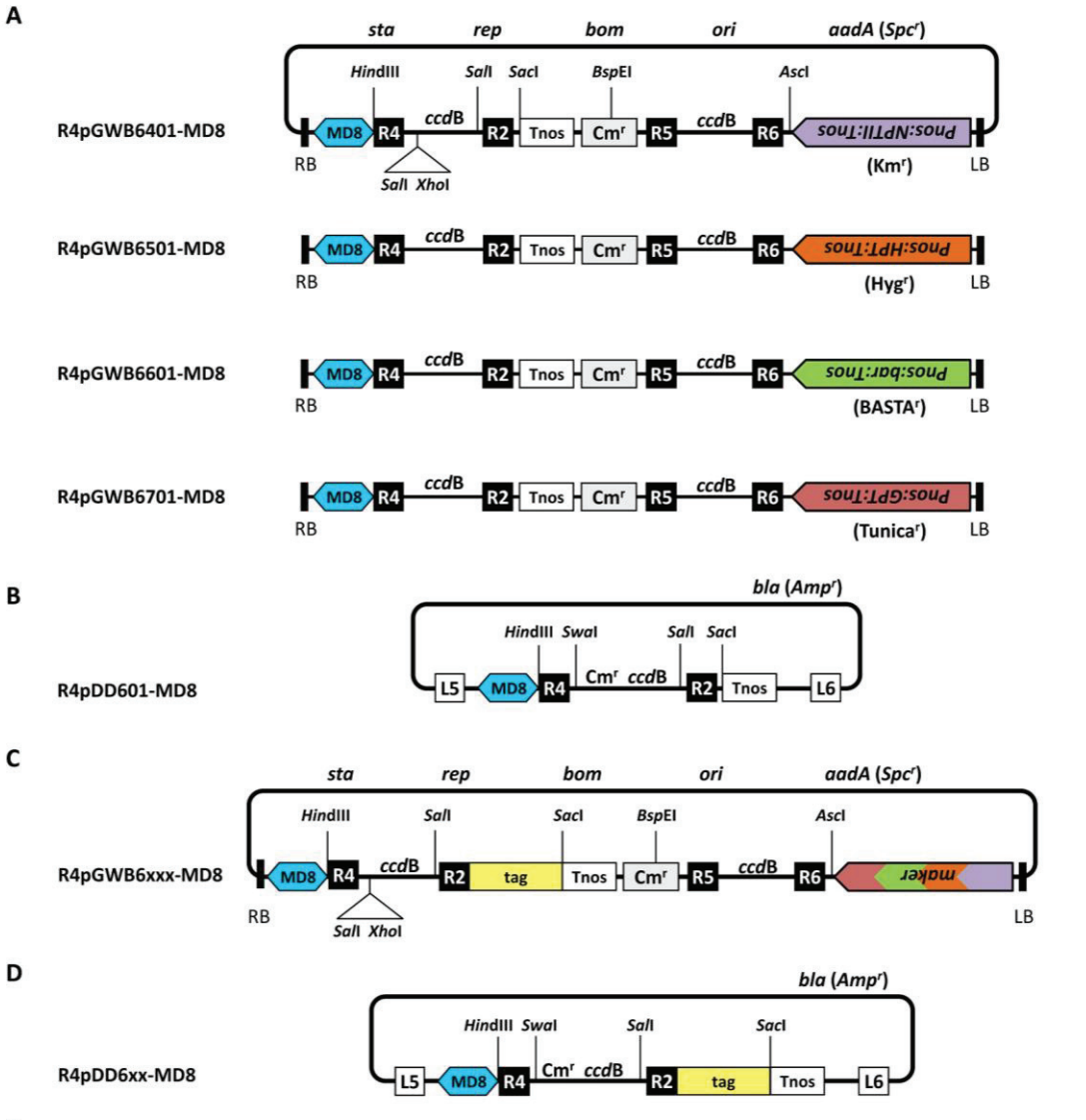

E

sGFP	6xHis	FLAG	3xHA	4xMyc	10xMyc
R4pGWB6404-MD8	R4pGWB6407-MD8	R4pGWB6410-MD8	R4pGWB6413-MD8	R4pGWB6416-MD8	R4pGWB6419-MD8
R4pGWB6504-MD8	R4pGWB6507-MD8	R4pGWB6510-MD8	R4pGWB6513-MD8	R4pGWB6516-MD8	R4pGWB6519-MD8
R4pGWB6604-MD8	R4pGWB6607-MD8	R4pGWB6610-MD8	R4pGWB6613-MD8	R4pGWB6616-MD8	R4pGWB6619-MD8
R4pGWB6704-MD8	R4pGWB6707-MD8	R4pGWB6710-MD8	R4pGWB6713-MD8	R4pGWB6716-MD8	R4pGWB6719-MD8
R4pDD604-MD8	R4pDD607-MD8	R4pDD610-MD8	R4pDD613-MD8	R4pDD616-MD8	R4pDD619-MD8

GST	T7	GUS	LUC	EYFP	ECFP
R4pGWB6422-MD8	R4pGWB6425-MD8	R4pGWB6433-MD8	R4pGWB6435-MD8	R4pGWB6440-MD8	R4pGWB6443-MD8
R4pGWB6522-MD8	R4pGWB6525-MD8	R4pGWB6533-MD8	R4pGWB6535-MD8	R4pGWB6540-MD8	R4pGWB6543-MD8
R4pGWB6622-MD8	R4pGWB6625-MD8	R4pGWB6633-MD8	R4pGWB6635-MD8	R4pGWB6640-MD8	R4pGWB6643-MD8
R4pGWB6722-MD8	R4pGWB6725-MD8	R4pGWB6733-MD8	R4pGWB6735-MD8	R4pGWB6740-MD8	R4pGWB6743-MD8
R4pDD622-MD8	R4pDD625-MD8	R4pDD633-MD8	R4pDD635-MD8	R4pDD640-MD8	R4pDD643-MD8

G3GFP	mRFP	TagRFP	nYFP	cYFP
R4pGWB6450-MD8	R4pGWB6453-MD8	R4pGWB6459-MD8	R4pGWB6400-MD8-NY2	R4pGWB6400-MD8-CY2
R4pGWB6550-MD8	R4pGWB6553-MD8	R4pGWB6559-MD8	R4pGWB6500-MD8-NY2	R4pGWB6500-MD8-CY2
R4pGWB6650-MD8	R4pGWB6653-MD8	R4pGWB6659-MD8	R4pGWB6600-MD8-NY2	R4pGWB6600-MD8-CY2
R4pGWB6750-MD8	R4pGWB6753-MD8	R4pGWB6759-MD8	R4pGWB6700-MD8-NY2	R4pGWB6700-MD8-CY2
R4pDD650-MD8	R4pDD653-MD8	R4pDD659-MD8	R4pDD600-MD8-NY2	R4pDD600-MD8-CY2

Fig. 4-2. Line-up of R4DSB vectors (R4pGWB6xxx-MD8) and R4DD vectors (R4pDD6xx-MD8). (A) Structural diagrams of the four no tag-type R4DSB vectors: R4pGWB6401-MD8, R4pGWB6501-MD8, R4pGWB6601-MD8, and R4pGWB6701-MD8. Backbone and restriction sites were shown in R4pGWB6401-MD8. The only difference between these four vectors is the selection marker for plants. LB, left border; RB, right border; *sta*, the region conferring stability in *Agrobacterium tumefaciens*; *rep*, broad host range replication origin; *bom*, cis-acting element for conjugational transfer; *ori*, ColE1 replication origin; Pnos, nopaline synthase promoter; Tnos, nopaline synthase terminator. (B) Structural diagram of the no tag-type R4DD vector, R4pDD601-MD8. (C) Structural diagram of tag fusion-type R4DSB vectors (R4pGWB6xxx-MD8). These vectors have the same structure as the no tag-type vector R4pGWB6x01 represented in A, except for a tag downstream of *att*R2. (D) Structural diagram of tag fusion-type R4DD vectors (R4pDD6xx-MD8). These vectors have the same structure as no tag-type R4pDD601-MD8 represented in B, except for a tag downstream of *att*R2. (E) Tags carried in R4pGWB6xxx-MD8 and R4pDD6xx-MD8. Figures in A-D are not drawn to scale.

Most previous vector systems, particularly those for multi-gene expression, were equipped with a limited number of commonly used constitutive promoters such as the cauliflower mosaic virus 35S promoter, *A. thaliana UBIQUITIN10* promoter, and *A. thaliana ACTIN2* promoter [208-210]. These promoters are often pre-cloned in vectors, and replacing them with other promoters is difficult and requires extra cloning steps. However, the expression of transgenes by various promoters, such as their own promoters, inducible promoters, tissue- or cell-specific promoters, and developmental stage-specific promoters, is required in many plant transgenic experiments. In the R4DS Gateway cloning system, many types of promoter entry clones (*att*L4-promoter-*att*R1) that have accumulated in the plant research community [142, 211-214] can be used for the desired expression of two transgenes. Also, these promoter entry clones are compatible with the large number of ORF entry clones (*att*Ll-ORF-*att*L2) currently available [212, 213, 215, 216]. Various two-gene constructs can be easily generated by LR reactions with the combination of two promoters, two ORFs, and seventeen tags in this system.

The complete nucleotide sequences of R4pGWB6xxx-MD8 and R4pDD6xx-MD8 are available in the GenBank/EML/DDBJ databases under the accession numbers indicated in Table 4-2. R4DD and R4DSB vectors developed in this work will be available through RIKEN BioResource Center (http://epd.brc.riken.jp/en/).

Table 4-2. Backbone, bacterial selection, plant selection, tag, restriction enzyme for linearization, and accession numbers of R4pDD6xx-MD8 and R4pGWB6xxx-MD8. Amp^r, ampicillin resistance; Cm^r, chloramphenicol resistance; Spc^r, spectinomycin resistance; the NPTII gene for kanamycin resistance (Km^r), the HPT gene for hygromycin B resistance (Hyg^r), the bar gene for BASTA resistance (BASTA^r), and the GPT gene for tunicamycin resistance (Tunica^r).

Plasmid name	Backbone	Bacterial selection	Plant selection	Tag	Restriction enzyme for linearization	Accession number
R4pDD601-MD8	pUC119	Amp^r, Cm^r	None	None	*Sal*I	LC171733
R4pDD604-MD8	pUC119	Amp^r, Cm^r	None	sGFP	*Sal*I	LC171734
R4pDD607-MD8	pUC119	Amp^r, Cm^r	None	6xHis	*Sal*I	LC171735
R4pDD610-MD8	pUC119	Amp^r, Cm^r	None	FLAG	*Sal*I	LC171736
R4pDD613-MD8	pUC119	Amp^r, Cm^r	None	3xHA	*Sal*I	LC171737
R4pDD616-MD8	pUC119	Amp^r, Cm^r	None	4xMyc	*Sal*I	LC171738
R4pDD619-MD8	pUC119	Amp^r, Cm^r	None	10xMyc	*Sal*I	LC171739
R4pDD622-MD8	pUC119	Amp^r, Cm^r	None	GST	*Sal*I	LC171740
R4pDD625-MD8	pUC119	Amp^r, Cm^r	None	T7	*Sal*I	LC171741
R4pDD633-MD8	pUC119	Amp^r, Cm^r	None	GUS	*Sal*I	LC171742
R4pDD635-MD8	pUC119	Amp^r, Cm^r	None	LUC	*Sal*I	LC171743
R4pDD640-MD8	pUC119	Amp^r, Cm^r	None	EYFP	*Sal*I	LC171744
R4pDD643-MD8	pUC119	Amp^r, Cm^r	None	ECFP	*Sal*I	LC171745
R4pDD650-MD8	pUC119	Amp^r, Cm^r	None	G3GFP	*Sal*I	LC171746
R4pDD653-MD8	pUC119	Amp^r, Cm^r	None	mRFP	*Sal*I	LC171747
R4pDD659-MD8	pUC119	Amp^r, Cm^r	None	TagRFP	*Sal*I	LC171748
R4pDD600-MD8-NY2	pUC119	Amp^r, Cm^r	None	nYFP	*Sal*I	LC171749
R4pDD600-MD8-CY2	pUC119	Amp^r, Cm^r	None	cYFP	*Sal*I	LC171750
R4pGWB6401-MD8	pPZP	Spc^r, Cm^r	Pnos:NPTII (Km^r)	None	*Sal*I or *Xho*I	LC171751
R4pGWB6404-MD8	pPZP	Spc^r, Cm^r	Pnos:NPTII (Km^r)	sGFP	*Sal*I or *Xho*I	LC171752
R4pGWB6407-MD8	pPZP	Spc^r, Cm^r	Pnos:NPTII (Km^r)	6xHis	*Sal*I or *Xho*I	LC171753
R4pGWB6410-MD8	pPZP	Spc^r, Cm^r	Pnos:NPTII (Km^r)	FLAG	*Sal*I or *Xho*I	LC171754
R4pGWB6413-MD8	pPZP	Spc^r, Cm^r	Pnos:NPTII (Km^r)	3xHA	*Sal*I or *Xho*I	LC171755
R4pGWB6416-MD8	pPZP	Spc^r, Cm^r	Pnos:NPTII (Km^r)	4xMyc	*Sal*I or *Xho*I	LC171756
R4pGWB6419-MD8	pPZP	Spc^r, Cm^r	Pnos:NPTII (Km^r)	10xMyc	*Sal*I or *Xho*I	LC171757
R4pGWB6422-MD8	pPZP	Spc^r, Cm^r	Pnos:NPTII (Km^r)	GST	*Sal*I or *Xho*I	LC171758
R4pGWB6425-MD8	pPZP	Spc^r, Cm^r	Pnos:NPTII (Km^r)	T7	*Sal*I or *Xho*I	LC171759
R4pGWB6433-MD8	pPZP	Spc^r, Cm^r	Pnos:NPTII (Km^r)	GUS	*Sal*I or *Xho*I	LC171760
R4pGWB6435-MD8	pPZP	Spc^r, Cm^r	Pnos:NPTII (Km^r)	LUC	*Sal*I or *Xho*I	LC171761
R4pGWB6440-MD8	pPZP	Spc^r, Cm^r	Pnos:NPTII (Km^r)	EYFP	*Sal*I or *Xho*I	LC171762
R4pGWB6443-MD8	pPZP	Spc^r, Cm^r	Pnos:NPTII (Km^r)	ECFP	*Sal*I or *Xho*I	LC171763
R4pGWB6450-MD8	pPZP	Spc^r, Cm^r	Pnos:NPTII (Km^r)	G3GFP	*Sal*I or *Xho*I	LC171764
R4pGWB6453-MD8	pPZP	Spc^r, Cm^r	Pnos:NPTII (Km^r)	mRFP	*Sal*I or *Xho*I	LC171765
R4pGWB6459-MD8	pPZP	Spc^r, Cm^r	Pnos:NPTII (Km^r)	TagRFP	*Sal*I or *Xho*I	LC171766
R4pGWB6400-MD8-NY2	pPZP	Spc^r, Cm^r	Pnos:NPTII (Km^r)	nYFP	*Sal*I or *Xho*I	LC171767
R4pGWB6400-MD8-CY2	pPZP	Spc^r, Cm^r	Pnos:NPTII (Km^r)	cYFP	*Sal*I or *Xho*I	LC171768
R4pGWB6501-MD8	pPZP	Spc^r, Cm^r	Pnos:HPT (Hyg^r)	None	*Sal*I or *Xho*I	LC171769
R4pGWB6504-MD8	pPZP	Spc^r, Cm^r	Pnos:HPT (Hyg^r)	sGFP	*Sal*I or *Xho*I	LC171770
R4pGWB6507-MD8	pPZP	Spc^r, Cm^r	Pnos:HPT (Hyg^r)	6xHis	*Sal*I or *Xho*I	LC171771
R4pGWB6510-MD8	pPZP	Spc^r, Cm^r	Pnos:HPT (Hyg^r)	FLAG	*Sal*I or *Xho*I	LC171772
R4pGWB6513-MD8	pPZP	Spc^r, Cm^r	Pnos:HPT (Hyg^r)	3xHA	*Sal*I or *Xho*I	LC171773
R4pGWB6516-MD8	pPZP	Spc^r, Cm^r	Pnos:HPT (Hyg^r)	4xMyc	*Sal*I or *Xho*I	LC171774

R4pGWB6519-MD8	pPZP	Spc^r, Cm^r	Pnos:HPT (Hyg^r)	10xMyc	*Sal*I or *Xho*I	LC171775
R4pGWB6522-MD8	pPZP	Spc^r, Cm^r	Pnos:HPT (Hyg^r)	GST	*Sal*I or *Xho*I	LC171776
R4pGWB6525-MD8	pPZP	Spc^r, Cm^r	Pnos:HPT (Hyg^r)	T7	*Sal*I or *Xho*I	LC171777
R4pGWB6533-MD8	pPZP	Spc^r, Cm^r	Pnos:HPT (Hyg^r)	GUS	*Sal*I or *Xho*I	LC171778
R4pGWB6535-MD8	pPZP	Spc^r, Cm^r	Pnos:HPT (Hyg^r)	LUC	*Sal*I or *Xho*I	LC171779
R4pGWB6540-MD8	pPZP	Spc^r, Cm^r	Pnos:HPT (Hyg^r)	EYFP	*Sal*I or *Xho*I	LC171780
R4pGWB6543-MD8	pPZP	Spc^r, Cm^r	Pnos:HPT (Hyg^r)	ECFP	*Sal*I or *Xho*I	LC171781
R4pGWB6550-MD8	pPZP	Spc^r, Cm^r	Pnos:HPT (Hyg^r)	G3GFP	*Sal*I or *Xho*I	LC171782
R4pGWB6553-MD8	pPZP	Spc^r, Cm^r	Pnos:HPT (Hyg^r)	mRFP	*Sal*I or *Xho*I	LC171783
R4pGWB6559-MD8	pPZP	Spc^r, Cm^r	Pnos:HPT (Hyg^r)	TagRFP	*Sal*I or *Xho*I	LC171784
R4pGWB6500-MD8-NY2	pPZP	Spc^r, Cm^r	Pnos:HPT (Hyg^r)	nYFP	*Sal*I or *Xho*I	LC171785
R4pGWB6500-MD8-CY2	pPZP	Spc^r, Cm^r	Pnos:HPT (Hyg^r)	cYFP	*Sal*I or *Xho*I	LC171786
R4pGWB6601-MD8	pPZP	Spc^r, Cm^r	Pnos:bar (BASTA^r)	None	*Xho*I	LC171787
R4pGWB6604-MD8	pPZP	Spc^r, Cm^r	Pnos:bar (BASTA^r)	sGFP	*Xho*I	LC171788
R4pGWB6607-MD8	pPZP	Spc^r, Cm^r	Pnos:bar (BASTA^r)	6xHis	*Xho*I	LC171789
R4pGWB6610-MD8	pPZP	Spc^r, Cm^r	Pnos:bar (BASTA^r)	FLAG	*Xho*I	LC171790
R4pGWB6613-MD8	pPZP	Spc^r, Cm^r	Pnos:bar (BASTA^r)	3xHA	*Xho*I	LC171791
R4pGWB6616-MD8	pPZP	Spc^r, Cm^r	Pnos:bar (BASTA^r)	4xMyc	*Xho*I	LC171792
R4pGWB6619-MD8	pPZP	Spc^r, Cm^r	Pnos:bar (BASTA^r)	10xMyc	*Xho*I	LC171793
R4pGWB6622-MD8	pPZP	Spc^r, Cm^r	Pnos:bar (BASTA^r)	GST	*Xho*I	LC171794
R4pGWB6625-MD8	pPZP	Spc^r, Cm^r	Pnos:bar (BASTA^r)	T7	*Xho*I	LC171795
R4pGWB6633-MD8	pPZP	Spc^r, Cm^r	Pnos:bar (BASTA^r)	GUS	*Xho*I	LC171796
R4pGWB6635-MD8	pPZP	Spc^r, Cm^r	Pnos:bar (BASTA^r)	LUC	*Xho*I	LC171797
R4pGWB6640-MD8	pPZP	Spc^r, Cm^r	Pnos:bar (BASTA^r)	EYFP	*Xho*I	LC171798
R4pGWB6643-MD8	pPZP	Spc^r, Cm^r	Pnos:bar (BASTA^r)	ECFP	*Xho*I	LC171799
R4pGWB6650-MD8	pPZP	Spc^r, Cm^r	Pnos:bar (BASTA^r)	G3GFP	*Xho*I	LC171800
R4pGWB6653-MD8	pPZP	Spc^r, Cm^r	Pnos:bar (BASTA^r)	mRFP	*Xho*I	LC171801
R4pGWB6659-MD8	pPZP	Spc^r, Cm^r	Pnos:bar (BASTA^r)	TagRFP	*Xho*I	LC171802
R4pGWB6600-MD8-NY2	pPZP	Spc^r, Cm^r	Pnos:bar (BASTA^r)	nYFP	*Xho*I	LC171803
R4pGWB6600-MD8-CY2	pPZP	Spc^r, Cm^r	Pnos:bar (BASTA^r)	cYFP	*Xho*I	LC171804
R4pGWB6701-MD8	pPZP	Spc^r, Cm^r	Pnos:GPT (Tunica^r)	None	*Sal*I	LC171805
R4pGWB6704-MD8	pPZP	Spc^r, Cm^r	Pnos:GPT (Tunica^r)	sGFP	*Sal*I	LC171806
R4pGWB6707-MD8	pPZP	Spc^r, Cm^r	Pnos:GPT (Tunica^r)	6xHis	*Sal*I	LC171807
R4pGWB6710-MD8	pPZP	Spc^r, Cm^r	Pnos:GPT (Tunica^r)	FLAG	*Sal*I	LC171808
R4pGWB6713-MD8	pPZP	Spc^r, Cm^r	Pnos:GPT (Tunica^r)	3xHA	*Sal*I	LC171809
R4pGWB6716-MD8	pPZP	Spc^r, Cm^r	Pnos:GPT (Tunica^r)	4xMyc	*Sal*I	LC171810
R4pGWB6719-MD8	pPZP	Spc^r, Cm^r	Pnos:GPT (Tunica^r)	10xMyc	*Sal*I	LC171811
R4pGWB6722-MD8	pPZP	Spc^r, Cm^r	Pnos:GPT (Tunica^r)	GST	*Sal*I	LC171812
R4pGWB6725-MD8	pPZP	Spc^r, Cm^r	Pnos:GPT (Tunica^r)	T7	*Sal*I	LC171813
R4pGWB6733-MD8	pPZP	Spc^r, Cm^r	Pnos:GPT (Tunica^r)	GUS	*Sal*I	LC171814
R4pGWB6735-MD8	pPZP	Spc^r, Cm^r	Pnos:GPT (Tunica^r)	LUC	*Sal*I	LC171815
R4pGWB6740-MD8	pPZP	Spc^r, Cm^r	Pnos:GPT (Tunica^r)	EYFP	*Sal*I	LC171816
R4pGWB6743-MD8	pPZP	Spc^r, Cm^r	Pnos:GPT (Tunica^r)	ECFP	*Sal*I	LC171817
R4pGWB6750-MD8	pPZP	Spc^r, Cm^r	Pnos:GPT (Tunica^r)	G3GFP	*Sal*I	LC171818
R4pGWB6753-MD8	pPZP	Spc^r, Cm^r	Pnos:GPT (Tunica^r)	mRFP	*Sal*I	LC171819
R4pGWB6759-MD8	pPZP	Spc^r, Cm^r	Pnos:GPT (Tunica^r)	TagRFP	*Sal*I	LC171820
R4pGWB6700-MD8-NY2	pPZP	Spc^r, Cm^r	Pnos:GPT (Tunica^r)	nYFP	*Sal*I	LC171821
R4pGWB6700-MD8-CY2	pPZP	Spc^r, Cm^r	Pnos:GPT (Tunica^r)	cYFP	*Sal*I	LC171822

Construction of two-gene fusion driven by stomatal lineage-specific promoters for the visualization of intracellular organelles

In order to test the performance of the R4DS Gateway cloning system, the author employed a combination of two stomatal lineage-specific promoters, *MUTE* promoter (P_{MUTE}) [46, 217] and *STOMATAL DENSITY AND DISTRIBUTION1* (*SDD1*) promoter (P_{SDD1}) [218, 219], and three organelle-targeting signals, a mitochondria-targeting signal of the *A. thaliana* F_1-ATPase γ subunit (Mt) [220], peroxisome-targeting signal type 2 of pumpkin citrate synthase (PTS2) [221], and a plastid-targeting signal of the *A. thaliana* RuBisCO small subunit [222]. The author selected R4pDD650-MD8 (G3GFP) and R4pDD659-MD8 (TagRFP) as R4DD vectors, and R4pGWB6450-MD8 (G3GFP) and R4pGWB6459-MD8 (TagRFP) as R4DSB vectors. By using successive first and second LR reactions, 10 constructs carrying two sets of organelle-targeting signal-fluorescent protein genes driven by stomatal lineage-specific promoters were constructed (Fig. 4-3, Table 4-3). In order to increase recombination efficiency, the R4DD and R4DSB vectors were linearized prior to the LR reaction. Table 4-2 summarized the recommended restriction enzymes for the linearization of R4pDD6xx-MD8 and R4pGWB6xxx-MD8. In order to confirm the structure of the ten binary constructs, the author analyzed them by restriction digestion. As shown in gel electrophoresis (Fig. 4-3D), DNA fragments generated by *Hin*dIII digestion from all tested clones migrated to the positions of the expected sizes, as shown in Fig. 4-3A, 3B, and 3C and Table 4-3, indicating the successful preparation of two-gene constructs. All these ten two-gene binary clones were constructed with 80-100% success rate. Out of five randomly chosen colonies, four to five were constructed successfully with the two-gene expression cassettes assembled in the desired combination. These clones were introduced into *A. tumefaciens*, and then used for the transformation of *A. thaliana*. The author obtained transgenic lines for all constructs showing segregation of 3:1 on kanamycin selection plates in the T2 generation. These lines indicating the integration of transgenes at a single locus were used in subsequent experiments.

Table 4-3. Binary clones constructed in this study. Ten binary clones containing different combinations of Pro1:ORF1-tag1-Pro2:ORF2-tag2 were constructed. The total vector size and size of *Hin*dIII fragments are indicated in base pairs (bp). P_{MUTE}, *MUTE* promoter; P_{SDD1}, *SDD1* promoter; Mt, mitochondria-targeting signal; PTS2, peroxisome-targeting signal type 2; Pt, plastid-targeting signal.

Binary clone	Total size (bp)	*Hin*dIII				
		Fragment 1	Fragment 2	Fragment 3	Fragment 4	Fragment 5
P_{MUTE}:Mt-G3GFP-P_{SDD1}:Mt-TagRFP	17,972	2,965	2,123	135	965	11,784
P_{MUTE}:PTS2-G3GFP-P_{SDD1}:PTS2-TagRFP	18,008	2,983	2,123	135	965	11,802
P_{MUTE}:Pt-G3GFP-P_{SDD1}:Pt-TagRFP	18,050	3,004	2,123	135	965	11,823
P_{MUTE}:Mt-G3GFP-P_{SDD1}:PTS2-TagRFP	17,990	2,965	2,123	135	965	11,802
P_{MUTE}:Mt-G3GFP-P_{SDD1}:Pt-TagRFP	18,011	2,965	2,123	135	965	11,823
P_{MUTE}:Mt-TagRFP-P_{SDD1}:Mt-G3GFP	17,972	5,085	135	965	1,913	9,874
P_{MUTE}:PTS2-TagRFP-P_{SDD1}:PTS2-G3GFP	18,008	5,103	135	965	1,931	9,874
P_{MUTE}:Pt-TagRFP-P_{SDD1}:Pt-G3GFP	18,050	5,124	135	965	1,952	9,874
P_{MUTE}:Pt-TagRFP-P_{SDD1}:PTS2-G3GFP	18,029	5,124	135	965	1,931	9,874
P_{SDD1}:Mt- TagRFP-P_{MUTE}:Mt-G3GFP	17,972	135	965	4,033	2,965	9,874

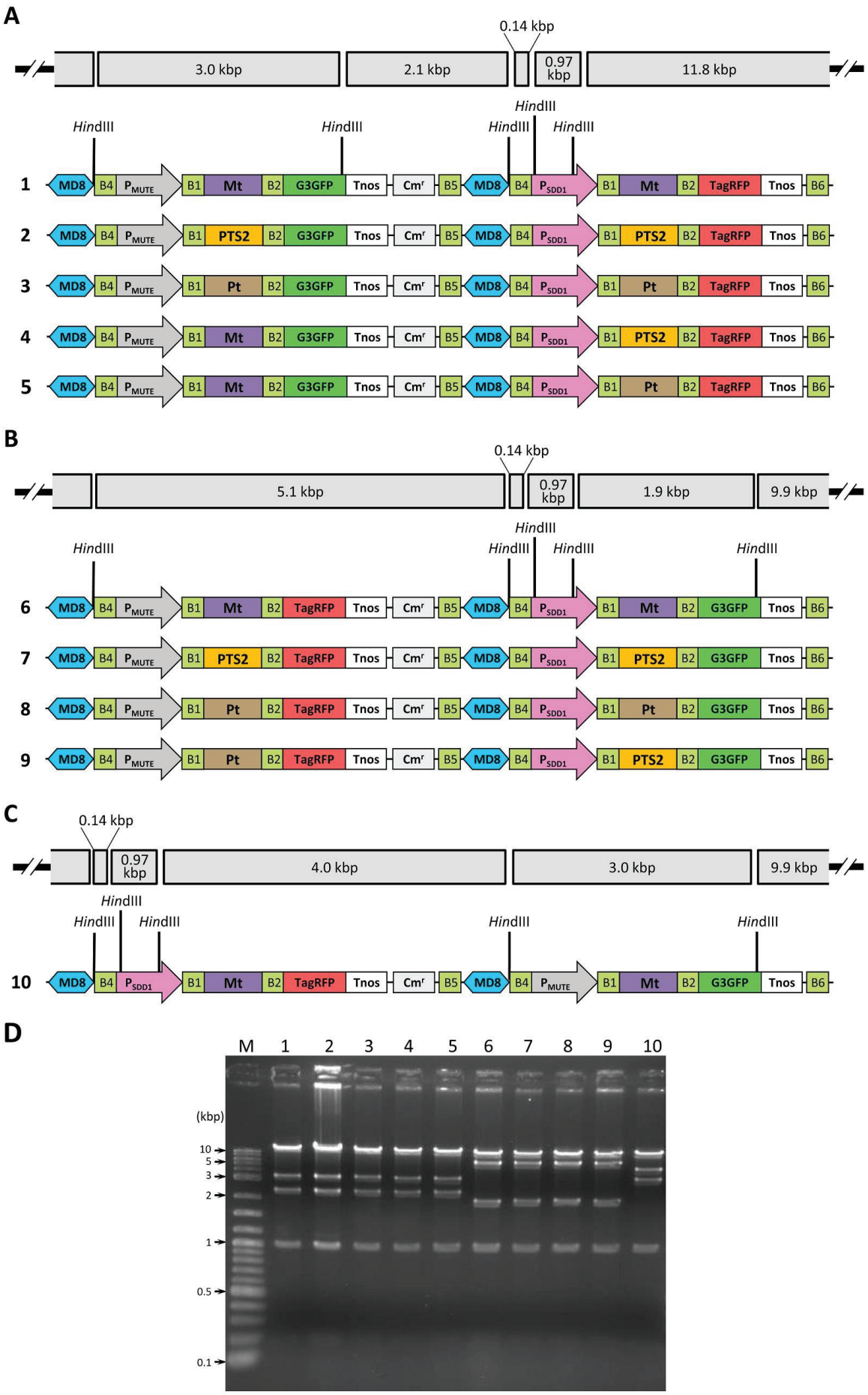
A
0.14 kbp
3.0 kbp
2.1 kbp
0.97 kbp
11.8 kbp
HindIII
1
2
3
4
5
MD8
B4
P MUTE
B1
Mt
PTS2
Pt
B2
G3GFP
TagRFP
Tnos
Cm r
B5
P SDD1
B6
B
5.1 kbp
1.9 kbp
9.9 kbp
6
7
8
9
C
4.0 kbp
3.0 kbp
10
D
M
(kbp)
10
5
3
2
1
0.5
0.1

Fig. 4-3. Illustration of ten R4pGWB64xx-MD8 constructs carrying Pro1:ORF1-tag1-Pro2:ORF2-tag2 and confirmation of structures by restriction digestion. (A) Structure of P_{MUTE}:ORF1-G3GFP-P_{SDD1}:ORF2-TagRFP constructed with R4pGWB6450-MD8 and R4pDD659-MD8 (binary clones 1-5). (B) Structure of P_{MUTE}:ORF1-TagRFP-P_{SDD1}:ORF2-G3GFP constructed with R4pGWB6459-MD8 and R4pDD650-MD8 (binary clones 6-9). (C) Structure of P_{SDD1}:Mt-TagRFP-P_{MUTE}:Mt-G3GFP constructed with R4pGWB6459-MD8 and R4pDD650-MD8 (binary clone 10). The positions of *Hin*dIII sites are indicated and the sizes of restriction fragments are shown in kilobase pairs (kbp). (D) Binary clones 1-10 were digested by *Hin*dIII and electrophoresed on 1.5% agarose gel. Lanes 1-10 show binary clones 1-10. Lane M shows the DNA ladder marker. The positions of 10, 5, 3, 2, 1, 0.5, and 0.1 kbp are indicated. P_{MUTE}, *MUTE* promoter; P_{SDD1}, *SDD1* promoter; Mt, mitochondria-targeting signal; PTS2, peroxisome-targeting signal type 2; Pt, plastid-targeting signal.

Promoter-directed expression and organelle targeting of fluorescent proteins in transgenic *A. thaliana*

Confocal laser scanning microscopy was used to detect the fluorescent signals of G3GFP and TagRFP in transgenic *A. thaliana* plants. The author analyzed the co-expression rate of two fluorescent proteins in 10 lines for each construct (constructs 1 to 10 in Fig. 4-3) and detected the expression of G3GFP and TagRFP in all lines examined. Binary clones constructed using the R4DS Gateway cloning system showed markedly higher co-expression efficiencies under the experimental conditions described herein than previously reported two-gene expression vectors that showed 10 to 88% of the co-expression efficiency of the two transgenes in transformed *A. thaliana* [208-210]. All the observed lines showed the expression of both fluorescent proteins, indicating 100% co-expression efficiency. The author then analyzed the precise expression timing and subcellular localization of G3GFP and TagRFP for each construct carrying a combination of two stomatal lineage-specific promoters (*MUTE* and *SDD1* promoters) and three organelle-targeting signals (mitochondria-, peroxisome-, and plastid-targeting signals). In *A. thaliana*, the development of stomata goes through a specialized cell lineage, stomatal lineage, which consists of the following five stages; meristemoid mother cells, meristemoids, guard mother cells (GMCs), immature guard cells (immature GCs), and mature GCs [223, 224]. MUTE is a basic helix–loop–helix protein that plays a role in the termination of stem cell behavior by triggering differentiation from meristemoids to GMCs. P_{MUTE} initiates the expression of downstream genes at the meristemoid stage [217]. SDD1 is a subtilisin-like serine protease that negatively regulates stomatal density [218]. P_{SDD1} is activated slightly later than P_{MUTE} around the GMC stage

[219]. The author demonstrated the difference of P_{MUTE} and P_{SDD1} activities by showing the fluorescence of mitochondria-targeted G3GFP and TagRFP in stomatal lineage cells in the leaf epidermis. Fig. 4-4A shows the construct, P_{MUTE}:Mt-G3GFP-P_{SDD1}:Mt-TagRFP (construct 1 in Fig. 4-3), carrying a mitochondria-targeting signal fused with G3GFP (Mt-G3GFP) under the control of P_{MUTE} at the first cloning site (the cloning site upstream of Cm^r) and mitochondria-targeting signal fused with TagRFP (Mt-TagRFP) under the control of P_{SDD1} at the second cloning site (the cloning site downstream of Cm^r). The second construct used for comparison was P_{MUTE}:Mt-TagRFP-P_{SDD1}:Mt-G3GFP (construct 6), in which Mt-G3GFP and Mt-TagRFP of construct 1 were replaced with each other (Fig. 4-4B). At the meristemoid stage, only G3GFP was detected in the mitochondria of plants transformed with construct 1, while only TagRFP was detected in the mitochondria of plants transformed with construct 6. At the GMC and immature GC stages and weakly at the mature GC stage, G3GFP and TagRFP were both observed in the mitochondria of plants transformed with both constructs (Fig. 4-4D and 4E). These results coincide with the expression patterns of the *MUTE* and *SDD1* genes. Similar results were obtained in experiments in which the mitochondria-targeting signal was replaced with the peroxisome-targeting signal [P_{MUTE}:PTS2-G3GFP-P_{SDD1}:PTS2-TagRFP (construct 2, Fig. 4-5A and 5C) and P_{MUTE}:PTS2-TagRFP-P_{SDD1}:PTS2-G3GFP (construct 7, Fig. 4-5B and 5D)] or with the plastid-targeting signal [P_{MUTE}:Pt-G3GFP-P_{SDD1}:Pt-TagRFP (construct 3, Fig. 4-5E and 5G) and P_{MUTE}:Pt-TagRFP-P_{SDD1}:Pt-G3GFP (construct 8, Fig. 4-5F and 5H)]. In order to confirm that differences in expression timing are not dependent on the position of the two cloning sites in the vectors, the location of expression units were exchanged in the constructs [P_{MUTE}:Mt-G3GFP-P_{SDD1}:Mt-TagRFP (construct 1, Fig. 4-4A) to P_{SDD1}:Mt-TagRFP-P_{MUTE}:Mt-G3GFP (construct 10, Fig. 4-4C)]. The same expression patterns were observed in both constructs (Fig. 4-4D and 4F), indicating that the cloning sites of R4DSB vectors are equivalent.

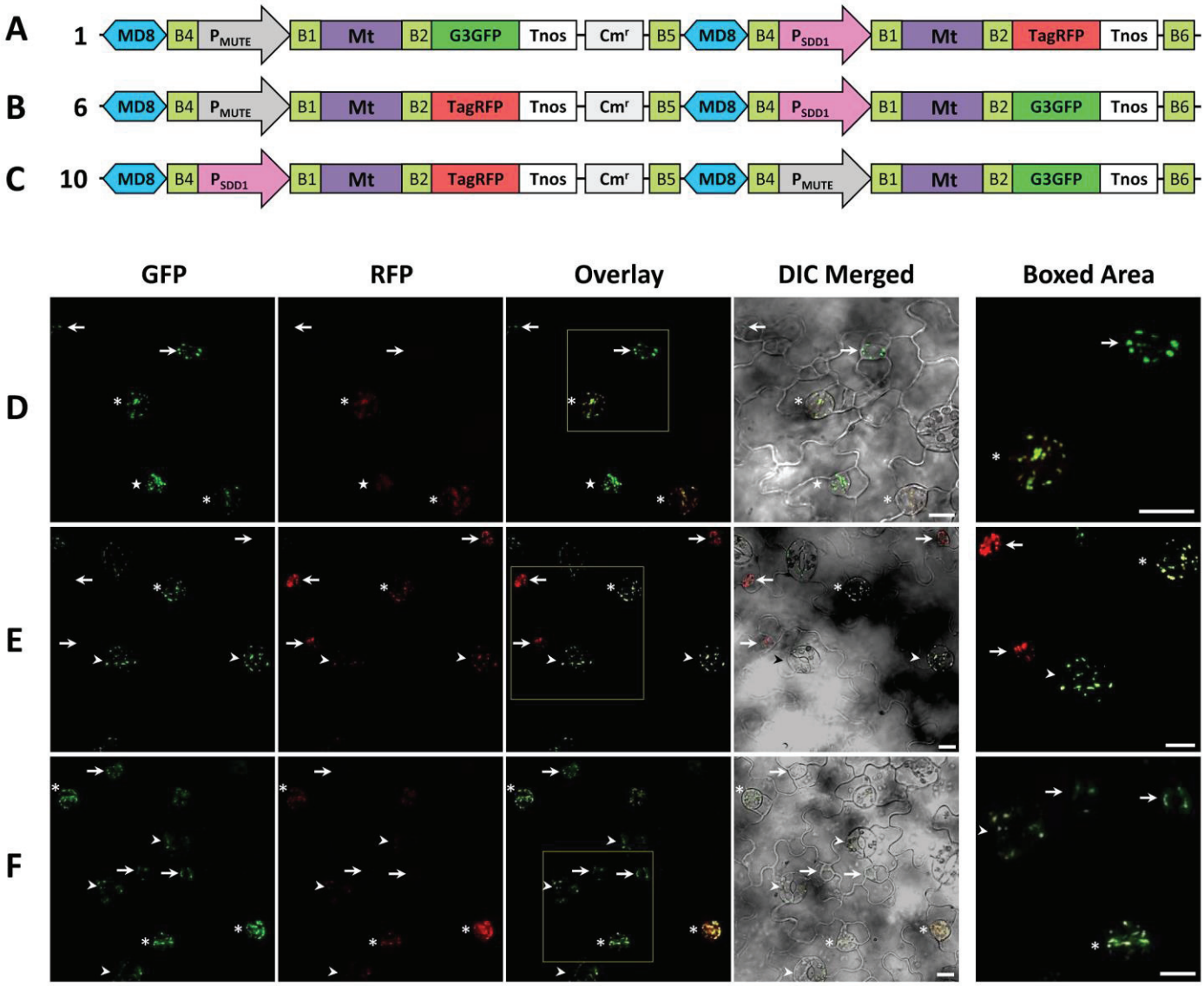

Fig. 4-4. Expression and intracellular localization of G3GFP and TagRFP fused with the mitochondria-targeting signal in transformed *A. thaliana* with different arrangements of promoters and cloning positions. (A-C) Structural diagram of the binary constructs 1, 6, and 10 used in expression experiments. (D-F) Fluorescent images of the leaf epidermis of *A. thaliana* transformed with construct 1 (D), 6 (E), or 10 (F). Different developmental stages in stomatal lineages are indicated by arrows (meristemoids), stars (GMCs), asterisks (immature GCs), or arrowheads (mature GCs). In meristemoids, only the expression of the fluorescent protein directed by P_{MUTE} was observed, while both signals were detected in later stages. GFP, signal of G3GFP; RFP, signal of TagRFP; Overlay, overlay of GFP and RFP; DIC Merged, differential interference contrast (DIC) merged with GFP and RFP; Boxed Area, enlargement of the boxed area in the overlay. Scale bars =10 μm.

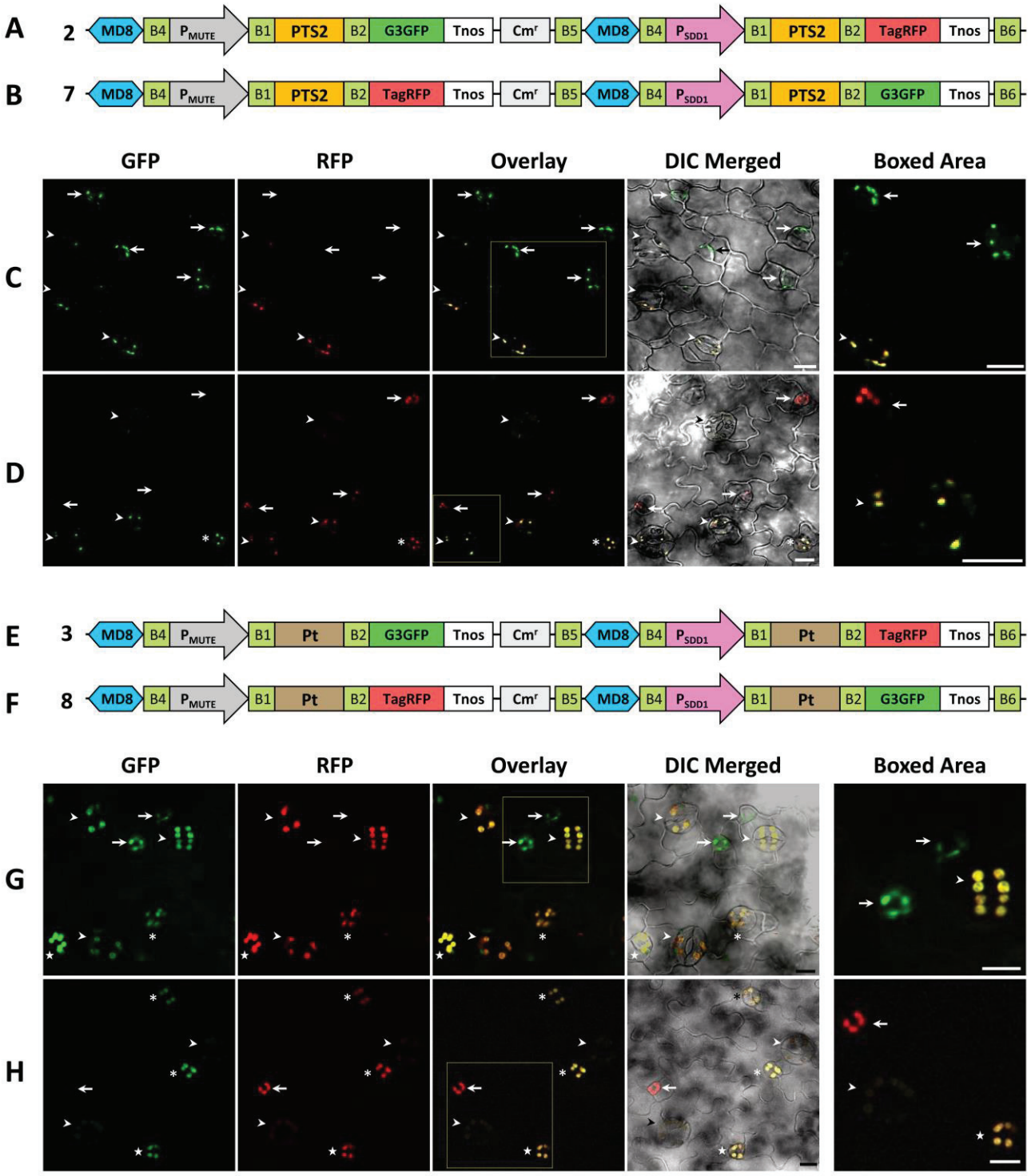

Fig. 4-5. Expression and intracellular localization of G3GFP and TagRFP fused with peroxisome- or plastid-targeting signals in transformed *A. thaliana* with different combinations of promoters. (A, B) Structural diagram of the binary constructs with peroxisome-targeting signals (constructs 2 and 7). (C, D) Fluorescent images of the leaf epidermis of *A. thaliana* transformed with construct 2 (C) or 7 (D). (E, F) Structural diagram of the binary constructs with plastid-targeting signals (constructs 3 and 8). (G, H) Fluorescent images of the leaf epidermis of *A. thaliana* transformed with construct 3 (G) or 8 (H). Different developmental stages in stomatal lineages are indicated by arrows (meristemoids), stars (GMCs), asterisks (immature GCs), or arrowheads (mature GCs). In meristemoids, only the expression of the fluorescent protein directed by P_{MUTE} was observed, while both signals were detected in later stages. GFP, signal of G3GFP; RFP, signal of TagRFP; Overlay, overlay of GFP and RFP; DIC Merged, differential interference contrast (DIC) merged with GFP and RFP; Boxed Area, enlargement of the boxed area in the overlay. Scale bars =10 μm.

The author also examined the constructs carrying G3GFP and TagRFP fused with different organelle-targeting signals and driven by different promoters. In plants transformed with construct 4 (P_{MUTE}:Mt-G3GFP-P_{SDD1}:PTS2-TagRFP, Fig. 4-6A), only the mitochondria-targeted G3GFP signal was detected in meristemoids. In GMCs, immature GCs, and weakly in mature GCs, the G3GFP signal and TagRFP signal were both detected, but localized in different subcellular compartments (Fig. 4-6D). P_{MUTE}:Mt-G3GFP-P_{SDD1}:Pt-TagRFP (construct 5, Fig. 4-6B) and P_{MUTE}:Pt-TagRFP-P_{SDD1}:PTS2-G3GFP (construct 9, Fig. 4-6C) also showed consistent fluorescence images corresponding to their targeting signals and promoters (Fig. 4-6E and 6F). These results indicate that the two genes cloned by the R4DS Gateway cloning system are independently regulated.

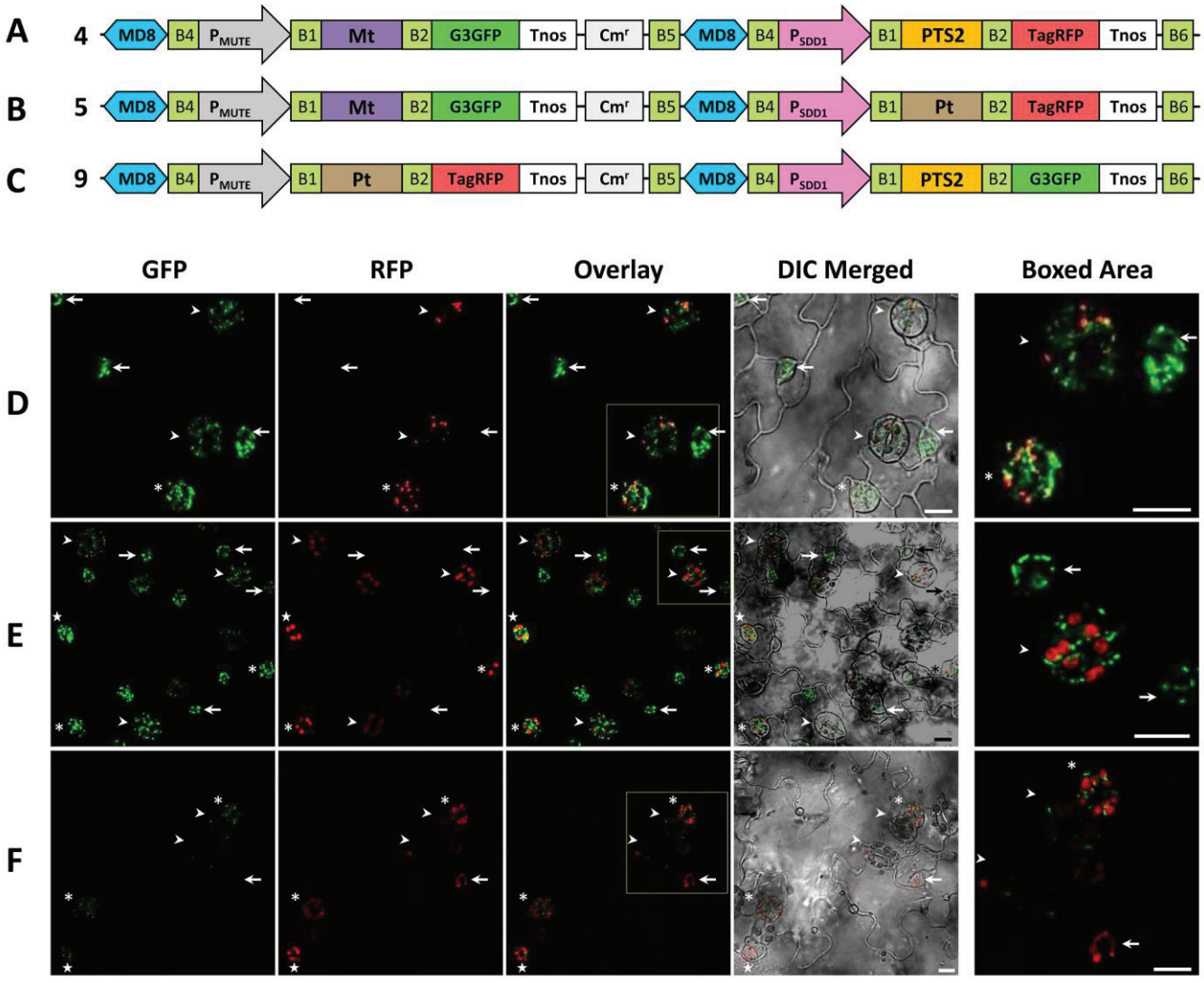

Fig. 4-6. Expression and intracellular localization of G3GFP and TagRFP fused with different combinations of mitochondria-, peroxisome-, and plastid-targeting signals in transformed *A. thaliana* with different promoters. (A-C) Structural diagram of the binary constructs 4, 5, and 9 with different targeting signals. (D-F) Fluorescent images of the leaf epidermis of *A. thaliana* transformed with construct 4 (D), 5 (E), or 9 (F). Different developmental stages in stomatal lineages are indicated by arrows (meristemoids), stars (GMCs), asterisks (immature GCs), or arrowheads (mature GCs). In meristemoids, only the expression of the fluorescent protein directed by P_{MUTE} was observed, while both signals were detected in later stages. GFP, signal of G3GFP; RFP, signal of TagRFP; Overlay, overlay of GFP and RFP; DIC Merged, differential interference contrast (DIC) merged with GFP and RFP; Boxed Area, enlargement of the boxed area in the overlay. Scale bars =10 μm.

In the present study, the author developed the R4DS Gateway cloning system with the following desirable features; [140] Compatible with universal-type entry clones (*att*L4-promoter-*att*R1 and *att*L1-ORF-*att*L2); therefore, the resources of promoter and ORF entry clones in the research community can be directly used in any combination for cloning. (2) Two-gene cloning can be accomplished easily using two rounds of Gateway LR reactions. (3) The 17 different tags including visible proteins and epitope tags can be fused at the C-terminal of each ORF in any combination. (4) Four kinds of resistance markers conferring Km^r, Hyg^r, $BASTA^r$, and $Tunica^r$ are available, and, thus, are useful for the re-transformation of plants already carrying a selection marker(s). The author made 10 different two-gene constructs using R4pGWB6xxx-MD8 and found efficient and accurate cloning performance. Expression experiments with P_{MUTE} and P_{SDD1} confirmed the promoter-specific independent expression of two ORFs, regardless of the combination of the promoters used or position of cloning sites, in *A. thaliana*. The R4DS Gateway cloning system is a powerful tool for plant transformation and will contribute to a better understanding of molecular gene functions and protein intracellular dynamics, e.g., comparing two transgene expression patterns, elucidating subcellular co-localization, analyzing protein complex formation, and detecting protein-protein interactions.

Chapter 5

A dual-site gateway cloning system for simultaneous cloning of two genes for plant transformation

Introduction

All physiological processes including DNA replication, protein trafficking, and different metabolic and signaling pathways require coordinated expression of genes and a huge network of protein functions and interactions. Innovative systems designed to deliver two or more expression cassettes simultaneously could facilitate the dissection of the complex network of protein functions and interactions. Plant vector systems enabling the cloning of two or more expression cassettes on a single T-DNA and deliver them simultaneously to the plant genome provide a technical advance in multiplication of transgenes over other methods, i.e., crossing between individual transgenic plants, co-transformation of plants, and re-transformation of established transgenic plants [43, 45, 208]. Such plant vector systems minimize the time and labor, reduce gene dosage effects, eliminate independent segregation of introduced genes in next generations, and enable the use of only one selection marker to screen the transformants.

In research areas using transgenic plants, promoter selection is one of the key factors for successful expression of transgenic genes and obtaining appropriate transgenic plants for various research purposes. For coordinated expression of two or more genes, two strategies are available when designing expression vectors: either using different promoters to drive the expression of transgenes (diverse promoter strategy) or using the same promoter for all multiple genes (repetitive promoter strategy). The diverse promoter strategy may be useful in pyramiding multiple transgenes for trait improvement, but finding different promoters with identical activities is extremely difficult [225]. In contrast, although in some cases it has been linked with gene silencing issues due to sequence homology, the repetitive promoter strategy often works effectively and there are several studies reported the successful use of same promoter to guide two or more transgene expressions [208, 226-228]. Constitutive promoters are frequently used for the repetitive promoter strategy to ensure expression of transgenes in most cell types, most stages of development, in a wide range of plant species. The cauliflower mosaic virus 35S promoter (P35S) is the most prevalently used among constitutive promoters with high expression levels of transgenes in many plants [229, 230]. However, strong overexpression by P35S may lead to mislocalization of investigated protein(s) and the enhancer sequence exists in P35S may alter the expression levels of nearly located transgenes [231]. Furthermore, the frequent methylation of P35S may cause transcriptional inactivation [232, 233] or gene silencing in stable transformants [234-237], especially when used

repetitively for multi-gene constructs [45, 235]. Such problems associated with the strong activity of P35S can be avoided by using a less active promoter, i.e., a promoter that provides a moderate level of constitutive expression such as nopaline synthase promoter (Pnos) [238]. The Pnos showed a 20-30 fold lower expression levels [239, 240] and much lower methylation frequency [235] when compared with P35S. Although some binary vectors enabling two-gene constitutive expression have been developed, they were equipped with diverse promoters [209, 210] or two P35S [208], which limits their usage in experiments requiring similar and moderate expression of the tested two genes. Thus, there is a need for an effective cloning system for two-gene construction utilizing a moderate constitutive promoter such as Pnos to simultaneously drive the transgenes. Besides promoters, other sequences are also known to affect expression of transgenes. Several reports have shown the use of matrix attachment regions (MARs) to increase overall expressions of transgenes [193-195, 241] and reduce the variations in expressions levels among transformants [190-193].

In recent years, bimolecular fluorescence complementation (BiFC) has been extensively used for identification and visualization of protein complex formation and protein interactions in living organisms including plants (Reviewed in: [242-245]). However, improper fusion orientation of amino- (N-) or carboxyl- (C-)terminal fragments of a fluorescent protein, e.g. enhanced yellow fluorescent protein (EYFP), may affect the protein binding or block the targeting information of that protein [244]. To this end, trying all the eight combinations of fusion patterns for the two tested proteins is highly recommended even necessary in some cases [246-248].

Here, the author created the dual-site (DS) Gateway cloning system for simple assembly and cloning of two transgenes driven by the moderate Pnos on a single T-DNA. The DS Gateway cloning system permits the N-terminal labeling of tested proteins with various tags (6 fluorescent proteins and 7 epitope tags) providing a suitability for subcellular localization analysis and co-precipitation experiments. The DS Gateway cloning system also enables both N- and C-terminal labeling of tested proteins with N- or C-terminal fragments of EYFP (n/cYFP) with all possible tagging patterns for analysis of protein-protein interactions by the BiFC assay. The DS Gateway cloning system provides a choice for selection of transformants by 4 different plant resistance markers (kanamycin resistance (Km^r), hygromycin resistance (Hyg^r), BASTA resistance ($BASTA^r$) and Tunicamycin ($Tunica^r$)). The author confirmed the stable co-expression and subcellular localization of two soluble *N*-ethylmaleimide-sensitive factor attachment protein receptors (SNAREs) in *Arabidopsis*

thaliana. Furthermore, the author detected the interaction of two cage subunits of coat protein complex II (COPII) by a BiFC assay in both transient expression system using Japanese leek and stable expression system using *A. thaliana*. Taken together, the newly developed DS Gateway cloning system should be an efficient multipurpose two-gene expression system in plant research with multiple applications, e.g., analysis of co-localization patterns of transgenes and investigation of protein-protein interactions by BiFC or co-immunoprecipitation.

Materials and methods

Plasmid manipulation and bacterial strains

Plasmid manipulations were performed according to standard molecular procedures [183]. KOD-Plus-Neo DNA polymerase (Toyobo, Osaka, Japan) was used to make amplified products with blunt ends. Nucleotide sequences of adaptors and primers are listed in Table 5-1. In all cloning steps, plasmids were confirmed by digestion with restriction enzymes and sequencing. Escherichia coli strains One Shot® ccdB survival™ 2T1R (Thermo Fisher Scientific, Kanagawa, Japan) or DH5α (Toyobo) were used for manipulation of plasmids with or without ccdB, respectively. The binary constructs were transferred to Agrobacterium tumefaciens strain C58C1 (pMP90) by electroporation.

Plasmid construction

The dual-site binary (DSB) vectors were constructed as follows. MD8, a MAR of *A. thaliana* [187] and Pnos were introduced into binary vectors pGWB400, pGWB500 [141], pGWB600 [184], and pGWB700 [185] to make pGWB400-, 500-, 600-, and 700-MD8-Pnos, respectively. Next, dual-site Gateway cassette (*att*R1-*ccd*B-*att*R2-Tnos-Cm^r-*att*R5-*ccd*B-*att*R6) constructed based on pUC119 (TaKaRa, Shiga, Japan) was introduced into pGWB400-, 500-, 600-, and 700-MD8-Pnos to make DSB vectors pGWB6402-, 6502-, 6602-, and 6702-MD8-Pnos (MD8-Pnos-*att*R1-*ccd*B-*att*R2-Tnos-Cm^r-*att*R5-*ccd*B-*att*R6), respectively. Tnos is the terminator of nopaline synthase and Cm^r is the chloramphenicol resistance. The *att*R1-*ccd*B-*att*R2 of resulting plasmids was replaced with tag-*att*R1-*ccd*B-*att*R2 to make DSB vectors for N-terminal fusion (MD8-Pnos-tag-*att*R1-*ccd*B-*att*R2-Tnos-Cm^r-*att*R5-*ccd*B-*att*R6). The *att*R1-*ccd*B-*att*R2 of pGWB6402-, 6502-, 6602-, and 6702-MD8-Pnos were replaced with n/cYFP-*att*R1-*ccd*B-*att*R2 or *att*R1-*ccd*B-*att*R2-n/cYFP to

make DSB vectors for the BiFC assay (MD8-Pnos-n/cYFP-*att*R1-*ccd*B-*att*R2-Tnos-Cm^r-*att*R5-*ccd*B-*att*R6 or MD8-Pnos-*att*R1-*ccd*B-*att*R2-n/cYFP-Tnos-Cm^r-*att*R5-*ccd*B-*att*R6). The destination donor (DD) vectors were constructed as follows. An *att*L5, *att*L6, MD8, Pnos, and Tnos were cloned into pUC119 to make pDD600-MD8-Pnos (*att*L5-MD8-Pnos-Tnos-*att*L6). The *att*R1-Cm^r-*ccd*B-*att*R2 from pGWB402 was introduced into pDD600-MD8-Pnos to make pDD602-MD8-Pnos (*att*L5-MD8-Pnos-*att*R1-Cm^r-*ccd*B-*att*R2-Tnos-*att*L6). The tag-*att*R1-Cm^r-*ccd*B-*att*R2 was introduced into pDD600-MD8-Pnos to make DD vectors for N-terminal fusion (*att*L5-MD8-Pnos-tag-*att*R1-Cm^r-*ccd*B-*att*R2-Tnos-*att*L6). The n/cYFP-*att*R1-Cm^r-*ccd*B-*att*R2 and *att*R1-Cm^r-*ccd*B-*att*R2-n/cYFP were introduced into pDD600-MD8-Pnos to make DD vectors for the BiFC assay. The detailed description of plasmid construction methods were as follows.

Generation of no tag-type DSB vectors (pGWB6x02-MD8-Pnos)

The Pnos sequence was amplified by PCR using pRED56-MD8-Pnos (unpublished work) as a template with the primers *Hin*dIII-Pnos-F and Pnos-*Xba*I-Cm^r(ATG)-R (Table 5-1). The Cm^r sequence was amplified by PCR using pGWB401 [141] as a template with the primers Cm^r-F and Cm^r-*Xba*I-*Sac*I-R (Table 5-1). These products were diluted, mixed, and subjected to a second PCR with the *Hin*dIII-Pnos-F and Cm^r-*Xba*I-*Sac*I-R primers to make *Hin*dIII-Pnos-*Xba*I-Cm^r-*Xba*I-*Sac*I. The amplified product was digested with *Hin*dIII and *Sac*I and introduced into pGWB400-MD8, pGWB500-MD8, pGWB600-MD8 and pGWB700-MD8 (MD8-*Hin*dIII-*Sac*I-Tnos-*Asc*I; unpublished work) to make pGWB400-MD8-Pnos-*Xba*I-Cm^r-*Xba*I, pGWB500-MD8-Pnos-*Xba*I-Cm^r-*Xba*I, pGWB600-MD8-Pnos-*Xba*I-Cm^r-*Xba*I, and pGWB700-MD8-Pnos-*Xba*I-Cm^r-*Xba*I, respectively. Next, the *Xba*I-Cm^r-*Xba*I fragment was removed by *Xba*I digestion followed by self-ligation to make pGWB400-MD8-Pnos, pGWB500-MD8-Pnos, pGWB600-MD8-Pnos and pGWB700-MD8-Pnos, respectively (MD8-*Hin*dIII-Pnos-*Xba*I-*Sac*I-Tnos-*Asc*I). The *att*R1-*ccd*B-*att*R2-Tnos-Cm^r-*att*R5-*ccd*B-*att*R6 sequence was prepared from pUGW6001 (*Hin*dIII-*att*R1-*ccd*B-*att*R2-Tnos-Cm^r-*att*R5-*ccd*B-*att*R6-*Asc*I; unpublished work) and then introduced into the *Hin*dIII-*Asc*I sites of pGWB400-MD8-Pnos, pGWB500-MD8-Pnos, pGWB600-MD8-Pnos, and pGWB700-MD8-Pnos to make pGWB6402-MD8-Pnos, pGWB6502-MD8-Pnos, pGWB6602-MD8-Pnos, and pGWB6702-MD8-Pnos, respectively (MD8-Pnos-*att*R1-*ccd*B-*att*R2-Tnos-Cm^r-*att*R5-*ccd*B-*att*R6).

Generation of DSB vectors for N-terminal tagging and BiFC assay

In order to construct DSB vectors for N-terminal tagging, the Cm^r fragment of pUGW6, 9, 12, 15, 18, 21, 24, 27, 42, 45, 52, 55, and 61 [141, 188] was removed by *Bam*HI digestion to make pUGW6-, 9-, 12-, 15-, 18-, 21-, 24-, 27-, 42-, 45-, 52-, 55-, and 61-ΔCm^r, respectively. The *Xba*I-*Sac*I fragments containing tag-*att*R1-*ccd*B-*att*R2 were prepared from pUGW6-, 9-, 12-, 15-, 18-, 21-, 24-, 27-, 42-, 45-, 52-, 55-, 61-ΔCm^r and replaced with the *att*R1-*ccd*B-*att*R2 of pUGW3002 (P35S-*att*R1-*ccd*B-*att*R2-Tnos-Cm^r-*att*R4-*ccd*B-*att*R3; unpublished work) to make the corresponding pUGW30xx vectors (P35S-tag-*att*R1-*ccd*B-*att*R2-Tnos-Cm^r-*att*R4-*ccd*B-*att*R3). *Xba*I-*Bsp*EI adaptor was introduced in pGWB6402-MD8-Pnos, pGWB6602-MD8-Pnos and pGWB6702-MD8-Pnos to make pGWB6402-MD8-Pnos/*Xba*I-*Bsp*EI, pGWB6602-MD8-Pnos/*Xba*I-*Bsp*EI and pGWB6702-MD8-Pnos/*Xba*I-*Bsp*EI, respectively. The *Xba*I-*Bsp*EI fragment containing tag-*att*R1-*ccd*B-*att*R2-Tnos-Cm^r was prepared from pUGW30xx vectors and inserted into pGWB6402-MD8-Pnos/*Xba*I-*Bsp*EI to make pGWB6406-MD8-Pnos to pGWB6461-MD8-Pnos (MD8-Pnos-tag-*att*R1-*ccd*B-*att*R2-Tnos-Cm^r-*att*R5-*ccd*B-*att*R6). By using the same method, the author constructed pGWB6606-MD8-Pnos to pGWB6661-MD8-Pnos and pGWB6706-MD8-Pnos to pGWB6761-MD8-Pnos by inserting the *Xba*I-*Bsp*EI fragment containing tag-*att*R1-*ccd*B-*att*R2-tag-Tnos-Cm^r into pGWB6602-MD8-Pnos/*Xba*I-*Bsp*EI and pGWB6702-MD8-Pnos/*Xba*I-*Bsp*EI, respectively. For construction of pGWB6506-MD8-Pnos to pGWB6561-MD8-Pnos, the *Xba*I-*Asc*I fragment containing tag-*att*R1-*ccd*B-*att*R2-Tnos-Cm^r-*ccd*B-*att*R6-*Asc*I was prepared from pGWB6406-MD8-Pnos to pGWB6461-MD8-Pnos and inserted into pGWB500-MD8-Pnos.

In order to construct DSB vectors for BiFC assay, the Cm^r fragment of pnYGW, pcYGW, pGWnY, and pGWcY [143] was removed by *Bam*HI digestion to make pnYGW-ΔCm^r, pcYGW-ΔCm^r, pGWnY-ΔCm^r, and pGWcY-ΔCm^r, respectively. The *Xba*I-*Sac*I fragments containing n/cYFP-*att*R1-*ccd*B-*att*R2 or *att*R1-*ccd*B-*att*R2-n/cYFP were prepared from pnYGW-ΔCm^r, pcYGW-ΔCm^r, pGWnY-ΔCm^r, or pGWcY-ΔCm^r and replaced with *att*R1-*ccd*B-*att*R2 of pUGW3002 to make pUGW3000-NY0, pUGW3000-CY0, pUGW3000-NY2, and pUGW3000-CY2, respectively. The *Xba*I-*Bsp*EI fragments containing n/cYFP-*att*R1-*ccd*B-*att*R2-Tnos-Cm^r were prepared from pUGW3000-NY0 or pUGW3000-CY0, and inserted into pGWB6402-MD8-Pnos/*Xba*I-*Bsp*EI to make pGWB6400-MD8-Pnos-NY0 and pGWB6400-MD8-Pnos-CY0, respectively (MD8-Pnos-n/cYFP-*att*R1-*ccd*B-*att*R2-Tnos-Cm^r-*att*R5-*ccd*B-*att*R6). The *Xba*I-*Bsp*EI fragments containing *att*R1-*ccd*B-*att*R2-n/cYFP-Tnos-Cm^r were prepared from pUGW3000-NY2 or pUGW3000-CY2, and inserted into

pGWB6402-MD8-Pnos/*Xba*I-*Bsp*EI to make pGWB6400-MD8-Pnos-NY2 and pGWB6400-MD8-Pnos-CY2, respectively (MD8-Pnos-*att*R1-*ccd*B-*att*R2-n/cYFP-Tnos-Cm^r-*att*R5-*ccd*B-*att*R6). By using the same method, pGWB6600-MD8-Pnos-NY0, pGWB6600-MD8-Pnos-CY0, pGWB6600-MD8-Pnos-NY2, and pGWB6600-MD8-Pnos-CY2 were constructed by inserting the *Xba*I-*Bsp*EI fragments containing n/cYFP-*att*R1-*ccd*B-*att*R2-Tnos-Cm^r or *att*R1-*ccd*B-*att*R2-n/cYFP-Tnos-Cm^r into pGWB6602-MD8-Pnos/*Xba*I-*Bsp*EI. Likewise, pGWB6700-MD8-Pnos-NY0, pGWB6700-MD8-Pnos-CY0, pGWB6700-MD8-Pnos-NY2, and pGWB6700-MD8-Pnos-CY2 were constructed by inserting the *Xba*I-*Bsp*EI fragments containing n/cYFP-*att*R1-*ccd*B-*att*R2-Tnos-Cm^r or *att*R1-*ccd*B-*att*R2-n/cYFP-Tnos-Cm^r into pGWB6702-MD8-Pnos/*Xba*I-*Bsp*EI. For construction of pGWB6500-MD8-Pnos-NY0, pGWB6500-MD8-Pnos-CY0, pGWB6500-MD8-Pnos-NY2, and pGWB6500-MD8-Pnos-CY2, the *Xba*I-*Asc*I fragments containing n/cYFP-*att*R1-*ccd*B-*att*R2-Tnos-Cm^r-*ccd*B-*att*R6 or *Xba*I-*att*R1-*ccd*B-*att*R2-n/cYFP-Tnos-Cm^r-*ccd*B-*att*R6 were prepared from pGWB6400-MD8-Pnos-NY0, pGWB6400-MD8-Pnos-CY0, pGWB6400-MD8-Pnos-NY2, and pGWB6400-MD8-Pnos-CY2 and inserted into pGWB500-MD8-Pnos.

Generation of DD vectors

The Pnos fragment prepared from pGWB700-MD8-Pnos was introduced into the *Hin*dIII-*Sac*I sites of pDD600-MD8 (*att*L5-MD8-Tnos-*att*L6; unpublished work) to make pDD600-MD8-Pnos (*att*L5-MD8-Pnos-Tnos-*att*L6). The *Xba*I-*Sac*I fragment containing *att*R1-Cm^r-*ccd*B-*att*R2 prepared from pGWB402 [141] was introduced into pDD600-MD8-Pnos to make pDD602-MD8-Pnos (*att*L5-MD8-Pnos-*att*R1-Cm^r-*ccd*B-*att*R2-Tnos-*att*L6).

For construction of DD vectors for N-terminal tagging, the *Xba*I-*Sac*I fragments containing tag-*att*R1-Cm^r-*ccd*B-*att*R2 were prepared from pGWB406 to pGWB461 [141], and introduced into pDD600-MD8-Pnos to make pDD606-MD8-Pnos to pDD661-MD8-Pnos (*att*L5-MD8-Pnos-tag-*att*R1-Cm^r-*ccd*B-*att*R2-Tnos-*att*L6).

For construction of DD vectors for BiFC assay, the *Xba*I-*Sac*I fragments containing n/cYFP-*att*R1-Cm^r-*ccd*B-*att*R2 were prepared from pnYGW and pcYGW [143], and introduced into pDD600-MD8-Pnos to make pDD600-MD8-Pnos-NY0 and pDD600-MD8-Pnos-CY0 (*att*L5-MD8-Pnos-n/cYFP-*att*R1-Cm^r-*ccd*B-*att*R2-Tnos-*att*L6). The *Xba*I-*Sac*I fragments containing *att*R1-Cm^r-*ccd*B-*att*R2-n/cYFP were prepared from pGWnY, and pGWcY [143], and introduced into pDD600-MD8-Pnos to make pDD600-MD8-Pnos-NY2

and pDD600-MD8-Pnos-CY2 (*att*L5-MD8-Pnos-*att*R1-Cm^r-*ccd*B-*att*R2-n/cYFP-Tnos-*att*L6).

Sequence files of all DSB and DD vectors were submitted to GenBank/EML/DDBJ and are available under accession numbers shown in Table 5-2.

Preparation of entry clones and Gateway cloning of two genes in the DS Gateway cloning system

The *A. thaliana* SNARE protein AtSYP43 (AT3G05710, a *trans*-Golgi network (TGN) marker) was used to construct ORF entry clone. Two step adaptor PCR was carried out to amplify the AtSYP43 fragment from Col-0 wild-type genomic DNA with AtSYP43-*att*B1 and AtSYP43-*att*B2 primers (Table 5-1). The obtained DNA fragment was further amplified with *att*B1 adaptor and *att*B2 adaptor primers to add *att*B1 and *att*B2 sequences to their 5' and 3' ends, respectively. The resulting amplified fragment *att*B1-AtSYP43-*att*B2 was subjected to a BP reaction with pDONR201 (Thermo Fisher Scientific) to construct pDONR201-AtSYP43 entry clone.

Generation of two-gene constructs in DSB vectors for subcellular localization analysis was performed by two rounds of LR reactions and transformations. A pDONR201-AtSYP43 entry clone was subjected to an LR reaction with *Sal*I-linearized pDD645-MD8-Pnos to make pDD645-MD8-Pnos-AtSYP43. Next, the resultant pDD645-MD8-Pnos-AtSYP43, the pDONR201-AtSYP31 (a *cis*-Golgi marker; [91]), and *Xho*I-linearized pGWB6642-MD8-Pnos were subjected to an LR reaction (tripartite LR reaction) to make a final binary construct Pnos:EYFP-AtSYP31-Pnos:ECFP-AtSYP43 (MD8-Pnos-EYFP-*att*B1-AtSYP31-*att*B2-Tnos-Cm^r-*att*B5-MD8-Pnos-ECFP-*att*B1-AtSYP43-*att*B2-Tnos-*att*B6). With the same method, Pnos:EYFP-AtSYP43-Pnos:ECFP-AtSYP31 (MD8-Pnos-EYFP-*att*B1-AtSYP43-*att*B2-Tnos-Cm^r-*att*B5-MD8-Pnos-ECFP-*att*B1-AtSYP31-*att*B2-Tnos-*att*B6) was constructed.

For generation of two-gene constructs in DSB vectors for the BiFC assay, the pDONR201-AtSEC13A, pDONR201-AtSEC13B entry clones [143] or pDONR201-β-glucuronidase (GUS) entry clone [188] were individually subjected to LR reactions with *Sal*I-linearized pDD600-MD8-Pnos-CY2 to make pDD600-MD8-Pnos-CY2-AtSEC13A, pDD600-MD8-Pnos-CY2-AtSEC13B and pDD600-MD8-Pnos-CY2-GUS, respectively. The resulting plasmids were individually subjected to an LR reaction (tripartite LR reaction) with

AtSEC31B entry clone [143] and *Xho*I-linearized pGWB6400-MD8-Pnos-NY2, to make final binary constructs Pnos:AtSEC31B-nYFP-Pnos:AtSEC13A-cYFP (MD8-Pnos-*att*B1-AtSEC31B-*att*B2-nYFP-Tnos-Cm^r-*att*B5-MD8-Pnos-*att*B1-AtSEC13A-*att*B2-cYFP-Tnos-*att*B6), Pnos:AtSEC31B-nYFP-Pnos:AtSEC13B-cYFP (MD8-Pnos-*att*B1-AtSEC31B-*att*B2-nYFP-Tnos-Cm^r-*att*B5-MD8-Pnos-*att*B1-AtSEC13B-*att*B2-cYFP-Tnos-*att*B6), and Pnos:AtSEC31B-nYFP-Pnos:GUS-cYFP (MD8-Pnos-*att*B1-AtSEC31B-*att*B2-nYFP-Tnos-Cm^r-*att*B5-MD8-Pnos-*att*B1-GUS-*att*B2-cYFP-Tnos-*att*B6), respectively. The AtSEC31B entry clone used here was differently named in Hino et al., 2011 as AtSEC31A entry clone.

Generation of transgenic A. thaliana for co-expression, subcellular localization, and protein-protein interaction analyses

A. thaliana ecotype Col-0 seeds were vernalized at 4˚C for 2-3 days on a Murashige and Skoog (MS) agar medium and grown at 22˚C under 24-hr continuous light for two weeks, then seedlings were transplanted to Jiffy-7 (Jiffy Preforma Production K. K, Yokohama, Japan) under long-day conditions (16/8-hr). Six-week-old *A. thaliana* were used for transformation by floral dip method [10] and treated plants were allowed to grow and set seeds under the same conditions. For the co-expression and subcellular localization analysis of SNARE proteins in a stable expression system, seeds were germinated for 10 days on MS agar plates containing (54 μL/L) BASTA and (100 mg/L) cefotax. Selected transformants were moved to new BASTA-cefotax free plates to boost root elongation for more 7 days before examining with confocal microscopy. For the protein-protein interaction analysis of COPII proteins by the BiFC assay in a stable expression system, seeds were germinated for 14 days on MS agar plates containing (30 mg/L) kanamycin and (100 mg/L) cefotax and selected transformants were examined by confocal microscopy.

Transient expression assay in Japanese leek

Two-gene constructs assembled on pGWB6400-MD8-Pnos-NY2 were introduced into leek epidermal cells using biolistic bombardment technique as described in Hino et al., 2011. A pUGW45 [188] encoding enhanced cyan fluorescent protein (ECFP) driven by the P35S was used as an internal reference [247]. Each experiment was independently performed 3-4 times under the same conditions.

Analyses of co-expression, subcellular localization, and protein-protein interactions by confocal microscopy

The fluorescent signals in the co-expression and subcellular localization analysis, and in the protein-protein interaction analysis were detected in *A. thaliana* or Japanese leek by a TCS SP5 confocal microscope (Leica Microsystems, Wetzlar, Germany) equipped with an HCX IRAPO L 25.0 X 0.95 water-immersion objective lens. The ECFP and EYFP were excited with the argon laser line with wavelengths of 458 nm and 514 nm, respectively. The fluorescence of ECFP and EYFP was captured at 465-500 nm and 520-555 nm, respectively. The images were acquired using the sequential scanning mode with a resolution of 512×512 pixels and scanning speed at 400 Hz for *A. thaliana* and with a resolution of 1024×256 pixels and bidirectional scanning speed at 200 Hz for Japanese leek epidermal cells.

Table 5-1. Adaptors and primers used in this study.

Oligos	Sequence
Adaptors	
*Xba*I-*Bsp*EI-F	5'-CTAGAGAGCCCTGAGT-3'
*Xba*I-*Bsp*EI-R	5'-CCGGACTCAGGGCTCT-3'
Primers	
*Hin*dIII-Pnos-F	5'-CTAAGCTTATCATGAGCGGAGAATTAAGG-3'
Pnos-*Xba*I-Cm^r(ATG)-R	5'-GAAGCATAAAGTGTAAAGCCTTCTAGACGGTGCAGATTATTG-3'
Cm^r-F	5'-AGGCTTTACACTTTATGCTTC-3'
Cm^r-*Xba*I-*Sac*I-R	5'-CTGAGCTCTTTCTAGACCTTACCAGACCGGAGATAT-3'
AtSYP43-*att*B1	5'-AAAAAGCAGGCTCGATGGCGACTAGGAATCGTACGCT-3'
AtSYP43-*att*B2	5'-AGAAAGCTGGGTTTCACAACAGAATCTCCTTGAGGATTAAGA-3'
*att*B1 adaptor	5'-GGGGACAAGTTTGTACAAAAAAGCAGGCT -3'
*att*B2 adaptor	5'-GGGGACCACTTTGTACAAGAAAGCTGGGT-3'

Table 5-2. List of plasmids constructed in this study. Backbone, bacterial selection, plant selection, tag, fusion type, restriction enzyme for linearization and accession numbers of DD vectors (pDD6xx-MD8-Pnos) and DSB vectors (pGWB6xxx-MD8-Pnos) are shown. Amp^r, ampicillin resistance; Cm^r, Chloramphenicol resistance**;** Spc^r, spectinomycin resistance; MD8, a matrix attachement region MD8 of *Arabidopsis thaliana*; Pnos, nopaline synthase promoter; the NPTII gene for kanamycin resistance (Km^r), the HPT gene for hygromycin resistance (Hyg^r), the bar gene for BASTA resistance ($BASTA^r$) and the GPT gene for tunicamycin resistance ($Tunica^r$).

Plasmid name	Backbone	Bacterial selection	Plant selection	Tag	Fusion type	Restriction enzyme for linearization	Accession number
pDD602-MD8-Pnos	pUC119	Amp^r, Cm^r	None	None	No fusion	*Sal*I	LC221303
pDD606-MD8-Pnos	pUC119	Amp^r, Cm^r	None	sGFP	N-terminal	*Sal*I	LC221304
pDD609-MD8-Pnos	pUC119	Amp^r, Cm^r	None	6xHis	N-terminal	*Sal*I	LC221305
pDD612-MD8-Pnos	pUC119	Amp^r, Cm^r	None	FLAG	N-terminal	*Sal*I	LC221306
pDD615-MD8-Pnos	pUC119	Amp^r, Cm^r	None	3xHA	N-terminal	*Sal*I	LC221307
pDD618-MD8-Pnos	pUC119	Amp^r, Cm^r	None	4xMyc	N-terminal	*Sal*I	LC221308
pDD621-MD8-Pnos	pUC119	Amp^r, Cm^r	None	10xMyc	N-terminal	*Sal*I	LC221309
pDD624-MD8-Pnos	pUC119	Amp^r, Cm^r	None	GST	N-terminal	*Sal*I	LC221310
pDD627-MD8-Pnos	pUC119	Amp^r, Cm^r	None	T7	N-terminal	*Sal*I	LC221311
pDD642-MD8-Pnos	pUC119	Amp^r, Cm^r	None	EYFP	N-terminal	*Sal*I	LC221312
pDD645-MD8-Pnos	pUC119	Amp^r, Cm^r	None	ECFP	N-terminal	*Sal*I	LC221313
pDD652-MD8-Pnos	pUC119	Amp^r, Cm^r	None	G3GFP	N-terminal	*Sal*I	LC221314
pDD655-MD8-Pnos	pUC119	Amp^r, Cm^r	None	mRFP	N-terminal	*Sal*I	LC221315
pDD661-MD8-Pnos	pUC119	Amp^r, Cm^r	None	TagRFP	N-terminal	*Sal*I	LC221316
pDD600-MD8-Pnos-NY0	pUC119	Amp^r, Cm^r	None	nYFP	N-terminal	*Sal*I	LC221317
pDD600-MD8-Pnos-CY0	pUC119	Amp^r, Cm^r	None	cYFP	N-terminal	*Sal*I	LC221318
pDD600-MD8-Pnos-NY2	pUC119	Amp^r, Cm^r	None	nYFP	C-terminal	*Sal*I	LC221319
pDD600-MD8-Pnos-CY2	pUC119	Amp^r, Cm^r	None	cYFP	C-terminal	*Sal*I	LC221320
pGWB6402-MD8-Pnos	pPZP	Spc^r, Cm^r	Pnos:NPTII (Km^r)	None	No fusion	*Sal*I or *Xho*I	LC221321
pGWB6406-MD8-Pnos	pPZP	Spc^r, Cm^r	Pnos:NPTII (Km^r)	sGFP	N-terminal	*Sal*I or *Xho*I	LC221322
pGWB6409-MD8-Pnos	pPZP	Spc^r, Cm^r	Pnos:NPTII (Km^r)	6xHis	N-terminal	*Sal*I or *Xho*I	LC221323
pGWB6412-MD8-Pnos	pPZP	Spc^r, Cm^r	Pnos:NPTII (Km^r)	FLAG	N-terminal	*Sal*I or *Xho*I	LC221324
pGWB6415-MD8-Pnos	pPZP	Spc^r, Cm^r	Pnos:NPTII (Km^r)	3xHA	N-terminal	*Sal*I or *Xho*I	LC221325
pGWB6418-MD8-Pnos	pPZP	Spc^r, Cm^r	Pnos:NPTII (Km^r)	4xMyc	N-terminal	*Sal*I or *Xho*I	LC221326
pGWB6421-MD8-Pnos	pPZP	Spc^r, Cm^r	Pnos:NPTII (Km^r)	10xMyc	N-terminal	*Sal*I or *Xho*I	LC221327
pGWB6424-MD8-Pnos	pPZP	Spc^r, Cm^r	Pnos:NPTII (Km^r)	GST	N-terminal	*Sal*I or *Xho*I	LC221328
pGWB6427-MD8-Pnos	pPZP	Spc^r, Cm^r	Pnos:NPTII (Km^r)	T7	N-terminal	*Sal*I or *Xho*I	LC221329
pGWB6442-MD8-Pnos	pPZP	Spc^r, Cm^r	Pnos:NPTII (Km^r)	EYFP	N-terminal	*Sal*I or *Xho*I	LC221330
pGWB6445-MD8-Pnos	pPZP	Spc^r, Cm^r	Pnos:NPTII (Km^r)	ECFP	N-terminal	*Sal*I or *Xho*I	LC221331
pGWB6452-MD8-Pnos	pPZP	Spc^r, Cm^r	Pnos:NPTII (Km^r)	G3GFP	N-terminal	*Sal*I or *Xho*I	LC221332
pGWB6455-MD8-Pnos	pPZP	Spc^r, Cm^r	Pnos:NPTII (Km^r)	mRFP	N-terminal	*Sal*I or *Xho*I	LC221333
pGWB6461-MD8-Pnos	pPZP	Spc^r, Cm^r	Pnos:NPTII (Km^r)	TagRFP	N-terminal	*Sal*I or *Xho*I	LC221334
pGWB6400-MD8-Pnos-NY0	pPZP	Spc^r, Cm^r	Pnos:NPTII (Km^r)	nYFP	N-terminal	*Sal*I or *Xho*I	LC221335
pGWB6400-MD8-Pnos-CY0	pPZP	Spc^r, Cm^r	Pnos:NPTII (Km^r)	cYFP	N-terminal	*Sal*I or *Xho*I	LC221336
pGWB6400-MD8-Pnos-NY2	pPZP	Spc^r, Cm^r	Pnos:NPTII (Km^r)	nYFP	C-terminal	*Sal*I or *Xho*I	LC221337
pGWB6400-MD8-Pnos-CY2	pPZP	Spc^r, Cm^r	Pnos:NPTII (Km^r)	cYFP	C-terminal	*Sal*I or *Xho*I	LC221338
pGWB6502-MD8-Pnos	pPZP	Spc^r, Cm^r	Pnos:HPT (Hyg^r)	None	No fusion	*Sal*I or *Xho*I	LC221339
pGWB6506-MD8-Pnos	pPZP	Spc^r, Cm^r	Pnos:HPT (Hyg^r)	sGFP	N-terminal	*Sal*I or *Xho*I	LC221340
pGWB6509-MD8-Pnos	pPZP	Spc^r, Cm^r	Pnos:HPT (Hyg^r)	6xHis	N-terminal	*Sal*I or *Xho*I	LC221341
pGWB6512-MD8-Pnos	pPZP	Spc^r, Cm^r	Pnos:HPT (Hyg^r)	FLAG	N-terminal	*Sal*I or *Xho*I	LC221342
pGWB6515-MD8-Pnos	pPZP	Spc^r, Cm^r	Pnos:HPT (Hyg^r)	3xHA	N-terminal	*Sal*I or *Xho*I	LC221343

pGWB6518-MD8-Pnos	pPZP	Spc^r, Cm^r	Pnos:HPT (Hyg^r)	4xMyc	N-terminal	*Sal*I or *Xho*I	LC221344
pGWB6521-MD8-Pnos	pPZP	Spc^r, Cm^r	Pnos:HPT (Hyg^r)	10xMyc	N-terminal	*Sal*I or *Xho*I	LC221345
pGWB6524-MD8-Pnos	pPZP	Spc^r, Cm^r	Pnos:HPT (Hyg^r)	GST	N-terminal	*Sal*I or *Xho*I	LC221346
pGWB6527-MD8-Pnos	pPZP	Spc^r, Cm^r	Pnos:HPT (Hyg^r)	T7	N-terminal	*Sal*I or *Xho*I	LC221347
pGWB6542-MD8-Pnos	pPZP	Spc^r, Cm^r	Pnos:HPT (Hyg^r)	EYFP	N-terminal	*Sal*I or *Xho*I	LC221348
pGWB6545-MD8-Pnos	pPZP	Spc^r, Cm^r	Pnos:HPT (Hyg^r)	ECFP	N-terminal	*Sal*I or *Xho*I	LC221349
pGWB6552-MD8-Pnos	pPZP	Spc^r, Cm^r	Pnos:HPT (Hyg^r)	G3GFP	N-terminal	*Sal*I or *Xho*I	LC221350
pGWB6555-MD8-Pnos	pPZP	Spc^r, Cm^r	Pnos:HPT (Hyg^r)	mRFP	N-terminal	*Sal*I or *Xho*I	LC221351
pGWB6561-MD8-Pnos	pPZP	Spc^r, Cm^r	Pnos:HPT (Hyg^r)	TagRFP	N-terminal	*Sal*I or *Xho*I	LC221352
pGWB6500-MD8-Pnos-NY0	pPZP	Spc^r, Cm^r	Pnos:HPT (Hyg^r)	nYFP	N-terminal	*Sal*I or *Xho*I	LC221353
pGWB6500-MD8-Pnos-CY0	pPZP	Spc^r, Cm^r	Pnos:HPT (Hyg^r)	cYFP	N-terminal	*Sal*I or *Xho*I	LC221354
pGWB6500-MD8-Pnos-NY2	pPZP	Spc^r, Cm^r	Pnos:HPT (Hyg^r)	nYFP	C-terminal	*Sal*I or *Xho*I	LC221355
pGWB6500-MD8-Pnos-CY2	pPZP	Spc^r, Cm^r	Pnos:HPT (Hyg^r)	cYFP	C-terminal	*Sal*I or *Xho*I	LC221356
pGWB6602-MD8-Pnos	pPZP	Spc^r, Cm^r	Pnos:bar (BASTA^r)	None	No fusion	*Xho*I	LC221357
pGWB6606-MD8-Pnos	pPZP	Spc^r, Cm^r	Pnos:bar (BASTA^r)	sGFP	N-terminal	*Xho*I	LC221358
pGWB6609-MD8-Pnos	pPZP	Spc^r, Cm^r	Pnos:bar (BASTA^r)	6xHis	N-terminal	*Xho*I	LC221359
pGWB6612-MD8-Pnos	pPZP	Spc^r, Cm^r	Pnos:bar (BASTA^r)	FLAG	N-terminal	*Xho*I	LC221360
pGWB6615-MD8-Pnos	pPZP	Spc^r, Cm^r	Pnos:bar (BASTA^r)	3xHA	N-terminal	*Xho*I	LC221361
pGWB6618-MD8-Pnos	pPZP	Spc^r, Cm^r	Pnos:bar (BASTA^r)	4xMyc	N-terminal	*Xho*I	LC221362
pGWB6621-MD8-Pnos	pPZP	Spc^r, Cm^r	Pnos:bar (BASTA^r)	10xMyc	N-terminal	*Xho*I	LC221363
pGWB6624-MD8-Pnos	pPZP	Spc^r, Cm^r	Pnos:bar (BASTA^r)	GST	N-terminal	*Xho*I	LC221364
pGWB6627-MD8-Pnos	pPZP	Spc^r, Cm^r	Pnos:bar (BASTA^r)	T7	N-terminal	*Xho*I	LC221365
pGWB6642-MD8-Pnos	pPZP	Spc^r, Cm^r	Pnos:bar (BASTA^r)	EYFP	N-terminal	*Xho*I	LC221366
pGWB6645-MD8-Pnos	pPZP	Spc^r, Cm^r	Pnos:bar (BASTA^r)	ECFP	N-terminal	*Xho*I	LC221367
pGWB6652-MD8-Pnos	pPZP	Spc^r, Cm^r	Pnos:bar (BASTA^r)	G3GFP	N-terminal	*Xho*I	LC221368
pGWB6655-MD8-Pnos	pPZP	Spc^r, Cm^r	Pnos:bar (BASTA^r)	mRFP	N-terminal	*Xho*I	LC221369
pGWB6661-MD8-Pnos	pPZP	Spc^r, Cm^r	Pnos:bar (BASTA^r)	TagRFP	N-terminal	*Xho*I	LC221370
pGWB6600-MD8-Pnos-NY0	pPZP	Spc^r, Cm^r	Pnos:bar (BASTA^r)	nYFP	N-terminal	*Xho*I	LC221371
pGWB6600-MD8-Pnos-CY0	pPZP	Spc^r, Cm^r	Pnos:bar (BASTA^r)	cYFP	N-terminal	*Xho*I	LC221372
pGWB6600-MD8-Pnos-NY2	pPZP	Spc^r, Cm^r	Pnos:bar (BASTA^r)	nYFP	C-terminal	*Xho*I	LC221373
pGWB6600-MD8-Pnos-CY2	pPZP	Spc^r, Cm^r	Pnos:bar (BASTA^r)	cYFP	C-terminal	*Xho*I	LC221374
pGWB6702-MD8-Pnos	pPZP	Spc^r, Cm^r	Pnos:GPT (Tunica^r)	None	No fusion	*Sal*I	LC221375
pGWB6706-MD8-Pnos	pPZP	Spc^r, Cm^r	Pnos:GPT (Tunica^r)	sGFP	N-terminal	*Sal*I	LC221376
pGWB6709-MD8-Pnos	pPZP	Spc^r, Cm^r	Pnos:GPT (Tunica^r)	6xHis	N-terminal	*Sal*I	LC221377
pGWB6712-MD8-Pnos	pPZP	Spc^r, Cm^r	Pnos:GPT (Tunica^r)	FLAG	N-terminal	*Sal*I	LC221378
pGWB6715-MD8-Pnos	pPZP	Spc^r, Cm^r	Pnos:GPT (Tunica^r)	3xHA	N-terminal	*Sal*I	LC221379
pGWB6718-MD8-Pnos	pPZP	Spc^r, Cm^r	Pnos:GPT (Tunica^r)	4xMyc	N-terminal	*Sal*I	LC221380
pGWB6721-MD8-Pnos	pPZP	Spc^r, Cm^r	Pnos:GPT (Tunica^r)	10xMyc	N-terminal	*Sal*I	LC221381
pGWB6724-MD8-Pnos	pPZP	Spc^r, Cm^r	Pnos:GPT (Tunica^r)	GST	N-terminal	*Sal*I	LC221382
pGWB6727-MD8-Pnos	pPZP	Spc^r, Cm^r	Pnos:GPT (Tunica^r)	T7	N-terminal	*Sal*I	LC221383
pGWB6742-MD8-Pnos	pPZP	Spc^r, Cm^r	Pnos:GPT (Tunica^r)	EYFP	N-terminal	*Sal*I	LC221384
pGWB6745-MD8-Pnos	pPZP	Spc^r, Cm^r	Pnos:GPT (Tunica^r)	ECFP	N-terminal	*Sal*I	LC221385
pGWB6752-MD8-Pnos	pPZP	Spc^r, Cm^r	Pnos:GPT (Tunica^r)	G3GFP	N-terminal	*Sal*I	LC221386
pGWB6755-MD8-Pnos	pPZP	Spc^r, Cm^r	Pnos:GPT (Tunica^r)	mRFP	N-terminal	*Sal*I	LC221387
pGWB6761-MD8-Pnos	pPZP	Spc^r, Cm^r	Pnos:GPT (Tunica^r)	TagRFP	N-terminal	*Sal*I	LC221388
pGWB6700-MD8-Pnos-NY0	pPZP	Spc^r, Cm^r	Pnos:GPT (Tunica^r)	nYFP	N-terminal	*Sal*I	LC221389
pGWB6700-MD8-Pnos-CY0	pPZP	Spc^r, Cm^r	Pnos:GPT (Tunica^r)	cYFP	N-terminal	*Sal*I	LC221390
pGWB6700-MD8-Pnos-NY2	pPZP	Spc^r, Cm^r	Pnos:GPT (Tunica^r)	nYFP	C-terminal	*Sal*I	LC221391
pGWB6700-MD8-Pnos-CY2	pPZP	Spc^r, Cm^r	Pnos:GPT (Tunica^r)	cYFP	C-terminal	*Sal*I	LC221392

Results and discussion

DS Gateway cloning system for expression of two ORFs with two distinct N-terminal fusions

The DS Gateway cloning system was developed to enable a rapid cloning of two ORFs in a binary vector with the commonly used entry clones (*att*L1-ORF-*att*L2) and to allow constitutive expression using the Pnos. The N-terminal fusion with diverse tags (fluorescent proteins and epitope tags) is available in this system. The DS Gateway cloning system uses two types of vectors, dual-site binary (DSB) vectors and destination donor (DD) vectors. Fig.1 shows a line-up of DSB vectors (pGWB6xxx-MD8-Pnos) and DD vectors (pDD6xx-MD8-Pnos) for no-tag cloning (Fig. 5-1A and B) and for N-terminal fusion with fluorescent proteins and epitope tags (Fig. 5-1C and D). pGWB6xxx-MD8-Pnos are composed of four selection-marker series; pGWB64xx-MD8-Pnos with Km^r, pGWB65xx-MD8-Pnos with Hyg^r, pGWB66xx-MD8-Pnos with $BASTA^r$ and pGWB67xx-MD8-Pnos with $Tunica^r$ (Fig. 5-1A and C). Availability of a range of selection markers is beneficial in various transformation experiments, especially in retransformation of plants that already contain one or more selection marker(s). All these selection markers use Pnos and Tnos for expression and termination of the resistance genes (Fig. 5-1A and C). The pGWB6xxx-MD8-Pnos comprise four-digits where 6xxx refers the dual-site type and the 4xx, 5xx, 6xx, and 7xx refer to the kind of resistance marker (Km^r, Hyg^r, $BASTA^r$, and $Tunica^r$, respectively). The pDD6xx-MD8-Pnos comprise three digits where 6xx refers the type of DD vector compatible with pGWB6xxx-MD8-Pnos. The last two digits in both pGWB6xxx-MD8-Pnos and pDD6xx-MD8-Pnos indicate the type of tag equipped in these vectors and they are following the same nomenclature system of the previously developed Gateway Binary vectors (pGWBs) [141, 184, 185]. The DSB and DD vectors contain 13 different tags including 6 fluorescent proteins and 7 epitope tags for N-terminal fusions with ORFs (Fig. 5-1E). The fluorescent proteins enable direct visualization of subcellular localizations of two different gene products; namely synthetic green fluorescent protein (sGFP) [196], EYFP, ECFP [203], G3 green fluorescent protein (G3GFP) [204], monomeric red fluorescent protein (mRFP) [205], and tag red fluorescent protein (TagRFP) [206]. While the epitope tags are employed to allow applications such as co-purification, co-immunoprecipitation, and western blotting analyses; namely hexahistidine tag (6xHis) [197], FLAG tag (FLAG) [198], triple HA tag (3xHA), four repeats of Myc tag (4xMyc), ten repeats of Myc tag (10xMyc) [197],

glutathione *S*-transferase (GST) [199] and T7 epitope tag (T7) [200]. All DSB and DD vectors contained MD8, a MAR of *A. thaliana* [187] upstream of Pnos of both expression cassettes (Figs. 5-1 and 5-3).

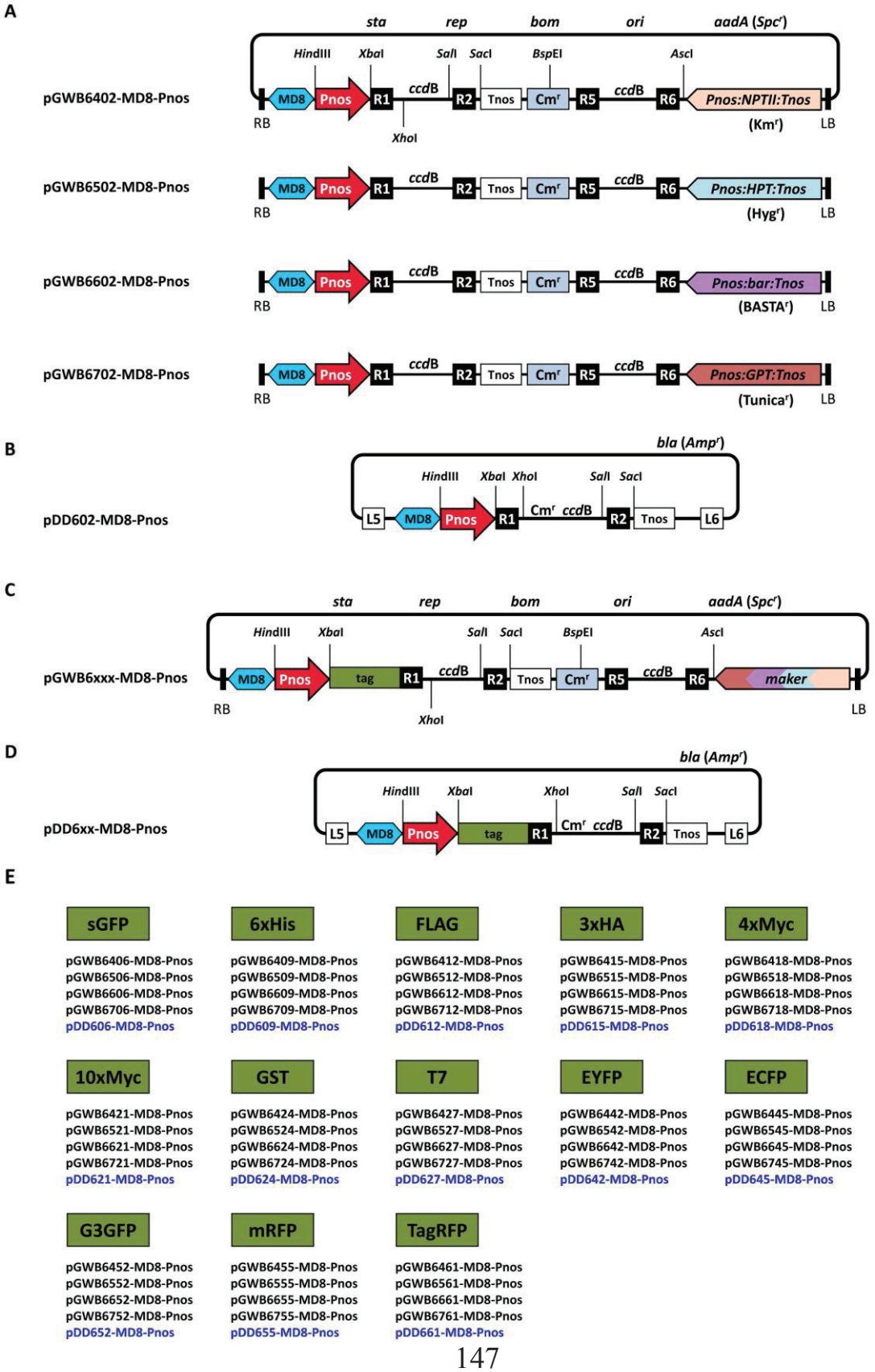

Fig. 5-1. Structures of no tag-type and N-terminal tag fusion-type vectors in the DS Gateway cloning system. (A) Illustration of the no tag-type DSB vectors. Four vectors, pGWB6402-MD8-Pnos, pGWB6502-MD8-Pnos, pGWB6602-MD8-Pnos, and pGWB6702-MD8-Pnos, with 4 different plant selection markers, were established. pGWB6402-MD8-Pnos has the neomycin phosphotransferase II (NPTII) gene for kanamycin resistance (Km^r), pGWB6502-MD8-Pnos contains the hygromycin phosphotransferase (HPT) gene for hygromycin resistance (Hyg^r), pGWB6602-MD8-Pnos has the bar gene for BASTA resistance ($BASTA^r$) and pGWB6702-MD8-Pnos contains the UDP-*N*-acetylglucosamine: dolichol phosphate *N*-acetylglucosamine-1-P transferase (GPT) gene for tunicamycin resistance ($Tunica^r$). The restriction enzyme cleavage sites were shown in the pGWB6402-MD8-Pnos. LB, left border; RB; right border; MD8, a matrix attachment region MD8 of *A. thaliana*; Pnos, nopaline synthase promoter; Tnos, nopaline synthase terminator; R1, *att*R1; R2, *att*R2; R5, *att*R5; R6, *att*R6; *ccd*B, negative selection marker for bacteria; Cm^r, chloramphenicol resistance; *aadA*, gene for spectinomycin resistance (Spc^r) in bacteria; *sta*, region conferring stability in *Agrobacterium tumefaciens*; *rep*, broad host range replication origin; *bom*, *cis*-acting element for conjugational transfer; *ori*, ColE1 replication origin (B) Illustration of no tag-type DD vector, pDD602-MD8-Pnos. L5, *att*L5; L6, *att*L6; *bla*, gene for ampicillin resistance (Amp^r) in bacteria. (C) Illustration of N-terminal tag fusion-type DSB vectors (pGWB6xxx-MD8-Pnos). These vectors are almost the same as the no tag-type vectors pGWB6x02-MD8-Pnos demonstrated in A, except for having a tag upstream of the *att*R1. (D) Illustration of N-terminal tag fusion-type pDD series (pDD6xx-MD8-Pnos). These vectors are almost the same as the no tag-type vector pDD602-MD8-Pnos demonstrated in B, except for a tag upstream of the *att*R1. (E) Different N-terminal tags in pGWB6xxx-MD8-Pnos and pDD6xx-MD8-Pnos. sGFP, synthetic green fluorescent protein; 6xHis, hexahistidine tag; FLAG, FLAG tag; 3xHA, triple HA tag; 4xMyc, four repeats of Myc tag; 10xMyc, ten repeats of Myc tag; GST, glutathione *S*-transferase; T7, T7 epitope tag; EYFP, enhanced yellow fluorescent protein; ECFP, enhanced cyan fluorescent protein; G3GFP, G3 green fluorescent protein; mRFP, monomeric red fluorescent protein; TagRFP, tag red fluorescent protein. Note that figures are not drawn to scale.

The cloning procedure and N-terminally tagging of two ORFs in the DS Gateway cloning system are shown in Fig. 5-2. Two ORF entry clones can be cloned easily and effectively into a DSB vector by two rounds of LR reactions. ORF2 is incorporated into DD vectors by the first LR reaction to obtain an intermediate clone *att*L5-MD8-Pnos-tag2-*att*B1-ORF2-*att*B2-Tnos-*att*L6 (pDD6xx-MD8-Pnos:tag2-ORF2 in Fig. 5-2). The second LR reaction (tripartite LR reaction) incorporates ORF1 and the MD8-Pnos:tag2-ORF2 expression unit into a DSB vector for preparation of the final construct MD8-Pnos-tag1-*att*B1-ORF1-*att*B2-Tnos-Cm^r-*att*B5-MD8-Pnos-tag2-*att*B1-ORF2-*att*B2-Tnos-*att*B6 (pGWB6xxx-MD8-Pnos:tag1-ORF1-Pnos:tag2-ORF2 in Fig. 5-2). Linearization of DD vectors in the first LR reaction and DSB vectors in the second LR reaction, by digestion with the proper restriction enzyme shown in Table 5-2 before the LR reactions, is recommended for efficient recombination. The DS Gateway cloning system utilizes the commonly used ORF entry clones (*att*L1-ORF-*att*L2) for the preparation of two-gene constructs, and does not require specialized entry clones such as *att*L1-ORF-*att*L4 and *att*L3-ORF-*att*L2 utilized in 2in1 cloning systems [208, 249].

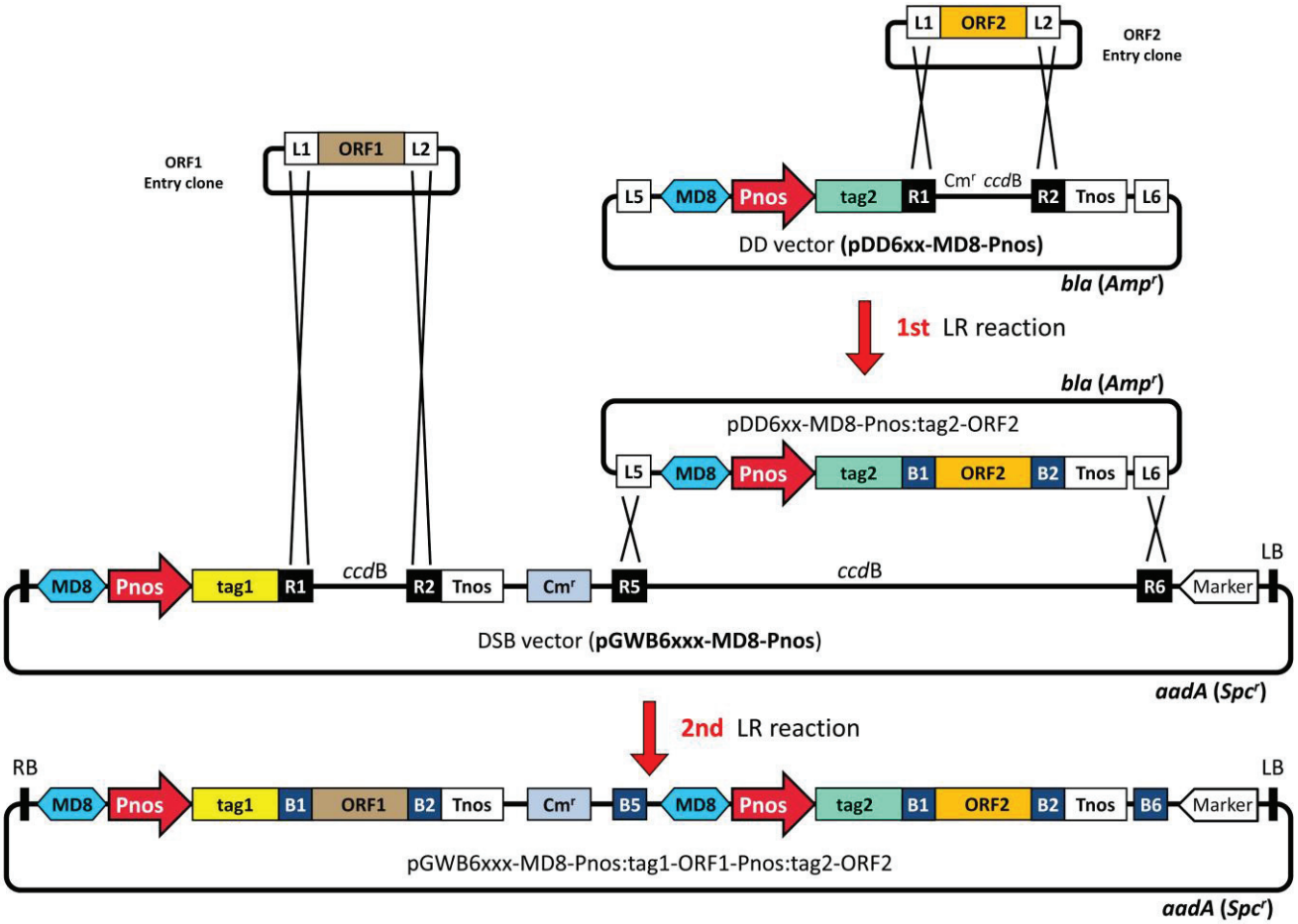

Fig. 5-2. Construction of two N-terminally tagged fusion genes using the DS Gateway cloning system. In order to assemble two expression cassettes in a DSB vector, two LR reactions are used. In the first LR reaction, ORF2 is transferred into a DD vector to make pDD6xx-MD8-Pnos:tag2-ORF2. In the second LR reaction (tripartite LR reaction), ORF1 and the obtained product of the first LR reaction are transferred into a DSB vector to make pGWB6xxx-MD8-Pnos:tag1-ORF1-Pnos:tag2-ORF2. Note that figures are not drawn to scale.

DS Gateway cloning system for BiFC assays; cloning of two ORFs with all possible tagging patterns

The author also made DSB and DD vectors for fusion with the N-terminal fragment of EYFP (nYFP) or the C-terminal fragments of EYFP (cYFP) [143] at either 5'- or 3'-terminus of ORFs (N- or C-fusion) to facilitate BiFC assays in living plant cells. Fig. 5-3 shows DSB and DD vectors for N-terminal fusion with nYFP (pGWB6x00-MD8-Pnos-NY0 and pDD600-MD8-Pnos-NY0) or with cYFP (pGWB6x00-MD8-Pnos-CY0 and pDD600-MD8-Pnos-CY0) (Fig. 5-3 A and B), and for C-terminal fusion with nYFP (pGWB6x00-MD8-Pnos-NY2 and pDD600-MD8-Pnos-NY2) or with cYFP (pGWB6x00-MD8-Pnos-CY2 and pDD600-MD8-Pnos-CY2) (Fig. 5-3 D and E). These vectors permit the construction of all possible tagging patterns of n/cYFP in a single T-DNA.

A

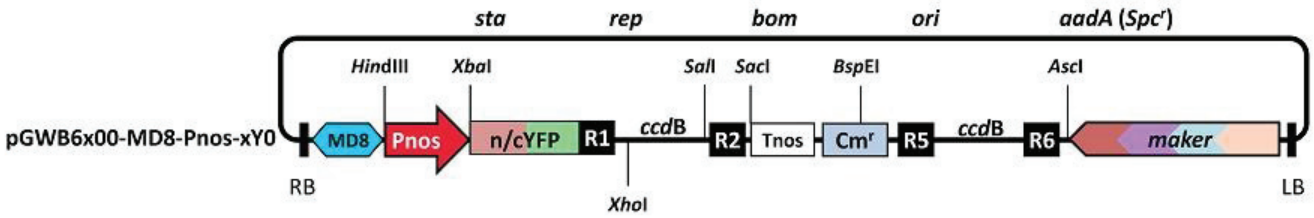

B

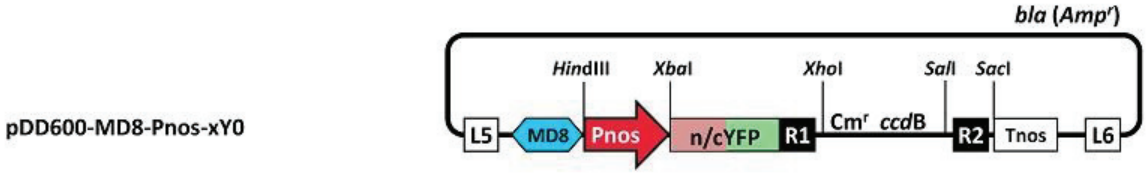

C

nYFP

pGWB6400-MD8-Pnos-NY0
pGWB6500-MD8-Pnos-NY0
pGWB6600-MD8-Pnos-NY0
pGWB6700-MD8-Pnos-NY0
pDD600-MD8-Pnos-NY0

cYFP

pGWB6400-MD8-Pnos-CY0
pGWB6500-MD8-Pnos-CY0
pGWB6600-MD8-Pnos-CY0
pGWB6700-MD8-Pnos-CY0
pDD600-MD8-Pnos-CY0

D

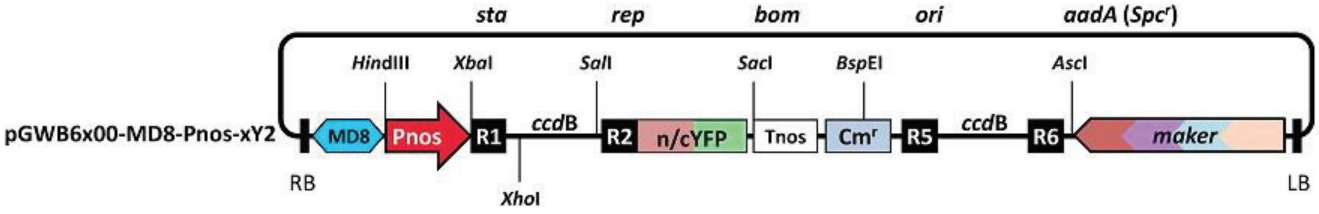

E

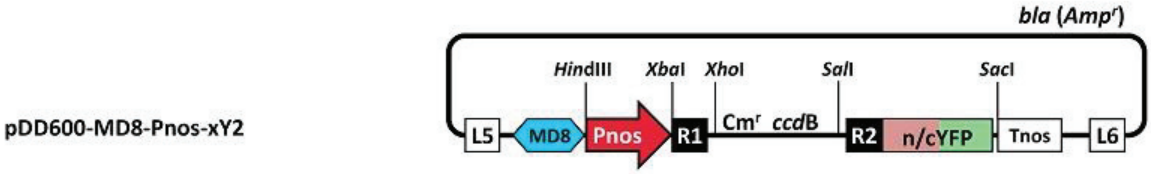

F

nYFP

pGWB6400-MD8-Pnos-NY2
pGWB6500-MD8-Pnos-NY2
pGWB6600-MD8-Pnos-NY2
pGWB6700-MD8-Pnos-NY2
pDD600-MD8-Pnos-NY2

cYFP

pGWB6400-MD8-Pnos-CY2
pGWB6500-MD8-Pnos-CY2
pGWB6600-MD8-Pnos-CY2
pGWB6700-MD8-Pnos-CY2
pDD600-MD8-Pnos-CY2

Fig. 5-3. Structure of DSB and DD vectors with fusions to N- or C-terminal fragments of EYFP (n/cYFP) for the BiFC assay. (A) Illustration of N-terminal n/cYFP fusion-type DSB vectors (pGWB6x00-MD8-Pnos-NY0 and (-CY0)). These vectors are almost the same as the no tag-type vectors pGWB6x02-MD8-Pnos demonstrated in Fig. 5-1A, except for having n/cYFP as a tag upstream of the *att*R1. (B) Illustration of N-terminal n/cYFP fusion-type DD vectors (pDD600-MD8-Pnos-NY0 and (-CY0)). These vectors are almost the same as the no tag-type vector pDD602-MD8-Pnos demonstrated in Fig. 5-1B, except for having n/cYFP as a tag upstream of the *att*R1. (C) N-terminal tags in pGWB6x00-MD8-Pnos-NY0 (-CY0) and pDD600-MD8-Pnos-NY0 (-CY0). nYFP, N-terminal fragment of enhanced yellow fluorescent protein; cYFP, C-terminal fragment of enhanced yellow fluorescent protein. (D) Illustration of C-terminal n/cYFP fusion-type DSB vectors (pGWB6x00-MD8-Pnos-NY2 and (-CY2)). These vectors are almost the same as the no tag-type vectors pGWB6x02-MD8-Pnos demonstrated in Fig. 5-1A, except for having n/cYFP as a tag downstream of the *att*R2. (E) Illustration of C-terminal n/cYFP fusion-type DD vectors (pDD600-MD8-Pnos-NY2 and (-CY2)). These vectors are almost the same as the no tag-type vector pDD602-MD8-Pnos demonstrated in Fig. 5-1B, except for having n/cYFP as a tag downstream of the *att*R2. (F) C-terminal tags in pGWB6x00-MD8-Pnos-NY2 (-CY2) and pDD600-MD8-Pnos-NY2 (-CY2). Note that figures are not drawn to scale.

The cloning procedure of two ORFs for the BiFC assay is shown in Fig. 5-4A. The main principle of the cloning procedure is similar with that in Fig. 5-2. However, both N- and C-terminal tagging is possible by these vectors. In the first LR reaction, ORF2 is cloned into a DD vector having either n/cYFP fused upstream of *att*R1 (N-fusion) or downstream of *att*R2 (C-fusion) to make one of the intermediate clones *att*L5-MD8-Pnos-n/cYFP-*att*B1-ORF2-*att*B2-Tnos-*att*L6 (N-fusion) or *att*L5-MD8-Pnos-*att*B1-ORF2-*att*B2-n/cYFP-Tnos-*att*L6 (C-fusion). In the second LR reaction, ORF1 and the obtained intermediate clone of first LR reaction are cloned into a DSB vector having either n/cYFP fused upstream of *att*R1 (N-fusion) or downstream of *att*R2 (C-fusion) to make a final binary construct with two ORFs fused in different combinations with nYFP and cYFP. All possible arrangements of tag fusions at each end should be tested in protein-protein interaction studies using BiFC systems [247, 250]. For example, YFP complementation occurred only when the PP2C-type phosphatases AP2C1 was fused with the N-terminus of n/cYFP in the BiFC assay with two members of mitogen-activated protein kinase (MAPK) family, MPK4 or MPK6 [251]. Also, it is necessary for the peroxisome targeting signal 2 to be N-terminally tagged to cYFP to function and obtain a fluorescent signal [189]. By using different combinations of pGWB6x00-MD8-Pnos-xYx and pDD600-MD8-Pnos-xYx, all the eight possible tagging patterns can be accomplished (Fig. 5-4B).

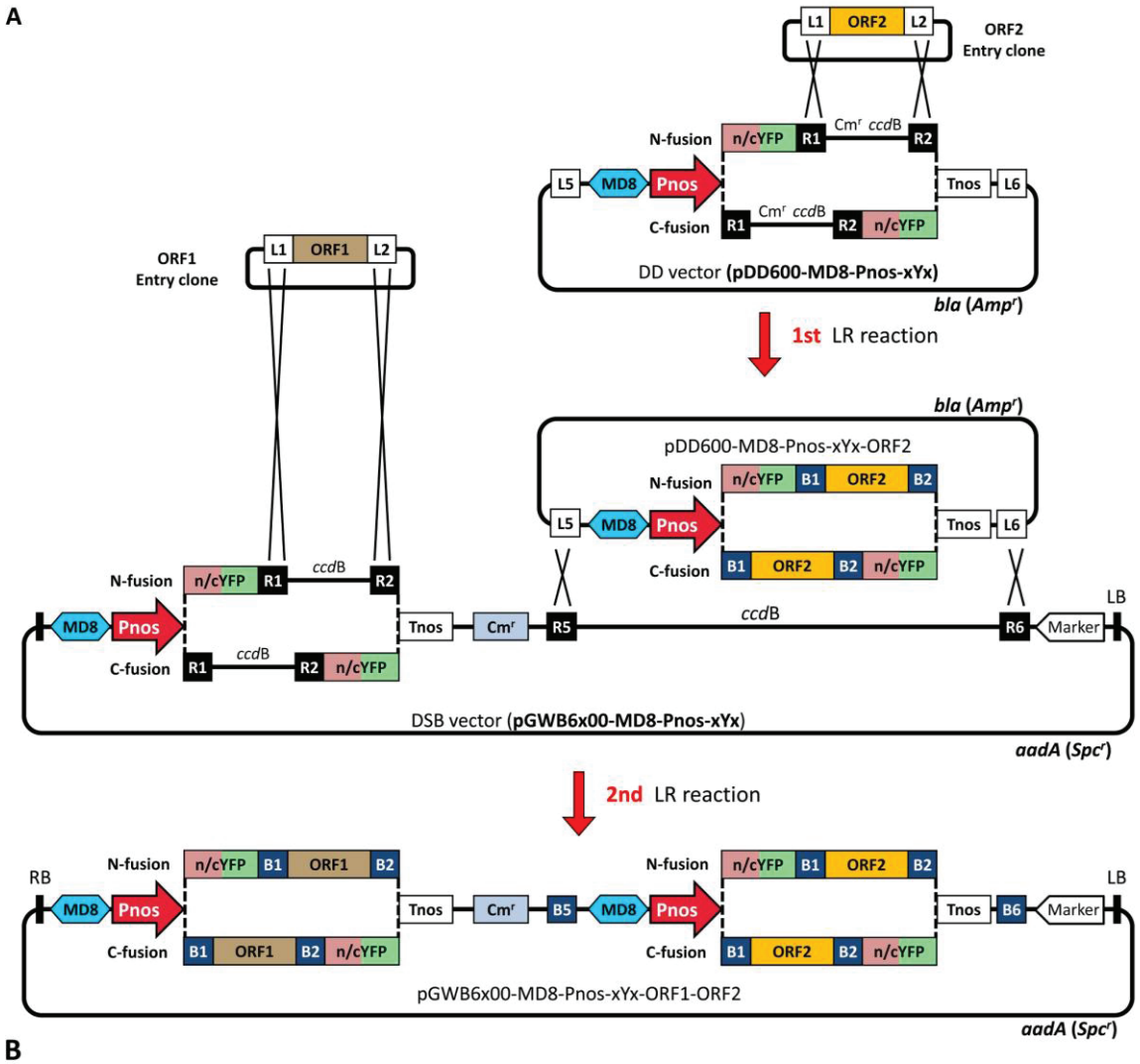
A
L1 ORF2 L2
ORF2 Entry clone
N-fusion n/cYFP R1 Cmr ccdB R2
L5 MD8 Pnos Tnos L6
C-fusion R1 Cmr ccdB R2 n/cYFP
DD vector (pDD600-MD8-Pnos-xYx)
bla (Ampr)
1st LR reaction
ORF1 Entry clone
L1 ORF1 L2
bla (Ampr)
pDD600-MD8-Pnos-xYx-ORF2
N-fusion n/cYFP B1 ORF2 B2
C-fusion B1 ORF2 B2 n/cYFP
N-fusion n/cYFP R1 ccdB R2
MD8 Pnos Tnos Cmr R5 ccdB R6 Marker LB
C-fusion R1 ccdB R2 n/cYFP
DSB vector (pGWB6x00-MD8-Pnos-xYx)
aadA (Spcr)
2nd LR reaction
RB
N-fusion n/cYFP B1 ORF1 B2
MD8 Pnos Tnos Cmr B5 MD8 Pnos Tnos B6 Marker LB
C-fusion B1 ORF1 B2 n/cYFP
N-fusion n/cYFP B1 ORF2 B2
C-fusion B1 ORF2 B2 n/cYFP
pGWB6x00-MD8-Pnos-xYx-ORF1-ORF2
aadA (Spcr)
B
N-N fusions
C-C fusions
N-C fusions
C-N fusions

Fig. 5-4 Two-gene cloning for the BiFC assay and possible tagging combinations with n/cYFP in the DS Gateway cloning system. (A) The cloning strategy of two ORFs in the DS Gateway cloning system for the BiFC assay. The principal idea for cloning of two ORFs in the DS Gateway cloning system for the BiFC assay is similar to that illustrated in Fig. 5-2 but with a possibility for both N- and C-terminal tagging. (B) Possible tagging patterns in the DS Gateway cloning system for the BiFC assay. The eight different patterns of tagging with n- and cYFP resulted from using different combinations of pGWB6x00-MD8-Pnos-xYx and pDD600-MD8-Pnos-xYx vectors are illustrated. Note that figures are not drawn to scale.

DS Gateway cloning system effectively enables cloning and stable co-expression of two genes for localization analysis in A. thaliana

To evaluate the flexibility of the DS Gateway cloning system in two-gene expression analyses, the author made two binary constructs Pnos:EYFP-AtSYP31-Pnos:ECFP-AtSYP43 and Pnos:EYFP-AtSYP43-Pnos:ECFP-AtSYP31 using pDONR201-AtSYP31, pDONR201-AtSYP43, pDD645-MD8-Pnos and pGWB6642-MD8-Pnos (Fig. 5-5A and B). Many SNARE proteins are known to serve as organelle markers because of their specific and distinct subcellular localization to particular organelles. AtSYP31 and AtSYP43 are two SNAREs being localized specifically to the *cis*-Golgi and the *trans*-Golgi network (TGN), respectively, in *A. thaliana* [154, 252]. The obtained two constructs were analyzed by digestion with *Hin*dIII and *Sac*I to confirm their structure. As shown in Fig. 5-5C, restriction fragments of expected sizes (Fig. 5-5A and B) were observed after the digestion with *Hin*dIII and *Sac*I, indicating correct cloning of AtSYP31 and AtSYP43 genes into a DSB vector. The two binary constructs were introduced into *A. thaliana* using Agrobacterium-mediated transformation.

Confocal microscopy was performed to analyze the expression and subcellular localization of the two SNAREs in *A. thaliana* plants. Firstly, the author analyzed the co-expression efficiency of these two fusion proteins and found all BASTA-resistant T1 and T2 plants have shown both YFP and CFP fluorescence, indicating the capability of the DS Gateway cloning system for efficient and reliable expression of two genes in transgenic plants. Next, the author observed their subcellular localization in detail. Both combinations, EYFP-AtSYP31+ECFP-AtSYP43 and EYFP-AtSYP43+ECFP-AtSYP31, have exhibited the expected subcellular localization patterns in the *A. thaliana* root cells as distinct dot-like structures. Some molecules of AtSYP43 were present in close vicinity to those of AtSYP31 but not completely overlapped (Fig. 5-6). These results were in agreement with a previous work in which subcellular localizations of the *cis*-Golgi-marker AtSYP31 and the TGN-

marker AtSYP41 were analyzed by transient expression in the protoplast of *A. thaliana* cultured cells [252]. They also reported the co-localization of AtSYP41 and AtSYP43. The author successfully generated *A. thaliana* transgenic lines expressing both the *cis*-Golgi and the TGN markers visualized by EYFP and ECFP. Such transgenic lines are expected to be useful for examining the detailed localization patterns of uncharacterized proteins in Golgi apparatus by fusions with other fluorescent proteins such as GFP or RFP.

A

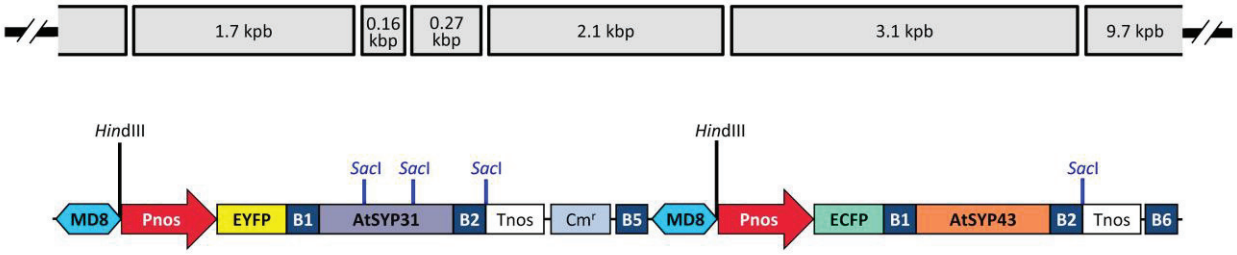

B

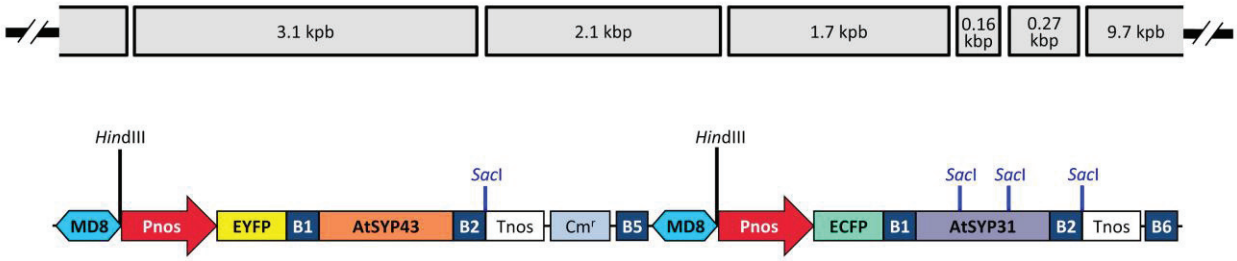

C

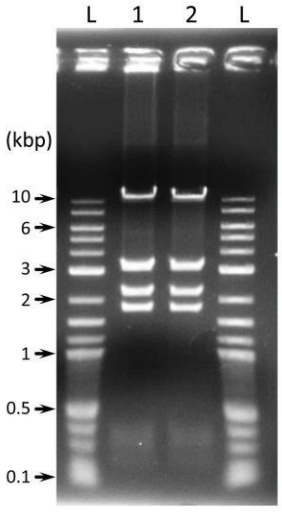

Fig. 5-5 Demonstration of two-gene constructs in pGWB6642-MD8-Pnos and confirmation of their structures. (A) Illustration of pGWB6642-MD8-Pnos carrying AtSYP31 in the first cloning site (cloning site upstream of Cm^r) and AtSYP43 in the second cloning site (cloning site downstream of Cm^r) (Pnos:EYFP-AtSYP31-Pnos:ECFP-AtSYP43) and expected sizes of fragments after the digestion with *Hin*dIII and *Sac*I. (B) Illustration of pGWB6642-MD8- Pnos carrying AtSYP43 in the first cloning site and AtSYP31 in the second cloning site (Pnos:EYFP-AtSYP43-Pnos:ECFP-AtSYP31) and expected sizes of fragments after the digestion with *Hin*dIII and *Sac*I. The size of resulting fragments is shown in kilobase pairs (kbp) (upper panel of A and B). The cleavage sites, which are recognized with *Hin*dIII and *Sac*I are shown in both constructs (lower panel of A and B). (C) Analysis of *Hin*dIII- and *Sac*I-digested fragments on 1.0% agarose gel. Lanes L show 2-log DNA ladder (New England Biolabs, Massachusetts, USA). Lanes 1 and 2 show the two-gene construct represented in A and B, respectively. The fragments equal 10, 6, 3, 2, 1, 0.5 and 0.1 kbp are indicated.

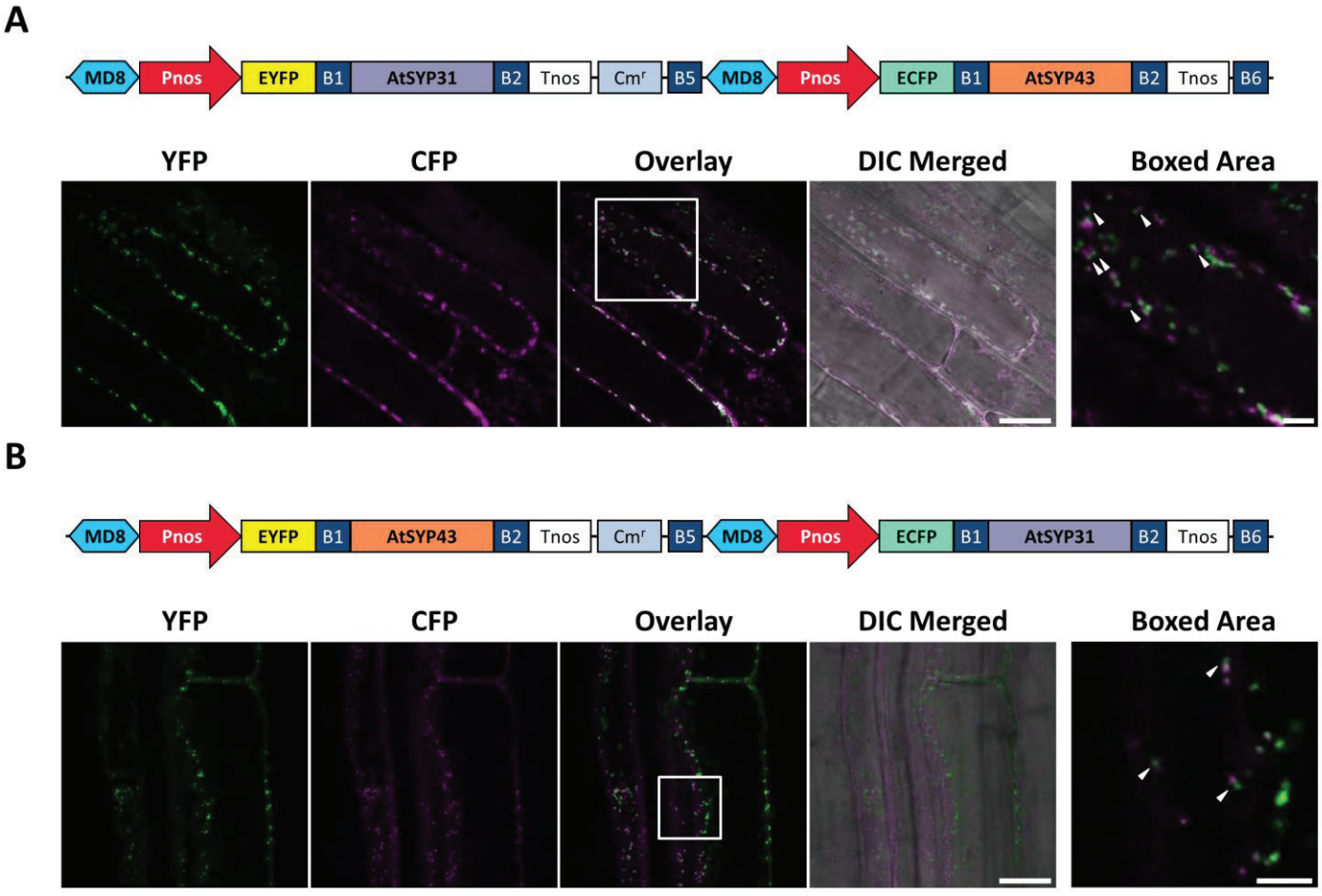

Fig. 5-6 Analysis of co-expression and subcellular localization of two SNAREs in a stable expression system using *A. thaliana*. (A) Structural diagram of Pnos:EYFP-AtSYP31-Pnos:ECFP-AtSYP43 construct (upper panel) and representative fluorescent images in *A. thaliana* root epidermal cells (lower panel). (B) Structural diagram of Pnos:EYFP-AtSYP43-Pnos:ECFP-AtSYP31 construct (upper panel) and representative fluorescent images in *A. thaliana* root epidermal cells (lower panel). YFP, signal of EYFP; CFP, signal of ECFP; Overlay, overlay of EYFP and ECFP signals; DIC Merged, differential interference contrast (DIC) merged with EYFP and ECFP; Boxed Area, enlargement of the boxed area in overlay. Bars: 20 µm. Bar in Boxed Area: 5 µm.

Detection of protein-protein interaction by BiFC using transient and stable expression systems

SEC31 and SEC13 are cage subunits of COPII, and they cooperate with other COPII members to form a coat complex for transport of cargo proteins from the endoplasmic reticulum to the Golgi apparatus in budding yeast [253]. *A. thaliana* genome contains two homologs of SEC31, AtSEC31A (AT1G18830) and AtSEC31B (AT3G63460), and two homologs of SEC13, AtSEC13A (AT2G30050) and AtSEC13B (AT3G01340). The interaction between AtSEC31B and AtSEC13A (or AtSEC13B) by BiFC was previously reported using transient expression systems [138, 143]. However, to the author's knowledge, the interaction between these proteins has not yet been performed in any stable expression system. In order to confirm availability of the DS Gateway cloning system for detection of protein-protein interactions in both transient and stable expression systems, the author applied AtSEC31B and AtSEC13s for the BiFC assay in Japanese leek and *A. thaliana*. The author made three binary constructs Pnos:AtSEC31B-nYFP-Pnos:AtSEC13A-cYFP, Pnos:AtSEC31B-nYFP-Pnos:AtSEC13B-cYFP and Pnos:AtSEC31B-nYFP-Pnos:GUS-cYFP (Figs. 5-7 and 5-8) using pDONR201-AtSEC31B, pDONR201-AtSEC13A, pDONR201-AtSEC13B, pDONR201-GUS, pDD600-MD8-Pnos-CY2 and pGWB6400-MD8-Pnos-NY2. Appropriate negative controls are required to distinguish the specific protein-protein interactions from non-specific ones. The author used GUS, an unrelated non-interacting protein as a negative control. In the transient expression experiment, the author bombarded a two-gene construct with pUGW45 (P35S:CFP; for identification of bombarded cells) into epidermal cells of Japanese leek and observed the fluorescence by confocal microscopy. Reconstituted YFP fluorescence signals were detected in the interacting couples AtSEC31B-nYFP and AtSEC13A-cYFP, and AtSEC31B-nYFP and AtSEC13B-cYFP (Fig. 5-7A, B) but not in case of the AtSEC31B-nYFP and GUS-cYFP couple (Fig. 5-7C). Unlike the CFP being detected in both nuclei and cytoplasm, reconstituted YFP was excluded from nuclei and localized only in the cytoplasm, indicating that interaction of AtSEC31B and AtSEC13s occurred only in the cytoplasm as shown previously [143].

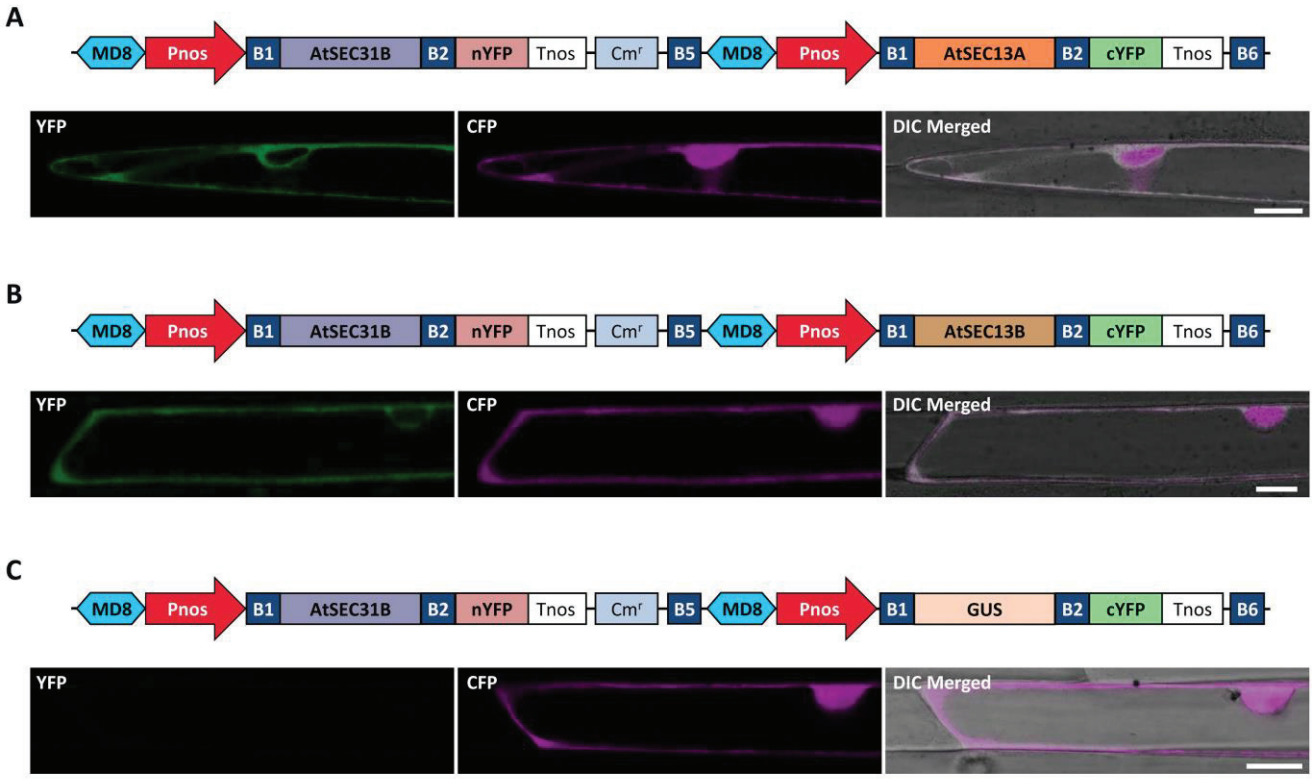

Fig. 5-7 Analysis of interactions between AtSEC31B and AtSEC13s by the BiFC assay in a transient expression system using Japanese leek. (A-C) Observation of fluorescent signals from reconstituted EYFP in Japanese leek epidermal cells. (A) AtSEC31B-nYFP with AtSEC13A-cYFP. (B) AtSEC31B-nYFP with AtSEC13B-cYFP. (C) AtSEC31B-nYFP with GUS-cYFP. Upper panels show the structural diagram of two-gene construct assembled in pGWB6400-MD8-Pnos-NY2 and bombarded into leek epidermal cells. Lower panels show representative fluorescent images by confocal microscopy. ECFP signals represent internal reference of bombardment. YFP, signal of EYFP; CFP, signal of ECFP; DIC Merged, differential interference contrast (DIC) merged with EYFP and ECFP. Bars: 20 µm.

Next, the author performed a BiFC assay to confirm the interaction of AtSEC31B with AtSEC13s in *A. thaliana* plants stably expressing those couples. The author detected the interaction of AtSEC31B with both AtSEC13A and AtSEC13B as a reconstituted YFP fluorescence observed in *A. thaliana* root cells including root hairs (Fig. 5-8A, B) while no interaction was detected between AtSEC31B and GUS (Fig. 5-8C), being consistent with the results obtained from the BiFC assay in the transient expression system.

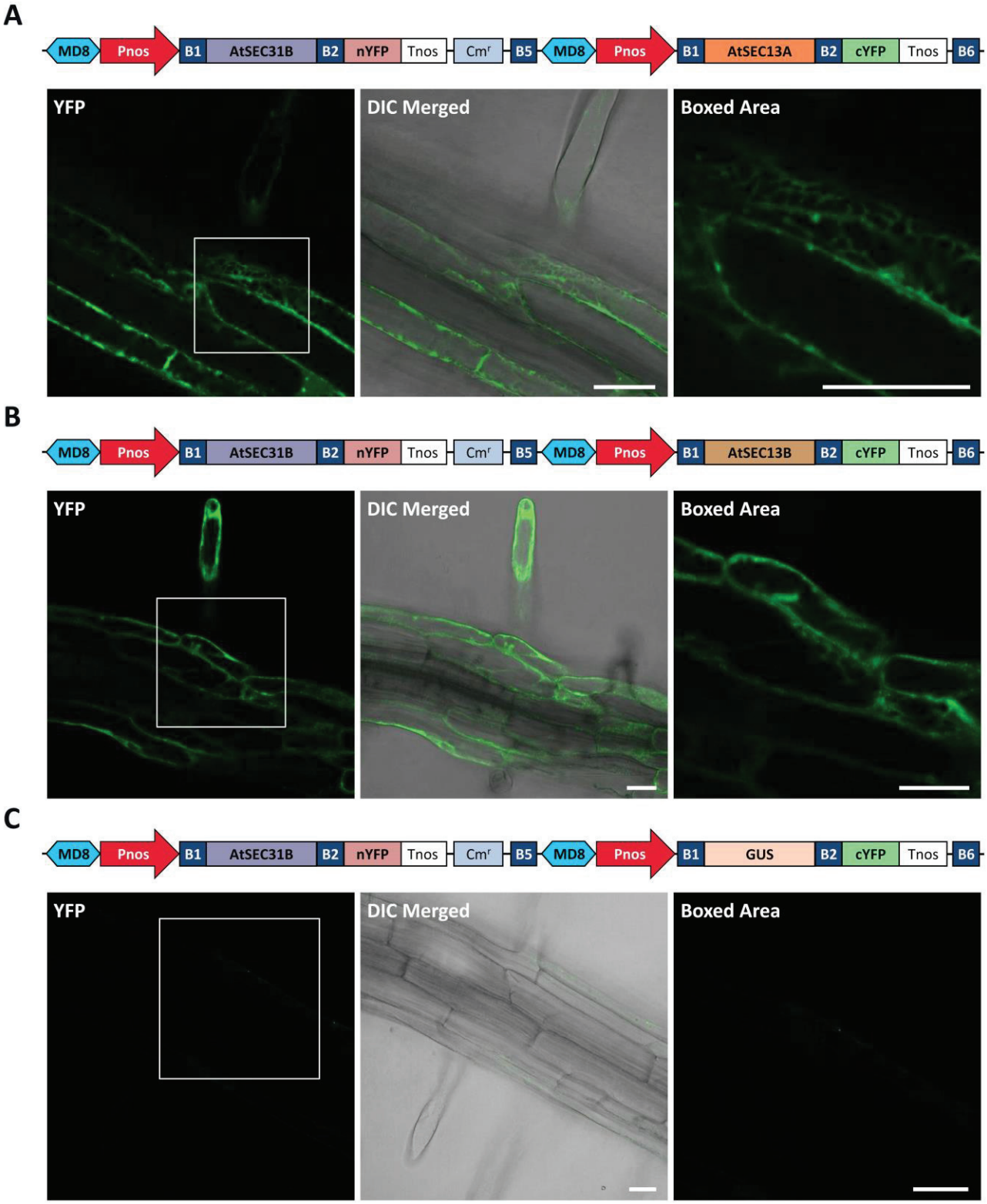

Fig. 5-8 Analysis of interaction between AtSEC31B and AtSEC13s by the BiFC assay in a stable **expression system using *A. thaliana*.** (A-C) Observation of fluorescent signals from reconstituted EYFP in root epidermal cells. (A) AtSEC31B-nYFP with AtSEC13A-cYFP. (B) AtSEC31B-nYFP with AtSEC13B-cYFP. (C) AtSEC31B-nYFP with GUS-cYFP. Upper panels show the structural diagram of two-gene construct assembled in pGWB6400-MD8-Pnos-NY2 and introduced into *A. thaliana* by Agrobacterium-mediated transformation. Lower panels show representative fluorescent images by confocal microscopy. YFP, signal of EYFP; DIC Merged, differential interference contrast merged with EYFP; Boxed Area, enlargement of the boxed area in YFP. Bars: 30 μm.

Although many vector systems were constructed to facilitate the BiFC assay in plants, only two systems have enabled the analysis of interactions between proteins expressed through a single T-DNA [249, 254]. Compared to those, the DS Gateway cloning system has an advantage of availability for Gateway cloning with commonly used entry clones; hence n/cYFP can be fused to either N- or C-terminus of the candidate two proteins simultaneously by LR reactions. The results showed that the DS Gateway cloning system is a simple and powerful tool for detecting protein-protein interactions between partner proteins assembled on a single T-DNA using the BiFC assay in both transient and stable expression systems.

In this study, the author demonstrated the construction and validation of a versatile vector system named "DS Gateway cloning system" that facilitates the cloning of two genes simultaneously on a single T-DNA by LR reactions with commonly used entry clones (attL1-ORF-attL2) accumulated in the research community. The binary vectors of four selection marker-series (Kmr, Hygr, BASTAr, Tunicar) can be used for various plant transformation experiments. The two cloned genes are constitutively expressed by Pnos which is suitable for localization analysis. Fusion with a wide range of fluorescent proteins and epitope tags are available in the DS Gateway cloning system for direct visualization of gene products, co-purification, co-immunoprecipitation and western blotting analyses. The author showed high performance of the DS Gateway cloning system in cloning and expression experiments in Japanese leek and A. thaliana. The DS Gateway cloning system is an effective multipurpose tool in plant genetic research, enables the simultaneous co-expression of two genes, the co-localization analysis of two proteins, and facilitates the investigation of protein-protein interactions in vivo by BiFC not only in transient expression systems including biolistic bombardment, protoplast transformation, and agroinfiltration but also in transgenic plants stably expressing these proteins.

Chapter 6

Proposed conclusions

The author proposes the conclusions of this thesis as follows:

(i) Several mutants with a range of defects in anther/pollen development and exine wall formation were recovered, some of them showing novel phenotypes.

The large scale screening (~ 10,000) using scanning electron microscopy at a high-magnification level was successful to isolate multiple mutant plants defective in anther/pollen development and exine wall formation. This screening strategy was effective to isolate mutants with mild defects in the exine surface structure that would be neglected with using other screening strategies e.g., visual screen by the naked eye, dissecting microscope-based, or confocal microscope-based screens.

(ii) Twenty-three mutations were successfully mapped to specific regions of particular chromosomes of the Arabidopsis genome.

The identification of the mutation location was performed by bulked-segregant analysis using a high-throughput sequencing technique (next generation sequencing) rather than using the traditional mapping methods. Only in one case, the identification was identified by capillary sequencing in the *quartet-like* mutant.

(iii) The isolated mutants provide an additional resource for plant researchers.

Characterization and analyzing of the genes responsible for these mutants will help to dissect the processes of anther/pollen development and exine wall formation.

(iv) *AtSEC23A* and *AtSEC23D* are required for proper pollen wall formation, exine patterning, and tapetum development.

Single *atsec23a and atsec23d* mutant plants exhibited a compromised pollen wall formation with less sporopollenin deposition in the outer exine layer. Double *atsec23ad* mutant plants showed defective pollen walls, and altered development of tapetal cells with morphological abnormalities of the ER, Golgi, elaioplasts, and tapetosomes.

(v) *AtSEC23A* and *AtSEC23D* may organize pollen wall development and exine patterning by regulating ER export of lipid and proteins necessary for pollen wall formation in tapetal cells.

AtSEC23A and *AtSEC23D* were highly expressed in the tapetal cells. *AtSEC23A* and *AtSEC23D* are functional COPII proteins exhibiting the characteristic COPII localization at

ER exit sites. To investigate the expression and co-localization patterns of *AtSEC23A* and *AtSEC23D* necessitate developing new systems to deliver the two expression cassettes simultaneously.

(vi) The developed vector systems are valuable experimental tools with multiple applications in plant research.

The author successfully developed two new vector systems named R4DS Gateway cloning system and DS Gateway cloning system. These two systems have multiple flexibility features, e.g., multiple types of tags and 4 kinds of plant selection markers. Both systems are effective multipurpose tools in plant research, enabling the simultaneous co-expression of two genes, the co-localization analysis of two proteins, and facilitating the investigation of protein-protein interactions *in vivo* by BiFC or co-immunoprecipitation.

(vii) The developed vector systems are suitable for exploring the functions and molecular mechanisms underlying various biological processes including pollen development and exine wall formation.

The R4DS cloning system was successfully used in exploring the expression and co-localizations patterns of two Arabidopsis genes required for pollen wall development, *AtSEC23A* and *AtSEC23D*, as well as in the co-localization of each of *AtSEC23A* and *AtSEC23D* with other organelle markers (e.g., endoplasmic reticulum, Golgi, and plastid markers).

References

1. Alonso-Blanco, C., and Koornneef, M. (2000). Naturally occurring variation in *Arabidopsis*: an underexploited resource for plant genetics. Trends in plant science *5*, 22-29.
2. Hoffmann, M.H. (2002). Biogeography of *Arabidopsis thaliana* (L.) Heynh.(Brassicaceae). Journal of Biogeography *29*, 125-134.
3. Al-Shehbaz, I.A., and O'Kane Jr, S.L. (2002). Taxonomy and phylogeny of *Arabidopsis* (Brassicaceae). The Arabidopsis book/American Society of Plant Biologists *1*.
4. Meinke, D.W., Cherry, J.M., Dean, C., Rounsley, S.D., and Koornneef, M. (1998). Arabidopsis thaliana: A model plant for genome analysis. Science *282*, 662-682.
5. Koornneef, M., and Meinke, D. (2010). The development of *Arabidopsis* as a model plant. The plant journal *61*, 909-921.
6. Alonso, J.M., Stepanova, A.N., Leisse, T.J., Kim, C.J., Chen, H., Shinn, P., Stevenson, D.K., Zimmerman, J., Barajas, P., Cheuk, R., et al. (2003). Genome-wide insertional mutagenesis of *Arabidopsis thaliana*. Science *301*, 653-657.
7. Laibach, F. (1943). *Arabidopsis thaliana* (L.) Heynh. als Objekt für genetische und entwicklungsphysiologische Untersuchungen. Bot. Archiv *44*, 439-455.
8. Meyerowitz, E.M. (1989). *Arabidopsis*, a useful weed. Cell *56*, 263-269.
9. Meyerowitz, E.M., and Pruitt, R.E. (1985). *Arabidopsis thaliana* and plant molecular genetics. Science *229*, 1214-1218.
10. Clough, S.J., and Bent, A.F. (1998). Floral dip: a simplified method for Agrobacterium-mediated transformation of Arabidopsis thaliana. The Plant Journal *16*, 735-743.
11. Arabidopsis Genome Initiative (2000). Analysis of the genome sequence of the flowering plant *Arabidopsis thaliana*. Nature *408*, 796.
12. Greene, E.A., Codomo, C.A., Taylor, N.E., Henikoff, J.G., Till, B.J., Reynolds, S.H., Enns, L.C., Burtner, C., Johnson, J.E., Odden, A.R., et al. (2003). Spectrum of chemically induced mutations from a large-scale reverse-genetic screen in Arabidopsis. Genetics *164*, 731-740.

13. Li, X., Song, Y., Century, K., Straight, S., Ronald, P., Dong, X., Lassner, M., and Zhang, Y. (2001). A fast neutron deletion mutagenesis-based reverse genetics system for plants. The Plant Journal *27*, 235-242.
14. Sundaresan, V., Springer, P., Volpe, T., Haward, S., Jones, J.D., Dean, C., Ma, H., and Martienssen, R. (1995). Patterns of gene action in plant development revealed by enhancer trap and gene trap transposable elements. Genes & development *9*, 1797-1810.
15. Kim, Y., Schumaker, K.S., and Zhu, J.-K. (2006). EMS Mutagenesis of Arabidopsis. In Arabidopsis Protocols, J. Salinas and J.J. Sanchez-Serrano, eds. (Totowa, NJ: Humana Press), pp. 101-103.
16. Maple, J., and Moller, S.G. (2007). Mutagenesis in Arabidopsis. In Circadian Rhythms: Methods and Protocols, E. Rosato, ed. (Totowa, NJ: Humana Press), pp. 197-206.
17. Krysan, P.J., Young, J.C., and Sussman, M.R. (1999). T-DNA as an insertional mutagen in Arabidopsis. The Plant Cell *11*, 2283-2290.
18. Liu, Y.-G., Mitsukawa, N., Oosumi, T., and Whittier, R.F. (1995). Efficient isolation and mapping of Arabidopsis thaliana T-DNA insert junctions by thermal asymmetric interlaced PCR. The Plant Journal *8*, 457-463.
19. Krysan, P.J., Young, J.C., Tax, F., and Sussman, M.R. (1996). Identification of transferred DNA insertions within Arabidopsis genes involved in signal transduction and ion transport. Proceedings of the National Academy of Sciences of the United States of America *93*, 8145-8150.
20. De Muyt, A., Pereira, L., Vezon, D., Chelysheva, L., Gendrot, G., Chambon, A., Lainé-Choinard, S., Pelletier, G., Mercier, R., Nogué, F., et al. (2009). A high throughput genetic screen identifies new early meiotic recombination functions in Arabidopsis thaliana. PLOS Genetics *5*, e1000654.
21. Dobritsa, A.A., Geanconteri, A., Shrestha, J., Carlson, A., Kooyers, N., Coerper, D., Urbanczyk-Wochniak, E., Bench, B.J., Sumner, L.W., Swanson, R., et al. (2011). A large-scale genetic screen in Arabidopsis to identify genes involved in pollen exine production. Plant Physiology *157*, 947-970.
22. Krieg, D.R. (1963). Ethyl methanesulfonate-induced reversion of bacteriophage T4rii mutants. Genetics *48*, 561-580.
23. Goldberg, R.B., Beals, T.P., and Sanders, P.M. (1993). Anther development: basic principles and practical applications. The Plant Cell *5*, 1217-1229.

24. Sanders, P.M., Bui, A.Q., Weterings, K., McIntire, K.N., Hsu, Y.-C., Lee, P.Y., Truong, M.T., Beals, T.P., and Goldberg, R.B. (1999). Anther developmental defects in Arabidopsis thaliana male-sterile mutants. Sexual Plant Reproduction *11*, 297-322.
25. Bedinger, P. (1992). The remarkable biology of pollen. The Plant Cell *4*, 879-887.
26. Blackmore, S., Wortley, A.H., Skvarla, J.J., and Rowley, J.R. (2007). Pollen wall development in flowering plants. New Phytologist *174*, 483-498.
27. Suzuki, T., Masaoka, K., Nishi, M., Nakamura, K., and Ishiguro, S. (2008). Identification of kaonashi mutants showing abnormal pollen exine structure in Arabidopsis thaliana. Plant and Cell Physiology *49*, 1465-1477.
28. Ariizumi, T., and Toriyama, K. (2011). Genetic regulation of sporopollenin synthesis and pollen exine development. Annual review of plant biology *62*, 437-460.
29. Paxson-Sowders, D., Owen, H., and Makaroff, C. (1997). A comparative ultrastructural analysis of exine pattern development in wild-typeArabidopsis and a mutant defective in pattern formation. Protoplasma *198*, 53-65.
30. Zhou, Q., Zhu, J., Cui, Y.-L., and Yang, Z.-N. (2015). Ultrastructure analysis reveals sporopollenin deposition and nexine formation at early stage of pollen wall development in Arabidopsis. Science Bulletin *60*, 273-276.
31. Quilichini, T.D., Douglas, C.J., and Samuels, A.L. (2014). New views of tapetum ultrastructure and pollen exine development in Arabidopsis thaliana. Annals of Botany *114*, 1189-1201.
32. Matsuoka, K., Orci, L., Amherdt, M., Bednarek, S.Y., Hamamoto, S., Schekman, R., and Yeung, T. (1998). COPII-coated vesicle formation reconstituted with purified coat proteins and chemically defined liposomes. Cell *93*, 263-275.
33. Lord, C., Ferro-Novick, S., and Miller, E.A. (2013). The highly conserved COPII coat complex sorts cargo from the endoplasmic reticulum and targets it to the Golgi. Cold Spring Harbor Perspectives in Biology *5*.
34. Nakano, A., Brada, D., and Schekman, R. (1988). A membrane glycoprotein, Sec12p, required for protein transport from the endoplasmic reticulum to the Golgi apparatus in yeast. The Journal of Cell Biology *107*, 851-863.
35. Barlowe, C., and Schekman, R. (1993). SEC12 encodes a guanine-nucleotide-exchange factor essential for transport vesicle budding from the ER. Nature *365*, 347-349.
36. Bi, X., Corpina, R.A., and Goldberg, J. (2002). Structure of the Sec23/24-Sar1 pre-budding complex of the COPII vesicle coat. Nature *419*, 271-277.

37. Shaywitz, D.A., Espenshade, P.J., Gimeno, R.E., and Kaiser, C.A. (1997). COPII subunit interactions in the assembly of the vesicle coat. Journal of Biological Chemistry *272*, 25413-25416.

38. Bi, X., Mancias, J.D., and Goldberg, J. (2007). Insights into COPII coat nucleation from the structure of Sec23•Sar1 complexed with the active fragment of Sec31. Developmental Cell *13*, 635-645.

39. Hartley, J.L., Temple, G.F., and Brasch, M.A. (2000). DNA cloning using in vitro site-specific recombination. Genome Research *10*, 1788-1795.

40. Walhout, A.J., Temple, G.F., Brasch, M.A., Hartley, J.L., Lorson, M.A., van den Heuvel, S., and Vidal, M. (2000a). GATEWAY recombinational cloning: application to the cloning of large numbers of open reading frames or ORFeomes. Methods in enzymology *328*, 575-592.

41. Sasaki, Y., Sone, T., Yoshida, S., Yahata, K., Hotta, J., Chesnut, J.D., Honda, T., and Imamoto, F. (2004). Evidence for high specificity and efficiency of multiple recombination signals in mixed DNA cloning by the multisite gateway system. Journal of Biotechnology *107*, 233-243.

42. Cheo, D.L., Titus, S.A., Byrd, D.R., Hartley, J.L., Temple, G.F., and Brasch, M.A. (2004). Concerted assembly and cloning of multiple DNA segments using in vitro site-specific recombination: functional analysis of multi-segment expression clones. Genome research *14*, 2111-2120.

43. Buntru, M., Gärtner, S., Staib, L., Kreuzaler, F., and Schlaich, N. (2013). Delivery of multiple transgenes to plant cells by an improved version of MultiRound Gateway technology. Transgenic Research *22*, 153-167.

44. Ren, F., Chen, Q.-J., Xie, M., Li, L.-J., Wu, W.-H., Chen, J., and Wang, X.-C. (2010). Engineering the K+ uptake regulatory pathway by MultiRound Gateway. Journal of Plant Physiology *167*, 1412-1417.

45. Kimura, T., Nakao, A., Murata, S., Kobayashi, Y., Tanaka, Y., Shibahara, K., Kawazu, T., and Nakagawa, T. (2013). Development of the gateway recycling cloning system for multiple linking of expression cassettes in a defined order, and direction on gateway compatible binary vectors. Bioscience, Biotechnology, and Biochemistry *77*, 430-434.

46. Pillitteri, L.J., Bogenschutz, N.L., and Torii, K.U. (2008). The bHLH protein, MUTE, controls differentiation of stomata and the hydathode pore in Arabidopsis. Plant and Cell Physiology *49*, 934-943.

47. Bergmann, D.C., and Sack, F.D. (2007). Stomatal development. Annu. Rev. Plant Biol. *58*, 163-181.
48. Nadeau, J.A., and Sack, F.D. (2002). Stomatal development in Arabidopsis. The Arabidopsis book/American Society of Plant Biologists *1*, e0066.
49. Pillitteri, L.J., and Torii, K.U. (2012). Mechanisms of stomatal development. Annual review of plant biology *63*, 591-614
50. Serna, L. (2009). Emerging parallels between stomatal and muscle cell lineages. Plant physiology *149*, 1625-1631.
51. Pillitteri, L.J., and Dong, J. (2013). Stomatal development in Arabidopsis. The Arabidopsis book/American Society of Plant Biologists *11*.
52. Owen, H.A., and Makaroff, C. (1995). Ultrastructure of microsporogenesis and microgametogenesis in Arabidopsis thaliana (L.) Heynh. ecotype Wassilewskija (Brassicaceae). Protoplasma *185*, 7-21.
53. Smyth, D.R., Bowman, J.L., and Meyerowitz, E.M. (1990). Early flower development in Arabidopsis. The Plant Cell *2*, 755-767.
54. de Azevedo Souza, C., Kim, S.S., Koch, S., Kienow, L., Schneider, K., McKim, S.M., Haughn, G.W., Kombrink, E., and Douglas, C.J. (2009). A novel fatty Acyl-CoA synthetase is required for pollen development and sporopollenin biosynthesis in Arabidopsis. The Plant Cell *21*, 507-525.
55. Dong, X., Hong, Z., Sivaramakrishnan, M., Mahfouz, M., and Verma, D.P.S. (2005). Callose synthase (CalS5) is required for exine formation during microgametogenesis and for pollen viability in Arabidopsis. The Plant Journal *42*, 315-328.
56. Aarts, M.G., Hodge, R., Kalantidis, K., Florack, D., Wilson, Z.A., Mulligan, B.J., Stiekema, W.J., Scott, R., and Pereira, A. (1997). The Arabidopsis MALE STERILITY 2 protein shares similarity with reductases in elongation/condensation complexes. The Plant Journal *12*, 615-623.
57. Morant, M., Jorgensen, K., Schaller, H., Pinot, F., Moller, B.L., Werck-Reichhart, D., and Bak, S. (2007). CYP703 is an ancient Cytochrome P450 in land plants catalyzing in-chain hydroxylation of lauric acid to provide building blocks for sporopollenin synthesis in pollen. The Plant Cell *19*, 1473-1487.
58. Dobritsa, A.A., Shrestha, J., Morant, M., Pinot, F., Matsuno, M., Swanson, R., Moller, B.L., and Preuss, D. (2009). CYP704B1 is a long-chain fatty acid ω-hydroxylase essential for sporopollenin synthesis in pollen of Arabidopsis. Plant Physiology *151*, 574-589.

59. Zhang, Z.-B., Zhu, J., Gao, J.-F., Wang, C., Li, H., Li, H., Zhang, H.-Q., Zhang, S., Wang, D.-M., Wang, Q.-X., et al. (2007). Transcription factor AtMYB103 is required for anther development by regulating tapetum development, callose dissolution and exine formation in Arabidopsis. The Plant Journal *52*, 528-538.

60. Garcia, V., Bruchet, H., Camescasse, D., Granier, F., Bouchez, D., and Tissier, A. (2003). AtATM is essential for meiosis and the somatic response to DNA damage in plants. The Plant Cell *15*, 119-132.

61. Preuss, D., Rhee, S., and Davis, R. (1994). Tetrad analysis possible in Arabidopsis with mutation of the QUARTET (QRT) genes. Science *264*, 1458-1460.

62. Rhee, S.Y., and Somerville, C.R. (1998). Tetrad pollen formation in quartet mutants of Arabidopsis thaliana is associated with persistence of pectic polysaccharides of the pollen mother cell wall. The Plant Journal *15*, 79-88.

63. Rhee, S.Y., Osborne, E., Poindexter, P.D., and Somerville, C.R. (2003). Microspore separation in the quartet 3 mutants of Arabidopsis is impaired by a defect in a developmentally regulated polygalacturonase required for pollen mother cell wall degradation. Plant Physiology *133*, 1170-1180.

64. Guan, Y.-F., Huang, X.-Y., Zhu, J., Gao, J.-F., Zhang, H.-X., and Yang, Z.-N. (2008). RUPTURED POLLEN GRAIN1, a member of the MtN3/saliva gene family, is crucial for exine pattern formation and cell integrity of microspores in Arabidopsis. Plant Physiology *147*, 852-863.

65. Ariizumi, T., Hatakeyama, K., Hinata, K., Sato, S., Kato, T., Tabata, S., and Toriyama, K. (2003). A novel male-sterile mutant of Arabidopsis thaliana, faceless pollen-1, produces pollen with a smooth surface and an acetolysis-sensitive exine. Plant Molecular Biology *53*, 107-116.

66. Paxson-Sowders, D.M., Dodrill, C.H., Owen, H.A., and Makaroff, C.A. (2001). DEX1, a novel plant protein, is required for exine pattern formation during pollen development in Arabidopsis. Plant Physiology *127*, 1739-1749.

67. Ariizumi, T., Hatakeyama, K., Hinata, K., Inatsugi, R., Nishida, I., Sato, S., Kato, T., Tabata, S., and Toriyama, K. (2004). Disruption of the novel plant protein NEF1 affects lipid accumulation in the plastids of the tapetum and exine formation of pollen, resulting in male sterility in Arabidopsis thaliana. The Plant Journal *39*, 170-181.

68. Oh, S.A., Johnson, A., Smertenko, A., Rahman, D., Park, S.K., Hussey, P.J., and Twell, D. (2005). A divergent cellular role for the FUSED Kinase family in the plant-specific cytokinetic phragmoplast. Current Biology *15*, 2107-2111.

69. Oh, S.A., Bourdon, V., Dickinson, H.G., Twell, D., and Park, S.K. (2014). Arabidopsis Fused kinase TWO-IN-ONE dominantly inhibits male meiotic cytokinesis. Plant Reproduction *27*, 7-17.

70. Hulskamp, M., Parekh, N.S., Grini, P., Schneitz, K., Zimmermann, I., Lolle, S.J., and Pruitt, R.E. (1997). The STUD gene is required for male-specific cytokinesis after telophase II of meiosis in Arabidopsis thaliana. Developmental Biology *187*, 114-124.

71. Spielman, M., Preuss, D., Li, F.L., Browne, W.E., Scott, R.J., and Dickinson, H.G. (1997). TETRASPORE is required for male meiotic cytokinesis in Arabidopsis thaliana. Development *124*, 2645-2657.

72. Yang, C.Y., Spielman, M., Coles, J.P., Li, Y., Ghelani, S., Bourdon, V., Brown, R.C., Lemmon, B.E., Scott, R.J., and Dickinson, H.G. (2003). TETRASPORE encodes a kinesin required for male meiotic cytokinesis in Arabidopsis. The Plant Journal *34*, 229-240.

73. Dobritsa, A.A., Lei, Z., Nishikawa, S.-i., Urbanczyk-Wochniak, E., Huhman, D.V., Preuss, D., and Sumner, L.W. (2010). LAP5 and LAP6 encode anther-specific proteins with similarity to chalcone synthase essential for pollen exine development in Arabidopsis. Plant Physiology *153*, 937-955.

74. Kim, S.S., Grienenberger, E., Lallemand, B., Colpitts, C.C., Kim, S.Y., Souza, C.d.A., Geoffroy, P., Heintz, D., Krahn, D., Kaiser, M., et al. (2010). LAP6/POLYKETIDE SYNTHASE A and LAP5/POLYKETIDE SYNTHASE B encode hydroxyalkyl α-pyrone synthases required for pollen development and sporopollenin biosynthesis in Arabidopsis thaliana. The Plant Cell *22*, 4045-4066.

75. Tang, L.K., Chu, H., Yip, W.K., Yeung, E.C., and Lo, C. (2009). An anther-specific dihydroflavonol 4-reductase-like gene (DRL1) is essential for male fertility in Arabidopsis. New Phytologist *181*, 576-587.

76. Grienenberger, E., Kim, S.S., Lallemand, B., Geoffroy, P., Heintz, D., Souza, C.d.A., Heitz, T., Douglas, C.J., and Legrand, M. (2010). Analysis of TETRAKETIDE α-PYRONE REDUCTASE function in Arabidopsis thaliana reveals a previously unknown, but conserved, biochemical pathway in sporopollenin monomer biosynthesis. The Plant Cell *22*, 4067-4083.

77. Quilichini, T.D., Friedmann, M.C., Samuels, A.L., and Douglas, C.J. (2010). ATP-binding cassette transporter G26 is required for male fertility and pollen exine formation in Arabidopsis. Plant Physiology *154*, 678-690.

78. Choi, H., Jin, J.-Y., Choi, S., Hwang, J.-U., Kim, Y.-Y., Suh, M.C., and Lee, Y. (2011). An ABCG/WBC-type ABC transporter is essential for transport of sporopollenin precursors for exine formation in developing pollen. The Plant Journal *65*, 181-193.

79. Suzuki, T., Narciso, J.O., Zeng, W., van de Meene, A., Yasutomi, M., Takemura, S., Lampugnani, E.R., Doblin, M.S., Bacic, A., and Ishiguro, S. (2017). KNS4/UPEX1: A type II arabinogalactan β-(1,3)-galactosyltransferase required for pollen exine development. Plant Physiology *173*, 183-205.

80. Li, W.L., Liu, Y., and Douglas, C.J. (2017). Role of glycosyltransferases in pollen wall primexine formation and exine patterning. Plant Physiology *173*, 167-182.

81. Quilichini, T.D., Grienenberger, E., and Douglas, C.J. (2015). The biosynthesis, composition and assembly of the outer pollen wall: A tough case to crack. Phytochemistry *113*, 170-182.

82. Shi, J., Cui, M., Yang, L., Kim, Y.-J., and Zhang, D. (2015). Genetic and biochemical mechanisms of pollen wall development. Trends in Plant Science *20*, 741-753.

83. Veen, J., and Wirtz, P. (1968). EMS-induced genic male sterility in Arabidopsis thaliana: a model selection experiment. Euphytica *17*, 371-377.

84. Moffatt, B., and Somerville, C. (1988). Positive selection for male-sterile mutants of Arabidopsis lacking adenine phosphoribosyl transferase activity. Plant Physiology *86*, 1150-1154.

85. Chaudhury, A.M., Craig, S., Dennis, E.S., Lavithis, M., Taylor, P.E., Singh, M.B., Knox, R.B., and Signer, E.R. (1994). Genetic control of male fertility in Arabidopsis thaliana: structural analysis of premeiotic developmental mutants. Sexual Plant Reproduction *7*, 17-28.

86. Glover, J.A., Blömer, K.C., Farrell, L.B., Chaudhury, A.M., and Dennis, E.S. (1996). Searching for tagged male-sterile mutants of arabidopsis. Plant Molecular Biology Reporter *14*, 330.

87. Peirson, B.N., Owen, H.A., Feldmann, K.A., and Makaroff, C.A. (1996). Characterization of three male-sterile mutants of Arabidopsis thaliana exhibiting alterations in meiosis. Sexual Plant Reproduction *9*, 1-16.

88. Aarts, M.G.M., Dirkse, W.G., Stiekema, W.J., and Pereira, A. (1993). Transposon tagging of a male sterility gene in Arabidopsis. Nature *363*, 715-717.

89. Dawson, J., Wilson, Z.A., Aarts, M.G.M., Braithwaite, A.F., Briarty, L.G., and Mulligan, B.J. (1993). Microspore and pollen development in six male-sterile mutants of Arabidopsis thaliana. Canadian Journal of Botany *71*, 629-638.

90. Taylor, P.E., Glover, J.A., Lavithis, M., Craig, S., Singh, M.B., Knox, R.B., Dennis, E.S., and Chaudhury, A.M. (1998). Genetic control of male fertility in Arabidopsis thaliana: structural analyses of postmeiotic developmental mutants. Planta *205*, 492-505.

91. Tanaka, Y., Nishimura, K., Kawamukai, M., Oshima, A., and Nakagawa, T. (2013). Redundant function of two Arabidopsis COPII components, AtSec24B and AtSec24C, is essential for male and female gametogenesis. Planta *238*, 561-575.

92. Bowman, J.L., Smyth, D.R., and Meyerowitz, E.M. (1991). Genetic interactions among floral homeotic genes of Arabidopsis. Development *112*, 1-20.

93. Coen, E.S., and Meyerowitz, E.M. (1991). The war of the whorls: genetic interactions controlling flower development. Nature *353*, 31-37.

94. Jack, T., Brockman, L.L., and Meyerowitz, E.M. (1992). The homeotic gene APETALA3 of Arabidopsis thaliana encodes a MADS box and is expressed in petals and stamens. Cell *68*, 683-697.

95. Goto, K., and Meyerowitz, E.M. (1994). Function and regulation of the Arabidopsis floral homeotic gene PISTILLATA. Genes & Development *8*, 1548-1560.

96. Yang, Y., Xiang, H., and Jack, T. (2003). pistillata-5, an Arabidopsis B class mutant with strong defects in petal but not in stamen development. The Plant Journal *33*, 177-188.

97. Schruff, M.C., Spielman, M., Tiwari, S., Adams, S., Fenby, N., and Scott, R.J. (2006). The AUXIN RESPONSE FACTOR 2 gene of Arabidopsis links auxin signalling, cell division, and the size of seeds and other organs. Development *133*, 251-261.

98. Sanders, P.M., Lee, P.Y., Biesgen, C., Boone, J.D., Beals, T.P., Weiler, E.W., and Goldberg, R.B. (2000). The Arabidopsis DELAYED DEHISCENCE1 gene encodes an enzyme in the jasmonic acid synthesis pathway. The Plant Cell *12*, 1041-1061.

99. Peng, Y.-J., Shih, C.-F., Yang, J.-Y., Tan, C.-M., Hsu, W.-H., Huang, Y.-P., Liao, P.-C., and Yang, C.-H. (2013). A RING-type E3 ligase controls anther dehiscence by activating the jasmonate biosynthetic pathway gene DEFECTIVE IN ANTHER DEHISCENCE1 in Arabidopsis. The Plant Journal *74*, 310-327.

100. Shih, C.-F., Hsu, W.-H., Peng, Y.-J., and Yang, C.-H. (2014). The NAC-like gene ANTHER INDEHISCENCE FACTOR acts as a repressor that controls anther

dehiscence by regulating genes in the jasmonate biosynthesis pathway in Arabidopsis. Journal of Experimental Botany *65*, 621-639.

101. Thevenin, J., Pollet, B., Letarnec, B., Saulnier, L., Gissot, L., Maia-Grondard, A., Lapierre, C., and Jouanin, L. (2011). The simultaneous repression of CCR and CAD, two enzymes of the lignin biosynthetic pathway, results in sterility and dwarfism in Arabidopsis thaliana. Molecular Plant *4*, 70-82.
102. Hao, Z., Avci, U., Tan, L., Zhu, X., Glushka, J., Pattathil, S., Eberhard, S., Sholes, T., Rothstein, G.E., Lukowitz, W., et al. (2014). Loss of Arabidopsis GAUT12/IRX8 causes anther indehiscence and leads to reduced G lignin associated with altered matrix polysaccharide deposition. Frontiers in Plant Science *5*, 357.
103. Feng, X., and Dickinson, H.G. (2010). Tapetal cell fate, lineage and proliferation in the *Arabidopsis* anther. Development *137*, 2409-2416.
104. Pacini, E., Franchi, G., and Hesse, M. (1985). The tapetum: Its form, function, and possible phylogeny in Embryophyta. Plant Systematics and Evolution *149*, 155-185.
105. Van Damme, D., Coutuer, S., De Rycke, R., Bouget, F.-Y., Inzé, D., and Geelen, D. (2006). Somatic cytokinesis and pollen maturation in Arabidopsis depend on TPLATE, which has domains similar to coat proteins. The Plant Cell *18*, 3502-3518.
106. Zhang, J., Teng, C., and Liang, Y. (2011). Programmed cell death may act as a surveillance mechanism to safeguard male gametophyte development in Arabidopsis. Protein & Cell *2*, 837-844.
107. Yang, M., Nadeau, J.A., Zhao, L., and Sack, F.D. (1999). Characterization of a cytokinesis defective (cyd1) mutant of Arabidopsis. Journal of Experimental Botany *50*, 1437-1446.
108. Gillmor, C.S., Roeder, A.H.K., Sieber, P., Somerville, C., and Lukowitz, W. (2016). A Genetic screen for mutations affecting cell division in the Arabidopsis thaliana embryo identifies seven loci required for cytokinesis. PLOS ONE *11*, e0146492.
109. Scott, R.J., Spielman, M., and Dickinson, H.G. (2004). Stamen structure and function. The Plant Cell *16*, S46-S60.
110. Ahlers, F., Bubert, H., Steuernage, S., and Wiermann, R. (2000). The nature of oxygen in sporopollenin from the pollen of Typha angustifolia L. Zeitschrift für Naturforschung C *55*, 129-136.
111. Ahlers, F., Lambert, J., and Wiermann, R. (2003). Acetylation and silylation of piperidine solubilized sporopollenin from pollen of Typha angustifolia L. Zeitschrift für Naturforschung C *58*, 807-811.

112. Descolas-Gros, C., and Schölzel, C. (2007). Stable isotope ratios of carbon and nitrogen in pollen grains in order to characterize plant functional groups and photosynthetic pathway types. New Phytologist *176*, 390-401.
113. Prahl, A., Rittscher, M., and Wiermann, R. (1986). New aspects of sporopollenin biosynthesis. In Biotechnology and ecology of pollen. (Springer), pp. 313-318.
114. Verma, D.P.S., and Hong, Z. (2001). Plant callose synthase complexes. Plant molecular biology *47*, 693-701.
115. Stieglitz, H. (1977). Role of β-1, 3-glucanase in postmeiotic microspore release. Developmental biology *57*, 87-97.
116. Liu, L., and Fan, X.-d. (2013). Tapetum: regulation and role in sporopollenin biosynthesis in Arabidopsis. Plant Molecular Biology *83*, 165-175.
117. Kawanabe, T., Ariizumi, T., Kawai-Yamada, M., Uchimiya, H., and Toriyama, K. (2006). Abolition of the tapetum suicide program ruins microsporogenesis. Plant and Cell Physiology *47*, 784-787.
118. Wilson, Z.A., Morroll, S.M., Dawson, J., Swarup, R., and Tighe, P.J. (2001). The Arabidopsis MALE STERILITY1 (MS1) gene is a transcriptional regulator of male gametogenesis, with homology to the PHD‐finger family of transcription factors. The Plant Journal *28*, 27-39.
119. Sorensen, A.M., Kröber, S., Unte, U.S., Huijser, P., Dekker, K., and Saedler, H. (2003). The Arabidopsis ABORTED MICROSPORES (AMS) gene encodes a MYC class transcription factor. The Plant Journal *33*, 413-423.
120. Xu, J., Yang, C., Yuan, Z., Zhang, D., Gondwe, M.Y., Ding, Z., Liang, W., Zhang, D., and Wilson, Z.A. (2010). The ABORTED MICROSPORES regulatory network is required for postmeiotic male reproductive development in Arabidopsis thaliana. The Plant Cell *22*, 91-107.
121. Ito, T., and Shinozaki, K. (2002). The MALE STERILITY1 gene of Arabidopsis, encoding a nuclear protein with a PHD-finger motif, is expressed in tapetal cells and is required for pollen maturation. Plant and cell physiology *43*, 1285-1292.
122. Yang, S.-L., Xie, L.-F., Mao, H.-Z., Puah, C.S., Yang, W.-C., Jiang, L., Sundaresan, V., and Ye, D. (2003). TAPETUM DETERMINANT1 is required for cell specialization in the Arabidopsis anther. The Plant Cell *15*, 2792-2804.
123. Zhang, W., Sun, Y., Timofejeva, L., Chen, C., Grossniklaus, U., and Ma, H. (2006). Regulation of Arabidopsis tapetum development and function by DYSFUNCTIONAL

TAPETUM1(DYT1) encoding a putative bHLH transcription factor. Development *133*, 3085-3095.

124. Zhu, J., Chen, H., Li, H., Gao, J.-F., Jiang, H., Wang, C., Guan, Y.-F., and Yang, Z.-N. (2008). Defective in Tapetal Development and Function 1 is essential for anther development and tapetal function for microspore maturation in Arabidopsis. The Plant Journal *55*, 266-277.

125. Schekman, R., and Orci, L. (1996). Coat proteins and vesicle budding. Science *271*, 1526-1533.

126. Vitale, A., and Denecke, J. (1999). The endoplasmic reticulum—gateway of the secretory pathway. The Plant Cell *11*, 615-628.

127. Foresti, O., and Denecke, J. (2008). Intermediate organelles of the plant secretory pathway: identity and function. Traffic *9*, 1599-1612.

128. Kuehn, M.J., Herrmann, J.M., and Schekman, R. (1998). COPII-cargo interactions direct protein sorting into ER-derived transport vesicles. Nature *391*, 187-190.

129. Mancias, J.D., and Goldberg, J. (2007). The transport signal on Sec22 for packaging into COPII-coated vesicles is a conformational epitope. Molecular Cell *26*, 403-414.

130. Fromme, J.C., Orci, L., and Schekman, R. (2008). Coordination of COPII vesicle trafficking by Sec23. Trends in Cell Biology *18*, 330-336.

131. Boyadjiev, S.A., Fromme, J.C., Ben, J., Chong, S.S., Nauta, C., Hur, D.J., Zhang, G., Hamamoto, S., Schekman, R., Ravazzola, M., et al. (2006). Cranio-lenticulo-sutural dysplasia is caused by a SEC23A mutation leading to abnormal endoplasmic-reticulum-to-Golgi trafficking. Nat Genet *38*, 1192-1197.

132. Fromme, J.C., Ravazzola, M., Hamamoto, S., Al-Balwi, M., Eyaid, W., Boyadjiev, S.A., Cosson, P., Schekman, R., and Orci, L. (2007). The genetic basis of a craniofacial disease provides insight into COPII coat assembly. Developmental Cell *13*, 623-634.

133. Zeng, Y., Chung, K.P., Li, B., Lai, C.M., Lam, S.K., Wang, X., Cui, Y., Gao, C., Luo, M., Wong, K.-B., et al. (2015). Unique COPII component AtSar1a/AtSec23a pair is required for the distinct function of protein ER export in Arabidopsis thaliana. Proceedings of the National Academy of Sciences *112*, 14360-14365.

134. Conger, R., Chen, Y., Fornaciari, S., Faso, C., Held, M.A., Renna, L., and Brandizzi, F. (2011). Evidence for the involvement of the Arabidopsis SEC24A in male transmission. Journal of Experimental Botany *62*, 4917-4926.

135. Faso, C., Chen, Y.-N., Tamura, K., Held, M., Zemelis, S., Marti, L., Saravanan, R., Hummel, E., Kung, L., Miller, E., et al. (2009). A missense mutation in the Arabidopsis COPII coat protein Sec24A induces the formation of clusters of the endoplasmic reticulum and Golgi apparatus. The Plant Cell *21*, 3655-3671.

136. Nakano, R.T., Matsushima, R., Ueda, H., Tamura, K., Shimada, T., Li, L., Hayashi, Y., Kondo, M., Nishimura, M., and Hara-Nishimura, I. (2009). GNOM-LIKE1/ERMO1 and SEC24a/ERMO2 are required for maintenance of endoplasmic reticulum morphology in Arabidopsis thaliana. The Plant Cell *21*, 3672-3685.

137. Qu, X., Chatty, P.R., and Roeder, A.H.K. (2014). Endomembrane trafficking protein SEC24A regulates cell size patterning in Arabidopsis. Plant Physiology *166*, 1877-1890.

138. Zhao, B., Shi, H., Wang, W., Liu, X., Gao, H., Wang, X., Zhang, Y., Yang, M., Li, R., and Guo, Y. (2016). Secretory COPII protein SEC31B is required for pollen wall development. Plant Physiology *172*, 1625-1642.

139. Narusaka, M., Shiraishi, T., Iwabuchi, M., and Narusaka, Y. (2010). The floral inoculating protocol: a simplified Arabidopsis thaliana transformation method modified from floral dipping. Plant Biotechnology *27*, 349-351.

140. Edwards, K., Johnstone, C., and Thompson, C. (1991). A simple and rapid method for the preparation of plant genomic DNA for PCR analysis. Nucleic acids research *19*, 1349.

141. Nakagawa, T., Suzuki, T., Murata, S., Nakamura, S., Hino, T., Maeo, K., Tabata, R., Kawai, T., Tanaka, K., Niwa, Y., et al. (2007). Improved gateway binary vectors: high-performance vectors for creation of fusion constructs in transgenic analysis of plants. Bioscience, Biotechnology, and Biochemistry *71*, 2095-2100.

142. Nakagawa, T., Nakamura, S., Tanaka, K., Kawamukai, M., Suzuki, T., Nakamura, K., Kimura, T., and Ishiguro, S. (2008). Development of R4 gateway binary vectors (R4pGWB) enabling high-throughput promoter swapping for plant research. Bioscience, Biotechnology, and Biochemistry *72*, 624-629.

143. Hino, T., Tanaka, Y., Kawamukai, M., Nishimura, K., Mano, S., and Nakagawa, T. (2011). Two Sec13p homologs, AtSec13A and AtSec13B, redundantly contribute to the formation of COPII transport vesicles in Arabidopsis thaliana. Bioscience, Biotechnology, and Biochemistry *75*, 1848-1852.

144. Nakamura, S., Suzuki, T., Kawamukai, M., and Nakagawa, T. (2012). Expression analysis of Arabidopsis thaliana small secreted protein genes. Bioscience, Biotechnology, and Biochemistry *76*, 436-446.

145. Boavida, L.C., and McCormick, S. (2007). Temperature as a determinant factor for increased and reproducible in vitro pollen germination in Arabidopsis thaliana. The Plant Journal *52*, 570-582.

146. Shah, K.H., Almaghrabi, B., and Bohlmann, H. (2013). Comparison of expression vectors for transient expression of recombinant proteins in plants. Plant Molecular Biology Reporter *31*, 1529-1538.

147. Huang, M.-D., Chen, T.-L.L., and Huang, A.H.C. (2013). Abundant type III lipid transfer proteins in Arabidopsis tapetum are secreted to the locule and become a constituent of the pollen exine. Plant Physiology *163*, 1218-1229.

148. Robinson, D.G., Herranz, M.-C., Bubeck, J., Pepperkok, R., and Ritzenthaler, C. (2007). Membrane dynamics in the early secretory pathway. Critical Reviews in Plant Sciences *26*, 199-225.

149. Chung, K.P., Zeng, Y., and Jiang, L. (2016). COPII paralogs in plants: functional redundancy or diversity? Trends in Plant Science *21*, 758-769.

150. Preuss, D., Rhee, S.Y., and Davis, R.W. (1994). Tetrad analysis possible in Arabidopsis with mutation of the QUARTET (QRT) genes. Science *264*, 1458-1459.

151. Alexander, M.P. (1969). Differential staining of aborted and nonaborted pollen. Stain Technology *44*, 117-122.

152. Hanton, S.L., Chatre, L., Renna, L., Matheson, L.A., and Brandizzi, F. (2007). De novo formation of plant endoplasmic reticulum export sites is membrane cargo induced and signal mediated. Plant Physiology *143*, 1640-1650.

153. Wei, T., and Wang, A. (2008). Biogenesis of cytoplasmic membranous vesicles for plant potyvirus replication occurs at endoplasmic reticulum exit sites in a COPI- and COPII-dependent manner. Journal of Virology *82*, 12252-12264.

154. Bubeck, J., Scheuring, D., Hummel, E., Langhans, M., Viotti, C., Foresti, O., Denecke, J., Banfield, D.K., and Robinson, D.G. (2008). The syntaxins SYP31 and SYP81 control ER–Golgi trafficking in the plant secretory pathway. Traffic *9*, 1629-1652.

155. Andersson, M.X., and Sandelius, A.S. (2004). A chloroplast-localized vesicular transport system: a bio-informatics approach. BMC Genomics *5*, 40.

156. Khan, N.Z., Lindquist, E., and Aronsson, H. (2013). New putative chloroplast vesicle transport components and cargo proteins revealed using a bioinformatics approach: an Arabidopsis model. PLOS ONE *8*, e59898.

157. Chebli, Y., Kaneda, M., Zerzour, R., and Geitmann, A. (2012). The cell wall of the Arabidopsis pollen tube—spatial distribution, recycling, and network formation of polysaccharides. Plant Physiology *160*, 1940-1955.

158. Lin, S., Dong, H., Zhang, F., Qiu, L., Wang, F., Cao, J., and Huang, L. (2014). BcMF8, a putative arabinogalactan protein-encoding gene, contributes to pollen wall development, aperture formation and pollen tube growth in Brassica campestris. Annals of Botany *113*, 777-788.

159. Lyu, M., Yu, Y., Jiang, J., Song, L., Liang, Y., Ma, Z., Xiong, X., and Cao, J. (2015). BcMF26a and BcMF26b are duplicated polygalacturonase genes with divergent expression patterns and functions in pollen development and pollen tube formation in Brassica campestris. PLOS ONE *10*, e0131173.

160. Ariizumi, T., Kawanabe, T., Hatakeyama, K., Sato, S., Kato, T., Tabata, S., and Toriyama, K. (2008). Ultrastructural characterization of exine development of the transient defective exine 1 mutant suggests the existence of a factor involved in constructing reticulate exine architecture from sporopollenin aggregates. Plant and Cell Physiology *49*, 58-67.

161. Ito, T., Nagata, N., Yoshiba, Y., Ohme-Takagi, M., Ma, H., and Shinozaki, K. (2007). Arabidopsis MALE STERILITY1 encodes a PHD-type transcription factor and regulates pollen and tapetum development. The Plant Cell *19*, 3549-3562.

162. Kim, S.S., and Douglas, C.J. (2013). Sporopollenin monomer biosynthesis in Arabidopsis. Journal of Plant Biology *56*, 1-6.

163. Lallemand, B., Erhardt, M., Heitz, T., and Legrand, M. (2013). Sporopollenin biosynthetic enzymes interact and constitute a metabolon localized to the endoplasmic reticulum of tapetum cells. Plant Physiology *162*, 616-625.

164. Takeuchi, M., Ueda, T., Sato, K., Abe, H., Nagata, T., and Nakano, A. (2000). A dominant negative mutant of sar1 GTPase inhibits protein transport from the endoplasmic reticulum to the Golgi apparatus in tobacco and Arabidopsis cultured cells. The Plant Journal *23*, 517-525.

165. Zheng, Z., Xia, Q., Dauk, M., Shen, W., Selvaraj, G., and Zou, J. (2003). Arabidopsis AtGPAT1, a member of the membrane-bound glycerol-3-phosphate acyltransferase

gene family, is essential for tapetum differentiation and male fertility. The Plant Cell *15*, 1872-1887.

166. Li, X.-C., Zhu, J., Yang, J., Zhang, G.-R., Xing, W.-F., Zhang, S., and Yang, Z.-N. (2012). Glycerol-3-phosphate acyltransferase 6 (GPAT6) is important for tapetum development in Arabidopsis and plays multiple roles in plant fertility. Molecular Plant *5*, 131-142.

167. Huang, C.Y., Chen, P.-Y., Huang, M.-D., Tsou, C.-H., Jane, W.-N., and Huang, A.H.C. (2013). Tandem oleosin genes in a cluster acquired in Brassicaceae created tapetosomes and conferred additive benefit of pollen vigor. Proceedings of the National Academy of Sciences *110*, 14480-14485.

168. Piffanelli, P., Ross, J.H., and Murphy, D. (1998). Biogenesis and function of the lipidic structures of pollen grains. Sexual plant reproduction *11*, 65-80.

169. Wu, S.S.H., Moreau, R.A., Whitaker, B.D., and Huang, A.H.C. (1999). Steryl esters in the elaioplasts of the tapetum in developing Brassica anthers and their recovery on the pollen surface. Lipids *34*, 517-523.

170. Fan, J., Zhai, Z., Yan, C., and Xu, C. (2015). Arabidopsis TRIGALACTOSYLDIACYLGLYCEROL5 Interacts with TGD1, TGD2, and TGD4 to Facilitate Lipid Transfer from the Endoplasmic Reticulum to Plastids. The Plant Cell *27*, 2941-2955.

171. Li, N., Xu, C., Li-Beisson, Y., and Philippar, K. (2016). Fatty acid and lipid transport in plant cells. Trends in Plant Science *21*, 145-158.

172. Samuels, L., and McFarlane, H.E. (2012). Plant cell wall secretion and lipid traffic at membrane contact sites of the cell cortex. Protoplasma *249*, 19-23.

173. Hsieh, K., and Huang, A.H.C. (2005). Lipid-rich tapetosomes in Brassica tapetum are composed of oleosin-coated oil droplets and vesicles, both assembled in and then detached from the endoplasmic reticulum. The Plant Journal *43*, 889-899.

174. Choi, H., Ohyama, K., Kim, Y.-Y., Jin, J.-Y., Lee, S.B., Yamaoka, Y., Muranaka, T., Suh, M.C., Fujioka, S., and Lee, Y. (2014). The role of arabidopsis ABCG9 and ABCG31 ATP binding cassette transporters in pollen fitness and the deposition of steryl glycosides on the pollen coat. The Plant Cell *26*, 310-324.

175. Halpin, C. (2005). Gene stacking in transgenic plants-the challenge for 21st century plant biotechnology. Plant Biotechnology Journal *3*, 141-155.

176. Dafny-Yelin, M., and Tzfira, T. (2007). Delivery of multiple transgenes to plant cells. Plant Physiology *145*, 1118-1128.

177. Xie, M., He, Y., and Gan, S. (2001). Bidirectionalization of polar promoters in plants. Nat Biotech *19*, 677-679.

178. Sun, Q., Liu, J., Li, Y., Zhang, Q., Shan, S., Li, X., and Qi, B. (2013). Creation and validation of a widely applicable multiple gene transfer vector system for stable transformation in plant. Plant Molecular Biology *83*, 391-404.

179. Li, M.V., Shukla, D., Rhodes, B.H., Lall, A., Shu, J., Moriarity, B.S., and Largaespada, D.A. (2014). HomeRun vector assembly system: a flexible and standardized cloning system for assembly of multi-modular DNA constructs. PLOS ONE *9*, e100948.

180. Karimi, M., Depicker, A., and Hilson, P. (2007). Recombinational cloning with plant gateway vectors. Plant Physiology *145*, 1144-1154.

181. Cheo, D.L., Titus, S.A., Byrd, D.R.N., Hartley, J.L., Temple, G.F., and Brasch, M.A. (2004). Concerted assembly and cloning of multiple DNA segments using in vitro site-specific recombination: functional analysis of multi-segment expression clones. Genome Research *14*, 2111-2120.

182. Petersen, L.K., and Stowers, R.S. (2011). A Gateway MultiSite recombination cloning toolkit. PloS one *6*, e24531.

183. Sambrook, J., and Russell, D.W. (2001). Molecular cloning: a laboratory manual 3rd edition. Coldspring-Harbour Laboratory Press, UK.

184. Nakamura, S., Mano, S., Tanaka, Y., Ohnishi, M., Nakamori, C., Araki, M., Niwa, T., Nishimura, M., Kaminaka, H., Nakagawa, T., et al. (2010). Gateway binary vectors with the bialaphos resistance gene, bar, as a selection marker for plant transformation. Bioscience, Biotechnology, and Biochemistry *74*, 1315-1319.

185. Tanaka, Y., Nakamura, S., Kawamukai, M., Koizumi, N., and Nakagawa, T. (2011). Development of a series of gateway binary vectors possessing a tunicamycin resistance gene as a marker for the transformation of Arabidopsis thaliana. Bioscience, Biotechnology, and Biochemistry *75*, 804-807.

186. Hajdukiewicz, P., Svab, Z., and Maliga, P. (1994). The small, versatile pPZP family of Agrobacterium binary vectors for plant transformation. Plant Molecular Biology *25*, 989-994.

187. Tachiki, K., Kodama, Y., Nakayama, H., and Shinmyo, A. (2009). Determination of the in vivo distribution of nuclear matrix attachment regions using a polymerase chain reaction-based assay in *Arabidopsis thaliana*. Journal of Bioscience and Bioengineering *108*, 11-19.

188. Nakagawa, T., Kurose, T., Hino, T., Tanaka, K., Kawamukai, M., Niwa, Y., Toyooka, K., Matsuoka, K., Jinbo, T., and Kimura, T. (2007). Development of series of gateway binary vectors, pGWBs, for realizing efficient construction of fusion genes for plant transformation. Journal of Bioscience and Bioengineering *104*, 34-41.

189. Singh, T., Hayashi, M., Mano, S., Arai, Y., Goto, S., and Nishimura, M. (2009). Molecular components required for the targeting of PEX7 to peroxisomes in Arabidopsis thaliana. The Plant Journal *60*, 488-498.

190. Spiker, S., and Thompson, W.F. (1996). Nuclear matrix attachment regions and transgene expression in plants. Plant Physiology *110*, 15-21.

191. Mlynarova, L., Loonen, A., Heldens, J., Jansen, R.C., Keizer, P., Stiekema, W.J., and Nap, J.P. (1994). Reduced position effect in mature transgenic plants conferred by the chicken lysozyme matrix-associated region. The Plant Cell *6*, 417-426.

192. Cheng, Z., Targolli, J., and Wu, R. (2001). Tobacco matrix attachment region sequence increased transgene expression levels in rice plants. Molecular Breeding *7*, 317-327.

193. Petersen, K., Leah, R., Knudsen, S., and Cameron-Mills, V. (2002). Matrix attachment regions (MARs) enhance transformation frequencies and reduce variance of transgene expression in barley. Plant Molecular Biology *49*, 45-58.

194. Verma, D., Verma, M., Dey, M., Jain, R.K., and Wu, R. (2005). Molecular dissection of the tobacco Rb7 matrix attachment region (MAR): Effect of 5' half on gene expression in rice. Plant Science *169*, 704-711.

195. Han, K.-H., Ma, C., and Strauss, S.H. (1997). Matrix attachment regions (MARs) enhance transformation frequency and transgene expression in poplar. Transgenic Research *6*, 415-420.

196. Chiu, W., Niwa, Y., Zeng, W., Hirano, T., Kobayashi, H., and Sheen, J. (1996). Engineered GFP as a vital reporter in plants. Current Biology *6*, 325-330.

197. Steever, A.B., Wach, A., Philippsen, P., and Pringle, J.R. (1998). Heterologous modules for efficient and versatile PCR-based gene targeting in *Schizosaccharomyces pombe*. Yeast *14*, 943-951.

198. Chubet, R.G. (1996). Vectors for expression and secretion of FLAG epitope-tagged proteins in mammalian cells. Biotechniques *20*, 136-141.

199. Smith, D.B., and Johnson, K.S. (1988). Single-step purification of polypeptides expressed in Escherichia coli as fusions with glutathione S-transferase. Gene *67*, 31-40.

200. Yano, D., Sato, M., Saito, C., Sato, M.H., Morita, M.T., and Tasaka, M. (2003). A SNARE complex containing SGR3/AtVAM3 and ZIG/VTI11 in gravity-sensing cells is important for Arabidopsis shoot gravitropism. Proceedings of the National Academy of Sciences of the United States of America *100*, 8589-8594.

201. Jefferson, R.A., Kavanagh, T.A., and Bevan, M.W. (1987). GUS fusions: beta-glucuronidase as a sensitive and versatile gene fusion marker in higher plants. The EMBO Journal *6*, 3901-3907.

202. Sherf, B.A., and Wood, K.V. (1994). Firefly luciferase engineered for improved genetic reporting. Promega notes *49*, 14-21.

203. Huang, J., Taylor, J.P., Chen, J.-G., Uhrig, J.F., Schnell, D.J., Nakagawa, T., Korth, K.L., and Jones, A.M. (2006). The plastid protein THYLAKOID FORMATION1 and the plasma membrane G-protein GPA1 interact in a novel sugar-signaling mechanism in Arabidopsis. The Plant Cell *18*, 1226-1238.

204. Kawakami, S., and Watanabe, Y. (1997). Use of green fluorescent protein as a molecular tag of protein movement in vivo. Plant Biotechnology *14*, 127-130.

205. Campbell, R.E., Tour, O., Palmer, A.E., Steinbach, P.A., Baird, G.S., Zacharias, D.A., and Tsien, R.Y. (2002). A monomeric red fluorescent protein. Proceedings of the National Academy of Sciences of the United States of America *99*, 7877-7882.

206. Shcherbo, D., Merzlyak, E.M., Chepurnykh, T.V., Fradkov, A.F., Ermakova, G.V., Solovieva, E.A., Lukyanov, K.A., Bogdanova, E.A., Zaraisky, A.G., Lukyanov, S., et al. (2007). Bright far-red fluorescent protein for whole-body imaging. Nat Methods *4*, 741-746.

207. Nakagawa, T., Ishiguro, S., and Kimura, T. (2009). Gateway vectors for plant transformation. Plant Biotechnology *26*, 275-284.

208. Hecker, A., Wallmeroth, N., Peter, S., Blatt, M.R., Harter, K., and Grefen, C. (2015). Binary 2in1 vectors improve in planta (co)localization and dynamic protein interaction studies. Plant Physiology *168*, 776-787.

209. Ghareeb, H., Laukamm, S., and Lipka, V. (2016). COLORFUL-circuit: a platform for rapid multigene assembly, delivery, and expression in plants. Frontiers in Plant Science *7*.

210. He, Z., Liu, B., Wang, X., Bian, M., He, R., Yan, J., Zhong, M., Zhao, X., and Liu, X. (2016). Construction and validation of a dual-transgene vector system for stable transformation in plants. Journal of Genetics and Genomics *43*, 207-215.

211. Benhamed, M., Martin-Magniette, M.-L., Taconnat, L., Bitton, F., Servet, C., De Clercq, R., De Meyer, B., Buysschaert, C., Rombauts, S., Villarroel, R., et al. (2008). Genome-scale Arabidopsis promoter array identifies targets of the histone acetyltransferase GCN5. The Plant Journal *56*, 493-504.

212. Siligato, R., Wang, X., Yadav, S.R., Lehesranta, S., Ma, G., Ursache, R., Sevilem, I., Zhang, J., Gorte, M., Prasad, K., et al. (2016). MultiSite Gateway-compatible cell type-specific gene-inducible system for plants. Plant Physiol. *170*, 627-641.

213. Karimi, M., Bleys, A., Vanderhaeghen, R., and Hilson, P. (2007). Building blocks for plant gene assembly. Plant Physiology *145*, 1183-1191.

214. Fernandez, A.I., Viron, N., Alhagdow, M., Karimi, M., Jones, M., Amsellem, Z., Sicard, A., Czerednik, A., Angenent, G., Grierson, D., et al. (2009). Flexible tools for gene expression and silencing in tomato. Plant Physiology *151*, 1729-1740.

215. Pruneda-Paz, Jose L., Breton, G., Nagel, Dawn H., Kang, S.E., Bonaldi, K., Doherty, Colleen J., Ravelo, S., Galli, M., Ecker, Joseph R., and Kay, Steve A. (2014). A Genome-Scale Resource for the Functional Characterization of Arabidopsis Transcription Factors. Cell Reports *8*, 622-632.

216. Gong, W., Shen, Y.-P., Ma, L.-G., Pan, Y., Du, Y.-L., Wang, D.-H., Yang, J.-Y., Hu, L.-D., Liu, X.-F., Dong, C.-X., et al. (2004). Genome-wide ORFeome cloning and analysis of Arabidopsis transcription factor genes. Plant Physiology *135*, 773-782.

217. Pillitteri, L.J., Sloan, D.B., Bogenschutz, N.L., and Torii, K.U. (2007). Termination of asymmetric cell division and differentiation of stomata. Nature *445*, 501-505.

218. Berger, D., and Altmann, T. (2000). A subtilisin-like serine protease involved in the regulation of stomatal density and distribution in Arabidopsis thaliana. Genes & Development *14*, 1119-1131.

219. von Groll, U., Berger, D., and Altmann, T. (2002). The subtilisin-like serine protease SDD1 mediates cell-to-cell signaling during Arabidopsis stomatal development. The Plant Cell *14*, 1527-1539.

220. Sakamoto, W., and Wintz, H. ((PGR) 1996). Nucleotide sequence of cDNAs encoding gamma, delta, delta-prime, and epsilon subunits of mitochondrial F1-ATPase in Arabidopsis thaliana. Plant Physiol. *112*, 1736.

221. Nishimura, M., Yamaguchi, J., Mori, H., Akazawa, T., and Yokota, S. (1986). Immunocytochemical analysis shows that glyoxysomes are directly transformed to leaf peroxisomes during greening of pumpkin cotyledons. Plant Physiology *81*, 313-316.

222. Kim, S., Lee, D.-S., Choi, I.S., Ahn, S.-J., Kim, Y.-H., and Bae, H.-J. (2010). Arabidopsis thaliana Rubisco small subunit transit peptide increases the accumulation of Thermotoga maritima endoglucanase Cel5A in chloroplasts of transgenic tobacco plants. Transgenic Research *19*, 489-497.

223. Bergmann, D.C., and Sack, F.D. (2007). Stomatal development. Annual Review of Plant Biology *58*, 163-181.

224. Pillitteri, L.J., and Torii, K.U. (2012). Mechanisms of stomatal development. Annual Review of Plant Biology *63*, 591-614.

225. Peremarti, A., Twyman, R.M., Gómez-Galera, S., Naqvi, S., Farré, G., Sabalza, M., Miralpeix, B., Dashevskaya, S., Yuan, D., Ramessar, K., et al. (2010). Promoter diversity in multigene transformation. Plant Mol. Biol. *73*, 363-378.

226. Naqvi, S., Zhu, C., Farre, G., Ramessar, K., Bassie, L., Breitenbach, J., Perez Conesa, D., Ros, G., Sandmann, G., Capell, T., et al. (2009). Transgenic multivitamin corn through biofortification of endosperm with three vitamins representing three distinct metabolic pathways. Proc. Natl. Acad. Sci. U.S.A. *106*, 7762-7767.

227. Paine, J.A., Shipton, C.A., Chaggar, S., Howells, R.M., Kennedy, M.J., Vernon, G., Wright, S.Y., Hinchliffe, E., Adams, J.L., Silverstone, A.L., et al. (2005). Improving the nutritional value of golden rice through increased pro-vitamin A content. Nat. Biotechnol. *23*, 482-487.

228. Zhu, C., Naqvi, S., Breitenbach, J., Sandmann, G., Christou, P., and Capell, T. (2008). Combinatorial genetic transformation generates a library of metabolic phenotypes for the carotenoid pathway in maize. Proc. Natl. Acad. Sci. U.S.A. *105*, 18232-18237.

229. Odell, J.T., Nagy, F., and Chua, N.-H. (1985). Identification of DNA sequences required for activity of the cauliflower mosaic virus 35S promoter. Nature *313*, 810-812.

230. Benfey, P.N., and Chua, N.-H. (1990). The cauliflower mosaic virus 35S promoter: combinatorial regulation of transcription in plants. Science *250*, 959-966.

231. Yoo, S.Y., Bomblies, K., Yoo, S.K., Yang, J.W., Choi, M.S., Lee, J.S., Weigel, D., and Ahn, J.H. (2005). The 35S promoter used in a selectable marker gene of a plant transformation vector affects the expression of the transgene. Planta *221*, 523-530.

232. Matzke, M.A., and Matzke, A. (1995). How and why do plants inactivate homologous (trans)genes? Plant Physiol. *107*, 679-685.

233. Stam, M., Mol, J.N.M., and Kooter, J.M. (1997). The silence of genes in transgenic plants. Ann. Bot. *79*, 3-12.

234. Dong, Y., and von Arnim, A.G. (2003). Novel plant activation-tagging vectors designed to minimize 35S enhancer-mediated gene silencing. Plant Mol. Biol. Rep. *21*, 349-358.

235. Mishiba, K.-i., Nishihara, M., Nakatsuka, T., Abe, Y., Hirano, H., Yokoi, T., Kikuchi, A., and Yamamura, S. (2005). Consistent transcriptional silencing of 35S-driven transgenes in gentian. Plant J *44*, 541-556.

236. Chalfun-Junior, A., Mes, J.J., Mlynárová, L., Aarts, M.G.M., and Angenent, G.C. (2003). Low frequency of T-DNA based activation tagging in Arabidopsis is correlated with methylation of CaMV 35S enhancer sequences. FEBS Lett. *555*, 459-463.

237. Curradi, M., Izzo, A., Badaracco, G., and Landsberger, N. (2002). Molecular mechanisms of gene silencing mediated by DNA methylation. Mol. Cell. Biol. *22*, 3157-3173.

238. Bevan, M., Barnes, W.M., and Chilton, M.D. (1983). Structure and transcription of the nopaline synthase gene region of T-DNA. Nucleic Acids Res. *11*, 369-385.

239. Sanders, P.R., Winter, J.A., Barnason, A.R., Rogers, S.G., and Fraley, R.T. (1987). Comparison of cauliflower mosaic virus 35S and nopaline synthase promoters in transgenic plants. Nucleic Acids Res. *15*, 1543-1558.

240. Harpster, M.H., Townsend, J.A., Jones, J.D.G., Bedbrook, J., and Dunsmuir, P. (1988). Relative strengths of the 35S califlower mosaic virus, 1', 2', and nopaline synthase promoters in transformed tobacco sugarbeet and oilseed rape callus tissue. Mol. Gen. Genet. *212*, 182-190.

241. Allen, G.C., Spiker, S., and Thompson, W.F. (2000). Use of matrix attachment regions (MARs) to minimize transgene silencing. Plant Mol. Biol. *43*, 361-376.

242. Tanaka, Y., Hikino, K., Nishimura, M., Goto, S., Mano, S., Kimura, T., and Nakagawa, T. (2012). Gateway vectors for plant genetic engineering: overview of plant vectors, application for bimolecular fluorescence complementation (BiFC) and multigene construction. (Croatia: InTech), pp. 35-68.

243. Kodama, Y., and Hu, C.-D. (2012). Bimolecular fluorescence complementation (BiFC): A 5-year update and future perspectives. Biotechniques *53*, 285-298.

244. Kudla, J., and Bock, R. (2016). Lighting the way to protein-protein interactions: recommendations on best practices for bimolecular fluorescence complementation analyses. Plant Cell *28*, 1002-1008.

245. Miller, K.E., Kim, Y., Huh, W.-K., and Park, H.-O. (2015). Bimolecular fluorescence complementation (BiFC) analysis: advances and recent applications for genome-wide interaction studies. J. Mol. Biol. *427*, 2039-2055.

246. Bhat, R.A., Lahaye, T., and Panstruga, R. (2006). The visible touch: in planta visualization of protein-protein interactions by fluorophore-based methods. Plant Methods *2*, 12.

247. Nishimura, K., Ishikawa, S., Matsunami, E., Yamauchi, J., Homma, K., Faulkner, C., Oparka, K., Jisaka, M., Nagaya, T., Yokota, K., et al. (2015). New Gateway-compatible vectors for a high-throughput protein–protein interaction analysis by a bimolecular fluorescence complementation (BiFC) assay in plants and their application to a plant clathrin structure analysis. Biosci. Biotechnol. Biochem. *79*, 1995-2006.

248. Kamigaki, A., Nito, K., Hikino, K., Goto-Yamada, S., Nishimura, M., Nakagawa, T., and Mano, S. (2016). Gateway vectors for simultaneous detection of multiple protein−protein interactions in plant cells using bimolecular fluorescence complementation. PLoS One *11*, e0160717.

249. Grefen, C., and Blatt, M.R. (2012). A 2in1 cloning system enables ratiometric bimolecular fluorescence complementation (rBiFC). Biotechniques *53*, 311-314.

250. Stellberger, T., Häuser, R., Baiker, A., Pothineni, V.R., Haas, J., and Uetz, P. (2010). Improving the yeast two-hybrid system with permutated fusions proteins: the Varicella Zoster Virus interactome. Proteome Sci *8*, 8.

251. Schweighofer, A., Shubchynskyy, V., Kazanaviciute, V., Djamei, A., and Meskiene, I. (2014). Bimolecular fluorescent complementation (BiFC) by MAP kinases and MAPK phosphatases. In Plant MAP Kinases: Methods and Protocols, G. Komis and J. Samaj, eds. (New York, NY: Springer New York), pp. 147-158.

252. Uemura, T., Ueda, T., Ohniwa, R.L., Nakano, A., Takeyasu, K., and Sato, M.H. (2004). Systematic analysis of SNARE molecules in Arabidopsis: dissection of the post-Golgi network in plant cells. Cell Struct. Funct. *29*, 49-65.

253. Barlowe, C., Orci, L., Yeung, T., Hosobuchi, M., Hamamoto, S., Salama, N., Rexach, M.F., Ravazzola, M., Amherdt, M., and Schekman, R. (1994). COPII: A membrane coat formed by Sec proteins that drive vesicle budding from the endoplasmic reticulum. Cell *77*, 895-907.

254. Gookin, T.E., and Assmann, S.M. (2014). Significant reduction of BiFC non-specific assembly facilitates in planta assessment of heterotrimeric G-protein interactors. Plant J *80*, 553-567.

List of publications

Chapter 4

Aboulela M, Tanaka Y, Nishimura K, Mano S, Nishimura M, Ishiguro S, Kimura T, Nakagawa T (2017) Development of an R4 dual-site (R4DS) gateway cloning system enabling the efficient simultaneous cloning of two desired sets of promoters and open reading frames in a binary vector for plant research. PLOS ONE 12 (5):e0177889. (DOI:10.1371/journal.pone.0177889).

Chapter 5

Aboulela M, Tanaka Y, Nishimura K, Mano S, Kimura T, Nakagawa T (2017) A dual-site gateway cloning system for simultaneous cloning of two genes for plant transformation. Plasmid 92:1-11. (DOI:10.1016/j.plasmid.2017.05.001).

Acknowledgements

In the first place, I would like to express my deepest gratitude to **Prof. Dr. Tsuyoshi NAKAGAWA**, Director of the Center of Integrated Research in Science, Shimane University, for constant encouragement, support, and invaluable suggestions which made this work successful. During my tenure, he contributed to widen my experience in many ways by giving me intellectual freedom in my work, and inspiring me with new ideas. I would also like to thank him for the careful consideration of my future-research continuity in my home country.

I wish to express my sincere thanks to **Prof. Dr. Makoto KAWAMUKAI, Associate Prof. Dr. Tomohiro KAINO,** and **Assistant Prof. Dr. Yasuhiro MATSUO**, (Shimane University), for providing me with invaluable advice and comments on my research in regular meetings and seminars throughout the course of this work.

I am very grateful to **Assistant Prof. Dr. Kohji NISHIMURA (**Shimane University), for the kind guidance and for the technical support especially concerning confocal microscopy imaging.

I would also like to thank the rest of my thesis committee, **Prof. Kazuhito AKAMA** (Shimane University), **Prof. Kinya AKASHI** (Tottori University) and **Prof. Akihiro ITAI** (Kyoto Pref. University) for their insightful suggestions and for kind guidance.

I wish also to express my sincere thanks to **Prof. Tetsuya KIMURA,** (Mie University**), Associate Prof. Sumie ISHIGURO** (Nagoya University**),** and **Assistant Prof. Shoji MANO**, (National Institute for Basic Biology), for the invaluable advice and their comments on the manuscripts.

I would also like to express my gratitude to **Associate Prof. Dr. Akinobu OSHIMA, (**Shimane University), for his technical support especially concerning scanning electron microscopy.

I would also like to express my special thanks to **Prof. Tetsuya HIGASHIYAMA** (Nagoya University) and **Dr. Takamasa SUZUKI** (Chubu University) for their great help with the Next generation sequencing.

My sincere thanks go to **Dr. Yuji TANAKA**, for his crucial contribution and technical support; without his efforts my work would have undoubtedly been more difficult.

Many thanks go to **Kanae KOIKE** (the Transmission Electron Microscopy Service, Center for Gene Science, Hiroshima University) for the help in ultrastructural analyses.

I would like to express my thanks to my present and past colleagues, Amit DUTTA, Sultana MOMTAZ, Toshiki SAISHO, Shoya YOKOYAMA, Aoi SHIBAHARA, Mihiko YAMAZAKI, Mayu KODANI, Kenta SHIBAHARA, Tomomi ODA, Chisato YAMADA, Kouhei KATSUYAMA, and all members of the laboratory of Life Science and Biotechnology, for their help and for being great friends throughout my stay in Japan.

Many thanks go to the Ministry of Education, Culture, Sports, Science and Technology of Japan (MEXT) for giving me this opportunity to study my Ph.D. degree at united graduate school of agricultural science and for the financial support.

At the end, I would like to express my thanks to my family for all their love and encouragement. And most of all for my supportive, encouraging, and patient wife MIADA and my son ADAM, thank you.

Summary

The research described in this thesis aimed to improve our understandings of the important processes of pollen development and exine wall formation and to isolate and characterize new genes involved in such complicated processes. Vast numbers of genes work cooperatively to regulate various biological processes including pollen development and exine wall formation. In order to understand the functions and molecular mechanisms underlying these processes, analyses of transgenic plants that concomitantly express two protein-coding genes are often required.

In **Chapter 1**, the author presents a general introduction to the work. **Chapter 2** describes a high-magnification level screening aimed to isolate new genes affecting anther and pollen development in *Arabidopsis thaliana*. Unlike most of the previous screens which were mainly based on isolating male sterile and semi-sterile plants neglecting a large number of mutants with severe to mild defects in pollen structure, however, still fertile; the screen described here using scanning electron microscopy could isolate such mutants. Several mutants with a range of defects in anther/pollen development and exine wall formation were recovered; some of them exhibit novel surface-structure phenotypes. A total of one hundred and one mutant plants were isolated (some of them were found to be allelic) and classified according to their phenotypic characters into three classes including multiple subclasses and types. The identification of the mutation location was performed mainly by the bulked-segregant analysis using next generation sequencing rather than using the traditional mapping methods. Twenty-three mutations were successfully mapped to specific regions of particular chromosomes of the Arabidopsis genome; thirteen of them were linked to specific genes. This work illustrates that high magnification level screens (i.e., using scanning electron microscopy) are highly beneficial and may even be required to isolate mutants with novel phenotypes, (i.e., most mutants with severe defects that can be found by naked-eye visual screen or dissecting microscope-level screen most likely will be alleles of previously identified genes). Characterization of the genes responsible for mutants isolated in this screen will expand our knowledge of the molecular mechanism underlying several vital processes in pollen development, including pollen wall formation, sporopollenin synthesis, polymerization and transport, and exine patterning. This screen provides an additional resource for plant researchers to analyze functions of genes involved in anther/pollen development and exine wall formation processes and will help unrevealing previously unknown players in such processes.

COPII proteins are involved in lipid and protein transport events from the endoplasmic reticulum to the Golgi in the early secretory pathway. **Chapter 3** provides phenotypic characterization of two components of the Arabidopsis coat protein complex II (COPII) proteins, *AtSEC23A* and *AtSEC23D*, and shows how these genes are involved in regulating plant growth and development. The study revealed that both *AtSEC23A* and *AtSEC23D* are essential for normal pollen and tapetum development. Single *atsec23a and atsec23d* mutant plants, although normally fertile, showed a compromised pollen wall formation with less sporopollenin deposition in the outer exine layer. Double *atsec23ad* mutant plants were semi-sterile and exhibited a wide range of developmental defects in pollen and tapetal cells. Pollen grains of *atsec23ad* plants had defective exine and intine layers and their cytoplasm have shown signs of degeneration or leakage. Moreover, the development of tapetal cells in *atsec23ad* plants was altered, with structural abnormalities in

inner organelles (i.e., ER, Golgi, elaioplasts, and tapetosomes). Both AtSEC23A and AtSEC23D exhibited the characteristic localization pattern of COPII proteins, indicating that they are functional COPII components. The results indicated that *AtSEC23A* and *AtSEC23D* may only share partial redundant functions and may have differing substrate preferences. Thus, this work suggests that *AtSEC23A* and *AtSEC23D* organize pollen wall development and exine patterning by regulating ER export of lipid and proteins necessary for pollen wall formation in tapetal cells. This work provides a direct link between the tapetum early secretory pathway and the processes of sporopollenin deposition and exine patterning. In addition, the results presented in this Chapter shed light on the functional heterogeneity of SEC23 homologs in plants.

To better understand the functions and molecular mechanisms underlying various biological processes including pollen development and exine wall formation, developing new systems to deliver two genes simultaneously are often required. For example, exploring the expression patterns and co-localizations of the two SEC23 proteins described in Chapter 3 required utilizing vector systems that enable simultaneous cloning of two expression cassettes. For these reasons, two vector systems allowing simple cloning of two expression cassettes simultaneously in plant cells were developed and presented in **Chapter 4** and **Chapter 5**. **Chapter 4** describes a vector system that enables the simultaneous cloning of two desired sets of promoters and open reading frames, named the R4 dual-site gateway cloning system. **Chapter 5** presents a vector system allows the simultaneous cloning of two genes under control of the moderate nopaline synthase promoter, named the dual-site gateway cloning system. These vectors have been used successfully not only in exploring the expression patterns and co-localizations of the two SEC23 proteins but also in the co-localization of each of AtSEC23A and AtSEC23D with other organelle markers (e.g., endoplasmic reticulum, Golgi, and plastid) as described in Chapter 3. These vectors also facilitate the protein-protein interaction analysis by bimolecular fluorescence complementation (BiFC) assay and co-immunoprecipitation. Investigating protein-protein interactions is required in many cases to dissect the functions and molecular mechanisms underlying multiple biological processes including pollen development and exine wall formation. In addition, the two developed vector series are versatile cloning tools with multiple flexibility features, including multiple types of tags and 4 kinds of plant selection markers. Both cloning systems will be invaluable experimental tools with multiple applications in plant research, e.g., analysis of co-localization patterns of transgenes and investigation of protein-protein interactions by BiFC or co-immunoprecipitation.

In the **final Chapter**, the author provides proposed conclusion remarks and discusses the findings presented in this study.

In sum, the large scale screening (~ 10,000) using scanning electron microscopy at a high-magnification level was successful to isolate mutants with mild defects in the exine surface structure that would be neglected with using other screening strategies. Multiple mutants with novel phenotypes were recovered. Two genes, *AtSEC23A* and *AtSEC23D*, were characterized in detail; both were found to be required for proper pollen wall development and exine patterning and they may function by regulating ER export of lipid and proteins necessary for pollen wall formation in the tapetal cells. Two novel vector systems were developed for analysis of the genes revealed in this study. These systems are beneficial tools in exploring the functions and molecular mechanisms underlying various biological processes including pollen development and exine wall formation.

概要

本論文は、花粉の発達やエキシン形成における複雑かつ重要なプロセスを分子レベルで理解するため、関与する遺伝子を新規に単離し解析を行うことを目的としたものである。花粉の発生やエキシンの形成をはじめとした様々な生物学的プロセスを調節するために膨大な数の遺伝子産物が協調して働いている。これら遺伝子産物の機能および分子メカニズムを理解するために、2 つの遺伝子を同時に発現するトランスジェニック植物を用いた解析がしばしば必要とされている。

第 1 章では、本論文の概要を述べる。第 2 章では、シロイヌナズナの葯や花粉の発生に影響を及ぼす新しい遺伝子の単離を目的とした高倍率顕微鏡スクリーニングについて述べる。これまでに行われた来た雄性不稔性および半不稔性を指標としたスクリーングでは、花粉の構造に欠陥を持つものの稔性を維持している多数の突然変異体が見逃されてきた。これらに比べ、本論文で述べる走査型電子顕微鏡を用いたスクリーニングでは、いままで見逃されていたタイプの突然変異体も単離することが可能で、葯/花粉の発達およびエキシンの形成に種々の欠陥を有する突然変異体が得られた。それらのいくつかは新規の花粉表面構造表現型を示した。変異部位の同定は、従来のマッピングではなく、次世代 DNA シークエンサーによる bulked-segregant analysis によって行われた。その結果、23 個の突然変異がシロイヌナズナ染色体の特定の領域に効率よくマッピングされた。それらのうち、13 種は特定の遺伝子と連鎖していることが示された。この研究は、高倍率顕微鏡によるスクリ−ニング（走査型電子顕微鏡スクリーニング）が非常に有効であり、新規な表現型の変異体を取得するのにすぐれた方法であることを示した。（従来行われて来た不稔性を指標とした目視スクリ−ニングで見いだされるような重篤な変異体は、その殆どが既に取得された変異の対立遺伝子であることが多い）。このスクリーニングで単離された突然変異体の原因遺伝子の解析により、花粉壁形成、スポロポレニン合成・重合・輸送、そしてエキシンパターン形成など、花粉発達におけるいくつかの重要なプロセスの分子メカニズムの理解が深まる。このスクリーニングは植物研究者が葯/花粉の発生およびエキシン形成プロセスに関する遺伝子の機能を分析するためのリソースを提供し、未知の遺伝子の発見を促すものである。

COPII タンパク質は、小胞体から初期分泌経路のゴルジ体への脂質およびタンパク質輸送事象に関与している。第 3 章では、シロイヌナズナのコートタンパク質複合体 II（COPII）タンパク質である

AtSEC23A および AtSEC23D の遺伝子破壊株表現型の解析を行い、これら遺伝子が植物の成長および発達を調節に関与することを示した。この研究は、AtSEC23A および AtSEC23D の両者が、正常な花粉およびタペタムの発生に必須であることを明らかにした。単一の *atsec23a* および *atsec23d* 変異体植物は稔性は正常であるが、花粉表層の外膜層におけるスポロポレニン沈着が少なく、花粉壁の形成が損なわれていることを示した。*atsec23ad* 二重突然変異植物は半不稔性であり、花粉およびタペート細胞において幅広い発生異常を示した。 *atsec23ad* 二重変異体植物の花粉は、exine および intine 層に欠陥があり、その細胞質は変性または漏出の様相を呈していた。さらに、*atsec23ad* 二重変異体植物ではタペート細胞の発達が異常となり、内部細胞小器官（ER、ゴルジ、エライオプラスト、およびタペトソーム）に構造異常が見られた。 AtSEC23A および AtSEC23D の両方が、COPII タンパク質の特徴的な細胞内局在パターンを示し、これらが COPII 成分として機能していることが示された。以上のことから、本研究ではタペート細胞において、花粉壁形成に必要な脂質およびタンパク質の ER 排出が AtSEC23A および AtSEC23D によって調節され、その結果花粉壁の発達およびエキシンのパターンが構成されていることが示された。さらに、本章で得られた結果は、植物における SEC23 相同遺伝子の機能的特異性を明らかにした。

花粉の発生やエキシンの形成をはじめとした様々な生物学的プロセスをよりよく理解するために、2 つの遺伝子を同時に導入するための新しいシステムの開発が望まれた。第 3 章に記載されている 2 つの SEC23 タンパク質の発現パターンおよび共局在を詳細に観察するためには、2 つの発現カセットの同時クローニングを可能にするベクターシステムの利用が必要であった。これらの理由から、2 つの発現カセットを同時に簡単にクローニングできるベクターシステムを二種類開発し、それらについて第 4 章および第 5 章で述べた。第 4 章では、2 つの任意のプロモーターおよびオープンリーディングフレームを組み合わせて同時にクローニングすることが可能な R4 dual-site Gateway cloning system について記した。第 5 章は、中程度の発現を示すノパリン合成酵素プロモーターの下流に 2 つの遺伝子を同時クローニングすることができる dual-site Gateway cloning system について記した。